Title	Theory and optimisation of metamorphic photonic devices
Authors	Bogusevschi, Silviu
Publication date	2018
Original Citation	Bogusevschi, S. 2018. Theory and optimisation of metamorphic photonic devices. PhD Thesis, University College Cork.
Type of publication	Doctoral thesis
Rights	© 2018, Silviu Bogusevschi. - http://creativecommons.org/licenses/by-nc-nd/3.0/
Download date	2025-07-05 07:50:33
Item downloaded from	https://hdl.handle.net/10468/7368

University College Cork, Ireland
Coláiste na hOllscoile Corcaigh

Theory and optimisation of metamorphic photonic devices

Silviu Bogușevschi

Thesis submitted in partial fulfilment of the requirements
of the degree of Doctor of Philosophy

at the
Department of Physics,
University College Cork,
National University of Ireland

Supervisor: Prof. Eoin P. O'Reilly
Head of Department: Prof. John G. McInerney

December 2018

Contents

Declaration of Authorship v

Dedication vi

Acknowledgements vii

Abstract viii

List of Publications ix

1 Introduction and overview 1
- 1.1 Background and motivation 1
  - 1.1.1 1.3 μm metamorphic quantum well lasers 3
  - 1.1.2 610 nm metamorphic light-emitting diodes 5
- 1.2 Structure of the thesis 6

2 Theory of electronic and optical properties of zinc blende heterostructures 11
- 2.1 Introduction to electronic structure of zinc blende semiconductors 11
- 2.2 $\mathbf{k}\cdot\mathbf{p}$ theory for electronic structure of zinc blende semiconductors 13
  - 2.2.1 First and second order perturbation theory 13
  - 2.2.2 8-band $\mathbf{k}\cdot\mathbf{p}$ Hamiltonian 17
- 2.3 The effects of strain on the electronic structure of zinc blende semiconductors 22
- 2.4 Theory of optical properties of semiconductor heterostructures 30
  - 2.4.1 Material and modal gain 30
  - 2.4.2 Spontaneous emission 37
- 2.5 Conclusions 39

3 Plane wave expansion method for electronic structure and optical properties calculations 41
- 3.1 Derivation of the method for quantum well based heterostructures 43
  - 3.1.1 1-band model 43
  - 3.1.2 8-band model 46
  - 3.1.3 Derivation of the method for multi-QW based heterostructures 49
- 3.2 Derivation of the method for quantum wire and dot based heterostructures 51
  - 3.2.1 $\mathbf{k}\cdot\mathbf{p}$ Hamiltonian 51
  - 3.2.2 Fourier transform of the strain tensor 54
  - 3.2.3 Pikus-Bir Hamiltonian 59

3.3 Carrier-induced self-consistent electrostatic potential 61
3.4 Momentum matrix elements 65
3.5 Conclusions 67

4 AlInGaAs 1.3 μm metamorphic quantum well lasers 69
4.1 Laser parameters and device modeling 70
4.2 Variable strain and well width 74
4.3 Variable barrier composition 84
4.4 Variable metamorphic buffer layer composition 86
4.5 Conclusions 89

5 AlGaInP 610 nm quantum wire based emitters on GaAs 91
5.1 Nanostructure formation 92
5.2 Strain distribution in a [110] QWR based supercell 93
5.3 Optical properties and photoluminescence measurements 97
5.4 Electroluminescence measurements under hydrostatic pressure 104
5.5 Conclusions 108

6 AlGaInP 610 nm metamorphic quantum well based light-emitting diodes 111
6.1 Band structure engineering 112
6.2 Electronic confinement 116
6.3 Spontaneous emission and photoluminescence measurements 118
6.4 Conclusions 120

7 Summary, conclusions, and future work 123
7.1 Summary and conclusions 123
7.2 Future work 127

A Material parameters for k·p calculations 129
A.1 Review of the material parameters for III-P compounds 131

B Second order perturbation theory 135

C Fermi's golden rule 139

D Useful characteristic functions for various quantum wire and quantum dot shapes 143

Bibliography 147

Declaration

This is to certify that the work I am submitting is my own and has not been submitted for another degree, either at University College Cork or elsewhere. All external references and sources are clearly acknowledged and identified within the contents. I have read and understood the regulations of University College Cork concerning plagiarism.

Signed: Silviu Boguszewschi

To my family

Acknowledgements

I would like to thank my colleagues in office A.3.1.50 and in Photonics Theory Group at Tyndall National Institute, starting with the people that very kindly welcomed me joining the group, and including all the members of the group that I had conversations with throughout my project.

I thank my collaborators who I worked closely with on the investigation of semiconductor lasers and light-emitting diodes presented in Chapters 4, 5 and 6 in this thesis. I thank Dr. Christopher A. Broderick, whose experience helped me gain significant understanding of theoretical simulation of semiconductor lasers and who strongly motivated me to improve my programming skills during the project. I also thank Dr. Emanuele Pelucchi and the Epitaxy and Physics of Nanostructures Group at Tyndall National Institute, and Prof. Stephen Sweeney from Advanced Technology Institute and Department of Physics at University of Surrey, UK, whose experimental input strongly improved my understanding of issues related with shorter wavelength red light-emitting diodes.

I thank the Irish Photonics Integration Centre (IPIC) and Science Foundation Ireland (SFI) for providing the funding that supported my research (Project no. 12/RC/2276).

I thank the members of my thesis committee, Dr. Emanuele Pelucchi and Mr. Brian Corbett for their time to review my progress of the research project and for their valuable feedback. I also thank my thesis examiners, Prof. Frank Peters from Tyndall National Institute and Prof. Stanko Tomić from University of Salford, for their time to review this thesis.

I thank my mother, Olga, for supporting my passion and interest in pursuing a degree in Physics, my father, Valeriu, for always reminding me to believe in my abilities, and my elder sister, Diana, who made me feel in Ireland like home. I also thank my wife, Ekaterina, for her priceless encouragement and motivation for me to be a better person and husband.

Finally, I would like to thank my supervisor Prof. Eoin P. O'Reilly not only for offering me this incredible research opportunity, but also for his highly valuable wisdom and guidance that helped me throughout the PhD project to perform the research presented in this thesis.

Abstract

Metamorphic growth of semiconductor materials – in which a “virtual” substrate with a desired lattice constant is obtained by growing a lattice-mismatched metamorphic buffer layer (MBL) on a conventional substrate such as InP or GaAs – is beginning to attract increasing interest due to its potential to facilitate the development of improved optoelectronic technologies. For example, by growing a relaxed $In_xGa_{1-x}As$ MBL on a GaAs substrate heterostructures can then be grown with a lattice constant intermediate between that of GaAs and InP, thereby providing enhanced scope for band structure engineering and semiconductor device design and optimization starting from a GaAs substrate. However, despite significant progress in material growth and device engineering, there has been very little theoretical analysis of metamorphic devices.

We are particularly interested in the development of metamorphic AlInGaAs-based lasers operating at the technologically important 1.3 μm wavelength, as well as efficient AlInGaP-based 610 nm Light-Emitting Diodes (LEDs) for maximised white light efficiency. In this thesis we investigate the electronic and optical properties of these emitters and compare their performance with existing photonic devices. Using the continuum based multiband $\mathbf{k}\cdot\mathbf{p}$ model within the planewave expansion method we quantify the potential of lattice mismatched MBLs and identify the trends in device performance.

We show that by employing an InGaAs MBL we can extend the ranges of strain and composition accessible for a direct band gap AlInGaAs or AlInGaP alloy, which allow the suppression of the amount of defects and CuPt atomic ordering created during the epitaxial growth. Using the model solid theory we demonstrate that the electron confinement strongly benefits from the use of an InGaAs MBL, bringing a reduced current leakage from the active region. After performing a detailed analysis over a series of metamorphic lasers and LEDs, which include such nanostructures in the active region as quantum wells, dots and wires, we identify the trends in electronic and optical properties which compare very favourably with existing devices, and we provide guidelines for the design of optimised devices.

Using the experimental data available in the literature for metamorphic lasers we are able to estimate the defect-related current losses in such devices, and find that there remains opportunity to further improve laser performance. In addition, the micro-photoluminescence measurements performed on a prototype 610 nm metamorphic LED confirm our prediction of enhanced internal quantum efficiency compared to GaAs-based structures, suggesting that this novel type of LEDs is an excellent candidate for efficient white light emission.

Publications

The following is a list of published work in which aspects of the research presented in this thesis have featured.

1. Refereed journal articles

- "Theory and optimization of 1.3–μm metamorphic quantum well lasers", Silviu Bogusevschi, Christopher A. Broderick, and Eoin P. O'Reilly, *IEEE Journal of Quantum Electronics* **52**, no. 3, pp. 1-11, (2016).
- "Three-dimensional Self-assembled Columnar Arrays of AlInP Quantum Wires for Polarized Amber Micron-sized Light Emitting Diodes", Andrea Pescaglini, Agnieszka Gocalinska, Silviu Bogusevschi, Stefano Moroni, Gediminas Juska, Enrica Mura, John Justice, Brian Corbett, Eoin O'Reilly, and Emanuele Pelucchi, *ACS Photonics*, published January 2018
- "Efficiency enhancements in 610 nm AlGaInP-based light-emitting diodes using metamorphic substrates", Silviu Bogusevschi, Andrea Pescaglini, Agnieszka Gocalinska, Enrica Mura, Gediminas Juska, Stefano Moroni, Emanuele Pelucchi, and Eoin P. O'Reilly, *to be submitted*, 2018

2. Conference proceedings

- "Theory and optimisation of 1.3 and 1.55 μm (Al)InGaAs metamorphic quantum well lasers" Christopher A. Broderick, Silviu Bogusevschi, and Eoin P. O'Reilly, in *Proceedings of the 16th International Conference on Numerical Simulations of Optoelectronic Devices* (NUSOD), Sydney, NSW, Australia (2016)
- "AlGaInP quantum well based 610 nm metamorphic LEDs as efficient red light emitters", Silviu Bogusevschi, Andrea Pescaglini, Emanuele Pelucchi, and Eoin P. O'Reilly, in *Proceedings of the 17th International Conference on Numerical Simulations of Optoelectronic Devices* (NUSOD), Copenhagen, Denmark (2017).

3. Conference talks

During the course of my doctoral research I have personally presented the following conference talk:

- “Theory and optimization of 1.3–μm metamorphic quantum well lasers”, Silviu Bogusevschi, Christopher A. Broderick, and Eoin P. O’Reilly, *29th Semiconductor and Integrated Optoelectronics Conference (SIOE)*, Cardiff, Wales (2015).

In addition to these talks I have also contributed to, and have had aspects of my work presented in, the following conference talk, which was presented by my colleague and collaborator:

- “Theory and optimisation of 1.3 and 1.55 μm (Al)InGaAs metamorphic quantum well lasers”, Christopher A. Broderick, Silviu Bogusevschi, and Eoin P. O’Reilly, *16th International Workshop on Numerical Simulations of Optoelectronic Devices*, Sydney, NSW, Australia (2016).

4. Conference posters

During the course of my doctoral research I have personally presented the following conference posters:

- “AlGaInP-based Quantum Dot LEDs as efficient red light sources”, Silviu Bogusevschi and Eoin P. O’Reilly, *Photonics Ireland*, Cork, Ireland (2015).
- “AlGaInP-based Quantum Dot LEDs as efficient red light sources”, Silviu Bogusevschi, Andrea Pescaglini, Emanuele Pelucchi, and Eoin P. O’Reilly, *Conference on Theory, Modelling, and Computational Methods for Semiconductors* (TMCS), Cork, Ireland (2017).
- “AlGaInP quantum well based 610 nm metamorphic LEDs as efficient red light emitters”, Silviu Bogusevschi, Andrea Pescaglini, Emanuele Pelucchi, and Eoin P. O’Reilly, *17th International Conference on Numerical Simulations of Optoelectronic Devices* (NUSOD), Copenhagen, Denmark (2017).
- “AlGaInP quantum well based 610 nm metamorphic LEDs as efficient red light emitters”, Silviu Bogusevschi, Andrea Pescaglini, Agnieszka Gocalinska, Enrica Mura, Gediminas Juska, Stefano Moroni, Emanuele Pelucchi, and Eoin P. O’Reilly, *Photonics Ireland*, Galway, Ireland (2017).

In addition to these posters I have also contributed to, and have had aspects of my work presented in, the following conference poster, which was presented by my colleagues and collaborators:

- “Self-assembled 3D arrays of AlInP nanowires for polarized amber microLEDs”, Andrea Pescaglini, Agnieszka Gocalinska, Silviu Bogusevschi, John Justice, Gediminas Juska, Stefano Moroni, Enrica Mura, Brian Corbett, Eoin P. O’Reilly, and Emanuele Pelucchi, *17th European Workshop on Metal-Organic Vapour Phase Epitaxy* (EW-MOVPE), Grenoble, France (2017).

5. Miscellaneous

- “Method to obtain efficient red light emitting diodes by exploiting metamorphic substrates”, Silviu Bogusevschi, Eoin P. O’Reilly, Andrea Pescaglini, and Emanuele Pelucchi (invention disclosure filed October 2016).

Chapter 1

Introduction and overview

In this chapter we begin with Section 1.1, where we present the background and motivation for the research in this thesis. Here we include an overview of the progress made for development of 1.3 μm lasers and 610 nm light-emitting diodes (LEDs) in Sections 1.1.1 and 1.1.2 respectively. Following this we provide an overview of the structure of this thesis in Section 1.2.

1.1 Background and motivation

Semiconductor photonic devices, such as lasers and LEDs, are currently based mostly on a $p - i - n$ design and produced using epitaxial growth on substrates like GaAs and InP [1]. These devices can be grown using III-P, III-As and III-Sb alloys, with the desired emission wavelength achieved by tuning the alloy composition of different epilayers of the separate confinement heterostructure (SCH) [2].

It is well established that the inclusion of a small amount of strain in the active or i (intrinsic) region can improve the emission of such devices [3]. This improvement occurs mainly because the strain can reduce the density of states close to the valence band edge [2, 4]. Consequently, strain engineering of the band structure of zinc blende materials and alloys has been widely used to enhance device characteristics [2, 5, 6]. However, the relatively thick epilayers in a heterostructure (e.g. barrier, cladding) limit the flexibility for band structure engineering using strain.

In order to incorporate strain in an epilayer due to lattice mismatch with respect to the substrate, its thickness has to be under a critical value to be thermodynamically stable; otherwise the excessive elastic energy releases as dislocations [3, 7, 8]. Therefore, during the growth of the semiconductor heterostructure the epilayers should have a lattice constant very close to the substrate for high quality growth [9]. For a very thin layer however, such as a Quantum

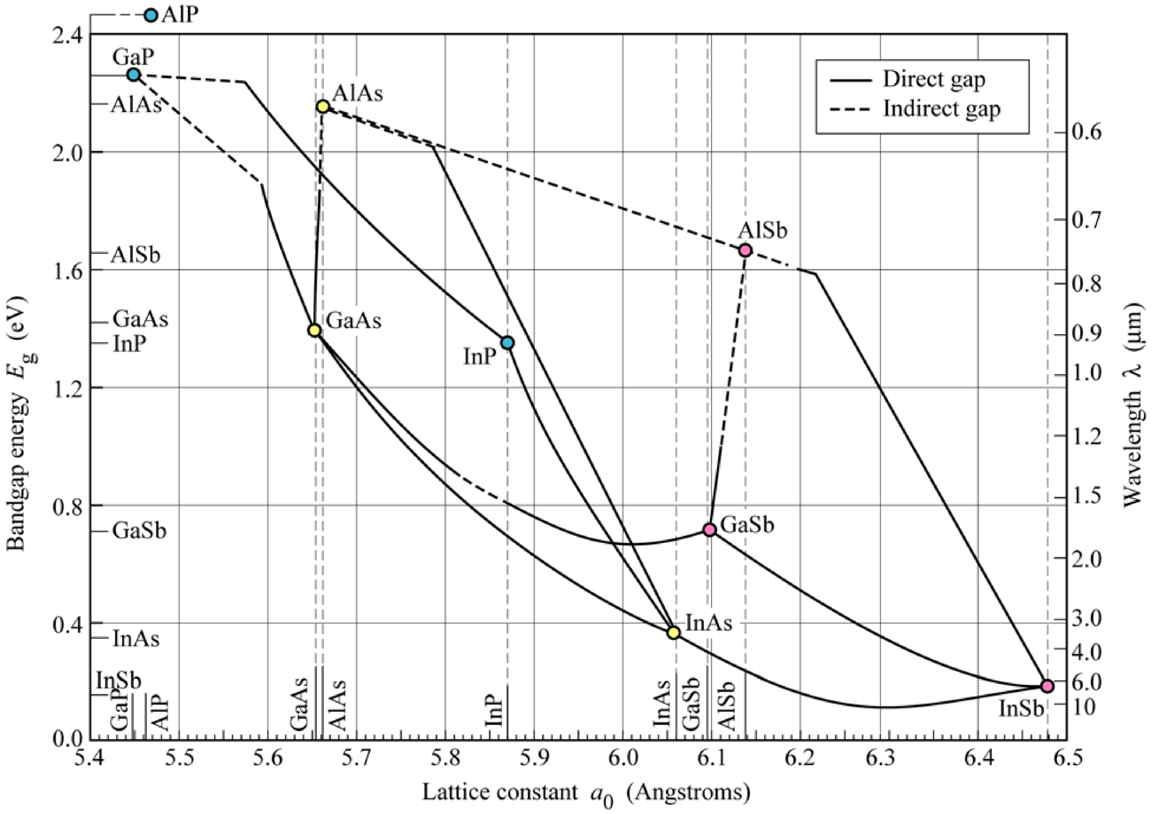

FIGURE 1.1: Variation of the band gap energy of III-V alloys as a function of lattice constant at 300 K (taken from Ref. [12]).

Well (QW) in the active region, it is possible to achieve larger values of strain, typically up to about 2%, to enhance the device characteristics. Strain can also be incorporated into the active region using self-assembled growth, which consists in nucleation of Quantum Wires (QWRs) and Quantum Dots (QDs) on the surface of an epilayer due to the lattice mismatch [10, 11].

Figure 1.1 shows the unstrained band gap energies of various III-V alloys as a function of lattice constant [12]. It can be seen that a range of band gaps can be achieved for a particular alloy when grown on a substrate. For example, InP, which is a conventional substrate for 1.3 μm lasers, allows growth of lattice-matched layers with a direct band gap between 0.7 and 1.5 eV (or between 0.83 μm and 1.78 μm in units of wavelength). Also, in a quaternary alloy, e.g. $\mathrm{Al}_{1-x-y}\mathrm{Ga}_y\mathrm{In}_x\mathrm{As}$, the lattice constant can be varied by adjusting the fraction of In x. This alloy is lattice-matched to InP for $x \approx 52\%$; its band gap can be tuned by adjusting the Al or Ga composition. Although growth of heterostructures based on these alloys on binary substrates has enabled high quality devices with efficient emission, there remains however room for efficiency improvements in many semiconductor photonic devices. Specifically, alloys with larger direct band gaps can be used as barrier layers to reduce current leakage in a device, thereby providing improved gain and threshold characteristics in a laser or more efficient emission in an LED. In order to achieve this, metamorphic growth can be used, where a buffer

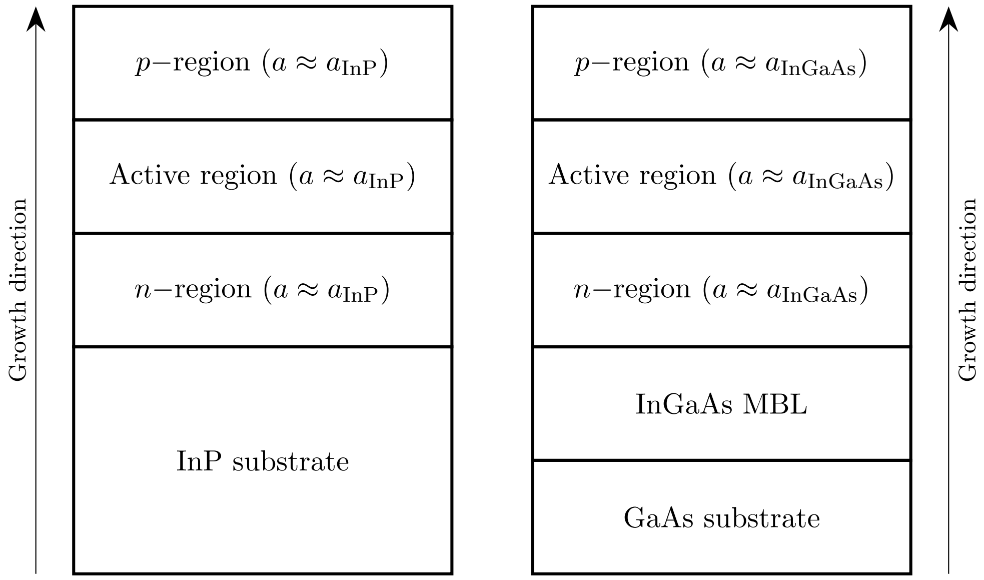
$p-$region $(a \approx a_{\text{InP}})$
Active region $(a \approx a_{\text{InP}})$
$n-$region $(a \approx a_{\text{InP}})$
InP substrate
$p-$region $(a \approx a_{\text{InGaAs}})$
Active region $(a \approx a_{\text{InGaAs}})$
$n-$region $(a \approx a_{\text{InGaAs}})$
InGaAs MBL
GaAs substrate
Growth direction
Growth direction

FIGURE 1.2: Schematic representation of a $p - i - n$ device grown on a conventional InP substrate (left panel) and on a relaxed InGaAs Metamorphic Buffer Layer (MBL, right panel). The arrows on the left and right denote the growth direction. In order to avoid dislocation defects due to strain relaxation, the layers in the structure from the left and right panel are nearly lattice-matched to the InP substrate and the InGaAs MBL respectively.

layer is grown in order to minimise the dislocations near the active region due to a potentially significant lattice mismatch with respect to the main substrate.

In metamorphic growth of semiconductor materials, a "virtual" substrate with a desired lattice constant is obtained by growing a lattice-mismatched metamorphic buffer layer (MBL) on a conventional substrate such as InP or GaAs [13], which is shown on the right panel of Fig. 1.2. This technique is beginning to attract increasing interest due to its potential to facilitate the development of improved optoelectronic technologies [9, 13]. Most commonly the metamorphic technique has been used to investigate GaAs-based semiconductor lasers operating at the technologically important 1.3 μm wavelength [9, 14–17]. For example, by growing a relaxed $\text{In}_x\text{Ga}_{1-x}\text{As}$ MBL on a GaAs substrate, heterostructures can then be grown with a lattice constant intermediate between that of GaAs and InP, thereby providing enhanced scope for band structure engineering and semiconductor laser design and optimisation starting from a GaAs substrate [9].

1.1.1 1.3 μm metamorphic quantum well lasers

The development of long-wavelength semiconductor lasers on GaAs substrates opens up the possibility to take advantage of the enhanced electronic and optical confinement offered by (Al)GaAs-based heterostructures. 1.3 μm QW lasers are typically grown on InP substrates and are based on the InGaAsP or AlInGaAs quaternary alloys [18–27]. While AlInGaAs/InP 1.3 μm lasers demonstrate reduced non-radiative recombination and reduced carrier spillover from the QW, leading to improved temperature stability as compared to their InGaAsP counterparts [28–31], uncooled operation has yet to be realised in practical applications and there remains a drive to improve the high-temperature and high-speed performance of 1.3 μm QW lasers. The enhanced electronic confinement in GaAs-based devices can be expected to reduce carrier spillover at high temperatures, thereby overcoming a limiting factor associated with InP-based technologies [26]. Furthermore, GaAs substrates are attractive due to their greater flexibility – e.g. the possibility to monolithically integrate long-wavelength optoelectronic devices with GaAs-based microelectronics – and are of lower cost than InP substrates, making the development of GaAs-based devices appealing from a commercial perspective.

Significant progress has been made in developing GaAs-based 1.3 μm semiconductor lasers. These efforts have centered mainly on (i) the GaInNAs dilute nitride alloy [32, 33], (ii) vertical cavity surface emitting lasers (VCSELs) incorporating strained InGaAs QWs [34, 35], and (iii) In(Ga)As QDs [36–40]. However, none of these approaches has, as yet, found its way through to widespread application. Lasers based on GaInNAs alloys suffer from strong defect-related recombination [41, 42], while the use of InGaAs QWs to obtain emission at 1.3 μm means the laser must be operated with a large detuning between the cavity mode and the gain peak [43] (in order to avoid the large In composition and associated lattice-mismatch required to produce an InGaAs/GaAs QW with a band gap close to 1.3 μm). Also, despite that individual QD lasers with ultra-low threshold current densities have been demonstrated [44–46], in practice many QDs layers are generally included to provide sufficient optical gain for laser applications [47, 48]. This, combined with the difficulty associated with uniform growth of QD heterostructures and arrays, means that QW-based devices continue to dominate practical applications.

Recently, there has been increasing interest in the development of GaAs-based 1.3 μm metamorphic QW lasers. The first 1.3 μm metamorphic QW laser – grown on GaAs, incorporating a graded $\text{In}_x\text{Ga}_{1-x}\text{As}$ MBL (up to $x = 30\%$) and based on the InGaAsP alloy – was demonstrated in 1994 by Uchida *et al.* [49]. Since then there have been a series of key developments, the first of which was the demonstration of a device based on the AlInGaAs alloy having improved high-temperature performance [50], with subsequent research on 1.3 μm metamorphic lasers focused almost exclusively on AlInGaAs devices.

There are a number of challenges associated with the growth of metamorphic laser structures. These include residual threading dislocations, as well as strain relaxation during the MBL growth that leads to cross-hatched surface morphologies and large roughness, which may impact the planarity of thin strained QWs [14, 51]. Despite these challenges, there has been significant progress in the development of GaAs-based 1.3 μm metamorphic QW lasers. In Ref. [17] Wu *et al.* demonstrated room temperature continuous-wave operation of a 1.3 μm AlInGaAs device having a low threshold current density of 205 A cm^{-2}. Uncooled operation at 10 Gb s^{-1} was demonstrated up to 85°C in 2009 [52], while Arai *et al.* reported a low areal density of threading dislocations, D, in a fully relaxed InGaAs MBL ($D < 4 \times 10^6$ cm^{-2}) [53] in 2009 and demonstrated operation up to 200°C with a high characteristic temperature of 220 K [54] in 2013. A recent review of GaAs-based 1.3 μm metamorphic QW lasers, as well as the associated development of metamorphic growth techniques, can be found in Ref. [9].

Despite significant progress in materials growth and device engineering, there has been very little theoretical analysis of metamorphic QW lasers at 1.3 μm. In Ref. [55] a comparative calculation for a pair of exemplar 1.3 μm InGaAsP devices (based on an InP substrate and on an $\mathrm{In}_{0.26}\mathrm{Ga}_{0.74}\mathrm{As}$ MBL) demonstrated that metamorphic QWs offer enhanced material gain due to their improved electronic confinement. While instructive, no general trends in the characteristics of 1.3 μm metamorphic lasers were identified. To our knowledge there has been no detailed theoretical investigation of metamorphic QW lasers based upon the AlInGaAs material system. As such, and also due to the improved high-temperature performance of InP-based AlInGaAs devices at 1.3 μm over their InGaAsP counterparts [28, 50], we focus our analysis in this research on AlInGaAs alloys.

1.1.2 610 nm metamorphic light-emitting diodes

Light-Emitting Diodes that produce white light for solid state light applications conventionally include a blue LED capped with green and red phosphors in the $\mathrm{R_B G_B B}$ design [56–58]. An alternative phosphor-free RGB design has been recently proposed which enables the maximisation of the white light efficiency by attenuating the non-radiative recombination, scattering and absorption losses, as well as energy losses associated with the Stokes shift [59, 60]. This technology is based on the use of three separate semiconductor emitters, each with narrow emission linewidth and including a red emitter with 614 nm emission wavelength. A blueshifted red light source compared to the conventional 630 – 650 nm commercial emitters is also expected to enhance the spectral eye sensitivity, with an up to 5 times larger luminous efficacy [61], thereby reducing the output power required from the LED devices.

Red semiconductor emitters can be grown using III-N alloys, and III-P based heterostructures on GaAs. Although the III-N alloys are currently deployed mostly for green and blue light sources, the best performing InGaN-based red LED was recently demonstrated with 1.1 mW light output power at 20 mA input current [62]. Because of the large amount of In required in the active region to produce red emission and the wurtzite crystal structure of these materials, the resulting built-in and strain-induced piezoelectric fields strongly suppress the radiative recombination rate [63–66], with the device ultimately having a very small External Quantum Efficiency (EQE). It has been shown that the built-in piezoelectric field can be avoided by growing the III-N based heterostructure on a different crystallographic plane [67]. This, as well as the use of III-N alloys with zinc-blende crystal structure offers a route to improve the device performance [68]. In reality, these approaches are currently very challenging to implement to achieve cost-efficient large-scale device manufacturing. Unlike the III-N materials, the piezoelectric field can be completely avoided in III-P heterostructures, due to the zinc-blende crystal structure of these compounds. AlGaInP-based heterostructures are, therefore, a more attractive alternative for shorter wavelength red emission, enabling a much higher EQE at high power operation [69].

The strong blueshift required for 614 nm emission compared to that in conventional 630 – 650 nm emitters brings a decreased EQE, mainly associated with the increased thermal leakage of electrons from the active region due to the reduced electronic confinement by the barriers [70, 71]. The weak electronic confinement in the active region has been confirmed by photoluminescence measurements performed on a series of devices by collaborations at Tyndall National Institute. The intrinsic limitation for the electronic confinement and the path for current leakage is associated with the direct-to-indirect band gap crossover in III-P alloys which occurs at around 2.3 eV at 300 K. One approach that was used to address this issue includes the incorporation of numerous QWs in the active region [72–75]; however emission in this case requires a large amount of carriers to be injected into the active region.

Metamorphic growth becomes a more attractive alternative due to its ability to extend the range of wavelengths available for semiconductor emitters. For example, by employing an InAsP MBL on InP it became possible to extend the range of wavelengths of InAs-based LEDs towards 2.50 – 2.94 μm [76], offering significant commercial advantages compared to the devices grown on GaSb. An AlGaN-based LED grown on an AlGaN MBL emitting at 310 nm studied by Young *et al.* [77] has demonstrated excellent electrical characteristics, low extended defect densities and promising optical emission for relatively unoptimised growth conditions. However to the best of our knowledge there has been no theoretical or experimental investigation to date of the use of an InGaAs MBL for red LED applications.

1.2 Structure of the thesis

We begin in Chapter 2 by presenting an overview of the theoretical models used to calculate the electronic structure of zinc blende semiconductors and the optical properties of semiconductor photonic devices, such as lasers and light-emitting diodes (LEDs). Here we introduce the well established 8-band $\mathbf{k}\cdot\mathbf{p}$ model [78], including the effects of strain, to calculate the electronic structure of zinc blende semiconductors. We then proceed to the theory of optical properties, where we derive the expression for gain and spontaneous emission spectra, which will complete our theoretical model for device simulation.

In Chapter 3 we present the semi-analytical plane wave expansion method [79], which is the computational technique used in this thesis to implement our theoretical model in a set of codes.

This method allows us to calculate the electronic and optical properties of QW, QWR and QD based heterostructures, by considering periodic boundary conditions. We introduce the method first by applying it to the 1-band model, where we show how the linear Schrödinger equation can be transformed into an eigenvalue problem with the position-dependent effective mass Hamiltonian being described by a square matrix, where matrix elements can be determined analytically using a Fourier transform approach. This matrix is then diagonalised numerically to calculate the eigenstates in the supercell; hence the *semi-analytical* name of the method. Here we introduce the characteristic function of the QW in order to calculate the Fourier expansion of the Hamiltonian matrix elements. In real space, the position-dependent characteristic function equals to unity (zero) inside (outside) the QW, and its Fourier transform is the main parameter required to calculate the electronic structure of a QW (or other nanostructure).

We then apply the method to the 8-band **k·p** Hamiltonian, which we will directly use to calculate the electronic structure of AlInGaAs- and AlGaInP-based heterostructure in Chapters 4, 5 and 6. Here we also briefly mention the application of the method for multiple QW-based supercells, where we show that the Fourier expansion of a single-QW Hamiltonian is a simplified case of a multi-QW expansion, for which a linear combination of multiple characteristic functions can be used.

We then present the implementation of the method to calculate the electronic properties of QD- or QWR-based supercells, which are periodic along all three Cartesian coordinate axes. Here we find the plane wave expansion of the **k·p** Hamiltonian to be similar to the QW case, and we show that the former is a special case of the general three-dimensional expansion. Because the strain distribution in a QWR- or QD-based heterostructure is more complex then in the QW-based case, we present the analytical expression for the Fourier transform of strain tensor elements in a supercell that contains a QD or QWR [80]. We then provide the analytical solution of Poisson's equation, by evaluating the Fourier transform of the carrier-induced electrostatic potential due to the spatial separation of electrons and holes within a supercell. The latter is calculated self-consistently using the Fourier coefficients of the calculated eigenstates directly [81].

The Fourier transform of the strain tensor and carrier-induced electrostatic potential can then be used to (i) estimate their real-space distribution within the supercell, and/or (ii) evaluate the plane wave expansion of the strain Hamiltonian matrix elements and the diagonal matrix elements associated with the electrostatic potential. We then provide analytical expressions to calculate the momentum matrix elements between a conduction and a valence energy state using the calculated Fourier coefficients of the corresponding eigenstates [82].

The 8-band **k·p** model and the plane wave expansion method are then used for the remainder of this thesis, which essentially consists of two parts.

In the first part of the research, presented in Chapter 4, we perform an analysis on threshold and gain characteristics of AlInGaAs-based 1.3 μm metamorphic QW lasers. We begin by identifying the ranges of strain and band gap accessible to pseudomorphically strained AlInGaAs alloys on $\text{In}_x\text{Ga}_{1-x}\text{As}$ MBLs. Having identified the alloy compositions of interest for the design of the laser active region, we then perform a detailed analysis and optimisation of a series of metamorphic QW laser structures. We focus primarily on laser structures containing compressively strained ternary InGaAs QWs with unstrained (Al)InGaAs barriers, grown on relaxed $\text{In}_{0.2}\text{Ga}_{0.8}\text{As}$ MBLs. We identify optimised laser structures by varying the strain and QW width while maintaining the QW band gap at 1.3 μm. This enables us to quantify the electronic and optical properties of GaAs-based 1.3 μm metamorphic QW lasers, as well as to identify general trends in their gain and threshold characteristics as functions of compressive strain, QW width and temperature. Additionally, we investigate the effect of varying the alloy compositions of (i) the $\text{In}_x\text{Ga}_{1-x}\text{As}$ MBL, and (ii) the AlInGaAs barrier layers, with the choice of barrier composition being critical for optimisation of both the carrier and optical confinement in the device.

We elucidate several general trends in GaAs-based 1.3 μm AlInGaAs metamorphic QW lasers. Firstly, we demonstrate through consideration of the strained AlInGaAs band structure that there is scope for the growth of compressively strained ternary (InGaAs) or quaternary (AlInGaAs) QWs, having either unstrained or tensile strained ternary or quaternary barriers. Secondly, our calculations show that the Al composition in quaternary AlInGaAs barrier layers can be varied over a much wider range than in equivalent InP-based devices, so that improved electronic confinement can be obtained. Thirdly, the ability to vary the Al composition over a wide range in AlInGaAs alloys which are lattice matched to the $\text{In}_x\text{Ga}_{1-x}\text{As}$ MBL means that an AlInGaAs separate-confinement heterostructure (SCH) can be engineered to enhance the optical confinement and hence reduce the material gain at threshold. Finally, our analysis of the threshold characteristics of a series of multi-QW devices shows that a low number of QWs (typically 1 and at most 2 – 3) is required to produce an optimised device; this is significantly less than the number of QWs (typically 4 – 6) required in an optimised InP-based 1.3 μm device [83]. Overall, our analysis quantifies the potential of the AlInGaAs material system for the development of GaAs-based 1.3 μm metamorphic QW lasers, and identifies routes towards realising optimised devices.

For the second part of this thesis, in Chapters 5 and 6, we perform an analysis on AlGaInP QWR- and QW-based LEDs for efficient 610 nm emission.

We first begin with Chapter 5, where we investigate the electronic and optical properties of [110]-oriented self-assembled AlGaInP QWR-based heterostructures for 610 nm emission. Here our calculations are based on geometry parameters extracted from Transmission Electron Microscopy (TEM) scans performed on devices grown at Tyndall National Institute, as well as using the nominal growth conditions. Having identified the main parameters for our model, we perform an analysis on the strain distribution in QWR-based supercells.

We then perform an analysis of the electronic and optical properties of QWR-based supercells. Here we examine the impact of the barrier thickness L_z on the radiative recombination in these heterostructures. Our calculations show that enhanced optical properties can be achieved by separating the QWR layers with a thinner barrier. This is a result of an improved electronic confinement, which then leads to (i) a smaller fraction of electrons occupying the barrier X states, and (ii) an improved ground electron-hole wavefunction overlap.

From the integrated photoluminescence (PL) measurements we find that thermal leakage of electrons from the QWR into the barrier is the primary cause of the large decrease in efficiency of shorter wavelength emitters. Our calculations also show that the QWRs, due to being elongated along the [110] direction, can be used to create emitters with a strong degree of linear polarisation. We calculated the radiative emission to be polarised nearly 100% along the QWR axis when the QWRs are surrounded by thin barrier layers ($L_z \approx 3$ nm), in good agreement with experimental measurements. This then makes such heterostructures attractive for display applications where, at present, filters are typically employed to achieve polarised emission.

Finally, we overview and analyse the results of electroluminescence measurements of QWR-based LED devices under hydrostatic pressure performed at University of Surrey, UK. These measurements confirmed the direct band gap nature of the radiative recombination. Based on the measurements, we conclude that $\Gamma - \text{X}$ leakage is indeed the dominant loss mechanism in the active region at room temperature.

Overall, these results confirm the significant thermal leakage of electrons from the active region due to a shallow electron confinement. These results serve as a precursor to Chapter 6 , where we investigate the possibility of improving the electron confinement for improved efficiency of 610 nm devices, by employing lattice-mismatched InGaAs MBLs.

In Chapter 6 we perform theoretical investigation of the electronic and optical properties of Al(Ga)InP QW-based LEDs for 610 nm emission grown on InGaAs MBLs, focusing on optimisation of device performance for 610 nm emission. Here we start by identifying the range of compositions accessible for direct band gap Al(Ga)InP on InGaAs MBLs, showing that growth on an MBL should enable the shift of the $\Gamma - \text{X}$ crossover towards larger band gap energies and also to increase the conduction band offset for an improved electron confinement. We then turn our attention to the electronic and optical properties, where we focus primarily on compressively strained AlInP QW structures surrounded by Al(Ga)InP barriers which are lattice-matched to the InGaAs MBL. We predict that the increased barrier band gap allows reduced leakage current at a fixed emission wavelength, and discuss how band offset changes with MBL composition may also be beneficial for LED operation. We also show that it should be possible to grow direct band-gap shorter wavelength LEDs on InGaAs MBLs with a reduced tendency to CuPt atomic ordering [84, 85], thereby providing higher quality growth of semiconductor emitters. Finally, we provide an experimental comparison between the micro-photoluminescence measurements peformed on comparable devices grown on GaAs and on an InGaAs MBL, which highlights the improvements achieved in PL emission at identical wavelengths.

Finally, we conclude and summarise our analysis in Chapter 7, where we also discuss some directions for further research.

Chapter 2

Theory of electronic and optical properties of zinc blende heterostructures

In this chapter we outline the theoretical methods we use to calculate the electronic and optical properties of zinc blende semiconductors and heterostructures. We start in Section 2.1 with an introduction of methods to calculate the electronic structure of a semiconductor, where we also provide the motivation for the method used in this thesis. We start with the first order perturbation theory for a free electron and second order perturbation theory for multiple electron states (bands) for a periodic unstrained crystal in Section 2.2. We later turn our attention to the application of a small strain to a zincblende semiconductor and analyse its effect on the electronic structure in Section 2.3. As we will show, the key input parameters for electronic structure calculations, including strain, can be derived from experimental measurements, reflecting the semi-empirical nature of the $\mathbf{k} \cdot \mathbf{p}$ method.

Then, in Section 2.4 we derive explicit expressions for absorption, gain and spontaneous emission as the main optical properties we are interested in in our calculations. Lastly, we conclude in Section 2.5.

2.1 Introduction to electronic structure of zinc blende semiconductors

Generally speaking, the electron-electron interaction has to be taken into account to calculate the band structure of a zinc blende semiconductor, leading to a many-body problem. This can be calculated using first principle methods such as Density-Functional Theory (DFT) [87].

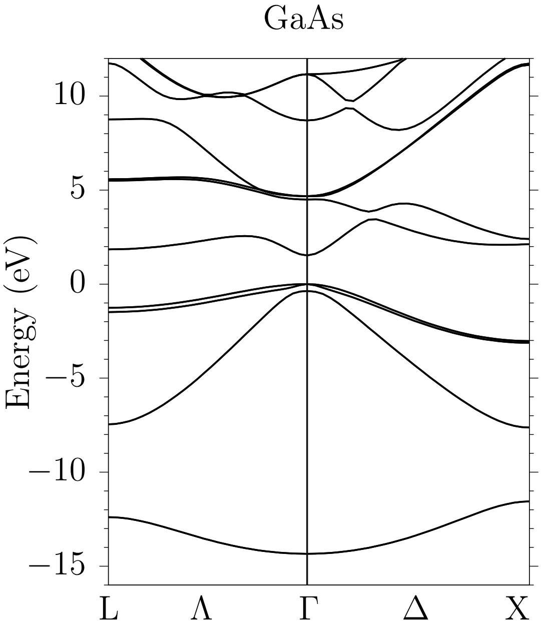

FIGURE 2.1: Calculated band structure of GaAs using hybrid functionals using the Density-Functional Theory (DFT) package VASP [86]. L, Γ and X denote the high symmetry points of the Brillouin zone, and the 0 eV energy corresponds to the valence band maximum.

Fig. 2.1 shows the calculated band structure of GaAs using the DFT package VASP (Vienna Ab-initio Simulation Package) [86]. Although first principle methods provide an accurate description of the band strucutre, the calculations can only be performed on very small supercells (typically up to 1000 atoms) since significant computational resources are required. For this reason, these methods are mostly used to investigate the band structure of a semiconductor compound.

The band gap of a semiconductor, which is the energy difference between the minimum of the conduction band (CB) and the maximum of the valence band (VB), is essentially the most important parameter extracted from both first principle calculations and experimental measurements. Depending on the compound, the minimum of the valence band can be located at (or near[1]) the L, Γ or X point of the Brillouin zone, while the maximum of the valence band (VB) is always located at the zone-centre of the Brillouin zone [88]. When the CB and VB extrema in a semiconductor are located at the same wave vector **k**, i.e. at Γ, it has a *direct* band gap, and *indirect* otherwise. This fact is particularly important for the design of photonic devices, where direct band gap semiconductors are preferred due to a much shorter recombination lifetime compared to indirect compounds and alloys. This is mainly associated with the fact that (i) the electrons at the Γ point have the lowest effective mass, and (ii) a phonon emission or absorption is required in order to transfer the electrons between different wave vectors **k**. Our goal therefore in this thesis is to design semiconductor lasers and light-emitting diodes with improved efficiency and based on direct band gap materials only.

---

[1] The conduction band minimum can also be located near a high symmetry point of the Brillouin zone, e.g. near X in Si or GaP.

For the purpose of optical properties calculations, instead of relying on the full band structure as shown in Fig. 2.1, the analysis can be restricted to a narrow set of bands close to the energy gap, and within a narrow range of wave vectors **k**, which are chosen to describe the energy states close to the conduction and valence band edges. In this case, perturbation theory [89] can be applied to give a sufficient description of the electronic structure. The 8-band **k·p** method is most commonly employed for such calculations [78], which enables the calculation of the electronic and optical properties of a heterostructure, and we also use it in this thesis. The scope of the method is restricted to one lowest CB and three topmost VBs, while also accounting for the double degeneracy due to spin (hence the *8-band* name of the method) and including the interaction between these bands explicitly[2]. The parameters required to construct the band structure using this method, such as band gap, electron and hole effective mass etc., can be obtained directly from experimental measurements. This method is presented in more detail starting with the next section, where we present the detailed derivation of the 8-band Hamiltonian, including the effects of strain, to calculate the electronic structure of III-As and III-P based heterostructures later in the thesis.

2.2 k·p theory for electronic structure of zinc blende semiconductors

In this section we present the first order perturbation theory for a free electron in a periodic crystal, following with the second order correction to account for the interaction between bands. Having derived the general form of the perturbation Hamiltonian we present the explicit form of the 8-band **k·p** Hamiltonian for the calculation of electronic structure of an unstrained semiconductor.

2.2.1 First and second order perturbation theory

For the derivation of the first-order perturbation theory we follow the method used by O'Reilly [88]. Here we start with the time-independent Schrödinger equation for a free electron in a periodic crystal at a particular wave vector **k**

$$\widehat{H}_0 \psi_n(\mathbf{k}, \mathbf{r}) = E_n(\mathbf{k}) \psi_n(\mathbf{k}, \mathbf{r}) \,, \tag{2.1}$$

where $\widehat{H}_0$ is given by

---

[2] The effect of X states on the optical properties of 610 nm LEDs is investigated in Chapters 5 and 6, where we use a 1-band model which does not include the interaction with other conduction or valence bands.

$$\widehat{H}_0 = -\frac{\hbar^2}{2m_0}\nabla^2 + V_0(\mathbf{r})\,. \tag{2.2}$$

For now, we ignore the spin-orbit interaction. Here $V_0(\mathbf{r})$ is the periodic potential of the unstrained crystal and its periodicity is described by $V_0(\mathbf{r}) = V_0(\mathbf{r} + \mathbf{R})$, where, for crystals with cubic symmetry, $\mathbf{R} = \sum_{i=x,y,z} c_i\mathbf{a}$ with $\mathbf{a}$ being the side length of the cubic unit cell (or the lattice constant) and $c_i \in \mathbb{Z}$. According to Bloch's theorem the electron wavefunction $\psi_{n\mathbf{k}}(\mathbf{r})$ can be expressed using a periodic function in the crystal $u_{n\mathbf{k}}(\mathbf{r})$ as [90]

$$\psi_n(\mathbf{k},\mathbf{r}) = e^{i\mathbf{k}\cdot\mathbf{r}}u_{n\mathbf{k}_0}(\mathbf{r})\,. \tag{2.3}$$

Here we assume that the periodic function $u_{n\mathbf{k}_0}$ does not vary with the wave vector $\mathbf{k}$ and corresponds to a reference value $\mathbf{k}_0$. By including Eq. (2.3) into the Schrödinger equation (2.1) we obtain

$$\widehat{H}_0\left[e^{i\mathbf{k}\cdot\mathbf{r}}u_{n\mathbf{k}_0}(\mathbf{r})\right] = E_n(\mathbf{k})e^{i\mathbf{k}\cdot\mathbf{r}}u_{n\mathbf{k}_0}(\mathbf{r})\,, \tag{2.4}$$

which, by considering the reference wave vector $\mathbf{k}_0$ and performing the substitution $\mathbf{k} \rightarrow \mathbf{k}-\mathbf{k}_0$, can be rewritten as

$$\left[-\frac{\hbar^2}{2m_0}\nabla^2 + V_0(\mathbf{r})\right]\left[e^{i(\mathbf{k}-\mathbf{k}_0)\cdot\mathbf{r}}u_{n\mathbf{k}_0}(\mathbf{r})\right] = E_n(\mathbf{k}-\mathbf{k}_0)e^{i(\mathbf{k}-\mathbf{k}_0)\cdot\mathbf{r}}u_{n\mathbf{k}_0}(\mathbf{r})\,. \tag{2.5}$$

Here we apply the Laplacian and recall the momentum operator $\mathbf{p} = -i\hbar\nabla$ to find the following $\mathbf{k}$-dependent Schrödinger equation for the periodic function $u_{n\mathbf{k}_0}$:

$$\left(\widehat{H}_0 + \widehat{H}'\right)u_{n\mathbf{k}_0} = E_n(\mathbf{k}-\mathbf{k}_0)u_{n\mathbf{k}_0}\,, \tag{2.6}$$

where

$$\widehat{H}' = \frac{\hbar^2}{2m_0}|\mathbf{k}-\mathbf{k}_0|^2 + \frac{\hbar}{m_0}(\mathbf{k}-\mathbf{k}_0)\cdot\mathbf{p}\,. \tag{2.7}$$

The goal of the $\mathbf{k}\cdot\mathbf{p}$ method is to solve Eq. (2.6) which includes the $\mathbf{k}$-dependent perturbation Hamiltonian $\widehat{H}'$ (referred to as $\mathbf{k}\cdot\mathbf{p}$ Hamiltonian hereafter). We can see that the general Schrödinger equation (2.1) is a reduced form of the perturbed equation (2.6) when $\mathbf{k} = \mathbf{k}_0$. Given a known value of $E_n(\mathbf{k}_0)$ and assuming a known periodic function in the crystal $u_{n\mathbf{k}_0}$ at the reference wave vector $\mathbf{k}_0$, we can then evaluate its dispersion in $\mathbf{k}$ at the vicinity of the reference wave vector $\mathbf{k}_0$. The energy dispersion $E_n(\mathbf{k}-\mathbf{k}_0)$ at $\mathbf{k}$ near the reference wave vector $\mathbf{k}_0$ can be written as:

$$\begin{aligned} E_n(\mathbf{k}-\mathbf{k}_0) &= \langle u_{n\mathbf{k}_0}|\widehat{H}_0+\widehat{H}'|u_{n\mathbf{k}_0}\rangle \\ &= E_n(\mathbf{k}_0)+\frac{\hbar^2|\mathbf{k}-\mathbf{k}_0|^2}{2m_0}\langle u_{n\mathbf{k}_0}|u_{n\mathbf{k}_0}\rangle+\frac{\hbar(\mathbf{k}-\mathbf{k}_0)}{m_0}\langle u_{n\mathbf{k}_0}|\mathbf{p}|u_{n\mathbf{k}_0}\rangle\,. \end{aligned} \tag{2.8}$$

Here and throughout the entire thesis we use Dirac's notation, i.e.

$$\langle u_m|u_n\rangle = \int_{\Omega_{\mathrm{uc}}} u_m^*(\mathbf{r})u_n(\mathbf{r})\mathrm{d}V = \delta_{mn}\,, \tag{2.9}$$

where the integration is performed over the volume of the periodic unit Ω_{uc} (in this case, the cubic unit cell). We note here that Eq. (2.9) equals to Kronecker delta δ_{mn} due to the orthonormality of the periodic functions $u_{n\mathbf{k}_0}$. The term linear in $\mathbf{k}$ in Eq. (2.8) includes the so-called momentum matrix element $\langle u_{n\mathbf{k}_0}|\mathbf{p}|u_{n\mathbf{k}_0}\rangle$ given by:

$$\langle u_{m\mathbf{k}_0}|\mathbf{p}|u_{n\mathbf{k}_0}\rangle = \mathbf{p}_{mn} = -i\hbar\int_{\Omega_{\mathrm{uc}}} u_{m\mathbf{k}_0}^*(\mathbf{r})\nabla u_{n\mathbf{k}_0}(\mathbf{r})\mathrm{d}V\,, \tag{2.10}$$

which vanishes in Eq. (2.8) due to the parity of the periodic functions $u_{n\mathbf{k}_0}$. Therefore the energy dispersion $E_n(\mathbf{k}-\mathbf{k}_0)$ can be written as a first order perturbation as:

$$E_n(\mathbf{k}-\mathbf{k}_0) = E_n(\mathbf{k}_0)+\frac{\hbar^2(\mathbf{k}-\mathbf{k}_0)^2}{2m_0} \tag{2.11}$$

As we mentioned, the first order perturbation theory can only be applied to a free electron in a periodic lattice that occupies a state in a conduction or valence band. For a more accurate representation of the actual band structure in a semiconductor using the $\mathbf{k}\cdot\mathbf{p}$ method the interaction between the bands has to be taken into account. Because of the large number of bands in the full band structure of a semiconductor, as shown in Fig. 2.1, it is useful to restrict the analysis of the electronic properties within the $\mathbf{k}\cdot\mathbf{p}$ method to the bands located close to the band gap. At the same time, the perturbative nature of the method gives an accurate quantitative description of the band structure within a narrow range of wave vector $\mathbf{k}$, although there are multiband $\mathbf{k}\cdot\mathbf{p}$ methods available in the literature that attempt to reproduce the entire band structure of a semiconductor [91–95].

It is therefore required to introduce a correction to the energy dispersion from Eq. (2.11) to account for the interaction between bands. Using Löwdin's renormalisation [2, 96], the main bands of interested are denoted as class A, and the interaction between them will be included explicitly in the Hamiltonian. Although we focus in this thesis on the description of class A states, we ensure that the effect of the remote bands, denoted as class B, on the energy dispersion of the main bands is considered. In the second-order perturbation theory for degenerate bands, the **k**·**p** Hamiltonian of an electron in a semiconductor is given by [2, 88]

$$\widehat{H}_{nm}(\mathbf{k}) = E_n(\mathbf{k}_0)\delta_{nm} + \widehat{H}'_{nm}(\mathbf{k}) + \sum_{l\in A\neq n} \frac{\widehat{H}'_{nl}(\mathbf{k})\widehat{H}'_{lm}(\mathbf{k})}{E_n(\mathbf{k}_0) - E_l(\mathbf{k}_0)} + \sum_{l\in B} \frac{\widehat{H}'_{nl}(\mathbf{k})\widehat{H}'_{lm}(\mathbf{k})}{E_A(\mathbf{k}_0) - E_l(\mathbf{k}_0)} \,. \tag{2.12}$$

where the interaction between the class A states and the effect of class B states are expressed using the first and second sum respectively. The reduced magnitude of the perturbation of the class B states, compared to the interaction between the class A states, in the Hamiltonian (2.12) is indicated by the denominator in the last summation, where we assumed that the class B energy levels lie far away in energy from the class A states E_A. The detailed derivation of the Hamiltonian (2.12) is also provided in Appendix B.

The Hamiltonian matrix (2.12) then allows us to evaluate the dispersion of the energy states at **k** by knowing (i) their energies at the reference wave vector $\mathbf{k}_0$, (ii) the interaction between the class A and B states through the perturbation Hamiltonian $\widehat{H}'$, and (iii) the periodic crystal function $u_{n\mathbf{k}_0}$ (referred to as *basis functions* hereafter). The second order perturbation theory is generally used for electronic structure calculations in the vicinity of high symmetry points in the Brillouin zone, e.g. Γ, X or L valley minima, close to the semiconductor energy gap. For the calculation of optical properties, in this thesis we are concerned about the energy dispersion near the Γ point of the Brillouin zone[3] (cf. Fig. 2.1), which corresponds to the reference wave vector $|\mathbf{k}_0| = 0$. As we will show in the following section, one advantage of the **k**·**p** method over, e.g., tight-binding or density functional theory, is that the Hamiltonian can be constructed using measurable parameters like band gap and electron and hole effective mass. In order to construct the **k**·**p** Hamiltonian the class A states in this thesis include one conduction and three valence bands, each being double degenerate to account for spin.

Considering for a moment that there is no interaction between the class A states, so the first sum in Eq. (2.12) vanishes, we end up with the single band model (which we use in this thesis to calculate the dispersion of the X states). In this case, the term linear in **k** vanishes due to symmetry. Therefore, for a particular wave vector $k = |\mathbf{k}|$ we can simplify the form of the energy dispersion [88]

$$E_n(k) = E_n(0) + \frac{\hbar^2 k^2}{2m_0} + \frac{\hbar^2}{m_0^2} \sum_{m\in A\neq n} \frac{|\mathbf{k}\cdot\mathbf{p}_{nm}|^2}{E_n(0) - E_m(0)} + \frac{\hbar^2}{m_0^2} \sum_{m\in B} \frac{|\mathbf{k}\cdot\mathbf{p}_{nm}|^2}{E_n(0) - E_m(0)} \,, \tag{2.13}$$

---

[3] We are also interested in the calculation of the X valley energy states, the impact of which on the electronic and optical properties will be discussed in Chapter 6.

It is also useful to write this equation in the so-called effective mass approximation [97], such as

$$E_n(k) = E_n(0) + \frac{\hbar^2}{2m_0} \sum_{i,j} \frac{k_i k_j}{m^*_{ij}} \tag{2.14}$$

where

$$\frac{1}{m^*_{ij}} = \delta_{ij} + \frac{1}{m_0} \sum_{m \in A \neq n} \frac{p^{(i)}_{nm} p^{(j)}_{mn} + p^{(j)}_{nm} p^{(i)}_{mn}}{E_n(0) - E_m(0)} + \frac{1}{m_0} \sum_{m \in B} \frac{p^{(i)}_{nm} p^{(j)}_{mn} + p^{(j)}_{nm} p^{(i)}_{mn}}{E_A(0) - E_m(0)}\,, \tag{2.15}$$

is the electron effective mass, expressed in units of the mass of free electron. Here we symmetrised the $i, j = x, y, z$ components of the momentum matrix p_{nm}. In case of a 1-band model for the conduction band, i.e. there is no interaction between the conduction and valence bands so the first sum in the Eq. (2.13) vanishes, the CB edge has a spherical dispersion in $\mathbf{k}$, thus the effective mass tensor in Eq. (2.15) is diagonal and can be rewritten as:

$$\frac{1}{m^*_{ii}} = 1 + \frac{2}{m_0} \sum_{m \in B} \frac{p^{(i)}_{nm} p^{(i)}_{mn}}{E_A(0) - E_m(0)} \tag{2.16}$$

2.2.2 8-band k·p Hamiltonian

In order to construct the 8-band **k·p** Hamiltonian which includes the effects of spin-orbit interaction, we need to define the basis functions $u_{n\mathbf{k}_0}$ at the Γ point. We start with one conduction state with an s-like symmetry $|u_{\mathrm{CB}}\rangle = |s\rangle$, and three degenerate valence states with p-like symmetry $|u^{(i)}_{\mathrm{VB}}\rangle = |v\rangle$, with $v = x, y, z$ and $i = 1, 2, 3$, and all states are spin degenerate. When the spin-orbit interaction is taken into account, the total Hamiltonian (2.7) for an unstrained crystal becomes:

$$\widehat{H} = \overbrace{\frac{\mathbf{p}^2}{2m_0} + V_0(\mathbf{r}) + \frac{\hbar}{4m_0^2c^2}\left(\nabla V_0 \times \mathbf{p}\right)\cdot\sigma}^{\widehat{H}_0} + \overbrace{\frac{\hbar^2k^2}{2m_0} + \frac{\hbar}{m_0}\mathbf{k}\cdot\mathbf{p} + \frac{\hbar}{4m_0^2c^2}\left(\nabla V_0 \times \hbar\mathbf{k}\right)\cdot\sigma}^{\widehat{H}'}\,, \tag{2.17}$$

where σ is the tensor containing the Pauli matrices

$$\sigma_x = \begin{pmatrix} 0 & 1 \\ 1 & 0 \end{pmatrix}, \qquad \sigma_y = \begin{pmatrix} 0 & -i \\ i & 0 \end{pmatrix}, \qquad \sigma_z = \begin{pmatrix} 1 & 0 \\ 0 & -1 \end{pmatrix}, \tag{2.18}$$

which, when acting upon the eigenspinors $|\uparrow\rangle$ and $|\downarrow\rangle$ yields:

$$\sigma_x|\uparrow\rangle = |\downarrow\rangle \qquad \sigma_x|\downarrow\rangle = |\uparrow\rangle \tag{2.19}$$

$$\sigma_y|\uparrow\rangle = i|\downarrow\rangle \qquad \sigma_y|\downarrow\rangle = -i|\uparrow\rangle \tag{2.20}$$

$$\sigma_z|\uparrow\rangle = |\uparrow\rangle \qquad \sigma_z|\downarrow\rangle = -|\downarrow\rangle \tag{2.21}$$

We note that generally the spin-orbit coupling term in Eq. (2.17) is linearly dependent on $\mathbf{k}$. However we do not include it in our analysis below since the crystal momentum $\hbar\mathbf{k}$ is much smaller compared to the electron momentum $\mathbf{p}$ in the far interior of the atom where most of the spin-orbit interaction occurs, and its influence has been discussed by Kane [89] where the wave vector dependent spin-orbit interaction was treated as an additional perturbation.

Here we use the set of basis functions

$$|u\rangle = (|s;\uparrow\rangle, |x;\uparrow\rangle, |y;\uparrow\rangle, |z;\uparrow\rangle, |s;\downarrow\rangle, |x;\downarrow\rangle, |y;\downarrow\rangle, |z;\downarrow\rangle) \tag{2.22}$$

to construct the Hamiltonian H_{nm} (2.12) as follows [98]:

$$\widehat{H}_{nm} = \begin{pmatrix} H^{(1)} & 0 \\ 0 & H^{(1)} \end{pmatrix} + \begin{pmatrix} H^{(2)} & 0 \\ 0 & H^{(2)} \end{pmatrix} + \begin{pmatrix} 0 & 0 & 0 & 0 & 0 & 0 & 0 & 0 \\ 0 & 0 & -i & 0 & 0 & 0 & 0 & 1 \\ 0 & i & 0 & 0 & 0 & 0 & 0 & -i \\ 0 & 0 & 0 & 0 & 0 & -1 & i & 0 \\ 0 & 0 & 0 & 0 & 0 & 0 & 0 & 0 \\ 0 & 0 & 0 & -1 & 0 & 0 & i & 0 \\ 0 & 0 & 0 & -i & 0 & -i & 0 & 0 \\ 0 & 1 & i & 0 & 0 & 0 & 0 & 0 \end{pmatrix} \frac{\Delta_{\mathrm{SO}}}{3}, \tag{2.23}$$

where

$$\begin{aligned} \Delta_{\mathrm{SO}} &= \frac{3i\hbar}{4m_0^2c^2}\left\langle x \left| \frac{\partial V}{\partial x}p_y - \frac{\partial V}{\partial y}p_x \right| y \right\rangle \\ &= \frac{3i\hbar}{4m_0^2c^2}\left\langle y \left| \frac{\partial V}{\partial y}p_z - \frac{\partial V}{\partial z}p_y \right| z \right\rangle \\ &= \frac{3i\hbar}{4m_0^2c^2}\left\langle z \left| \frac{\partial V}{\partial z}p_x - \frac{\partial V}{\partial x}p_z \right| x \right\rangle, \end{aligned} \tag{2.24}$$

is the spin-orbit splitting,

$$H^{(1)} = \begin{pmatrix} E_{\mathrm{CB}_0} + \frac{\hbar^2 k^2}{2m_0} & ik_x P & ik_y P & ik_z P \\ -ik_x P & E_{\mathrm{VB}_0} + \frac{\hbar^2 k^2}{2m_0} & 0 & 0 \\ -ik_y P & 0 & E_{\mathrm{VB}_0} + \frac{\hbar^2 k^2}{2m_0} & 0 \\ -ik_z P & 0 & 0 & E_{\mathrm{VB}_0} + \frac{\hbar^2 k^2}{2m_0} \end{pmatrix}, \tag{2.25}$$

and

$$H^{(2)} = \begin{pmatrix} Ak^2 & 0 & 0 & 0 \\ 0 & Lk_x^2 + M(k_y^2 + k_z^2) & Nk_x k_y & Nk_x k_z \\ 0 & Nk_x k_y & Lk_y^2 + M(k_x^2 + k_z^2) & Nk_y k_z \\ 0 & Nk_x k_z & Nk_y k_z & Lk_z^2 + M(k_x^2 + k_y^2) \end{pmatrix}. \tag{2.26}$$

Here the matrices [89] $H^{(1)}$ and $H^{(2)}$ include the first order interaction due to the terms linear in $\mathbf{k}$ and second order interaction between the class A states respectively, and $k^2 = |\mathbf{k}|^2$. The form of the Hamiltonians $H^{(1)}$ and $H^{(2)}$ suggests that the dispersion of the energy bands in $\mathbf{k}$ in [001], [010] and [100] directions will be identical, and the same applies to the [110], [101] and [011] directions. The parameters A, L, M and N are given by [89]:

$$\begin{aligned} A &= \frac{\hbar^2}{2m_0}\left(\frac{1}{m_c^*}\right) + \frac{3P^2}{E_{\mathrm{CB}_0} - E_{\mathrm{VB}_0}}\,, \\ L &= \frac{\hbar^2}{2m_0}\left(1 + \frac{2}{m_0}\sum_{m\in B}\frac{p_{xm}^{(x)}p_{mx}^{(x)}}{E_A(0) - E_m(0)}\right), \\ M &= \frac{\hbar^2}{2m_0}\left(1 + \frac{2}{m_0}\sum_{m\in B}\frac{p_{xm}^{(y)}p_{mx}^{(y)}}{E_A(0) - E_m(0)}\right), \\ N &= \frac{\hbar^2}{m_0^2}\sum_{m\in B}\frac{p_{xm}^{(x)}p_{my}^{(y)} + p_{xm}^{(y)}p_{my}^{(x)}}{E_A(0) - E_m(0)} \end{aligned} \tag{2.27}$$

where m_c^* is the electron effective mass from Eq. (2.16) and P is the Kane matrix element [99] which denotes the coupling between the s- and p-like states:

$$P = -i\frac{\hbar}{m_0}\langle s|\widehat{p}^{(j)}|j\rangle\,, \tag{2.28}$$

with $j = x, y, z$. The parameters L, M and N are closely related to the Luttinger parameters γ^L [100, 101] as follows:

$$\begin{aligned} \gamma_1^L &= -\frac{2m_0}{3\hbar^2}\left(L+2M\right) \\ \gamma_2^L &= -\frac{m_0}{3\hbar^2}\left(L-M\right) \\ \gamma_3^L &= -\frac{m_0}{3\hbar^2}N \end{aligned} \tag{2.29}$$

The Luttinger parameters $\gamma_1^L, \gamma_2^L, \gamma_3^L$ are also closely related to the heavy-, light- and spin-split-off hole effective masses (m_{hh}, m_{lh}, m_{so} respectively) along particular directions of the wave vector $\mathbf{k}$, and the relationship between them can be found in Refs. [102–104]. We note that the subscript x, y and superscript (x, y) next to p in Eq. (2.27) correspond to the x/y functions and the x/y component of the momentum matrix respectively. The eigenvectors of the Hamiltonian (2.23) are expressed as a mixture of s-like or p-like states due to (i) the spin-orbit interaction and (ii) the terms linear and quadratic in $\mathbf{k}$. For the purpose of optical property calculations it is more practical to define the basis functions in terms of conduction, heavy-hole, light-hole and spin-split-off bands (CB, HH, LH and SO respectively), because the mixing (or coupling) between them is a more useful factor that determines the optical performance of photonic devices of interest. We therefore set a new set of orthonormal basis functions which will transform the Hamiltonian (2.23) into a diagonal matrix at $|\mathbf{k}| = 0$, whose eigenvalues will also denote the reference energy position E_0 of the conduction (valence) band minima (maxima). A general practice is to use the basis functions in the angular momentum $|J; m_j\rangle$ notation [105], whose combinations of functions with s- or p-like symmetry are obtained using the unitary transformation matrix S:

$$\begin{pmatrix} |u_{\mathrm{CB}};\uparrow\rangle \\ |u_{\mathrm{HH}};\uparrow\rangle \\ |u_{\mathrm{LH}};\uparrow\rangle \\ |u_{\mathrm{SO}};\uparrow\rangle \\ |u_{\mathrm{CB}};\downarrow\rangle \\ |u_{\mathrm{HH}};\downarrow\rangle \\ |u_{\mathrm{LH}};\downarrow\rangle \\ |u_{\mathrm{SO}};\downarrow\rangle \end{pmatrix} = \begin{pmatrix} \left|\frac{1}{2};\ \frac{1}{2}\right\rangle \\ \left|\frac{3}{2};\ \frac{3}{2}\right\rangle \\ \left|\frac{3}{2};\ \frac{1}{2}\right\rangle \\ \left|\frac{1}{2};\ \frac{1}{2}\right\rangle \\ \left|\frac{1}{2};-\frac{1}{2}\right\rangle \\ \left|\frac{3}{2};-\frac{3}{2}\right\rangle \\ \left|\frac{3}{2};-\frac{1}{2}\right\rangle \\ \left|\frac{1}{2};-\frac{1}{2}\right\rangle \end{pmatrix} = iS \begin{pmatrix} |s;\uparrow\rangle \\ |x;\uparrow\rangle \\ |y;\uparrow\rangle \\ |z;\uparrow\rangle \\ |s;\downarrow\rangle \\ |x;\downarrow\rangle \\ |y;\downarrow\rangle \\ |z;\downarrow\rangle \end{pmatrix}, \tag{2.30}$$

where the i on the right-hand side is simply a phase constant, and S is given by [32]:

$$S = \begin{pmatrix} -i & 0 & 0 & 0 & 0 & 0 & 0 & 0 \\ 0 & \frac{1}{\sqrt{2}} & \frac{i}{\sqrt{2}} & 0 & 0 & 0 & 0 & 0 \\ 0 & 0 & 0 & -\frac{2}{\sqrt{6}} & 0 & \frac{1}{\sqrt{6}} & \frac{i}{\sqrt{6}} & 0 \\ 0 & 0 & 0 & \frac{1}{\sqrt{3}} & 0 & \frac{1}{\sqrt{3}} & \frac{i}{\sqrt{3}} & 0 \\ 0 & 0 & 0 & 0 & i & 0 & 0 & 0 \\ 0 & 0 & 0 & 0 & 0 & -\frac{1}{\sqrt{2}} & \frac{i}{\sqrt{2}} & 0 \\ 0 & \frac{1}{\sqrt{6}} & -\frac{i}{\sqrt{6}} & 0 & 0 & 0 & 0 & \frac{2}{\sqrt{6}} \\ 0 & \frac{1}{\sqrt{3}} & -\frac{i}{\sqrt{3}} & 0 & 0 & 0 & 0 & -\frac{1}{\sqrt{3}} \end{pmatrix}. \tag{2.31}$$

By diagonalising the Hamiltonian matrix at $|\mathbf{k}| = 0$ we find the set of reference energies E_{CB_0}, $E_{\text{HH}_0} = E_{\text{VB}_0} + \frac{\Delta_{\text{SO}}}{3}$, $E_{\text{LH}_0} = E_{\text{VB}_0} + \frac{\Delta_{\text{SO}}}{3}$, $E_{\text{SO}_0} = E_{\text{VB}_0} - 2\frac{\Delta_{\text{SO}}}{3}$ with each energy being double degenerate for spin. The coefficients for the "spin-down" states in the matrix (2.31) are obtained from the "spin-up" states by applying the time reversal operator which, for zinc blende semiconductors, is $\widehat{T} = -i\sigma_y \widehat{C}\widehat{J}$ [32], where $\widehat{C}$ is the complex conjugate operator and $\widehat{J}$ is the inversion operator about midpoint between nearest neighbours, i.e. $\widehat{J} : s \mapsto -s$, $\widehat{J} : p \mapsto p$. We then evaluate the Hamiltonian matrix using the basis functions due the transformation matrix S (2.31) and obtain [32]:

$$H_{\mathbf{k}\cdot\mathbf{p}} = \begin{pmatrix} E_{\text{CB}} & -\sqrt{3}T_+ & \sqrt{2}U & -U & 0 & 0 & -T_- & -\sqrt{2}T_- \\ & E_{\text{HH}} & \sqrt{2}S & -S & 0 & 0 & -R & -\sqrt{2}R \\ & & E_{\text{LH}} & Q & T_+^* & R & 0 & \sqrt{3}S \\ & & & E_{\text{SO}} & \sqrt{2}T_+^* & \sqrt{2}R & -\sqrt{3}S & 0 \\ & & & & E_{\text{CB}} & -\sqrt{3}T_- & \sqrt{2}U & -U \\ & & & & & E_{\text{HH}} & \sqrt{2}S^* & -S^* \\ & & & & & & E_{\text{LH}} & Q \\ & & & & & & & E_{\text{SO}} \end{pmatrix}, \tag{2.32}$$

We ignore here the bottom diagonal terms since the Hamiltonian (2.32) is a Hermitian matrix. The elements of the Hamiltonian are given here by:

$$E_{\text{CB}}(\mathbf{k}) = E_{\text{CB}_0} + \frac{\hbar^2}{2m_0} s_c \left(k_x^2 + k_y^2 + k_z^2\right) \tag{2.33a}$$

$$E_{\text{HH}}(\mathbf{k}) = E_{\text{HH}_0} - \frac{\hbar^2}{2m_0} (\gamma_1 + \gamma_2) \left(k_x^2 + k_y^2\right) - \frac{\hbar^2}{2m_0} (\gamma_1 - 2\gamma_2) k_z^2 \tag{2.33b}$$

$$E_{\text{LH}}(\mathbf{k}) = E_{\text{LH}_0} - \frac{\hbar^2}{2m_0} (\gamma_1 - \gamma_2) \left(k_x^2 + k_y^2\right) - \frac{\hbar^2}{2m_0} (\gamma_1 + 2\gamma_2) k_z^2 \tag{2.33c}$$

$$E_{\text{SO}}(\mathbf{k}) = E_{\text{SO}_0} - \frac{\hbar^2}{2m_0} \gamma_1 \left(k_x^2 + k_y^2 + k_z^2\right) \tag{2.33d}$$

$$T_{\pm}(\mathbf{k}) = \frac{1}{\sqrt{6}} P \left(k_x \pm i k_y\right) \tag{2.33e}$$

$$U(\mathbf{k}) = \frac{1}{\sqrt{3}} P k_z \tag{2.33f}$$

$$S(\mathbf{k}) = \sqrt{\frac{3}{2}} \frac{\hbar^2}{m_0} \gamma_3 k_z \left(k_x - i k_y\right) \tag{2.33g}$$

$$R(\mathbf{k}) = \frac{\sqrt{3}}{2} \frac{\hbar^2}{2m_0} \left[\left(\gamma_2 + \gamma_3\right)\left(k_x - i k_y\right)^2 - \left(\gamma_3 - \gamma_2\right)\left(k_x + i k_y\right)^2\right] \tag{2.33h}$$

$$Q(\mathbf{k}) = -\frac{1}{\sqrt{2}} \frac{\hbar^2}{m_0} \gamma_2 \left(k_x^2 + k_y^2\right) + \sqrt{2} \frac{\hbar^2}{m_0} \gamma_2 k_z^2 \,, \tag{2.33i}$$

The Hamiltonian (2.32) contains the modified expressions for the electron effective mass s_c and the Luttinger parameters γ due to the CB – VB coupling, and are given by:

$$\begin{aligned} s_c &= \frac{1}{m^*} - \frac{E_p}{3}\left(\frac{2}{E_g} + \frac{1}{E_g + \Delta_{\mathrm{SO}}}\right) \\ \gamma_1 &= \gamma_1^L - \frac{E_p}{3E_g} \\ \gamma_{2,3} &= \gamma_{2,3}^L - \frac{E_p}{6E_g} \,, \end{aligned} \tag{2.34}$$

where E_g is the band gap at the Γ point in the Brillouin zone of the unstrained crystal, and $E_p = \frac{2m_0|P|^2}{\hbar^2}$. We note here that the calculated eigenstates of the Hamiltonian (2.32) are slightly anisotropic in the $\mathbf{k}_{\|}$ plane (so-called band warping) and the dispersion depends on the polar angle $\theta = \arctan\frac{k_y}{k_x}$. For the calculation of optical properties in Chapters 4 and 6 we use the axial approximation [106], according to which the term $\gamma_3 - \gamma_2$ in R from Eq. (2.33h) is set as zero. In this case we simplify our calculations, in particular of the optical properties, by calculating the dispersion along one polar angle $\theta = \frac{\pi}{4}$, thereby allowing us to calculate the density of states and other quantities in polar coordinates only using the magnitude of the wave vector $\mathbf{k}$, i.e. $\frac{1}{4\pi^2}\int_{\mathbf{k}_{\|}} \mathrm{d}\mathbf{k}_{\|} \rightarrow \frac{1}{2\pi}\int_{k_{\|}} k_{\|}\mathrm{d}k_{\|}$.

2.3 The effects of strain on the electronic structure of zinc blende semiconductors

In this section we follow the method used by Pikus and Bir [107] to determine the effects of a small strain on the electronic structure of zincblende semiconductors, and we restrict our analysis here to the first order perturbation theory only.

A small homogeneous strain is given by the following strain tensor:

$$\epsilon_{ij} = \frac{1}{2}\left(\frac{\partial u_i}{\partial j} + \frac{\partial u_j}{\partial i}\right) , \tag{2.35}$$

where $\mathbf{u} = \sum_i u_i \mathbf{i}$ is the vector of displacement due to strain and $i, j = x, y, z$. The strain tensor ϵ_{ij} is also related with the stress tensor σ_{kl} using the elastic tensor C_{ijkl} as follows:

$$\sigma_{kl} = \sum_{ij} C_{ijkl}\epsilon_{ij} . \tag{2.36}$$

Taking into account the symmetry of the stress tensor σ_{kl}, the fourth order elastic tensor C_{ijkl} can be simplified to a second order tensor $C_{\alpha\beta}$ using the Voigt notation and making a substitution of indices $ij \to \alpha$, $kl \to \beta$. For crystals with cubic symmetry the elastic tensor $C_{\alpha\beta}$ is then given by:

$$C_{\alpha\beta} = \begin{pmatrix} C_{11} & C_{12} & C_{12} & 0 & 0 & 0 \\ C_{12} & C_{11} & C_{12} & 0 & 0 & 0 \\ C_{12} & C_{12} & C_{11} & 0 & 0 & 0 \\ 0 & 0 & 0 & C_{44} & 0 & 0 \\ 0 & 0 & 0 & 0 & C_{44} & 0 \\ 0 & 0 & 0 & 0 & 0 & C_{44} \end{pmatrix} . \tag{2.37}$$

In order to construct the Hamiltonian $\widehat{H}_\epsilon$ that determines the influence of a crystal lattice deformation on its electronic structure, we have to firstly determine the operator that describes the change in energy dispersion due to a homogeneous strain. The unperturbed Hamiltonian with spin-orbit interaction for a strained crystal is given by:

$$\widehat{H}_\epsilon = \frac{\mathbf{p}^2}{2m_0} + V_\epsilon(\mathbf{r}) + \frac{\hbar}{4m_0^2c^2}\left(\nabla V_\epsilon \times \mathbf{p}\right) \cdot \sigma , \tag{2.38}$$

with the eigenvalues $E_{n\epsilon}(\mathbf{k})$ and eigenvectors $\psi_{n\epsilon}(\mathbf{k}, \mathbf{r})$, V_ϵ is the periodic potential of the deformed cubic unit cell, and the Hamiltonian (2.38) is obtained from the unperturbed Hamiltonian from Eq. (2.17) simply by substituting V_0 with V_ϵ.

A small deformation can be regarded as an additional perturbation, and we can restrict our analysis here to the terms linear in strain, i.e. directly proportional to the components of the strain tensor ϵ_α. The position of a Bravais lattice point is given by

$$\mathbf{a} = \sum_{i=1}^{3} m_i \mathbf{a}_i \tag{2.39}$$

where $\mathbf{a}_i$ are the primitive unit vectors of the Bravais lattice and $m \in \mathbb{Z}$. If we consider, for instance, a fixed Bravais lattice point $\mathbf{a}_0$ at the origin, i.e. $m_1 = m_2 = m_3 = 0$, then the ith component of a Bravais lattice point $\mathbf{a}_0$ with $m_i \neq 0$, which in an unstrained crystal is given by (2.39), changes due to strain as follows:

$$\mathbf{a}^{(i)} = \mathbf{a}_0^{(i)} + (\epsilon \cdot \mathbf{a}_0)_i \ , \tag{2.40}$$

where the dot product $(\epsilon \cdot \mathbf{a}_0)_i$ is given by

$$(\epsilon \cdot \mathbf{a}_0)_i = \sum_{j=1}^{3} \epsilon_{ij} \mathbf{a}_0^{(j)} \ . \tag{2.41}$$

For suffiently large m_i the relative displacement $\Delta \mathbf{a}^{(i)} = \mathbf{a}^{(i)} - \mathbf{a}_0^{(i)} = (\epsilon \cdot \mathbf{a}_0)_i$ can be comparable with the lattice constant, and the difference between the potential of the strained and unstrained crystal $V_\epsilon - V_0$ in this case will of the order of V_0. Therefore the change in the crystal potential cannot be interpreted as a perturbation. At the same time the strain will also affect the periodicity of the unit cell, thus the basis functions $u_{n\mathbf{k}}$ of the unperturbed Hamiltonian from Eq. (2.17) and (2.38) will also be different. In order to address this issue, we perform a transformation of the coordinates such as the vector components of the Bravais lattice points in the strained crystal $\mathbf{a}'_m$ in the new system will coincide with the points in the unstrained lattice using the old coordinate system. In this case

$$\begin{aligned} \mathbf{x}^{(i)} &= \mathbf{x}'^{(i)} + \left(\epsilon \cdot \mathbf{x}'\right)_i \equiv (1 + \epsilon)\mathbf{x}' \\ \mathbf{x}'^{(i)} &= (1 + \epsilon)^{-1}\mathbf{x} \approx (1 - \epsilon)\mathbf{x} \, . \end{aligned} \tag{2.42}$$

From this transformation the momentum operator $\mathbf{p}$ becomes

$$p^{(i)} = (1 - \epsilon)\mathbf{p}' \ , \tag{2.43}$$

where $p'^{(i)} = -i\hbar \frac{\partial}{\partial x'^{(i)}}$,

$$p^2 \approx p'^2 - 2 \sum_{ij} p'^{(i)} \epsilon_{ij} p'_j \equiv p'^2 - 2\left(\mathbf{p}' \epsilon \mathbf{p}'\right) \ , \tag{2.44}$$

and $V_\epsilon(\mathbf{x}) = V_\epsilon \left[(1 + \epsilon)\mathbf{x}'\right]$. Going back to the unstrained coordinate system $\mathbf{x}$ we find that $V_\epsilon \left[(1 + \epsilon)\mathbf{x}\right]$ has the same periodicity as $V_0(\mathbf{x})$, and the difference between the potentials of the strained and unstrained crystal δV can be written as:

$$\delta V = V_\epsilon\left[(1+\epsilon)\mathbf{x}\right] - V_0(\mathbf{x}) = \sum_{ij} V_{ij}(\mathbf{x})\epsilon_{ij} \equiv (V\epsilon)\ , \tag{2.45}$$

where

$$V_{ij}(\mathbf{x}) = \frac{1}{2-\delta_{ij}} \lim_{\epsilon\to 0} \frac{V_\epsilon\left[(1+\epsilon)\mathbf{x}\right] - V_0(\mathbf{x})}{\epsilon_{ij}}\ . \tag{2.46}$$

Using the transformations (2.42) and (2.43), we rewrite the Schrödinger Equation (2.6) the following way:

$$\left(\widehat{H}_0 + \widehat{H}'\right)|\psi_{n\epsilon}(\mathbf{k},\mathbf{r})\rangle = E_{n\epsilon}(\mathbf{k})|\psi_{n\epsilon}(\mathbf{k},\mathbf{r})\rangle\ , \tag{2.47}$$

where $|\psi_{n\epsilon}(\mathbf{k},\mathbf{r})\rangle = \sum_{i=1}^{8} c_{n\epsilon i}|u_i\rangle$ and it has the same periodicity as the eigenvectors of the Hamiltonian (2.32). The unperturbed Hamiltonian $\widehat{H}_0$ is from (2.17). In order to evaluate the perturbation Hamiltonian due to strain $\widehat{H}_\epsilon$ we take into account the fact the potential of strained and unstrained crystal, $V_\epsilon\left[(1+\epsilon)\mathbf{x}\right]$ and $V_0(\mathbf{x})$ respectively, have the same periodicity. This means that, in order to maintain the periodicity of the basis functions $|u_{n\mathbf{k}_0}\rangle$ we simply substitute the momentum operator $\mathbf{p}$ with its corresponding transformation $(1-\epsilon)\mathbf{p}$. Consequently $\widehat{H}_\epsilon$ for $\mathbf{k}_0 = 0$ will be given by:

$$\begin{aligned}\widehat{H}' &= \frac{\hbar^2 k^2}{2m_0} + \frac{\hbar}{m_0}\mathbf{k}\cdot\mathbf{p} - \frac{\hbar}{m_0}\mathbf{k}\cdot(\epsilon\mathbf{p}) - \frac{(\mathbf{p}\epsilon\mathbf{p})}{m_0} + (V\epsilon) \\ &\equiv \widehat{H}_{\mathbf{k}\cdot\mathbf{p}} - \frac{\hbar}{m_0}\mathbf{k}\cdot(\epsilon\mathbf{p}) - \frac{(\mathbf{p}\epsilon\mathbf{p})}{m_0} + (V\epsilon) = \widehat{H}_{\mathbf{k}\cdot\mathbf{p}} + \widehat{H}_\epsilon\ .\end{aligned} \tag{2.48}$$

There are a few things to note here. Firstly, we do not include the effect of strain on the spin-orbit interaction for simplicity. Secondly, as we mentioned, we do not include in our analysis the terms proportional to the product of strain tensor elements $\epsilon_{\alpha_1}\epsilon_{\alpha_2}$ due to a small magnitude of strain, therefore we restrict our analysis here to the first order perturbation theory only.

Since in the derivation of the Hamiltonian matrix (2.32) we included the first two terms from (2.48), we focus here on the expansion of the terms depending on the strain which, in the first order perturbation theory, yields

$$\left(\widehat{H}_\epsilon\right)_{nm} = -\frac{\hbar}{m_0}\sum_{i=i}^{3} k_i\left(\epsilon\mathbf{p}_{nm}\right)_i + \sum_{ij}\left(-\frac{\left(p^{(i)}p^{(j)}\right)_{nm}}{m_0} + \left(V_{ij}\right)_{nm}\right)\epsilon_{ij}\ . \tag{2.49}$$

Using the set of basis functions (2.22) we evaluate the following Hamiltonian matrix

$$\left(\widehat{H}_\epsilon\right)_{nm} = \begin{pmatrix} H_\epsilon^{(1)} & 0 \\ 0 & H_\epsilon^{(1)} \end{pmatrix} , \tag{2.50}$$

where

$$H_\epsilon^{(1)} = \begin{pmatrix} a_c(\epsilon_{xx}+\epsilon_{yy}+\epsilon_{zz}) & -iP\sum_i k_i\epsilon_{xi} & -iP\sum_i k_i\epsilon_{yi} & -iP\sum_i k_i\epsilon_{zi} \\ iP\sum_i k_i\epsilon_{xi} & l\epsilon_{xx}+m(\epsilon_{yy}+\epsilon_{zz}) & n\epsilon_{xy} & n\epsilon_{xz} \\ iP\sum_i k_i\epsilon_{yi} & n\epsilon_{xy} & l\epsilon_{yy}+m(\epsilon_{xx}+\epsilon_{zz}) & n\epsilon_{yz} \\ iP\sum_i k_i\epsilon_{zi} & n\epsilon_{xz} & n\epsilon_{yz} & l\epsilon_{zz}+m(\epsilon_{xx}+\epsilon_{yy}) \end{pmatrix} . \tag{2.51}$$

Here a_c and l, m, n are deformation potentials for the s-like (conduction) states and p-like (valence) states respectively, and are given by:

$$\begin{aligned} a_c &= -\frac{\left(p^{(i)}p^{(i)}\right)_{ss}}{m_0} + (V_{ii})_{ss} \\ l &= -\frac{\left(p^{(x)}p^{(x)}\right)_{xx}}{m_0} + (V_{xx})_{xx} \\ m &= -\frac{\left(p^{(y)}p^{(y)}\right)_{xx}}{m_0} + (V_{yy})_{xx} \\ n &= -\frac{\left(p^{(x)}p^{(y)}\right)_{xy}}{m_0} + (V_{xy})_{xy} . \end{aligned} \tag{2.52}$$

Comparing the matrices (2.51), (2.25) and (2.26) we notice that the elements of the strain Hamiltonian can be obtain from the $\mathbf{k}\cdot\mathbf{p}$ interaction matrix with the following substitutions:

$$\begin{aligned} k_i k_j &\to \epsilon_{ij} \\ A &\to a_c \\ L, M, N &\to l, m, n \\ k_i &\to -\sum_j \epsilon_{ij} k_j . \end{aligned} \tag{2.53}$$

The valence band deformation potentials a_v, b, d are closely related with the deformation potentials of the p-like states l, m, n with the following expressions:

$$\begin{aligned} a_v &= \frac{l+2m}{3} \\ b &= \frac{l-m}{3} \\ d &= \frac{n}{\sqrt{3}}\,. \end{aligned} \tag{2.54}$$

Comparing the expressions above with the Luttinger parameters (2.29), we notice that for the evaluation of the strain Hamiltonian matrix in the $|J;m_j\rangle$ notation it is useful to transform the Luttinger parameters $\gamma_1, \gamma_2, \gamma_3$ into the valence band deformation potentials a_v, b, d as follows:

$$\begin{aligned} &\frac{\hbar^2}{2m_0}\gamma_1 \rightarrow -a_v \\ &\frac{\hbar^2}{m_0}\gamma_2 \rightarrow -b \\ &\frac{\hbar^2}{m_0}\gamma_3 \rightarrow -\frac{d}{\sqrt{3}}\,, \end{aligned} \tag{2.55}$$

thereby obtaining the following Hamiltonian matrix expansion:

$$H_\epsilon = \begin{pmatrix} a_c\epsilon_{hy} & -\sqrt{3}t_+ & \sqrt{2}u & -u & 0 & 0 & -t_- & -\sqrt{2}t_- \\ & -p+q & \sqrt{2}s & -s & 0 & 0 & -r & -\sqrt{2}r \\ & & -p-q & -\sqrt{2}q & t_+^* & r & 0 & \sqrt{2}s \\ & & & -p & \sqrt{2}t_+^* & \sqrt{2}r & -\sqrt{3}s & 0 \\ & & & & a_c\epsilon_{hy} & -\sqrt{3}t_- & \sqrt{2}u & -u \\ & & & & & -p+q & \sqrt{2}s^* & -s^* \\ & & & & & & -p-q & \sqrt{2}q \\ & & & & & & & -p \end{pmatrix}, \tag{2.56}$$

where

$$\begin{aligned}
\epsilon_{hy} &= \epsilon_{xx} + \epsilon_{yy} + \epsilon_{zz} \\
p &= -a_v \epsilon_{hy} \\
q &= -\frac{b}{2}(\epsilon_{xx} + \epsilon_{yy} - 2\epsilon_{zz}) \\
t_\pm &= -\frac{1}{\sqrt{6}} P \sum_j \left(\epsilon_{xj} \pm i\epsilon_{yj}\right) k_j \\
u &= -\frac{1}{\sqrt{3}} P \sum_j \epsilon_{zj} k_j \\
s &= -\frac{1}{\sqrt{2}} d\left(\epsilon_{xz} - i\epsilon_{yz}\right) \\
r &= -\frac{\sqrt{3}}{2} b(\epsilon_{xx} - \epsilon_{yy}) - id\epsilon_{xy}
\end{aligned} \tag{2.57}$$

Similarly to the Hamiltonian (2.32), the lower diagonal in the matrix (2.56) is the complex conjugate of the upper diagonal since it is also a Hermitian matrix.

We also note here that the 8-band strain Hamiltonian (2.56) can be simplified for an epitaxial layer, e.g. QW. Here we take into account the fact that the only non-zero components of the stress tensor σ_{kl} are σ_{xx} and σ_{yy}, which, due to the cubic structure of zinc blende heterostructures, will be equal. A lattice mismatch between the deposited layer and the substrate will result in an in-plane strain given by:

$$\epsilon_{xx} = \epsilon_{yy} = \frac{a_s - a_l}{a_l}\,, \tag{2.58}$$

where a_s and a_l are the unstrained lattice constants of the substrate and the epitaxially grown layers respectively. In this case, from Eq. (2.36) we can write:

$$\begin{aligned}
2C_{12}\epsilon_{xx} + C_{11}\epsilon_{zz} = \sigma_{zz} = 0 \\
\implies \epsilon_{zz} = -\frac{2C_{12}}{C_{11}}\epsilon_{xx}\,.
\end{aligned} \tag{2.59}$$

Also there are no shear forces acting during the pseudomorphic growth of such layers, therefore $\epsilon_{xy} = \epsilon_{xz} = \epsilon_{yz} = 0$ and the terms s and r in the strain Hamiltonian (2.56) vanish, as well as the terms t and u at $k = 0$.

The effects of strain on the electronic structure of a bulk III-V compound are shown in Fig. 2.2. Firstly we find that the HH and LH bands, which were originally degenerate in an unstrained lattice at the zone centre of the Brillouin zone, split due to the diagonal term q in the Hamiltonian (2.56), with the HH (LH) band being closer to the CB edge in a compressively (tensile) strained semiconductor (although the spin degeneracy is still maintained). As we will

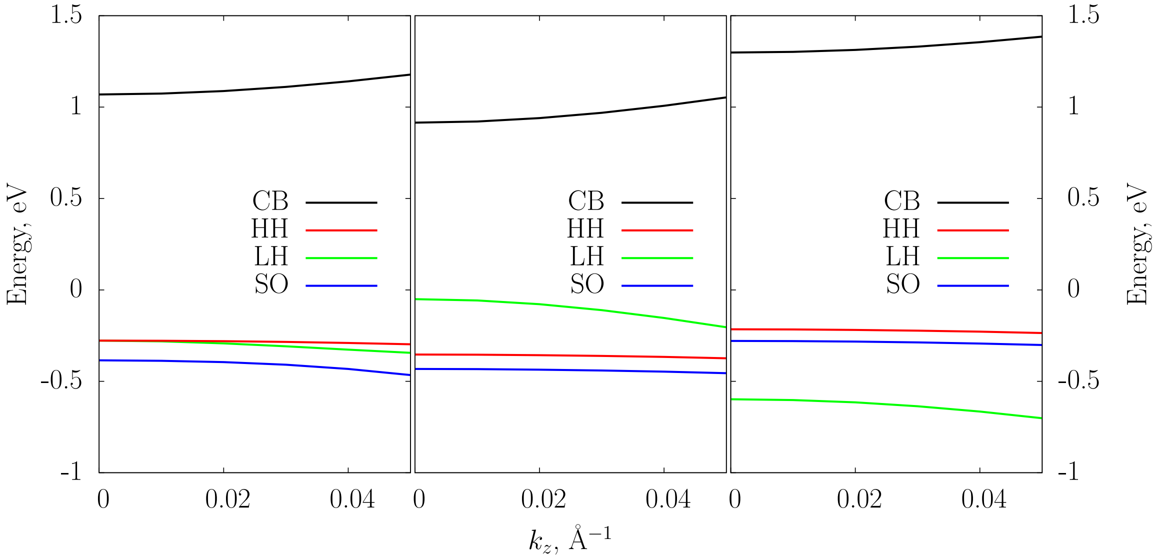

FIGURE 2.2: Calculated energy dispersion of the conduction (black line), heavy-hole (red line), light-hole (green line) and spin-split-off bands (blue line) along the [001] direction in an unstrained (left panel), tensile (middle panel) and compressively strained (right panel) InP epitaxial layer at 300 K.

show later, this is an important feature for the calculation of the optical properties, since the electron-hole recombination rate now will be strongly favoured by a particular polarisation of the incident electric field. This is not the case in an unstrained material, where, for instance, a photoluminescence response would be independent on the polarisation of the laser excitation. As we will also show in Section 4.2, by splitting the HH and LH bands we also affect the valence density of states, especially at energies close to the valence band maximum. Due to the Fermi-Dirac distribution of the carriers, the reduced density of states allows a more rapid population of the valence states per unit energy, thereby enhancing the threshold characteristics and differential gain of a laser.

Secondly, a slight change in volume due to the hydrostatic strain ϵ_{hy} causes a noticeable change in the band gap, and it increases (decreases) when compressive (tensile) strain is applied, as can be seen on the right (middle) panel in Fig. 2.2. This feature has to be taken into account for the design of heterostructure based devices, e.g. lasers and light-emitting diodes, with a particular emission wavelength. In order to maintain a constant emission wavelength, the effects of hydrostatic strain can be partially compensated with minor adjustments in the alloy composition of the active region, or, as we will show in Section 4.2, by changing the confinement of the carriers with a different nanostructure geometry.

Thirdly, the tensile strain increases the energy separation between the topmost valence band (light-hole, green line) and the spin-split-off band (blue line). This is particularly imporant for the CHSH Auger recombination process [108], which is the dominant recombination pathway in semiconductor lasers for telecom applications [109], especially at 300 K or higher temperatures. During this process, due to a smaller magnitude of the spin-orbit splitting Δ_{SO} compared to the band gap E_g, the released energy of the recombination of a conduction electron and a valence hole can excite a hole into the spin-split-off band [110]. The dilute bismide-based heterostructures have been suggested to have a suppressed Auger recombination due to a much larger spin-orbit splitting Δ_{SO} compared to the band gap E_g [111]. The theoretical estimations by Jones *et al.* [112] also indicate a suppressed Auger recombination for 1.5μm lasers when tensile strain is applied to the QWs in the active region.

Finally, unlike the material parameters for the $\mathbf{k}\cdot\mathbf{p}$ Hamiltonian (2.32) which are always positive, the sign convention becomes an important aspect when the effects of strain on the electronic structure are calculated using the Hamiltonian (2.56). In this thesis we follow the typically used sign convention for the lattice mismatched as shown in Eq. (2.58)[4], in which case the compressive (tensile) strain is negative (positive). This, in combination with the chosen sign of (i) the deformation potentials a_c, a_v, b, d, which are provided the III-As and III-P compounds in Appendix A, and (ii) the set of terms of the strain Hamiltonian from Eq. (2.57) has to result in a behaviour as previously discussed.

2.4 Theory of optical properties of semiconductor heterostructures

In this section we discuss the key optical properties which our analysis of device performance in Chapters 4 – 6 will be based on and provide explicit expressions for gain and spontaneous emission spectra, and we follow here the approach used by Chuang [2].

We start with the derivation of the expression for the gain spectrum in Section 2.4.1, where we also discuss (i) the requirements for an amplified emission to occur and (ii) the threshold condition for gain to overcome the internal losses of the cavity. Then, in Section 2.4.2 we provide the derivation for the spontaneous emission spectrum due to the relaxation of the conduction electrons.

2.4.1 Material and modal gain

Due to an incident electromagnetic wave, the Hamiltonian for a free electron (2.2) requires the substitution $\mathbf{p} \rightarrow \mathbf{p} - e\mathbf{A}$, where $\mathbf{A}$ is the magnetic vector potential, leading to the following operator:

---

[4] We use the opposite sign convention for strain in Chapter 4, where we provide detailed guidelines for optimised emission of metamorphic lasers and our analysis is primarily focused on an audience with epitaxial and device engineering background.

$$\begin{aligned}\widehat{H} &= \frac{(\mathbf{p}-e\mathbf{A})^2}{2m_0} + V_0(\mathbf{r}) \\ &= \widehat{H}_0 - \frac{e}{2m_0}(\mathbf{p}\cdot\mathbf{A} + \mathbf{A}\cdot\mathbf{p}) + \frac{e^2}{2m_0}|\mathbf{A}|^2\,,\end{aligned} \tag{2.60}$$

Here $\widehat{H}_0$ is the unperturbed Hamiltonian from Eq. (2.2) and e is the electron charge. Using the Coulomb gauge $\nabla\cdot\mathbf{A}=0$, such as $\mathbf{p}\cdot\mathbf{A}=\mathbf{A}\cdot\mathbf{p}$, and taking into account that the last term in Eq. (2.60) has a much smaller effect than the term linear in $\mathbf{A}$, we find

$$\widehat{H} = \widehat{H}_0 - \frac{e}{m_0}(\mathbf{p}\cdot\mathbf{A}) = \widehat{H}_0 + \widehat{H}'(\mathbf{r},t)\,. \tag{2.61}$$

The magnetic vector potential $\mathbf{A}$ is given here by

$$\mathbf{A} = \widehat{e}A_0\cos\left(\mathbf{k}_{op}\cdot\mathbf{r} - \omega t\right), \tag{2.62}$$

where $\widehat{e}$, A_0, $\mathbf{k}_{op}$ and ω are the polarisation vector, peak amplitude, wave vector and the angular frequency of the incident wave. Substituting the magnetic vector potential $\mathbf{A}$ (2.62) into the time-dependent perturbation Hamiltonian $\widehat{H}'(\mathbf{r},t)$ from Eq. (2.61) we find

$$\begin{aligned}\widehat{H}'(\mathbf{r},t) &= -\frac{eA_0}{m_0}\cos\left(\mathbf{k}_{op}\cdot\mathbf{r} - \omega t\right)\mathbf{p}\cdot\widehat{e} \\ &= -\frac{eA_0}{2m_0}\left(e^{i\mathbf{k}_{op}\cdot\mathbf{r}}e^{-i\omega t} + e^{-i\mathbf{k}_{op}\cdot\mathbf{r}}e^{i\omega t}\right)\mathbf{p}\cdot\widehat{e} = \widehat{H}'(\mathbf{r})e^{-i\omega t} + \widehat{H}'^{*}(\mathbf{r})e^{+i\omega t}\,,\end{aligned} \tag{2.63}$$

We now assume a two-level system, with energy levels E_1 and E_2, such as $E_1 < E_2$, as shown in Fig. 2.3. Using the Fermi's golden rule, the derivation of which is presented in Appendix C, the upward transition rate per unit volume can be written as

$$R_{1\to 2} = \frac{1}{V}\frac{2\pi}{\hbar}\left|\widehat{H}'_{21}\right|^2\delta(E_2 - E_1 - \hbar\omega)f_1(1-f_2)\,. \tag{2.64}$$

Here f_1 (f_2) denotes the probability of the state 1 (2) being occupied by an electron according to the Fermi-Dirac statistics

$$f_{1(2)} \equiv f(E_{1(2)}, F_{v(c)}) = \frac{1}{1+e^{\frac{E_{1(2)}-F_{v(c)}}{k_BT}}}\,, \tag{2.65}$$

where $F_{v(c)}$, k_B and T are the quasi-Fermi level in the vicinity of the valence (conduction) band edge, Boltzmann constant and temperature respectively. For a system with a set of valence

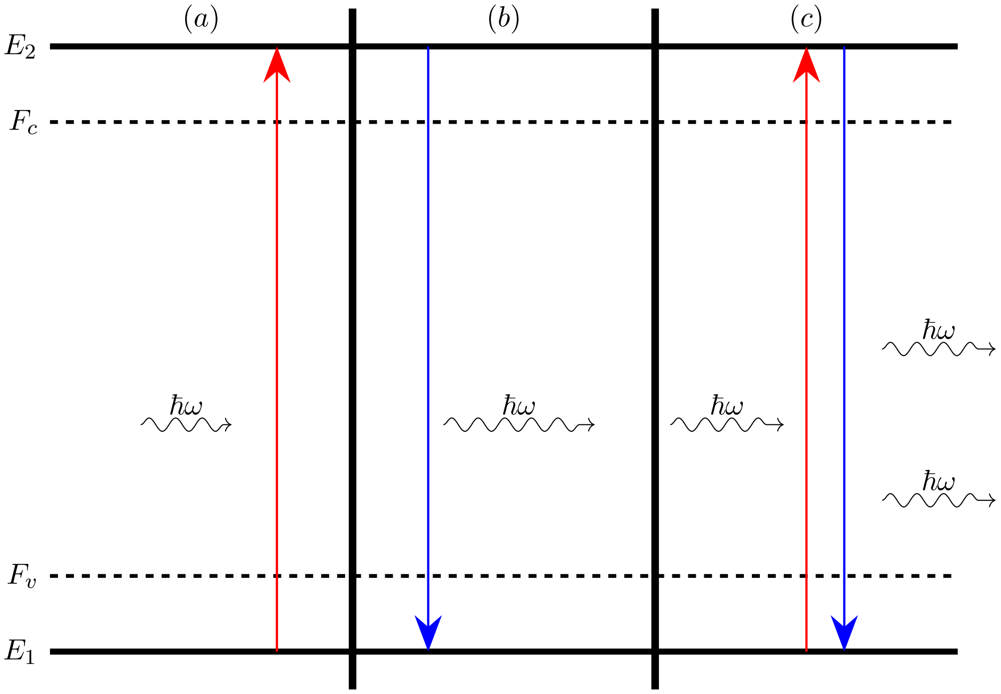

FIGURE 2.3: Schematic representation of the absorption (a), spontaneous emission (b) and stimulated emission (c) processes for a two level system E_1 and E_2, with $E_1 < E_2$.

and conduction states, E_v and E_c respectively, with $E_c > E_v$ the total transition rate per unit volume is the sum of all possible two level transitions, i.e.

$$R_{v\rightarrow c} = \frac{2}{V}\frac{2\pi}{\hbar}\sum_v\sum_c \left|\widehat{H}'_{cv}\right|^2 \delta(E_c - E_v - \hbar\omega) f_v(1-f_c)\,, \tag{2.66}$$

where the prefactor 2 is included to take into account the transitions between the states with the same spin. By analogy, the downward transition rate per unit volume between a set of conduction states c onto the valence states v is

$$R_{c\rightarrow v} = \frac{2}{V}\frac{2\pi}{\hbar}\sum_v\sum_c \left|\widehat{H}'^*_{vc}\right|^2 \delta(E_v - E_c + \hbar\omega) f_c(1-f_v)\,. \tag{2.67}$$

Taking into account the fact that $|\widehat{H}'_{cv}| = |\widehat{H}'^*_{vc}|$, the parity of the Dirac delta function $\delta(x) = \delta(-x)$, and the dipole approximation $\mathbf{k}_{op} \approx 0$ the net upward transition rate per unit volume is

$$\begin{aligned} R = R_{v\rightarrow c} - R_{c\rightarrow v} &= \frac{2}{V}\frac{2\pi}{\hbar}\sum_v\sum_c \left|\widehat{H}'_{cv}\right|^2 \delta(E_c - E_v - \hbar\omega)\,(f_v - f_c) \\ &= \frac{\pi e^2 A_0^2}{V\hbar m_0^2}\sum_v\sum_c \left|\mathbf{p}_{cv}\cdot\widehat{e}\right|^2 \delta(E_c - E_v - \hbar\omega)\,(f_v - f_c)\;. \end{aligned} \tag{2.68}$$

Here $\mathbf{p}_{cv} \cdot \widehat{e} = \langle \psi_c | \mathbf{p} \cdot \widehat{e} | \psi_v \rangle$ is the momentum matrix element between an initial state E_v and a final state E_c. From Eq. (2.68) we see that the sign of the difference between the state occupation $f_v - f_c$ is the only factor that determines whether the absorption or emission is the dominant process, with the positive (negative) sign corresponding to net absorption (emission).

The magnetic vector potential $\mathbf{A}$ (2.62) is related with the electric and magnetic fields, $\mathbf{E}$ and $\mathbf{H}$ respectively, as

$$\begin{aligned} \mathbf{E} &= -\nabla \phi - \frac{\partial \mathbf{A}}{\partial t} = -\widehat{e} A_0 \omega \sin\left(\mathbf{k}_{op} \cdot \mathbf{r} - \omega t\right) \\ \mathbf{H} &= \frac{1}{\mu_0} \nabla \times \mathbf{A} = -\frac{1}{\mu_0} \mathbf{k}_{op} \times \widehat{e} A_0 \sin\left(\mathbf{k}_{op} \cdot \mathbf{r} - \omega t\right) \end{aligned} \tag{2.69}$$

Here we set the scalar potential ϕ to be zero and use the magnetic permeability of the vaccum in the first and second equations respectively. The Poynting vector is given by

$$\mathbf{P} = \mathbf{E} \times \mathbf{H} = \widehat{k} k_{op} \frac{\omega A_0^2}{\mu_0} \sin^2(\mathbf{k}_{op} \cdot \mathbf{r} - \omega t)\,. \tag{2.70}$$

and we calculate the power density using the time average of the Poynting vector $\mathbf{P}$ [113]

$$P = |\langle \mathbf{P}(\mathbf{r}, t) \rangle| = \frac{\omega A_0^2}{2\mu_0} k_{op} = \frac{n_r c \epsilon_0 \epsilon_r \omega^2 A_0^2}{2}\,, \tag{2.71}$$

where n_r, c, ϵ_0 and ϵ_r are the refractive index, speed of light, vaccuum and relative permittivity[5] respectively. Here we took into account the fact that the time average of $\sin^2()$ is $1/2$. The absorption coefficient, which is the ratio between the rate of absorbed photons per unit volume and the rate of incident photons per unit area, can be written for a system with a set of states E_v and E_c as discussed above, as:

$$\alpha(\hbar\omega) = \frac{R}{P/\hbar\omega} = \frac{2R\hbar\omega}{n_r c \epsilon_0 \epsilon_r \omega^2 A_0^2}\,. \tag{2.72}$$

We substitute here the expression for the net transition rate (2.68) to find

$$\alpha(\hbar\omega) = \frac{e^2 \pi \hbar}{\epsilon_0 \epsilon_r m_0^2 n_r c \hbar\omega} \frac{2}{V} \sum_v \sum_c |\mathbf{p}_{cv} \cdot \widehat{e}|^2 \, \delta(E_c - E_v - \hbar\omega) \, (f_v - f_c)\,. \tag{2.73}$$

In the case when the final states E_c have a larger occupation compared to the initial states E_v, i.e. $f_v - f_c < 0$, the absorption is negative and represents the material gain

---

[5] Since the relative permittivity is position-dependent, we restrict our calculations by using the ϵ_r corresponding to the barrier material.

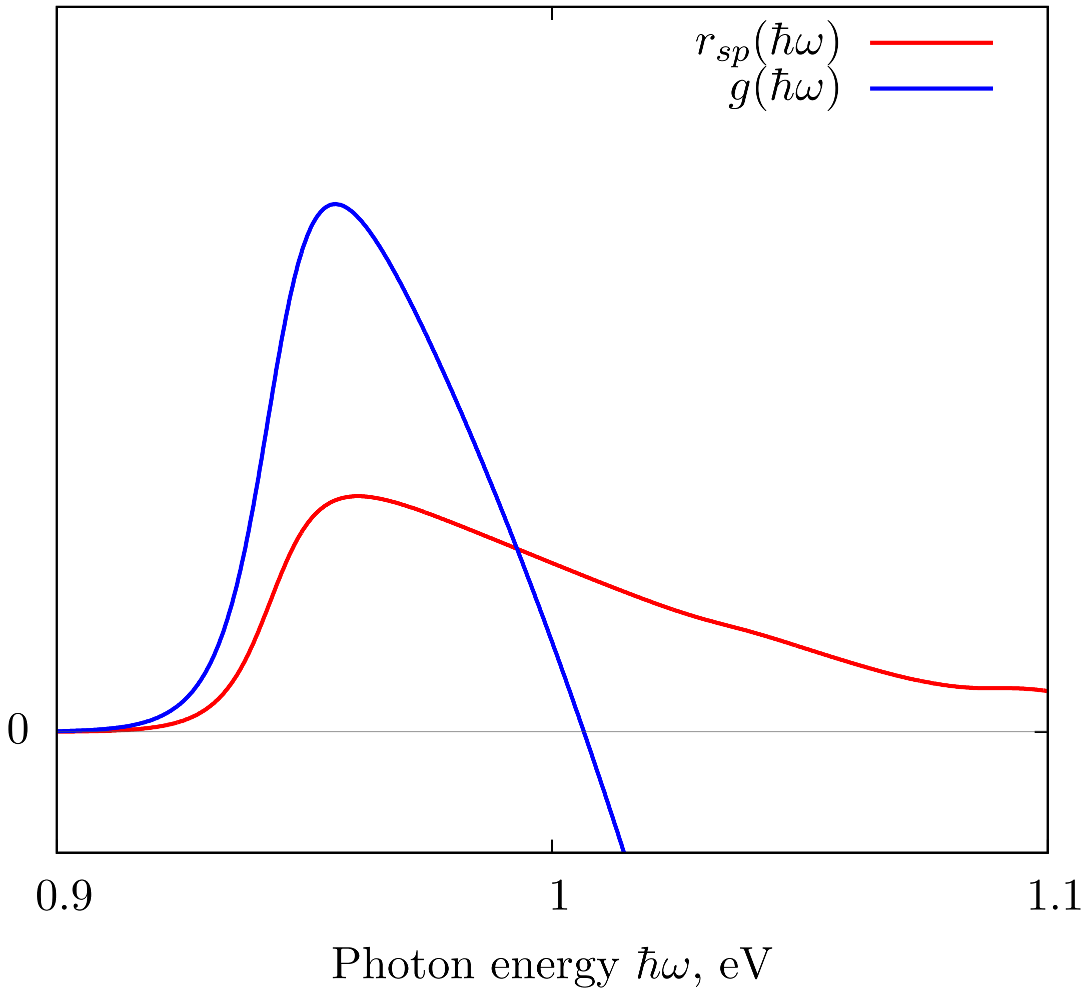

FIGURE 2.4: Spontaneous emission (red) and gain (blue) spectra for an InGaAs QW, at the injected areal carrier density $n^{2\mathrm{D}} = 1.51 \times 10^{12}\mathrm{cm}^{-2}$.

$$g(\hbar\omega) = -\alpha(\hbar\omega) = \frac{e^2\pi\hbar}{\epsilon_0\epsilon_r m_0^2 n_r c\hbar\omega}\frac{2}{V}\sum_v\sum_c |\mathbf{p}_{cv}\cdot\widehat{e}|^2\,\delta(E_c - E_v - \hbar\omega)\,(f_c - f_v)\ . \tag{2.74}$$

By looking at the definition of the Fermi-Dirac probability function (2.65), we find that the following condition has to be satisfied for the material gain to occur:

$$\Delta F = F_c - F_v > E_c - E_v \tag{2.75}$$

This is the so-called Bernard-Duraffourg condition, or population inversion, which indicates that the threshold for a pair of states E_c and E_v to produce amplified emission occurs when the difference $E_c - E_v$ is smaller than the energy difference in quasi-Fermi levels. A typical gain spectrum is shown in Fig. 2.4.

First thing we note here is that the expression for material gain (2.74) is valid for a system with a set of states in the conduction and valence band calculated at a single value of $\mathbf{k}$. Consequently, Eq. (2.74) can be in principle applied directly for the gain calculations of QD- or QWR-based heterostructures, where the electronic structure is calculated at the Γ point in the Brillouin zone (or $|\mathbf{k}| = 0$) [6].

However the electronic structure calculations for QW-based heterostructures bring about a dispersion of conduction and valence bands along $\mathbf{k}_{\|}$ (cf. Section 2.2.2). In this case, the transitions between conduction and valence states at all values of $\mathbf{k}_{\|}$ are taken into account for gain calculations, by applying the transformation $\frac{1}{V} \to \frac{1}{a}\frac{1}{(2\pi)^2}\int_{k_x,k_y} \mathrm{d}k_x \mathrm{d}k_y$ to Eq. (2.74), where a is the thickness of the active region. The axial approximation [106] allows us to transform this integration using polar coordinates and integrate over the magnitude of $\mathbf{k}_{\|}$, i.e. $\frac{1}{V} \to \frac{1}{a}\frac{1}{2\pi}\int_{k_{\|}} k_{\|}\mathrm{d}k_{\|}$, where $k_{\|} = |\mathbf{k}_{\|}|$.

Secondly, the Dirac delta function δ in Eq. (2.74) requires to be substituted with a normalised lineshape function to account for the effects of homogeneous broadening. In our calculation we use the hyperbolic secant as a lineshape function [32], i.e.

$$\delta(E) \to S(E) = \frac{\tau_{in}}{\pi\hbar}\mathrm{sech}\left(\frac{E\tau_{in}}{\hbar}\right) , \tag{2.76}$$

where τ_{in} is the interband relaxation time. The main advantage of the hyperbolic secant function compared to other lineshape functions, such as the Lorentzian, consists in removing the problem of absorption below the band gap [4]. Taking into account the integration over $\mathbf{k}_{\|}$ and the homogeneous broadening, the expression for material gain for a QW-based heterostructure becomes:

$$g(\hbar\omega) = \frac{e^2\hbar}{\epsilon_0\epsilon_r m_0^2 n_r c\hbar\omega}\frac{1}{a}\int_{k_{\|}}\sum_v\sum_c \left|\mathbf{p}_{cv}(k_{\|})\cdot\hat{e}\right|^2 S\left[E_c(k_{\|}) - E_v(k_{\|}\right]-\hbar\omega)\left[f_c(k_{\|}) - f_v(k_{\|})\right] k_{\|}\mathrm{d}k_{\|} \tag{2.77}$$

Since in the dipole approximation the electromagnetic wave does not carry (significant) momentum, we ensure here that the transitions occur between energy levels at the same $k_{\|}$, also known as k-selection rule.

Finally, for the derivation of the gain expression (2.77) we assumed that the time averaged Poynting vector of the incident electromagnetic wave contributes entirely to the energy transition of the electrons. In reality, only a fraction of the Poynting vector is "confined" in the active region where the carrier wavefunctions is localised, which is described by the optical confinement factor Γ given by:

---

[6] This is discussed in more details in Section 3.2.

$$\Gamma = \frac{\displaystyle\int_{\mathrm{AR}} \langle \mathbf{P} \rangle \cdot \widehat{e} \mathrm{d}z}{\displaystyle\int_{\mathrm{WG}} \langle \mathbf{P} \rangle \cdot \widehat{e} \mathrm{d}z} , \tag{2.78}$$

where the integration in the numerator (denominator) is performed over the active region (waveguide) length, and the actual modal (or optical) gain is

$$g_m(\hbar\omega) = \Gamma g(\hbar\omega) , \tag{2.79}$$

Unlike the material gain (2.77), the modal gain is, in fact, measurable, e.g. using the stripe-length method [114] or the Hakki-Paoli method [115, 116]. The optical confinement factor Γ in our calculations is evaluated using the effective index method [117].

Fourthly, in the perfect scenario the amplified emission in Eq. (2.77) is not attenuated while propagating in the optical cavity. In reality, the modal gain has to reach a certain threshold value $g_m^{(th)}$, so that it compensates (i) the internal absorption losses of the cavity, and (ii) the reflection losses of the facets. The threshold gain in this case is given by [118]:

$$g_m^{(th)} = \Gamma g_{th} = \alpha_i + \frac{1}{L} \ln \left(\frac{1}{R} \right) , \tag{2.80}$$

where α_i, L and R are the internal losses, cavity length and reflectivity of the facets. We notice here that, unlike the threshold material gain g_{th}, the modal gain at threshold $g_m^{(th)}$ does not depend on the optical confinement Γ. For the calculation of the quasi-Fermi levels in our work we consider an equal amount of injected electrons n_e and holes n_h (for charge neutrality) into the conduction and valence bands respectively and, for a set of discrete states with no dispersion in $\mathbf{k}$ is calculated iteratively as

$$n_{e(h)} = \sum_{E_{c(v)}} f_{e(h)} = \sum_{E_{c(v)}} f(E_{c(v)}, F_{n(h)}) , \tag{2.81}$$

or, in other words, the total sum of the probabilities finding an electron (hole) in a conduction state E_c (valence state E_v) equals the amount of injected electrons (holes). When the energy dispersion has to be take into account, e.g. in QWs along $k_\parallel$, an additional integration over the $k_\parallel$ space is required and, using the axial approximation, it is given by

$$n_{e(h)}^{\mathrm{2D}} = \frac{1}{2\pi} \sum_{E_{c(v)}} \int_{k_\parallel} f(E_{c(v)}(k_\parallel), F_{n(h)}) k_\parallel \mathrm{d}k_\parallel , \tag{2.82}$$

where $n^{\mathrm{2D}}_{e(h)}$ has units of number of electrons (holes) per unit area, i.e. $n^{\mathrm{2D}}_{e(h)}$ is the areal carrier density.

2.4.2 Spontaneous emission

We start by assuming a two level system as shown in Fig. 2.3, and define the upward transition rate due to an incident photon with energy $\hbar\omega$ using the Einstein stimulated emission coefficient B as

$$B_{12} = \frac{2\pi}{\hbar}\left|\widehat{H}'_{12}\right|^2 \delta(E_2 - E_1 - \hbar\omega)\,, \tag{2.83}$$

where we took into account the transition $1 \rightarrow 2$ due to resonance using the Dirac delta function. The total upward transition rate for a broad range of photons is given by:

$$R_{1\rightarrow 2} = B_{12}\rho_{ph}(\hbar\omega) f_{\text{B-E}}(\hbar\omega) f_1(1 - f_2)\,, \tag{2.84}$$

where we included the occupation probabilities of the two levels, $\rho_{ph}(\hbar\omega)$ is the density of photon states with energy $\hbar\omega$ in a bulk material [2, 119], given by:

$$\rho_{ph}(\hbar\omega) = \frac{n_r^3(\hbar\omega)^2}{\pi^2\hbar^3c^3}\,, \tag{2.85}$$

and $f_{\text{B-E}}(\hbar\omega)$ is the probability of finding a photon with energy $\hbar\omega$ using the Bose-Einstein statistics, given by:

$$f_{\text{B-E}}(\hbar\omega) = \frac{1}{e^{\frac{\hbar\omega}{k_BT}} - 1}\,. \tag{2.86}$$

Similarly to Eq. (2.84), the downward emission due to a range of incident photon energies (or stimulated emission) is given by:

$$R^{stim}_{2\rightarrow 1} = B_{21}\rho_{ph}(\hbar\omega) f_{\text{B-E}}(\hbar\omega) f_2(1 - f_1)\,. \tag{2.87}$$

The spontaneous downward transition rate (spontaneous emission) does not depend on the incident photons and is given by

$$R^{spon}_{2\rightarrow 1} = A_{21} f_2(1 - f_1)\,, \tag{2.88}$$

where A_{21} is the Einstein spontaneous emission coefficient. The quasi-equilibrium requires the rate of upward transitions to be equal with the total downward transitions, therefore

$$\begin{aligned} B_{12}\rho_{ph}(\hbar\omega)f_{\text{B-E}}(\hbar\omega)f_1(1-f_2) &= B_{21}\rho_{ph}(\hbar\omega)f_{\text{B-E}}(\hbar\omega)f_2(1-f_1) \\ &\quad + A_{21}f_2(1-f_1) \\ \implies \frac{A_{21}}{B_{21}}f_{\text{B-E}}(\hbar\omega) &= \rho_{ph}(\hbar\omega)f_{\text{B-E}}(\hbar\omega)\,, \end{aligned} \tag{2.89}$$

where we took into account the fact that $B_{12} = B_{21}$, and find $A_{21} = B_{21}\rho_{ph}(\hbar\omega)$. The net photon-assisted upward transition rate in a two level system can be written as

$$R_{abs} = R_{1\to 2} - R_{2\to 1} = B_{12}(f_1 - f_2)\rho_{ph}(\hbar\omega)f_{\text{B-E}}\,, \tag{2.90}$$

and the spectral absorption for a spectral width dE can be written as

$$\alpha(\hbar\omega)\mathrm{d}E = R_{abs}\mathrm{d}E = B_{12}(f_1 - f_2)\frac{n_r}{c}\,. \tag{2.91}$$

Taking the ratio between the spontaneous emission rate $R_{2\to 1} \equiv r_{sp}\mathrm{d}E$ (2.88) and the expression for absorption above we find

$$\begin{aligned} \frac{r_{sp}(\hbar\omega)\mathrm{d}E}{\alpha(\hbar\omega)\mathrm{d}E} &= \frac{A_{21}}{B_{12}}\frac{f_2(1-f_1)}{f_1-f_2}\frac{c}{n_r} \\ \implies r_{sp}(\hbar\omega) &= \rho_{ph}(\hbar\omega)f_2(1-f_1)\frac{\alpha(\hbar\omega)}{f_2-f_1}\frac{c}{n_r}\,. \end{aligned} \tag{2.92}$$

Eq. (2.92) shows the relationship between the spontaneous emission and absorption in a system with a conduction and a valence state. Here we substitute the absorption expression from Eq. (2.73), assuming a single two-level system. We then take into account the set of calculated states E_c and E_v, integrate over $\mathbf{k}_\parallel$ due to energy dispersion while taking into account the axial approximation, and find the explicit expression for the spontaneous emission for a QW-based active region with a set of states E_v and E_c as

$$\begin{aligned} r_{sp}(\hbar\omega) = \frac{e^2 n_r \hbar\omega}{\pi^2\epsilon_0\epsilon_r\hbar^2c^3m_0^2a}\int_{k_\parallel}\sum_v\sum_c \left|\mathbf{p}_{cv}(k_\parallel)\cdot\hat{e}\right|^2\delta\left[E_c(k_\parallel) - E_v(k_\parallel) - \hbar\omega\right] \\ \times f_c(k_\parallel)\left[1 - f_v(k_\parallel)\right]k_\parallel\mathrm{d}k_\parallel\,. \end{aligned} \tag{2.93}$$

Two essential differences appear when we compare the expressions (2.77) and (2.93), (i) a higher energy emission is associated with a reduced gain (enhanced spontaneous emission) since it is inversely (directly) proportional to the photon energy, and (ii) the probability of finding an electron-hole pair determines whether spontaneous emission occurs, whereas at quasi-equilibrium the gain requires a larger occupation of the conduction states compared to the valence band. For the calculation of spontaneous emission in our work we assume an inhomogeneous broadening of the emission. This is particularly relevant when self-assembled QDs and QWRs are considered, as the distribution in geometry and (potentially) composition of these nanostructures result in a broader emission spectrum compared to the modal gain. We therefore consider the Gaussian distribution

$$\delta(E) = \frac{1}{\sqrt{2\pi}\sigma} e^{-\frac{E^2}{2\sigma^2}} \,, \tag{2.94}$$

where σ is the inhomogeneous broadening factor. We do not consider the inhomogeneous broadening for the calculation of gain, since we ensure that the CB–VB transition energy is at resonance with the incident photon $\hbar\omega$. The spontaneous emission spectrum (2.93) can be translated into the total radiative electron-hole recombination rate per unit area, or radiative current density J_{rad}, simply by integrating over the emission wavelength

$$J_{rad} = ea \int_{\hbar\omega} r_{sp}(\hbar\omega) \mathrm{d}(\hbar\omega) \,. \tag{2.95}$$

2.5 Conclusions

In this chapter we discussed the theory of electronic and optical properties of semiconductors with zincblende crystal structure.

We started with the derivation of the $\mathbf{k} \cdot \mathbf{p}$ method for an unstrained crystal in Section 2.2, where we have shown the effects on the wave vector dependent energy dispersion due to (i) the electron momentum $\mathbf{p}$ as a first order perturbation, and (ii) the nearby and remote bands, class A and B respectively [96], according to the second order perturbation theory. The effect of class B states is particularly relevant for the calculation of the electron effective mass m^* and Luttinger parameters γ since the experimentally measured effective masses of electrons and holes are smaller compared to the free electron with a typical ratio $m_0/m^* \approx 5 - 20$. Knowing a set of energy states at a reference wave vector $\mathbf{k}_0$, typicall $k_0 = 0$ and having a set of eight orthonormal basis functions $|u_b\rangle$ (one conduction and three valence spin degenerate states), we can then evaluate the 8-band $\mathbf{k}{\cdot}\mathbf{p}$ Hamiltonian which explicitly includes the effects of class A states on the energy dispersion.

Following this, in Section 2.3 we discussed the effects of a small strain on the electronic structure of zincblende semiconductors. A transformation of the coordinate system was applied in order to maintain the periodicity of the basis functions $|u_b\rangle$ of the $\mathbf{k} \cdot \mathbf{p}$ Hamiltonian. Although the magnitude of strain is indeed small, typically up to about ± 2% for thin epitaxial layers e.g. QWs, noticeable changes in the electronic structure as a consequence occur, such as: (i) a noticeable increase (decrease) in the band gap due to the compressive (tensile); (ii) the originally degenerate HH and LH bands split due to biaxial strain with the CB-HH (CB-LH) transition begin the shortest in the compressive (tensile) case; (iii) increased transition energy between the topmost valence band (in this case LH) and the spin-split-off band when tensile strain is applied, and is potentially beneficial for suppressed Auger recombination [109–112]. The sign convention for strain and deformation potentials is another important aspect that has to be taken into account for strained electronic structure calculations.

Having derived the theoretical framework for the calculation of electronic properties, we turned our attention to the theory of optical properties in Section 2.4. Starting the the Fermi's golden rule, which enforces the energy transitions of electrons to be resonant with the energy of the incident photons, the explicit expressions for the absorption and gain spectra were found, leading to the Bernard-Duraffourg condition, or population inversion, for an amplified emission to occur. Using the optical confinement factor Γ we can then calculate the modal (or optical) gain which, unlike the material gain, is experimentally measurable, as well as the threshold gain due to internal and mirror losses in the optical cavity. We then derived the expression for spontaneous emission which shows that, unlike the gain spectrum, it cannot be negative and only depends on the population probability of the CB and VB states.

Having derived the necessary set of theoretical frameworks, we now proceed to its computational implementation in the next chapter, where we focus on the semi-analytical plane wave method.

Chapter 3

Plane wave expansion method for electronic structure and optical properties calculations

In this chapter we derive the semi-analytical plane wave expansion method [79] that can efficiently and accurately calculate the electronic and optical properties of QW-, QWR- and QD-based heterostructures using the theoretical methods we presented in Chapter 2. We start in Section 3.1.1 with the derivation of the method for a one-dimensional confinement using the 1-band effective mass Hamiltonian and then discuss in Section 3.1.2 its implementation in a multi-band Hamiltonian and its implementation for a multi-QW based heterostructure in Section 3.1.3. Following this we proceed to the derivation of the method for QD and QWR based heterostructures in Section 3.2.1. We will show that, in essence, the implementation of the method to calculate the eigenstates in a one dimensional potential represents a special case within the general derivation of the method for a multi dimensional confinement.

In Section 3.2.2 we discuss the Green's function based method to estimate the real space distribution of the strain tensor elements in a QD and QWR based heterostructure with zincblende crystal structure based on continuum elasticity theory, and then we derive the Pikus-Bir Hamiltonian matrix elements within the plane wave method in Section 3.2.3.

In Section 3.3 we describe the implementation of the plane wave method in order to solve Poisson's equation. This will allow us to estimate the electrostatic field due to the spatial separation of the confined electrons and holes in a heterostructure. We then show in Section 3.4 that the electronic eigenstates calculated using the plane wave expansion of the 8-band Hamiltonian can be used directly to calculate the momentum matrix element between an electron and hole state according to Szmulowicz's formalism [82]. The beauty of this method consists in the use of bulk material parameters to calculate the optical properties, such as spontaneous emission and gain, in an active region of a photonic device. Finally we summarise the chapter results in Section 3.5.

3.1 Derivation of the method for quantum well based heterostructures

In this section we present the fundamental idea of the method and present its implementation for electrons confined in a one-dimensional potential.

3.1.1 1-band model

Our goal here is to solve the one band effective mass Schrödinger equation:

$$\widehat{H} F_n(z) = E_n F_n(z)\,. \tag{3.1}$$

The effective mass Hamiltonian $\widehat{H}$ is given by:

$$\widehat{H} = -\frac{\hbar^2}{2m_0}\frac{\mathrm{d}}{\mathrm{d}z}\left(\frac{1}{m^*(z)}\frac{\mathrm{d}}{\mathrm{d}z}\right) + V(z)\,. \tag{3.2}$$

In order to solve Eq. (3.1) we define our heterostructure as a periodic supercell of length L, in this case along the z (or growth) direction, with a QW of thickness d, with a material parameter in the supercell $f_n(z) = f_n(z+mL)$, where $m \in \mathbb{Z}$, and the origin of the z coordinate is located at the centre of the supercell. This allows us to expand the envelope function as a Fourier series:

$$F_n(z) = \frac{1}{\sqrt{L}} \sum_{m=-M}^{+M} \widetilde{a}_n(G_m) e^{iG_m z}\,, \tag{3.3}$$

where $G_m = \frac{2m\pi}{L}$ is the one dimensional reciprocal vector of the supercell, $\widetilde{a}_n(G_m)$ are Fourier coefficients of $F_n(z)$ and $M \in \mathbb{Z}$.

Substituting Eqs. (3.3) and (3.2) into (3.1) we obtain

$$\frac{1}{\sqrt{L}} \sum_{m=-M}^{+M} \widehat{H} \widetilde{a}_n(G_m) e^{iG_m z} = E_n \frac{1}{\sqrt{L}} \sum_{m=-M}^{M} \widetilde{a}_n(G_m) e^{iG_m z}\,. \tag{3.4}$$

We then multiply both sides by $\frac{1}{\sqrt{L}} e^{-iG_{m'} z}$, where $m' \in [-M, +M]$ and integrate over the supercell

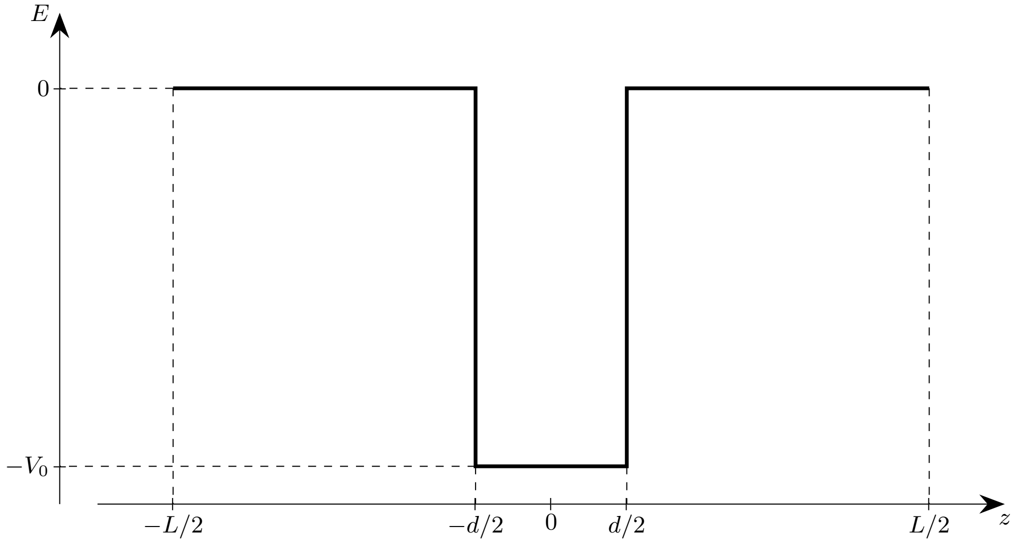

FIGURE 3.1: Schematic representation of a supercell with length L that contains a QW of thickness d. The centre of the QW is situated at 0 on the z axis, and $\chi(z) \in [-d/2, d/2]$.

$$\sum_{m=-M}^{+M} \left(\frac{1}{L} \int_{-L/2}^{L/2} e^{-iG_{m'}z} \widehat{H} e^{iG_m z} \mathrm{d}z \right) \widetilde{a}_n(G_m) = E_n \widetilde{a}_n(G_{m'}) \tag{3.5}$$

On the right-hand side we made use of the fact that

$$\frac{1}{L} \int_{-L/2}^{L/2} e^{-i(G_{m'}-G_m)z} = \delta_{mm'} \, , \tag{3.6}$$

where $\delta_{mm'}$ is the Kronecker delta. We notice that Eq. (3.5) is in fact an eigenvalue problem, with the solution found after diagonalising the matrix representation of the Hamiltonian

$$H_{m'm} = \frac{1}{L} \int_{-L/2}^{L/2} e^{-iG_{m'}z} \widehat{H} e^{iG_m z} \mathrm{d}z \tag{3.7}$$

In order to derive the matrix representation of the Hamiltonian, we solve the integral first for the position-dependent potential $V(z)$ part of the Hamiltonian, and then turn our attention to the kinetic term of Eq. (3.1). Firstly, we assume that the QW with thickness d is located in the supercell within $z \in \left[-\frac{d}{2}, \frac{d}{2}\right]$, as shown in Fig. 3.1, and we define the position-dependent characteristic function $\chi(z)$ to be

$$\chi(z) = \begin{cases} 1 \, , & |z| \leq \frac{d}{2} \\ 0 \, , & \text{otherwise} \end{cases} \tag{3.8}$$

The Fourier transform of the characteristic function is given by

$$\widetilde{\chi}(G_m) = \frac{1}{L}\int_{-L/2}^{L/2} \chi(z) e^{-iG_m z} \mathrm{d}z\,. \tag{3.9}$$

We can therefore express $V(z)$ using the characteristic function

$$V(z) = \chi(z)V_w + \left[1 - \chi(z)\right] V_b = V_b + \chi(z)\left(V_w - V_b\right) \tag{3.10}$$

The indices w and b in Eq. (3.10) correspond to the potential in the QW and surrounding barrier respectively, and will have the same meaning when used for a particular parameter hereafter. We also note that this equation can be applied for any position dependent parameter in the supercell, e.g. effective mass, Luttinger and Kane parameters etc., and it will be particularily important during the derivation of the plane wave method for the 8-band model for QWs, QDs and QWRs. We simplify Eq. (3.10) for the example here by defining $V_b = 0$ and $V_w = -V_0$ (cf. Fig. 3.1). We therefore obtain the following form of the integral using the Fourier transform of the characteristic function $\widetilde{\chi}$ from Eq. (3.9)

$$-\frac{1}{L}\int_{-d/2}^{d/2} V_0 e^{-i(G_{m'}-G_m)z} \mathrm{d}z = -V_0 \widetilde{\chi}(G_{m'} - G_m) \tag{3.11}$$

In order to find $\widetilde{\chi}$ we reduce the limits of the integral from $[-\frac{L}{2}, \frac{L}{2}]$ to $[-\frac{d}{2}, \frac{d}{2}]$ because outside of the QW the integral will be zero. For a QW which is located symmetrically relative to the centre of the supercell this function then becomes

$$\widetilde{\chi}(G_{m'} - G_m) = \frac{d}{L}\mathrm{sinc}\left[\frac{d(G_{m'} - G_m)}{2}\right] \tag{3.12}$$

In essence, a characteristic function and its Fourier transform will correspond to a nanostructure with a particular shape, e.g. QW, QWR or QD. It is important to note here that the sinc function in Eq. (3.12), unlike the sine, treats the singularity explicitly, and equals to unity at $G_{m'} - G_m = 0$. We will later show that these singularities will be particularily important when deriving $\widetilde{\chi}$ for a QWR or a QD shape.

In order to solve the integral of the kinetic part of the Hamiltonian (3.2), we use an approach similar to Eq. (3.10) for $m^*(z)$, i.e.

$$\frac{1}{m^*(z)} = \frac{1}{m_b^*} + \chi(z)\left(\frac{1}{m_w^*} - \frac{1}{m_b^*}\right)\,. \tag{3.13}$$

By substituting Eq. (3.13) into (3.7) we obtain

$$
\begin{aligned}
H_{m'm} = &\left(-\frac{\hbar^2}{2m_0}\frac{1}{m_b^*}\right)\frac{iG_m}{L}\int_{-L/2}^{L/2} e^{-iG_{m'}z}\frac{\mathrm{d}}{\mathrm{d}z}e^{iG_m z}\mathrm{d}z \\
&+\left(-\frac{\hbar^2}{2m_0}\right)\left(\frac{1}{m_w^*}-\frac{1}{m_b^*}\right)\frac{iG_m}{L}\int_{-L/2}^{L/2} e^{-iG_{m'}z}\frac{\mathrm{d}}{\mathrm{d}z}\left[\chi(z)e^{iG_m z}\right]\mathrm{d}z\,.
\end{aligned}
\tag{3.14}
$$

We focus for a moment on the integral in the first term here. By applying integration by parts it becomes

$$
\begin{aligned}
\frac{1}{L}\int_{-L/2}^{L/2} e^{-iG_{m'}z}\frac{\mathrm{d}}{\mathrm{d}z}e^{iG_m z}\mathrm{d}z = \left.\frac{e^{-i(G_{m'}-G_m)z}}{L}\right|_{-L/2}^{L/2} - \frac{1}{L}\int_{-L/2}^{L/2} e^{iG_m z}\frac{\mathrm{d}}{\mathrm{d}z}e^{-iG_{m'}z}\mathrm{d}z \\
= \left(G_{m'}-G_m\right)\delta_{mm'} + iG_{m'}\delta_{mm'}
\end{aligned}
\tag{3.15}
$$

Here for the first term we notice that it is zero due to the definition of the Kronecker delta. We then perform a similar procedure for the integral in the second term in Eq. (3.14), and substitute the results into Eq. (3.14) to find the final form of the matrix representation of the plane wave Hamiltonian (3.2):

$$
H_{m'm} = \frac{\hbar^2}{2m_0}\frac{G_m G_{m'}}{m_b^*}\delta_{mm'} + \left[\frac{\hbar^2 G_m G_{m'}}{2m_0}\left(\frac{1}{m_w^*}-\frac{1}{m_b^*}\right) - V_0\right]\widetilde{\chi}(G_{m'}-G_m)\,. \tag{3.16}
$$

In essence, using analytical methods we transformed the Schrödinger equation from a second order differential equation into a real symmetric $(2M+1)\times(2M+1)$ size matrix, which will be diagonalised numerically (hence the *semi-analytical* name of the method). The end result of the diagonalisation is a $2M+1$ size array that contains the eigenvalues E_n with $(2M+1)$ Fourier coefficients $\widetilde{a}_{nm}$ corresponding to the eigenvalue E_n. Using the Fourier series (3.3) we can then evaluate the position dependent eigenstate. This method has been shown to converge rapidly with the number of plane waves $2M+1$ [79], quickly approaching the exact solution of the Schrödinger equation (3.2) for the ground state, and first few excited states.

3.1.2 8-band model

The ultimate goal is to apply this method to solve the 8-band Schrödinger equation. Here we start by introducing the eigenstates for an in-plane wave vector $\mathbf{k}_{\|}$ as a set of envelope functions associated with a particular bulk band b, and we then expand it into a Fourier series using Eq. (3.3):

$$\psi_n(\mathbf{k}_\parallel, z) = \frac{1}{\sqrt{L}} \sum_{b=1}^{8} \sum_{m=-M}^{+M} \widetilde{a}_{nb}(\mathbf{k}_\parallel, G_m) e^{iG_m z} |u_b\rangle, \tag{3.17}$$

We then follow the procedure from the previous section by inserting Eq. (3.17) into Eq. (2.1)

$$\frac{1}{\sqrt{L}} \sum_{b=1}^{8} \sum_{m=-M}^{+M} \widehat{H}_{b'b}(\mathbf{k}_\parallel, z) \widetilde{a}_{nb}(\mathbf{k}_\parallel, G_m) e^{iG_m z} = E_n \frac{1}{\sqrt{L}} \sum_{b=1}^{8} \sum_{m=-M}^{+M} \widetilde{a}_{nb'}(\mathbf{k}_\parallel, G_m) e^{iG_m z}\,, \tag{3.18}$$

where $\widehat{H}_{b'b}$ is the Hamiltonian matrix element linking bands b and b' in the multiband Hamiltonian. Multiplying both sides by $\frac{1}{\sqrt{L}} e^{-iG_{m'} z}$ and integrating over the supercell space we obtain the following matrix representation of the Hamiltonian:

$$\left[\widehat{H}_{b'b}(\mathbf{k}_\parallel)\right]_{m'm} = \frac{1}{L} \int_{-L/2}^{L/2} e^{-iG_{m'} z} \widehat{H}_{b'b}(\mathbf{k}_\parallel, z) e^{iG_m z} \mathrm{d}z \tag{3.19}$$

By comparing Eqs. (3.7) and (3.19) we first notice that the plane wave expansion of our 8-band Hamiltonian yields a $8\,(2M+1) \times 8\,(2M+1)$ size matrix, where each element of the original Hamiltonian is expanded into a $(2M+1) \times (2M+1)$ matrix. The diagonalisation of $\left[\widehat{H}_{b'b}(\mathbf{k}_\parallel)\right]_{m'm}$ leads to a $8\,(2M+1)$ array of eigenvalues E_n with a set of $8\,(2M+1)$ Fourier coefficients $\widetilde{a}_{nb}$ corresponding to each eigenvalue. These coefficients allow us to determine the envelope function associated with each bulk band, and then use Eq. (3.17) to construct the QW eigenstate at a particular wave vector $\mathbf{k}_\parallel$.

The plane wave expansion of an element in the 8-band Hamiltonian matrix can be obtained following a similar method to that discussed in Section. 3.1.1. However, because the bulk Hamiltonian matrix elements contain terms that depend upon $\mathcal{A}(z)$, $\mathcal{A}(z)k_z$, and $\mathcal{A}(z)k_z^2$, the substitution $k_z \to -i\frac{\mathrm{d}}{\mathrm{d}z}$ for the quantisation along the z direction results in the evaluation of three different types of integrals which we discuss below.

Terms of $H_{b'b} \propto \mathcal{A}(z)$. Due to their being independent of k_z, and therefore lacking the differential operator, the plane wave expansion of the Hamiltonian matrix elements independent of k_z are the simplest to derive. Starting with the following integral:

$$\left[\widehat{H}_{b'b}(\mathbf{k}_\parallel)\right]_{m'm} \propto \frac{1}{L} \int_{-L/2}^{L/2} \mathcal{A}(z) e^{-i(G_{m'} - G_m)z} \mathrm{d}z \tag{3.20}$$

where $\mathcal{A}$ is any position dependent parameter that is constant across a particular layer, including the strain ϵ_{ii}[1], we can then expand the term $\mathcal{A}$ using the characteristic function from Eq. (3.10) and make the substitution into the integral:

$$\begin{aligned} \mathcal{A}_b \frac{1}{L}\int_{-L/2}^{L/2} e^{-i(G_{m'}-G_m)z}\mathrm{d}z + (\mathcal{A}_w - \mathcal{A}_b)\,\frac{1}{L}\int_{-d/2}^{d/2} e^{-i(G_{m'}-G_m)z}\mathrm{d}z \\ = \mathcal{A}_b\delta_{mm'} + (\mathcal{A}_w - \mathcal{A}_b)\,\widetilde{\chi}(G_{m'} - G_m)\,. \end{aligned} \tag{3.21}$$

Terms of $H_{b'b} \propto \mathcal{A}(z)k_z$. These are the terms that appear in the **k·p** Hamiltonian in the form $H_{b'b} \propto k_z$. By making the substitution $k_z \to -i\frac{\mathrm{d}}{\mathrm{d}z}$ and applying symmetrisation in order to ensure a Hermitian Hamiltonian matrix we obtain

$$\begin{aligned} \frac{1}{L}\int_{-L/2}^{L/2} e^{-iG_{m'}z}\frac{1}{2}\left[\mathcal{A}(z)\frac{\mathrm{d}}{\mathrm{d}z} + \frac{\mathrm{d}}{\mathrm{d}z}\left(\mathcal{A}(z)\right)\right] e^{iG_m z}\mathrm{d}z \\ = \frac{iG_m}{2L}\int_{-L/2}^{L/2} \mathcal{A}(z)e^{-i(G_{m'}-G_m)z}\mathrm{d}z + \frac{1}{2L}\int_{-L/2}^{L/2} e^{-iG_{m'}z}\frac{\mathrm{d}}{\mathrm{d}z}\left[\mathcal{A}(z)e^{iG_m z}\right]\mathrm{d}z\,. \end{aligned} \tag{3.22}$$

The first term of this integral is then evaluated in the same way as was done for Eq. (3.20). For the second term we use integration by parts to obtain

$$\begin{aligned} \frac{1}{2L}\int_{-L/2}^{L/2} e^{-iG_{m'}z}\frac{\mathrm{d}}{\mathrm{d}z}\left[\mathcal{A}(z)e^{iG_m z}\right]\mathrm{d}z = \frac{1}{2L}\mathcal{A}(z)e^{-i(G_{m'}-G_m)z}\Big|_{-L/2}^{L/2} \\ + \frac{iG_{m'}}{2L}\int_{-L/2}^{L/2} \mathcal{A}(z)e^{-i(G_{m'}-G_m)z}\mathrm{d}z\,. \end{aligned} \tag{3.23}$$

It is important to note here that although the parameter $\mathcal{A}(z)$ is a step function, i.e. discontinuous at the layer interfaces, the periodic boundary conditions and the fact that we can expand it into a Fourier series, allow us to to perform the integration by parts. This integral then yields

$$-\frac{i\mathcal{A}_b}{L}\sin\left[(m-m')\pi\right] + \frac{iG_{m'}}{2}\left[\mathcal{A}_b\delta_{mm'} + (\mathcal{A}_w - \mathcal{A}_b)\,\widetilde{\chi}(G_{m'} - G_m)\right] \tag{3.24}$$

where we used the fact that $\mathcal{A}(L/2) = \mathcal{A}(-L/2) = \mathcal{A}_b$ and $G_m = \frac{2m\pi}{L}$. With the first term here becoming zero, we obtain the final result:

---

[1] This is different in the case of a QD- or QWR-based supercell, where the strain has a certain profile, which we discuss in Section 3.2.

$$\frac{1}{L}\int_{-L/2}^{L/2} e^{-iG_{m'}z}\widehat{H}_{b'b}(\mathbf{k}_{\|})e^{iG_m z}\mathrm{d}z = \frac{i(G_m+G_{m'})}{2}\mathcal{A}_b\delta_{mm'}+\frac{i(G_m+G_{m'})}{2}(\mathcal{A}_w-\mathcal{A}_b)\widetilde{\chi}(G_{m'}-G_m) \tag{3.25}$$

Terms of $H_{b'b} \propto \mathcal{A}(z)k_z^2$. These are the terms that appear in the **k·p** Hamiltonian in the form $H_{b'b} \propto k_z^2$. For this type of Hamiltonian matrix element the derivation of the method follows the exact same way as we have shown for the kinetic energy term of the 1-band model in Section 3.1.1, with the expansion becoming

$$\frac{1}{L}\int_{-L/2}^{L/2} e^{-iG_{m'}z}\widehat{H}_{b'b}(\mathbf{k}_{\|})e^{iG_m z}\mathrm{d}z = G_m G_{m'}\mathcal{A}_b\delta_{mm'} + G_m G_{m'}(\mathcal{A}_w-\mathcal{A}_b)\widetilde{\chi}(G_{m'}-G_m)\,. \tag{3.26}$$

3.1.3 Derivation of the method for multi-QW based heterostructures

So far, we focused on the derivation of the method for single QW based heterostructures. Here we consider a set of N QWs with a thickness d_q each and with the following characteristic function

$$\chi_q(z) = \begin{cases} 1\,, & z \in \left[a_q - \frac{d_q}{2}, a_q + \frac{d_q}{2}\right] \\ 0\,, & \text{otherwise} \end{cases} \tag{3.27}$$

where a_q is the position of the centre of each QW as shown in Fig. 3.2. We then define a material parameter $\mathcal{A}(z)$ using a set of characteristic functions

$$\mathcal{A}(z) = \mathcal{A}_b\left[1-\sum_{q=1}^{N}\chi_q(z)\right] + \mathcal{A}_q\sum_{q=1}^{N}\chi_q(z) = \mathcal{A}_b + \sum_{q=1}^{N}\chi_q(z)\left(\mathcal{A}_q-\mathcal{A}_b\right) \tag{3.28}$$

or, in other words, $\mathcal{A}(z) = \mathcal{A}_q$ in a particular QW and $\mathcal{A}(z) = \mathcal{A}_b$ in the barrier material. As we have seen from the previous section during the derivation of the plane wave representation of any Hamiltonian term we ended up evaluating the integral in Eq. (3.20). We rewrite this integral for a multi-QW case to obtain

$$\mathcal{A}_b\frac{1}{L}\int_{-L/2}^{L/2} e^{-i(G_{m'}-G_m)z}\mathrm{d}z + \sum_{q=1}^{N}\left(\mathcal{A}_q-\mathcal{A}_b\right)\frac{1}{L}\int_q e^{-i(G_{m'}-G_m)z}\mathrm{d}z \tag{3.29}$$

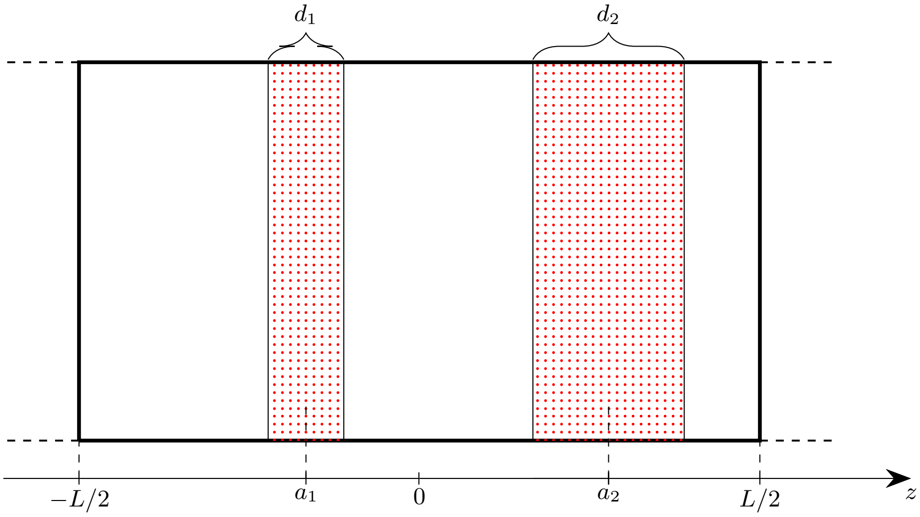

FIGURE 3.2: Schematic representation of a supercell with length L that contains two QWs of thickness d_1 and d_2. The centre of each QW is situated at a_1 and a_2 on the z axis, such that $\chi_1(z) \in [a_1 - d_1/2, a_1 + d_1/2]$ and $\chi_2(z) \in [a_2 - d_2/2, a_2 + d_2/2]$.

The integral in the first term here becomes the usual $\delta_{mm'}$. The domain of the second integral was changed from $\left[-\frac{L}{2}, \frac{L}{2}\right]$ to $q \in \left[a_q - \frac{d_q}{2}, a_q + \frac{d_q}{2}\right]$, because outside of this domain the integral is zero for a particular QW in the sum. When evaluating the different contributions to the second integral we assume for simplicity $G_{m'} - G_m = G$, to obtain

$$\begin{aligned} \frac{1}{L}\int_q e^{-iGz}\mathrm{d}z = -\frac{1}{L}\frac{1}{iG}e^{-iGz}\bigg|_q &= -\frac{1}{L}\frac{e^{-iGa_q}}{iG}\left(e^{-\frac{iGd_q}{2}} - e^{\frac{iGd_q}{2}}\right) \\ &= \frac{d_q}{L}\mathrm{sinc}\left(\frac{Gd_q}{2}\right)e^{-iGa_q} = \widetilde{\chi}_q(G)\,. \end{aligned} \tag{3.30}$$

We can see that Eq. (3.12) is a simplified form of (3.30) since in the former case we considered a symmetric QW with respect to the centre of the supercell ($a_q = 0$). Substituting this result into (3.20) we find the plane wave expansion for a material parameter $\mathcal{A}$ in a supercell with multiple QWs to be given by

$$\mathcal{A}_b\delta_{mm'} + \sum_{q=1}^{N}\left(\mathcal{A}_q - \mathcal{A}_b\right)\widetilde{\chi}_q(G_{m'} - G_m)\,. \tag{3.31}$$

3.2 Derivation of the method for quantum wire and dot based heterostructures

In this section we derive the semi-analytical expansion for three dimensional supercells that contain one or multiple QDs or QWRs. Here we define the characteristic function and its Fourier transform based on the periodic boundary conditions in three dimensions and provide the general expression for the expanded Hamiltonian matrix element. We then derive the Fourier transform of the strain tensor elements. Unlike in QW-based heterostructures where the strain tensor is assumed constant in a particular layer, the inclusion of a lattice-mismatched QD or QWR in the supercell results in a particular strain profile, which strongly depends upon the shape of the nanostructure. Having this expression derived, we then turn our attention to the expansion of the Pikus-Bir Hamiltonian matrix elements.

3.2.1 k·p Hamiltonian

We start the derivation of the method by considering a rectangular cuboid supercell with its body centre located at the origin of the Cartesian coordinate system, with the supercell size L_x, L_y, L_z along the x, y, z Cartesian axes respectively, and a material parameter $f(\mathbf{r}) = f(\mathbf{r}+\mathbf{R})$, with $\mathbf{R} = m_x L_x \mathbf{x} + m_y L_y \mathbf{y} + m_z L_z \mathbf{z}$, where $\mathbf{x}$, $\mathbf{y}$ and $\mathbf{z}$ are unit vectors along the corresponding Cartesian axes, and $m_x, m_y, m_z \in \mathbb{Z}$. Due to its periodicity along all three coordinate axes, the reciprocal vectors of the supercell are given by $\mathbf{G}_m = (G_{mx}, G_{my}, G_{mz})$ with

$$G_{mj} = \frac{2m_j\pi}{L_j} \tag{3.32}$$

where $j = x, y, z$. Using the vectors we then expand the 8-band eigenstate into the following series:

$$\psi_n(\mathbf{r}) = \frac{1}{\sqrt{\Omega_{\text{sc}}}} \sum_{m_x=-M_x}^{+M_x} \sum_{m_y=-M_y}^{+M_y} \sum_{m_z=-M_z}^{+M_z} \sum_{b=1}^{8} \widetilde{a}_{nb}(\mathbf{G}_m) e^{i\mathbf{G}_m\cdot\mathbf{r}} |u_b\rangle \,, \tag{3.33}$$

where Ω_{sc} is the volume of the supercell. In our QWR calculations later in the thesis, the wires are continous along the $x = \pm y$ direction; therefore we have to take into account the energy dispersion along $k_x = \pm k_y$. Because of the chosen Cartesian coordinate system (x, y, z), we ensure the periodic boudary conditions by having a set of reciprocal vectors $\mathbf{G}_j$ which include non-zero components for $j = x, y, z$. Consequently, computational expense to calculate $E_n(k_x = k_y)$ and $\psi_n(k_x = k_y)$ in a QWR increases significantly compared to a QW-based supercell given the three-dimensional expansion. Therefore, in our calculations we diagonalise the Hamiltonian only at $k_x = k_y = k_z = 0$ for both QD and QWR based heterostructures. One way to address this concern would be to use a different coordinate system (x', y', z), such that $x' = \frac{1}{\sqrt{2}}(x + y)$ and $y' = \frac{1}{\sqrt{2}}(-x + y)$. This would allow us to consider a two-dimensional supercell instead and to then only use two-dimensional reciprocal vectors. However, in this case we would need to rederive most of the method, including the expanded Hamiltonian and the Fourier transform of the strain tensor. Thus we use our existing plane wave framework, which will be consistent with all nanostructure shapes, including QWRs.

By looking at Eq. (3.33) we can already presume that the three-dimensional expansion will be more demanding computationally compared to the QW case due to the triple sum over m_x, m_y and m_z. In order to illustrate the evaluation of the integrals, in this section we will examine a supercell that contains a rectangular cuboid QD of size $d_x \times d_y \times d_z$, with its body centre located at the origin of the coordinate system and the coordinate axes perpendicular to its faces at the centre. As we have seen from Section 3.1, the shape of the nanostructure is incorporated using only the Fourier transform of its characteristic function. Fourier transforms of the characteristic functions used in this thesis will be given in Appendix D, where we also provide references for additional QD shapes. The characteristic function of the QD is expressed here then as

$$\chi_{\text{QD}}(\mathbf{r}) = \begin{cases} 1\,, & \mathbf{r} \in \Omega_{\text{QD}} \\ 0\,, & \text{otherwise} \end{cases} \tag{3.34}$$

where Ω_{QD} is the volume of the QD, and its Fourier transform is given by

$$\widetilde{\chi}_{\text{QD}}(\mathbf{G}) = \frac{1}{\Omega_{\text{sc}}} \int_{\Omega_{\text{QD}}} e^{-i\mathbf{G}\cdot\mathbf{r}} \mathrm{d}V\,, \tag{3.35}$$

with $\mathbf{G} = (G_x, G_y, G_z)$.

Following the procedure from Section 3.1.2, we introduce Eq. (3.34) and the expanded eigenstate (3.33) into Eq. (2.1), multiply both sides by $\frac{1}{\sqrt{\Omega_{\text{sc}}}} e^{-i\mathbf{G}_{m'}\cdot\mathbf{r}}$, integrate over the volume of the supercell and obtain the three dimensional plane wave expansion of the Hamiltonian matrix element:

$$(H_{b'b})_{m'm} = \frac{1}{\Omega_{\text{sc}}} \int_{\Omega_{\text{sc}}} e^{-i\mathbf{G}_{m'}\cdot\mathbf{r}} \widehat{H}_{b'b}(\mathbf{r}) e^{i\mathbf{G}_m\cdot\mathbf{r}} \mathrm{d}V\,. \tag{3.36}$$

Terms of $H_{b'b} \propto \mathcal{A}(\mathbf{r})$. Just like in the last section, the easiest point to start from is the expansion of the Hamiltonian matrix elements that are independent of the wave vector k_i. We define a position dependent parameter $\mathcal{A}(\mathbf{r})$ using Eq. (3.34)

$$\mathcal{A}(\mathbf{r}) = \mathcal{A}_b + \chi_{\text{QD}}(\mathbf{r})(\mathcal{A}_{\text{QD}} - \mathcal{A}_b) \tag{3.37}$$

where the index QD in $\mathcal{A}_{\text{QD}}$ indicates that this parameter corresponds to the QD structure. The plane wave representation of the Hamiltonian matrix term becomes

$$(H_{b'b})_{m'm} \propto \frac{1}{\Omega_{\text{sc}}} \int_{\Omega_{\text{sc}}} e^{-i\mathbf{G}_{m'}\cdot\mathbf{r}} \mathcal{A}(\mathbf{r}) e^{i\mathbf{G}_m\cdot\mathbf{r}} \mathrm{d}V\,. \tag{3.38}$$

By inserting Eq. (3.37) into (3.38) the integral becomes

$$\begin{aligned} &\mathcal{A}_b \delta_{xx'}\delta_{yy'}\delta_{zz'} + (\mathcal{A}_{\text{QD}} - \mathcal{A}_b)\frac{1}{\Omega_{\text{sc}}}\int_{\Omega_{\text{QD}}} e^{-i(\mathbf{G}_{m'}-\mathbf{G}_m)\cdot\mathbf{r}} \mathrm{d}V \\ &\qquad = \mathcal{A}_b\delta_{mm'} + (\mathcal{A}_{\text{QD}} - \mathcal{A}_b)\widetilde{\chi}_{\text{QD}}(\mathbf{G}_{m'} - \mathbf{G}_m) \end{aligned} \tag{3.39}$$

where the indices i and i' ($i = x, y, z$) in $\delta_{ii'}$ correspond to the ith component of the wave vectors $\mathbf{G}_m$ and $\mathbf{G}_{m'}$ respectively. To further simplify the form of the expanded terms we also made the substitution $\delta_{xx'}\delta_{yy'}\delta_{zz'} \to \delta_{mm'}$, i.e. the Kronecker delta equals to 1 when $\mathbf{G}_m = \mathbf{G}_{m'}$ and 0 otherwise. We then find the Fourier transform of the characteristic function of the cuboid QD:

$$\widetilde{\chi}_{\text{QD}}(\mathbf{G}) = \frac{\Omega_{\text{QD}}}{\Omega_{\text{sc}}} \text{sinc}\left(\frac{G_x d_x}{2}\right) \text{sinc}\left(\frac{G_y d_y}{2}\right) \text{sinc}\left(\frac{G_z d_z}{2}\right)\,. \tag{3.40}$$

Terms of $H_{b'b} \propto \mathcal{A}(\mathbf{r})k_j$. Unlike the previous section where we focused on the one-dimensional electron confinement along the growth direction z, the electronic structure calculations in a three-dimensional potential requires the substitution of all wave vectors k_j with their respective partial derivative $k_j \to -i\frac{\partial}{\partial j}$. By making this substitution into the corresponding Hamiltonian term, we apply here, by analogy with the previous section, matrix element symmetrisation and obtain the following expansion:

$$\begin{aligned} &\frac{iG_{mj}}{2\Omega_{\text{sc}}} \int_{\Omega_{\text{sc}}} \mathcal{A}(\mathbf{r}) e^{-i(\mathbf{G}_{m'}-\mathbf{G}_m)\cdot\mathbf{r}} \mathrm{d}V + \frac{1}{2\Omega_{\text{sc}}}\int_{\Omega_{\text{sc}}} e^{-i\mathbf{G}_{m'}\cdot\mathbf{r}} \frac{\partial}{\partial j}\left[\mathcal{A}(\mathbf{r})e^{i\mathbf{G}_m\cdot\mathbf{r}}\right] \mathrm{d}V \\ &= \frac{i(G_{mj} + G_{m'j})}{2}\mathcal{A}_b\delta_{mm'} + \frac{i(G_{mj} + G_{m'j})}{2}\left(\mathcal{A}_{\text{QD}} - \mathcal{A}_b\right)\widetilde{\chi}_{\text{QD}}(\mathbf{G}_{m'} - \mathbf{G}_m)\,. \end{aligned} \tag{3.41}$$

To evaluate the second integral here we used the fact that $\mathcal{A}(-L_j/2) = \mathcal{A}(L_j/2) = \mathcal{A}_b$.

Terms of $H_{b'b} \propto \mathcal{A}(\mathbf{r})k_j k_{j'}$ and $H_{b'b} \propto \mathcal{A}(\mathbf{r})k_j^2$. Here we start by deriving the plane wave expansion of $\mathbf{k}{\cdot}\mathbf{p}$ Hamiltonian matrix elements that depend upon the product of different wave vectors $k_j k_{j'}$. We expand the Hamiltonian matrix element by applying the symmetrisation in the following form:

$$\begin{aligned}
&-\frac{1}{2\Omega_{\mathrm{sc}}}\int_{\Omega_{\mathrm{sc}}} e^{-i\mathbf{G}_{m'}\cdot\mathbf{r}}\frac{\partial}{\partial j}\left[\mathcal{A}(\mathbf{r})\frac{\partial}{\partial j'}e^{i\mathbf{G}_m\cdot\mathbf{r}}\right]\mathrm{d}V-\frac{1}{2\Omega_{\mathrm{sc}}}\int_{\Omega_{\mathrm{sc}}} e^{-i\mathbf{G}_{m'}\cdot\mathbf{r}}\frac{\partial}{\partial j'}\left[\mathcal{A}(\mathbf{r})\frac{\partial}{\partial j}e^{i\mathbf{G}_m\cdot\mathbf{r}}\right]\mathrm{d}V\\
&\quad=-\frac{iG_{mj'}}{2\Omega_{\mathrm{sc}}}\int_{\Omega_{\mathrm{sc}}} e^{-i\mathbf{G}_{m'}\cdot\mathbf{r}}\frac{\partial}{\partial j}\left[\mathcal{A}(\mathbf{r})e^{i\mathbf{G}_m\cdot\mathbf{r}}\right]\mathrm{d}V-\frac{iG_{mj}}{2\Omega_{\mathrm{sc}}}\int_{\Omega_{\mathrm{sc}}} e^{-i\mathbf{G}_{m'}\cdot\mathbf{r}}\frac{\partial}{\partial j'}\left[\mathcal{A}(\mathbf{r})e^{i\mathbf{G}_m\cdot\mathbf{r}}\right]\mathrm{d}V\,.
\end{aligned}\tag{3.42}$$

We then use the integration by parts as we have done for Eq. (3.14) to obtain the expanded Hamiltonian matrix element:

$$\frac{G_{mj'}G_{m'j}+G_{mj}G_{m'j'}}{2}\mathcal{A}_b\delta_{mm'}+\frac{G_{mj'}G_{m'j}+G_{mj}G_{m'j'}}{2}\left(\mathcal{A}_{\mathrm{QD}}-\mathcal{A}_b\right)\widetilde{\chi}(\mathbf{G}_{m'}-\mathbf{G}_m)\tag{3.43}$$

We notice that when $j=j'$, i.e. the Hamiltonian term has the form $\widehat{H}\propto\mathcal{A}(\mathbf{r})k_j^2$ is a special case of Eq. (3.43) and the expanded Hamiltonian term looks very similar to Eq. (3.14)

$$(G_{mj}G_{m'j})\mathcal{A}_b\delta_{mm'}+(G_{mj}G_{m'j})\left(\mathcal{A}_{\mathrm{QD}}-\mathcal{A}_b\right)\widetilde{\chi}_{\mathrm{QD}}(\mathbf{G}_{m'}-\mathbf{G}_m)\,.\tag{3.44}$$

3.2.2 Fourier transform of the strain tensor

In this section we derive the Fourier transform of the strain tensor elements in a QD-based heterostructure with its components having zincblende crystal structure. Originally this method was used to evaluate the Fourier transform of Green's tensor by Lifshits and Rosenzweig [120], and later extended to the strain tensor by Andreev *et al.* [80]. We follow here the approach used in Ref. [80] to derive the Fourier transform of the strain tensor.

The Green's tensor G_{ln} at a point $\mathbf{r}$ denotes the displacement along the l direction due to a point force along the n direction at $\mathbf{r}$, and, given an infinte anisotropic elastic medium, is the solution of the equation [120]

$$C_{iklm}\frac{\partial^2 G_{ln}(\mathbf{r})}{\partial x_k\partial x_m}=-\delta(\mathbf{r})\delta_{in}\,,\tag{3.45}$$

where C_{iklm} is the elastic tensor, $\delta(\mathbf{r})$ and δ_{in} are the Dirac and Kronecker deltas respectively, and the boundary conditions are $|\mathbf{r}| \to \infty \implies G_{ln}(\mathbf{r}) \to 0$. Here we introduce the inverse Fourier transform of the Green's tensor

$$G_{ln}(\mathbf{r}) = \int_{-\infty}^{+\infty} \widetilde{G}_{ln}(\boldsymbol{\xi}) e^{i\boldsymbol{\xi}\cdot\mathbf{r}} \mathrm{d}\boldsymbol{\xi}\,, \tag{3.46}$$

and integral form of the Dirac delta

$$\delta(\mathbf{r}) = \frac{1}{(2\pi)^3} \int_{-\infty}^{+\infty} e^{i\boldsymbol{\xi}\cdot\mathbf{r}} \mathrm{d}\boldsymbol{\xi}\,, \tag{3.47}$$

where both integrals are performed over all space. We note here that throughout the derivation process G will denote the Green's tensor instead of the reciprocal vector from Section 3.2.1, though we will make use of the reciprocal vector $\mathbf{G}$ at a later point in this section. By substituting Eqs. (3.46) and (3.47) into (3.45) we obtain

$$C_{iklm} \widetilde{G}_{ln}(\boldsymbol{\xi}) \xi_k \xi_m = \frac{\delta_{in}}{(2\pi)^3}\,. \tag{3.48}$$

Here and throughout the entire chapter we use Einstein's notation for summation over 1–3 for the repeated indices, unless the summation is indicated explicitly. In order to find the strain in a QD structure, the method of inclusion proposed by Eshelby [121] is used here:

$$u_i^{(s)}(\mathbf{r}) = u_i^T \chi(\mathbf{r}) + \int G_{in}(\mathbf{r} - \mathbf{r'})\, \sigma_{nk}^T \, \mathrm{d}S_k'\,, \tag{3.49}$$

where $\sigma_{nk}^T = C_{nkpr} \epsilon_{pr}^T$, and σ_{nk}^T, ϵ_{pr}^T and u_i^T are the components of the stress and strain tensors and the displacement caused by the "initial" strain due to the lattice mismatch. The superscript (s) indicates that this expression means that there is only one QD in the anisotropic medium. Using Gauss' theorem, Eq. (3.49) can be written as:

$$u_i^{(s)}(\mathbf{r}) = u_i^T \chi(\mathbf{r}) + \int_{\mathrm{QD}} \frac{\partial}{\partial x_k} G_{in}(\mathbf{r} - \mathbf{r'})\, C_{nkpr}\, \epsilon_{pr}^T \mathrm{d}V'\,. \tag{3.50}$$

In order to find the final expression for the Fourier transform of the strain tensor we consider the elastic tensor C_{nkpr} to be constant throughout the entire medium and corresponding to the barrier material [2], thereby applying the divergence only to the Green's tensor. A method to calculate the Fourier transform of the strain tensor which takes into account different elastic tensors in the barrier and QD is presented in Ref. [122]. However the approximation in this section strongly reduces the computational expenses of strain calculations, and we expect that it will have an insignificant impact on the results of our calculations given the small difference between the actual strain tensors of the barrier and QD. Here we recall the definition of the elements of the strain tensor ϵ_{ij}

---

[2] We consider different elastic tensors in the barrier and QW for the electronic structure calculations under strain in Chapters 4 and 6, where we expand the step-like distribution of strain in the supercell using the QW characteristic function (cf. Section 3.1.2).

$$\epsilon_{ij}(\mathbf{r}) = \frac{1}{2}\left[\frac{\partial u_i(\mathbf{r})}{\partial x_j} + \frac{\partial u_j(\mathbf{r})}{\partial x_i}\right] . \tag{3.51}$$

By substituting Eq. (3.50) and a similar expression for $u_j^{(s)}$ into (3.51), we obtain

$$\epsilon_{ij}^{(s)}(\mathbf{r}) = \epsilon_{ij}^{T}\chi(\mathbf{r}) + \frac{1}{2}C_{nkpr}\epsilon_{pr}^{T}\int_{\text{QD}}\left[\frac{\partial^2 G_{in}(\mathbf{r}-\mathbf{r'})}{\partial x_j \partial x_k} + \frac{\partial^2 G_{jn}(\mathbf{r}-\mathbf{r'})}{\partial x_i \partial x_k}\right]\mathrm{d}V' . \tag{3.52}$$

For the first term in Eq. (3.52) we made use of the fact that the “initial” displacement (or lattice mismatch) is present only in the QD according to the definition of χ from Eq. (3.34). To evaluate the integral in the second term we apply the following substitution:

$$\begin{aligned} \frac{\partial^2 G_{in}(\mathbf{r}-\mathbf{r'})}{\partial x_k \partial x_j} &= G_{in,kj}(\mathbf{r}-\mathbf{r'}) , \\ \frac{\partial^2 G_{jn}(\mathbf{r}-\mathbf{r'})}{\partial x_k \partial x_i} &= G_{jn,ki}(\mathbf{r}-\mathbf{r'}) , \end{aligned} \tag{3.53}$$

and rewrite the integral to find

$$\int_{-\infty}^{+\infty}\chi(\mathbf{r'})\left[G_{in,jk}(\mathbf{r}-\mathbf{r'}) + G_{jn,ik}(\mathbf{r}-\mathbf{r'})\right]\mathrm{d}V' = \chi(\mathbf{r}) * \left[G_{in,jk}(\mathbf{r}) + G_{jn,ik}(\mathbf{r})\right] . \tag{3.54}$$

where the asterisk sign denotes the convolution. By substituting Eq. (3.54) into (3.52), using the definition of the Fourier transform (3.46) for $\epsilon(\mathbf{r})$ and $G(\mathbf{r})$, expressing $\chi(\mathbf{r})$ using (3.47) for normalisation and taking into account the convolution theorem, we obtain

$$\widetilde{\epsilon}_{ij}^{(s)}(\boldsymbol{\xi}) = \epsilon_{ij}^{T}\widetilde{\chi}(\boldsymbol{\xi}) - \frac{(2\pi)^3}{2}\widetilde{\chi}(\boldsymbol{\xi})C_{nkpr}\epsilon_{pr}^{T}\xi_k\left[\xi_j\widetilde{G}_{in}(\boldsymbol{\xi}) + \xi_i\widetilde{G}_{jn}(\boldsymbol{\xi})\right] . \tag{3.55}$$

Eq. (3.55) gives the general expression for the Fourier transform of the strain tensor in a structure containing a single QD of arbitrary shape, which is described by the Fourier transform of the characteristic function $\widetilde{\chi}$. We now treat the specific case of zincblende semiconductors which have a cubic crystal symmetry. Here the elastic tensor has three independent components and can be represented in the form

$$C_{iklm} = C_{12}\delta_{ik}\delta_{lm} + C_{44}\left(\delta_{il}\delta_{mk} + \delta_{im}\delta_{lk}\right) + C_{an}\sum_{p=1}^{3}\delta_{ip}\delta_{kp}\delta_{lp}\delta_{mp}\,. \tag{3.56}$$

where C_{11}, C_{12} and C_{44} are the elastic constants, and $C_{an} = C_{11} - C_{12} - 2\,C_{44}$ describes the anisotropic part of the tensor. In the isotropic case, i.e. $C_{an} = 0$, C_{12} and C_{44} represent the Lamé parameters λ and μ respectively [123]. By substituting Eq. (3.56) into (3.48) we derive

$$\sum_{l=1}^{3}\left[(C_{12}+C_{44})\xi_i\xi_l + C_{44}\delta_{il}|\boldsymbol{\xi}|^2 + C_{an}\delta_{il}\xi_i^2\right]\widetilde{G}_{ln}(\boldsymbol{\xi}) = \frac{\delta_{in}}{(2\pi)^3}\,. \tag{3.57}$$

The derivation of Eq. (3.57) involves algebraic operations with many Kronecker delta functions, which we will skip. We introduce here the dot product $\left[\boldsymbol{\xi}\cdot\widetilde{G}(\boldsymbol{\xi})\right]_n = \sum_{l=1}^{3}\xi_l\widetilde{G}_{ln}(\boldsymbol{\xi})$ and take into account the δ_{il} in the sum, which yields

$$(C_{12}+C_{44})\,\xi_i\left[\boldsymbol{\xi}\cdot\widetilde{G}(\boldsymbol{\xi})\right]_n + \left(C_{44}|\boldsymbol{\xi}|^2 + C_{an}\xi_i^2\right)\widetilde{G}_{in}(\boldsymbol{\xi}) = \frac{\delta_{in}}{(2\pi)^3}\,. \tag{3.58}$$

We rewrite this equation for $\widetilde{G}_{in}(\boldsymbol{\xi})$ to obtain

$$\widetilde{G}_{in}(\boldsymbol{\xi}) = \frac{\delta_{in}/(2\pi)^3 - (C_{12}+C_{44})\xi_i\left[\boldsymbol{\xi}\cdot\widetilde{G}(\boldsymbol{\xi})\right]_n}{C_{44}|\boldsymbol{\xi}|^2 + C_{an}\xi_i^2}\,. \tag{3.59}$$

We multiply both sides of Eq. (3.59) by ξ_i, perform the sum over i and solve for $\left[\boldsymbol{\xi}\cdot\widetilde{G}(\boldsymbol{\xi})\right]_n$:

$$\left[\boldsymbol{\xi}\cdot\widetilde{G}(\boldsymbol{\xi})\right]_n = \frac{1}{(2\pi)^3}\frac{\xi_n}{C_{44}|\xi|^2 + C_{an}\xi_n^2}\left[1 + (C_{12}+C_{44})\sum_{i=1}^{3}\frac{\xi_i^2}{C_{44}|\xi|^2 + C_{an}\xi_i^2}\right]^{-1}\,. \tag{3.60}$$

We then substitute Eq. (3.60) into (3.59) to obtain the final form of the Fourier transform of the Green's tensor

$$\begin{aligned}\widetilde{G}_{in}(\boldsymbol{\xi}) = \frac{\delta_{in}}{(2\pi)^3}\frac{1}{C_{44}|\xi|^2 + C_{an}\xi_n^2} - \frac{(C_{12}+C_{44})\xi_i\xi_n}{(C_{44}|\xi|^2 + C_{an}\xi_i^2)(C_{44}|\xi|^2 + C_{an}\xi_n^2)}\\ \times\left[1 + (C_{12}+C_{44})\sum_{i=1}^{3}\frac{\xi_i^2}{C_{44}|\xi|^2 + C_{an}\xi_i^2}\right]^{-1}\,.\end{aligned} \tag{3.61}$$

The "initial" strain in a crystal with cubic symmetry is given by:

$$\epsilon_{pr}^{T} = \frac{a_b - a_{\mathrm{QD}}}{a_{\mathrm{QD}}}\delta_{pr} = \epsilon_0 \delta_{pr}\,, \tag{3.62}$$

where a_b and a_{QD} are the unstrained lattice constants of the barrier and QD materials respectively. Combining this with the elastic tensor gives the following expression:

$$C_{nkpr}\epsilon_{pr}^{T} = \epsilon_0 (C_{11} + 2\,C_{12})\delta_{nk}\,. \tag{3.63}$$

By including Eqs. (3.62) and (3.63) into Eq. (3.55) we obtain

$$\widetilde{\epsilon}_{ij}^{(s)}(\boldsymbol{\xi}) = \epsilon_0 \widetilde{\chi}(\boldsymbol{\xi}) \left\{ \delta_{ij} - \frac{(2\pi)^3}{2}(C_{11} + 2\,C_{12}) \left[\xi_i \left[\boldsymbol{\xi} \cdot \widetilde{G}(\boldsymbol{\xi}) \right]_j + \xi_j \left[\boldsymbol{\xi} \cdot \widetilde{G}(\boldsymbol{\xi}) \right]_i \right] \right\}. \tag{3.64}$$

We substitute here Eq. (3.60) and obtain the final form the Fourier transform of the strain tensor for a single QD:

$$\begin{split}\widetilde{\epsilon}_{ij}^{(s)}(\boldsymbol{\xi}) = \epsilon_0 \widetilde{\chi}(\boldsymbol{\xi}) \Bigg\{ \delta_{ij} - \frac{1}{2}(C_{11} + 2\,C_{12}) \left[\frac{\xi_i \xi_j}{C_{44}|\boldsymbol{\xi}|^2 + C_{an}\xi_i^2} + \frac{\xi_i \xi_j}{C_{44}|\boldsymbol{\xi}|^2 + C_{an}\xi_j^2} \right] \\ \times \left[1 + (C_{12} + C_{44}) \sum_{p=1}^{3} \frac{\xi_p^2}{C_{44}|\xi|^2 + C_{an}\xi_p^2} \right]^{-1} \Bigg\}.\end{split} \tag{3.65}$$

Due to the linearity of the elastic problem, the strain field in an infinite medium that contains multiple QDs is simply expressed as the superposition of the strain field due to the individual QDs, i.e.

$$\epsilon_{ij}^{(m)}(\mathbf{r}) = \sum_{\infty} \epsilon_{ij}^{(s)}(\mathbf{r}) \tag{3.66}$$

In this work we consider infinitely periodic supercells with volume Ω_{sc} that contain one (or multiple, if necessary) QDs. Here we multiply both sides of Eq. (3.66) by $\frac{e^{-i\mathbf{G}\cdot\mathbf{r}}}{\Omega_{\mathrm{sc}}}$, where $\mathbf{G}$ is the reciprocal vector from Section 3.2.1, and we integrate over the supercell space

$$\begin{split}\widetilde{\epsilon}_{ij}^{(m)}(\mathbf{G}) = \sum_{\infty} \frac{1}{\Omega_{\mathrm{sc}}} \int_{\Omega_{\mathrm{sc}}} \epsilon_{ij}^{(s)}(\mathbf{r}) e^{-i\mathbf{G}\cdot\mathbf{r}} \mathrm{d}V = \sum_{\infty} \frac{1}{(2\pi)^3} \int_{\boldsymbol{\xi}} \widetilde{\epsilon}_{ij}^{(s)}(\boldsymbol{\xi}) \frac{1}{\Omega_{\mathrm{sc}}} \int_{\Omega_{\mathrm{sc}}} e^{-i(\mathbf{G}-\boldsymbol{\xi})\cdot\mathbf{r}} \mathrm{d}V \mathrm{d}\boldsymbol{\xi} \\ = \frac{1}{(2\pi)^3} \int_{\boldsymbol{\xi}} \widetilde{\epsilon}_{ij}^{(s)}(\mathbf{G}) \mathrm{d}\xi = \widetilde{\epsilon}_{ij}^{(s)}(\mathbf{G})\,,\end{split} \tag{3.67}$$

where $\widetilde{\epsilon}_{ij}^{(s)}(\mathbf{G})$ has the form of Eq. (3.65), in which $\widetilde{\chi}$ is now Eq. (3.35). For the left-hand side we also used the definition of the Fourier transform from Eq. (3.35).

From Eq. (3.65) we see that an apparent singularity occurs with $|\mathbf{G}| = 0$. In this case we assume for growth on a substrate with lattice constant a_b that the diagonal terms of the strain tensor are:

$$\begin{aligned} \widetilde{\epsilon}_{xx}(|\mathbf{G}|=0) = \widetilde{\epsilon}_{yy}(|\mathbf{G}|=0) &= \frac{a_b - a_{\mathrm{QD}}}{a_{\mathrm{QD}}} \widetilde{\chi}(|\mathbf{G}|=0) \\ \widetilde{\epsilon}_{zz}(|\mathbf{G}|=0) &= -\frac{2\,C_{12}}{C_{11}}\,\widetilde{\epsilon}_{xx}(|\mathbf{G}|=0)\,, \end{aligned} \tag{3.68}$$

and we set the off-diagonal terms to be zero. This expansion then allows us to treat pseudomorphic growth and to use the Fourier series to estimate the position dependent strain tensor, which we will discuss in the next section.

3.2.3 Pikus-Bir Hamiltonian

In this section we will be deriving the plane wave expansion of the Pikus-Bir Hamiltonian terms. As we mentioned in Section 2.3, the pseudomorphic strain in a supercell with a QW is assumed constant within a particular layer, therefore it can be expressed using the characteristic function $\chi(z)$ as

$$\epsilon_{\alpha\alpha}(z) = \epsilon^{b}_{\alpha\alpha} + \chi(z)\left(\epsilon^{w}_{\alpha\alpha} - \epsilon^{b}_{\alpha\alpha}\right)\,. \tag{3.69}$$

where $\alpha = x, y, z$, and the superscripts b and w correspond to the barrier and QW layer respectively. When a supercell with a QD is considered the strain follows a certain profile across the supercell. Hence, we define the elements of the strain tensor $\epsilon_{\alpha\beta}$ here using the Fourier series

$$\epsilon_{\alpha\beta}(\mathbf{r}) = \sum_{n_x=-M_x}^{+M_x}\sum_{n_y=-M_y}^{+M_y}\sum_{n_z=-M_z}^{+M_z} \widetilde{\epsilon}_{\alpha\beta}(\mathbf{G}_n)e^{i\mathbf{G}_n\cdot\mathbf{r}} = \sum_{n}\widetilde{\epsilon}_{\alpha\beta}(\mathbf{G}_n)e^{i\mathbf{G}_n\cdot\mathbf{r}} \tag{3.70}$$

where $\widetilde{\epsilon}_{\alpha\beta}(\mathbf{G}_n)$ is the Fourier transform of the strain, as derived in Section 3.2.2. The Fourier series here was written using a single sum over all possible reciprocal vectors in order to simplify the equations. By looking at the Pikus-Bir Hamiltonian from Section 2.3 we notice that it contains only two types of matrix elements, $H_{b'b} \propto \mathcal{A}(\mathbf{r})\epsilon_{\alpha\beta}(\mathbf{r})$ and $H_{b'b} \propto \mathcal{A}(\mathbf{r})\epsilon_{\alpha\beta}(\mathbf{r})k_j$.

Terms of $H_{b'b} \propto \mathcal{A}(\mathbf{r})\epsilon_{\alpha\beta}(\mathbf{r})$ We start with the matrix elements that are independent of k_j.

$$\begin{aligned} (H_{b'b})_{m'm} &\propto \frac{1}{\Omega_{\text{sc}}}\int_{\Omega_{\text{sc}}} e^{-i\mathbf{G}_{m'}\cdot\mathbf{r}}\mathcal{A}(\mathbf{r})\epsilon_{\alpha\beta}(\mathbf{r})e^{i\mathbf{G}_m\cdot\mathbf{r}}\mathrm{d}V \\ = \mathcal{A}_b\frac{1}{\Omega_{\text{sc}}}\int_{\Omega_{\text{sc}}} \epsilon_{\alpha\beta}(\mathbf{r})e^{-i(\mathbf{G}_{m'}-\mathbf{G}_m)\cdot\mathbf{r}}\mathrm{d}V &+ (\mathcal{A}_{\text{QD}}-\mathcal{A}_b)\frac{1}{\Omega_{\text{sc}}}\int_{\Omega_{\text{QD}}} \epsilon_{\alpha\beta}(\mathbf{r})e^{-i(\mathbf{G}_{m'}-\mathbf{G}_m)\cdot\mathbf{r}}\mathrm{d}V\,. \end{aligned} \tag{3.71}$$

We simplify the evaluation of these integrals by making the substitution $\mathbf{G}_{m'}-\mathbf{G}_m \rightarrow \mathbf{G}_\mu$, where $\mu_j \in [-2M_j, +2M_j]$. By inserting Eq. (3.70) with the reciprocal vectors limits $n_j \in [-M_j, +M_j]$ into the first integral we obtain

$$\begin{aligned} &\mathcal{A}_b\frac{1}{\Omega_{\text{sc}}}\sum_n \widetilde{\epsilon}_{\alpha\beta}(\mathbf{G}_n)\int_{\Omega_{\text{sc}}} e^{-i(\mathbf{G}_\mu-\mathbf{G}_n)\cdot\mathbf{r}}\mathrm{d}V \\ &= \mathcal{A}_b\sum_n \widetilde{\epsilon}_{\alpha\beta}(\mathbf{G}_n)\delta(G_{\mu x}, G_{nx})\delta(G_{\mu y}, G_{ny})\delta(G_{\mu z}, G_{nz}) \end{aligned} \tag{3.72}$$

Here δ represents the Kronecker delta, and taking into account that the domain of $\mathbf{G}_\mu$ is larger than $\mathbf{G}_n$, the result of the integration becomes

$$\begin{cases} \mathcal{A}_b\widetilde{\epsilon}_{\alpha\beta}(\mathbf{G}_\mu)\,, & |G_{\mu j}| \leq \frac{2n_j\pi}{L_j} \\ 0\,, & \text{otherwise} \end{cases} \tag{3.73}$$

We make the same substitutions into the second integral from Eq. (3.71) which becomes

$$\begin{aligned} &(\mathcal{A}_{\text{QD}}-\mathcal{A}_b)\frac{1}{\Omega_{\text{sc}}}\sum_n \widetilde{\epsilon}_{\alpha\beta}(\mathbf{G}_n)\int_{\Omega_{\text{QD}}} e^{-i(\mathbf{G}_\mu-\mathbf{G}_n)\cdot\mathbf{r}}\mathrm{d}V \\ &= (\mathcal{A}_{\text{QD}}-\mathcal{A}_b)\sum_n \widetilde{\epsilon}_{\alpha\beta}(\mathbf{G}_n)\widetilde{\chi}_{\text{QD}}(\mathbf{G}_\mu-\mathbf{G}_n)\,. \end{aligned} \tag{3.74}$$

The final result can be written in the following way:

$$\mathcal{A}_b\widetilde{\epsilon}_{\alpha\beta}(\mathbf{G}_{m'}-\mathbf{G}_m) + (\mathcal{A}_{\text{QD}}-\mathcal{A}_b)\sum_n \widetilde{\epsilon}_{\alpha\beta}(\mathbf{G}_n)\widetilde{\chi}_{\text{QD}}(\mathbf{G}_{m'}-\mathbf{G}_m-\mathbf{G}_n)\,, \tag{3.75}$$

where we keep in mind that the first term becomes 0 if $|G_{m'j}-G_{mj}| > \frac{2n_j\pi}{L_j}$. We can see that the plane wave expansion of the Pikus-Bir Hamiltonian matrix elements results in a sum over $(2M_x+1)\times(2M_y+1)\times(2M_z+1)$ reciprocal vectors. Compared to the expansion of the $\mathbf{k}{\cdot}\mathbf{p}$

Hamiltonian, the time it takes to computationally evaluate each term in the $(2M_x+1)\times(2M_y+1)\times(2M_z+1)$ order matrix increases considerably. Because the Fourier transform of the strain tensor matrix element decays rapidly at larger n_j, we decided to reduce the computational expenses by using the Fourier series with $n_j \in [-M_j, +M_j]$.

Terms of $H_{b'b} \propto \mathcal{A}(\mathbf{r})\epsilon_{\alpha\beta}(\mathbf{r})k_j$ In order to expand the Pikus-Bir Hamiltonian matrix elements that take the form $H_{b'b} \propto \mathcal{A}(\mathbf{r})\epsilon_{\alpha\beta}(\mathbf{r})k_j$ we use the symmetrisation technique when making the substitution $k_j \rightarrow -i\frac{\partial}{\partial j}$, leading to the the evaluation of the following two integrals

$$\begin{aligned}(H_{b'b})_{m'm} \propto & \frac{iG_{mj}}{2}\frac{1}{\Omega_{\text{sc}}}\int_{\Omega_{\text{sc}}} \epsilon_{\alpha\beta}(\mathbf{r})\mathcal{A}(\mathbf{r})e^{i(\mathbf{G}_{m'}-\mathbf{G}_m)\cdot\mathbf{r}}\mathrm{d}V \\ & +\frac{1}{2}\frac{1}{\Omega_{\text{sc}}}\int_{\Omega_{\text{sc}}} e^{-i\mathbf{G}_{m'}\cdot\mathbf{r}}\frac{\partial}{\partial j}\left[\epsilon_{\alpha\beta}(\mathbf{r})\mathcal{A}(\mathbf{r})e^{i\mathbf{G}_m\cdot\mathbf{r}}\right]\mathrm{d}V\,.\end{aligned} \tag{3.76}$$

The first term of this expansion can be found similarly to the terms discussed earlier. For the second term we perform the integration by parts and, taking into account the fact that $\epsilon_{\alpha\beta}(L_j/2)\mathcal{A}(L_j/2) = \epsilon_{\alpha\beta}(-L_j/2)\mathcal{A}(-L_j/2)$, the final result becomes

$$\frac{i\left(G_{mj}+G_{m'j}\right)}{2}\left[\mathcal{A}_b\widetilde{\epsilon}_{\alpha\beta}(\mathbf{G}_{m'}-\mathbf{G}_m)+(\mathcal{A}_{\text{QD}}-\mathcal{A}_b)\sum_n \widetilde{\epsilon}_{\alpha\beta}(\mathbf{G}_n)\widetilde{\chi}_{\text{QD}}(\mathbf{G}_{m'}-\mathbf{G}_m-\mathbf{G}_n)\right] \tag{3.77}$$

where the first term in the square bracket becomes 0 if $|G_{m'j}-G_{mj}| > \frac{2n_j\pi}{L_j}$.

3.3 Carrier-induced self-consistent electrostatic potential

Throughout this thesis we assume the thermal distribution of electrons and holes within their corresponding states in a QW that can be described using the Fermi-Dirac distribution, according to which the occupation probability of a particular state $E_{e,h}$ at a particular wave vector $\mathbf{k}_{\|}$ is expressed as:

$$f_{e,h}\left[E_{n_{e,h}}(\mathbf{k}_{\|}), F_{e,h}\right] = \frac{1}{1+\exp\frac{(-1)^p[E_{n_{e,h}}(\mathbf{k}_{\|})-F_{e,h}]}{k_BT}}\,, \tag{3.78}$$

where the indices e and h correspond to the electrons and holes respectively, $F_{e,h}$ is the quasi-Fermi level and $p = 0$ (1) for electrons (holes). Assuming that the band dispersion is isotropic in the QW plane (depending only on the magnitude of $\mathbf{k}_\parallel$, i.e. $k_\parallel = |\mathbf{k}_\parallel|$), the position-dependent electron and hole carrier density is then given by

$$n(z) = \frac{1}{2\pi L} \sum_{n_e} \int_{k_\parallel} \left|\psi_{n_e}(z, k_\parallel)\right|^2 f\left[E_{n_e}(k_\parallel), F_e\right] k_\parallel \mathrm{d}k_\parallel \tag{3.79}$$

$$p(z) = \frac{1}{2\pi L} \sum_{n_h} \int_{k_\parallel} \left|\psi_{n_h}(z, k_\parallel)\right|^2 f\left[E_{n_h}(k_\parallel), F_h\right] k_\parallel \mathrm{d}k_\parallel \,, \tag{3.80}$$

which determine the position dependent charge density $\rho(z) = e\left[p(z) - n(z)\right]$, with the choice of quasi-Fermi energies then determining the areal carrier density

$$\begin{aligned} \int_{-L/2}^{L/2} n(z)\mathrm{d}z &= n_{2\mathrm{D}} \\ \int_{-L/2}^{L/2} p(z)\mathrm{d}z &= p_{2\mathrm{D}} \end{aligned} \tag{3.81}$$

In our calculations we assume charge neutrality, i.e. $n_{2\mathrm{D}} = p_{2\mathrm{D}}$. In a typical type-I heterostructure, where both conduction and valence band offsets are large enough to not allow significant spillover of the bound eigenstates into the barrier layer, the magnitude of the position-dependent charge density $\rho(z)$ is close to 0 for all z. However, in type-I heterostructures with a very small magnitude of, e.g., conduction band offset, or type-II structures where the electrons and holes are confined in different layers, the resulting non-zero charge density generates an electrostatic potential across the supercell $\phi(z)$. This electrostatic potential can be understood as arising from the Coulomb attraction between opposite charges due to their spatial separation, and is described using Poisson's second order linear differential equation

$$\frac{\mathrm{d}}{\mathrm{d}z}\left[\varepsilon_r(z)\frac{\mathrm{d}}{\mathrm{d}z}\phi(z)\right] = \frac{\rho(z)}{\varepsilon_0} \,, \tag{3.82}$$

where $\rho(z)$ is the charge density, and $\varepsilon_r(z)$ and ε_0 are the relative permittivity and vacuum permittivity respectively. This electrostatic potential $\phi(z)$ then enters the Schrödinger equation (2.6) as a position-dependent potential energy term $V(z) = -e\phi(z)$, which needs to be calculated self-consistently. The structures we investigate in this thesis have type-I $\Gamma - \Gamma$ confinement, i.e. the bound Γ electrons and holes are confined in the same layer, e.g. QW. However, as we will show in Chapter 6, when considering AlGaInP red-emitting heterostructures (i) the bulk conduction band edges in the Γ and X valleys of the barrier layer ($E_{c_b}^{\Gamma}$ and $E_{c_b}^{\mathrm{X}}$ respectively) in our calculations are either close to degenerate or can even have $E_{c_b}^{\mathrm{X}} < E_{c_b}^{\Gamma}$, and (ii) the X conduction band offset is often negative, i.e. $\Delta E_c^{\mathrm{X}} = E_{c_b}^{\mathrm{X}} - E_{c_{qw}}^{\mathrm{X}} < 0$. The X band edge in the QW therefore acts as a potential barrier for the electrons in the barrier layer, and we assume in our calculations that a fraction of injected electrons will populate the resulting bound states with X character according to Eq. (3.78). Thus our goal here is to use the plane-wave method to solve the Poisson's equation (3.82) for the electrostatic potential $V(z)$. We will start the derivation of the solution for a QW-based heterostructure, and later present the solution for the QD case. Here for a simplified derivation we assume $\varepsilon_r(z) = \varepsilon_b$ throughout the entire supercell. We start by considering the Fourier series expansion of V

$$V(z) = \sum_m \widetilde{V}(G_m) e^{iG_m z} \tag{3.83}$$

with $m \in [-M, +M]$. By inserting Eq. (3.83) into Eq. (3.82), applying the Laplacian, multiplying both sides by $\frac{e^{-iG_p z}}{L}$ and integrating over the supercell we obtain

$$G_p^2 \widetilde{V}(G_p) = \frac{e}{\varepsilon_0 \varepsilon_b} \frac{1}{L} \int_L \rho(z) e^{-iG_p z} \mathrm{d}z \,. \tag{3.84}$$

with the domain of p being the same as for m. By inserting Eq. (3.17) into Eqs. (3.79) and (3.80), and keeping in mind the orthonormality of the zone centre basis functions $\langle u_a | u_b \rangle = \delta_{ab}$ we obtain

$$n(z) = \frac{1}{2\pi L} \sum_{n_e} \sum_{b=1}^{8} \sum_m \sum_{m'} \int_{k_\parallel} \widetilde{a}^*_{n_e b}(G_{m'}, k_\parallel) \widetilde{a}_{n_e b}(G_m, k_\parallel) e^{-i(G_{m'} - G_m)z} f\left[E_{n_e}(k_\parallel), F_e\right] k_\parallel \mathrm{d}k_\parallel \tag{3.85}$$

$$p(z) = \frac{1}{2\pi L} \sum_{n_h} \sum_{b=1}^{8} \sum_m \sum_{m'} \int_{k_\parallel} \widetilde{a}^*_{n_h b}(G_{m'}, k_\parallel) \widetilde{a}_{n_h b}(G_m, k_\parallel) e^{-i(G_{m'} - G_m)z} f\left[E_{n_h}(k_\parallel), F_h\right] k_\parallel \mathrm{d}k_\parallel \tag{3.86}$$

with $m'_j \in [-M, +M]$. We note here that the first equation includes the sum over the calculated Γ and X eigenstates, i.e. $n_e = 2(2M+1) + 3(2M+1)$. We then substitute these expansions into Eq. (3.84), evaluate the integral over the supercell on the right-hand side and solve it for $\widetilde{V}(G_p)$ [81]

$$\begin{aligned} \widetilde{V}(G_p) = \frac{e^2}{2\pi \varepsilon_0 \varepsilon_b L G_p^2} \sum_{b=1}^{8} \sum_m \int_{k_\parallel} \Bigg\{ & \sum_{n_h} f\left[E_{n_h}(k_\parallel), F_h\right] \widetilde{a}^*_{n_h b}(G_p - G_m, k_\parallel) \widetilde{a}_{n_h b}(G_m, k_\parallel) \\ & - \sum_{n_e} f\left[E_{n_e}(k_\parallel), F_e\right] \widetilde{a}^*_{n_e b}(G_p - G_m, k_\parallel) \widetilde{a}_{n_e b}(G_m, k_\parallel) \Bigg\} k_\parallel \mathrm{d}k_\parallel \,. \end{aligned} \tag{3.87}$$

Here we took into account the Kronecker delta $\delta(G_{m'}, G_p - G_m)$. There are a few things to discuss here. Firstly, we notice that the summation includes Fourier coefficients $\widetilde{a}$ that depend upon reciprocal vectors G that are outside of the domain $[-M, +M]$. The fact that the diagonalisation of the Hamiltonian yields a set of $2M + 1$ Fourier coefficients for a particular eigenstate and particular band $|u_b\rangle$ suggests that we should have to use then non-existent terms. However, we keep in mind that the Fourier coefficients $\widetilde{a}$ rapidly approach 0 at larger reciprocal vectors for convergence. Thus, for the calculation of the Fourier coefficients $\widetilde{V}(G_p)$ it is sufficient that the sum over m is performed only for the terms that depend upon $G_p - G_m$ with $p - m \in [-M, +M]$.

Secondly, for the expansion of the carrier-induced electrostatic potential Hamiltonian we need to evaluate an integral similar to Eq. (3.20), where the expanded terms will depend upon $G_{m'} - G_m$, which may also be outside of the original domain $[-M, +M]$. From Eq. (3.87) we notice that the Fourier coefficients rapidly approach 0 at larger wave vectors G since they are decaying at least as fast as $1/G_p^2$. Thus, the Fourier coefficients $\widetilde{V}(G_p)$ that are outside of the domain $[-M, +M]$ in our calculations do not need to be considered in the expansion of this Hamiltonian matrix element.

The last question arises regarding the singularity of $\widetilde{V}(G_p)$ at $|G_p| = 0$. In this case the right-hand side of Eq. (3.84) becomes zero due to the charge neutrality, and we obtain

$$|G_p|^2 \widetilde{V}(G_p)\Big|_{G_p=0} = 0\,, \tag{3.88}$$

therefore $\widetilde{V}(G_p = 0) \in \mathbb{R}$. In practice, a non-zero $\widetilde{V}(G_p = 0)$ will result in an equivalent shift of all energy bands and, ultimately, does not make a difference for the transition energy between any two states. Therefore in our calculations we set $\widetilde{V}(G_p = 0) = 0$ for simplicity.

For QD and QWR based heterostructures the electronic structure calculations are limited to the Γ and X valley minima, and the carrier density is given by

$$n_e(\mathbf{r}) = \frac{1}{\Omega_{\text{sc}}} \sum_{n_e} |\psi_{n_e}(\mathbf{r})|^2 f(E_{n_e}, F_e) \tag{3.89}$$

$$n_h(\mathbf{r}) = \frac{1}{\Omega_{\text{sc}}} \sum_{n_h} |\psi_{n_h}(\mathbf{r})|^2 f(E_{n_h}, F_h) \tag{3.90}$$

which, when integrated over the volume of the supercell, yields the total number of injected carriers:

$$n = \int_{\Omega_{\mathrm{sc}}} n_e(\mathbf{r})\mathrm{d}V \tag{3.91}$$

and similarly for holes. We will not provide the detailed derivation of the solution of Poisson's equation in this case, as we do not perform self-consistent calculations for QWR or QD structures, but, by analogy to the QW-based heterostructures, one finds the solution in the following form

$$\begin{aligned} \widetilde{V}(\mathbf{G}_p) = \frac{e^2}{\varepsilon_0\varepsilon_b\Omega_{\mathrm{sc}}|\mathbf{G}_p|^2}\sum_{b=1}^{8}\sum_{m}\Bigg[\sum_{n_h} f(E_{n_h},F_h)\widetilde{a}^*_{n_h b}(\mathbf{G}_p-\mathbf{G}_m)\widetilde{a}_{n_h b}(\mathbf{G}_m) \\ -\sum_{n_e} f(E_{n_e},F_e)\widetilde{a}^*_{n_e b}(\mathbf{G}_p-\mathbf{G}_m)\widetilde{a}_{n_e b}(\mathbf{G}_m)\Bigg]\,, \end{aligned} \tag{3.92}$$

where the summation index m indicates that it is performed over $(2M_x+1)\times(2M_y+1)\times(2M_z+1)$ reciprocal vectors.

3.4 Momentum matrix elements

Our goal here is to analytically calculate the momentum matrix element between an initial conduction state $\psi^{(i)}_{n_e}$ and a final valence state $\psi^{(f)}_{n_h}$ in a QW-based heterostructure, which is given by:

$$P_{e,h}(k_\|) = \left\langle \psi^{(i)}_{n_e}(k_\|)\,|\widehat{\mathbf{p}}\cdot\widehat{e}\,|\,\psi^{(f)}_{n_h}(k_\|)\right\rangle \tag{3.93}$$

where $\widehat{e}$ is the polarisation vector, and the product $\widehat{\mathbf{p}}\cdot\widehat{e}$, according to Szmulowicz's formalism [82], can be defined as:

$$\widehat{\mathbf{p}}\cdot\widehat{e} = \frac{m_0}{\hbar}\left(\frac{\partial\widehat{H}}{\partial k_\|}\widehat{e}_\| + \frac{\partial\widehat{H}}{\partial k_z}\widehat{e}_z\right)_{k_z\to -i\frac{\mathrm{d}}{\mathrm{d}z}}\cdot\widehat{e}\,. \tag{3.94}$$

Substituting Eqs. (3.94) and (3.17) into (3.93) we obtain

$$\begin{aligned} P_{e,h}^{(j)}(k_\parallel) &= \frac{m_0}{\hbar}\frac{1}{L}\sum_{b,b'}\sum_{m,m'}\widetilde{a}^*_{n_eb'}(G_{m'},k_\parallel)\widetilde{a}_{n_hb}(G_m,k_\parallel)\int_{-L/2}^{L/2}e^{-iG_{m'}z}\left\langle u_{b'}\left|\frac{\partial\widehat{H}}{\partial k_j}\cdot\widehat{e}_j\right|u_b\right\rangle e^{iG_mz}\mathrm{d}z \\ &= \frac{m_0}{\hbar}\frac{1}{L}\sum_{b,b'}\sum_{m,m'}\widetilde{a}^*_{n_eb'}(G_{m'},k_\parallel)\widetilde{a}_{n_hb}(G_m,k_\parallel)\int_{-L/2}^{L/2}e^{-iG_{m'}z}\left(\frac{\partial\widehat{H}_{b'b}}{\partial k_j}\cdot\widehat{e}_j\right)e^{iG_mz}\mathrm{d}z \\ &= \frac{m_0}{\hbar}\sum_{b,b'}\sum_{m,m'}\widetilde{a}^*_{n_eb'}(G_{m'},k_\parallel)\widetilde{a}_{n_hb}(G_m,k_\parallel)\left(\frac{\partial\widehat{H}_{b'b}}{\partial k_j}\cdot\widehat{e}_j\right)_{m'm}, \end{aligned} \tag{3.95}$$

where the superscript j in $P_{e,h}^{(j)}$ denotes the polarisation direction of the external electric field, $m,m'\in[-M,+M]$ and $b,b'\in[1,8]$, and $\left(\frac{\partial\widehat{H}_{b'b}}{\partial k_j}\cdot\widehat{e}_j\right)_{m'm}$ is defined similar to Eq. (3.19). The in-plane polarisation vector $\widehat{e}_\parallel$ denotes the transverse electric (TE) polarisation. In our calculations, the dispersion of the energy states are calculated along $k_\parallel = k_x\cos\theta + k_y\sin\theta$ with $\theta=\frac{\pi}{4}$. Therefore, to average over all in-plane directions, the TE polarisation vector is taken to lie along the k_x direction, whereas the transverse magnetic polarisation $\widehat{e}_z$ is simply $\widehat{e}_z=\widehat{z}$.

For a QWR or QD-based heterostructure, the momentum matrix element is calculated at the centre of the superlattice Brillouin zone

$$P_{e,h} = \left\langle \psi_{n_e}^{(i)}\left|\widehat{\mathbf{p}}\cdot\widehat{e}\right|\psi_{n_h}^{(f)}\right\rangle, \tag{3.96}$$

where, using the formalism of Szmulowicz

$$\widehat{\mathbf{p}} = \frac{m_0}{\hbar}\left(\frac{\partial\widehat{H}}{\partial k_x}\cdot\widehat{x}+\frac{\partial\widehat{H}}{\partial k_y}\cdot\widehat{y}+\frac{\partial\widehat{H}}{\partial k_z}\cdot\widehat{z}\right)_{k_j\to -i\frac{\partial}{\partial k_j}} \tag{3.97}$$

In analogy to Eq. (3.95), the momentum matrix element for a QWR or QD based heterostructures is calculated in the following way:

$$P_{e,h}^{(j)} = \frac{m_0}{\hbar}\sum_{b,b'}\sum_{m,m'}\widetilde{a}^*_{n_eb'}(G_{m'})\widetilde{a}_{n_hb}(G_m)\left(\frac{\partial\widehat{H}_{b'b}}{\partial k_j}\cdot\widehat{e}_j\right)_{m'm}, \tag{3.98}$$

where $m,m'\in(2M_x+1)\times(2M_y+1)\times(2M_z+1)$. Two different TE polarisation vectors are used here $\widehat{x}$ and $\widehat{y}$ because, depending on the shape of the nanostructure and its characteristic function $\chi(\mathbf{r})$, the resulting momentum matrix elements may differ. The TM polarisation is, similarly to the QW case, associated with the $\widehat{z}$ polarisation vector. The plane wave expansion of the partial derivative of the Hamiltonian matrix for either type of nanostructure follows the same way we described in Sections 3.1 and 3.2 and is, in fact, simpler due to the reduction of the Hamiltonian terms by one order.

3.5 Conclusions

In conclusion, we have derived in this chapter the semi-analytical plane wave expansion method for the calculation of electronic and optical properties of QW-, QWR- and QD-based heterostructures. In Section 3.1 we started with the general idea of the method and applied it to solve the 1-band effective mass Schrödinger equation, followed by the extension of the method to the 8-band $\mathbf{k}\cdot\mathbf{p}$ Hamiltonian in order to calculate the electronic structure of QW-based heterostructures.

We have discussed in Section 3.2 the implementation of the method for QD-based heterostructures and the main differences from a QW-based system. In particular, we presented the extended definition of the characteristic function for a QD, which is, essentially, a mathematical representation of a QD shape. We did not discuss QWRs explicitly in this chapter; however in our calculations we treat these structures as a particular QD shape. The Fourier transforms of the characteristic function for some QWR shapes we consider in our calculations are given in Appendix D. In Section 3.2.2 we derived the explicit form of the Fourier transform of the strain tensor for zincblende semiconductors using the Green's tensor method, followed by discussing the expansion of the Pikus-Bir Hamiltonian within the plane wave framework.

Due to the spatial separation of the electron and hole charge densities, we derived in Section 3.3 the analytical solution to Poisson's equation using the Fourier series expansion of the electron and hole eigenstates.

Finally, we have presented in Section 3.4 the analytical calculation of the momentum matrix elements using the plane wave method, that can be applied to either QW-, QWR- or QD-based structures. We showed that the momentum matrix elements between two states can be expressed using (i) the Fourier coefficients of the eigenstates and (ii) the bulk material parameters that we also used to solve the Schrödinger equation.

This set of analytical techniques was implemented in a suite of codes that was used to explicitly calculate the electronic and optical properties of different heterostructures. We start using the method to analyse the performance of 1.3-μm QW lasers grown on InGaAs metamorphic buffer layers, and present our analysis in Chapter 4. We extend the application of the method towards the calculation of the electronic and optical properties of QWR-based heterostructures in Chapter 5, and, based on the insights we obtain about their electronic properties, we investigate the performance of AlGaInP QW-based metamorphic light-emitting diodes (LEDs) for 610 nm emission in Chapter 6.

Chapter 4

AlInGaAs 1.3 μm metamorphic quantum well lasers

In this chapter we investigate the predicted characteristics of (Al)InGaAs QW-based lasers with 1.3 μm peak gain emission and grown on a relaxed InGaAs Metamorphic Buffer Layer (MBL) lattice-mismatched to the GaAs substrate. The goal of this chapter is to provide a set of parameters for an (Al)InGaAs-based laser grown on an InGaAs MBL with an optimised performance. We start with Section 4.1 where we provide the parameters required for the calculation of the laser properties at threshold.

We start our calculations in Section. 4.2 by evaluating the ranges of strain and band gaps accessible for pseudomorphically strained (Al)InGaAs layers grown on InGaAs MBLs. We focus here primarily on compressively strained ternary InGaAs QWs having unstrained InGaAs barriers grown on relaxed $In_{0.2}Ga_{0.8}As$ MBLs. We note here that throughout this chapter the in-plane strain $\epsilon_{xx} > 0$ and $\epsilon_{xx} < 0$ correspond to compressive and tensile strain respectively as the sign convention. Additionally, different elastic tensors for the barrier and QW are considered for the strain calculations in this chapter. As we will show, while changing the strain in the QW we can also adjust the QW thickness in order to maintain 1.3 μm emission. In order to find out how the strain and QW thickness affect the performance of our devices independently, we also performed an additional set of calculations where we consider quaternary AlInGaAs QWs with either a constant strain or well width.

In Section 4.3 we investigate the effect of increased barrier band gap by using quaternary AlInGaAs barrier layers lattice-matched to the InGaAs MBL. Because we consider an AlInGaAs Separate Confinement Heterostructure (SCH) layer with the same composition throughout the entire study, a choice of the barrier material will be critical for optimisation of both carrier and optical confinement in the device. We then discuss the effects of varying the InGaAs MBL composition on the device performance in Section 4.4.

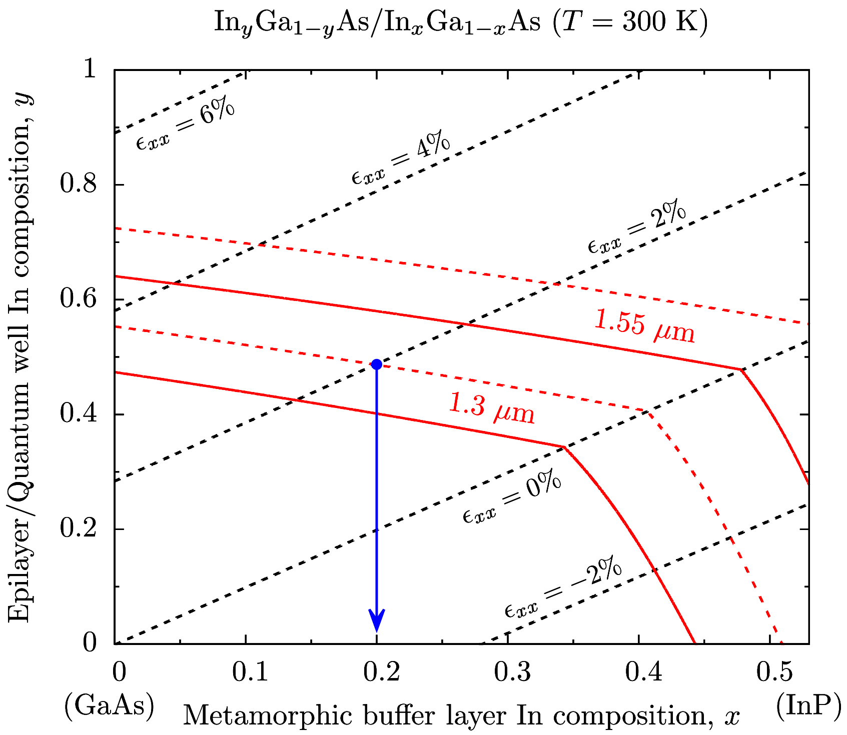

FIGURE 4.1: Composition space map showing the calculated variation of the in-plane strain (ϵ_{xx}) and room temperature strained bulk and quantum well (QW) band gaps for In$_y$Ga$_{1-y}$As grown pseudomorphically on an In$_x$Ga$_{1-x}$As metamorphic buffer layer (MBL). Dotted black and solid red lines respectively denote paths in the composition space along which ϵ_{xx} and the In$_y$Ga$_{1-y}$As strained bulk band gap are constant. The dotted red line lying above each solid red line denotes the path in the composition space along which the bulk band gap of the In$_y$Ga$_{1-y}$As/In$_x$Ga$_{1-x}$As QW material is constant, assuming a total confinement energy of 75 meV, so that the QW emission wavelength is the same as the bulk material denoted by the solid red line. The closed blue circle and vertical arrow show that an In$_y$Ga$_{1-y}$As QW with an emission wavelength of 1.3 μm can be grown with 2% compressive strain on an In$_{0.2}$Ga$_{0.8}$As MBL.

We provide a short summary at the end of each section, where we derive from the context the parameters required for an optimised metamorphic laser having 1.3 μm peak gain. Finally, we summarise the chapter conclusions in Section 4.5.

4.1 Laser parameters and device modeling

Paths of constant strain for an In$_y$Ga$_{1-y}$As layer grown pseudomorphically on In$_x$Ga$_{1-x}$As are shown in Fig. 4.1 using dotted black lines, while paths along which the strained bulk band gap of the In$_y$Ga$_{1-y}$As material is constant at 1.3 and 1.55 μm are shown using solid red lines. Dotted red lines show the corresponding compositions for the bulk band gaps of the In$_y$Ga$_{1-y}$As material required to form QWs emitting at 1.3 and 1.55 μm, assuming a total

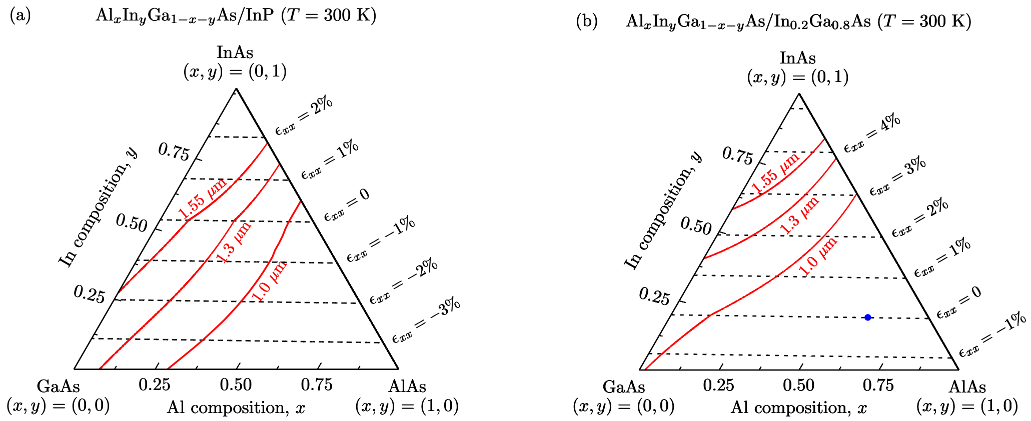

FIGURE 4.2: Composition space maps showing the variation of the in-plane strain (ϵ_{xx}) and strained bulk band gap for pseudomorphically strained Al$_x$In$_y$Ga$_{1-x-y}$As alloys grown epitaxially on (a) a conventional InP substrate, and (b) an In$_{0.2}$Ga$_{0.8}$As metamorphic buffer layer (MBL). Dashed black and solid red lines respectively denote paths in the composition space along which ϵ_{xx} and the Al$_x$In$_y$Ga$_{1-x-y}$As strained bulk room temperature band gap are constant. As discussed in the text, the closed blue circle in (b) denotes the alloy Al composition ($x = 62\%$) above which the Al$_x$In$_y$Ga$_{1-x-y}$As alloys which are lattice matched to an In$_{0.2}$Ga$_{0.8}$As MBL (satisfying $y = 0.2 - 0.02x$) have an indirect band gap.

confinement energy of 75 meV[1]. At $x = 0$ we see that a compressive strain close to 4% is required to produce 1.3 μm emission from an InGaAs QW on a GaAs substrate, which is too large a strain value to allow high quality pseudomorphic growth. However, employing an MBL with $x = 20\%$ we see that it is possible to grow In$_y$Ga$_{1-y}$As QWs under 2% compressive strain which have a 1.3 μm band gap (as highlighted by the closed blue circle and arrow). We further see that increasing the MBL In composition to approximately 34% should enable the growth of strained In$_y$Ga$_{1-y}$As QWs having a 1.55 μm band gap under 2% compressive strain.

Figures 4.2(a) and 4.2(b) show the calculated variation of the in-plane strain (dashed black lines) and band gap (solid red lines) as a function of the Al and In compositions x and y in the Al$_x$In$_y$Ga$_{1-x-y}$As composition space, calculated for strained AlInGaAs alloys grown on an InP substrate and on an In$_{0.2}$Ga$_{0.8}$As MBL, respectively. The variation of the alloy composition required to maintain a fixed bulk band gap is shown in each case for emission wavelengths of 1.3 and 1.55 μm, as well as 1 μm (a representative barrier material). Comparing Figs. 4.2(a) and 4.2(b) we note several important differences in the material parameter trends.

Firstly, while there is significant scope for the growth of tensile strained ($\epsilon_{xx} < 0$) QWs with 1.3 and 1.55 μm band gaps on the InP substrate, only compressively strained ($\epsilon_{xx} > 0$) 1.3 μm InGaAs QWs can be grown on the In$_{0.2}$Ga$_{0.8}$As MBL. This is because a much reduced In composition y is required to remain lattice matched to the In$_{0.2}$Ga$_{0.8}$As MBL ($\epsilon_{xx} = 0$ for $y =$

---

[1] The total confinement energy denotes here the difference between the QW ground state transition energy at $k_{\parallel} = 0$ and the bulk band gap of the QW material. The red dashed line in Fig. 4.1 is presented as a reminder that a higher composition and strain would be required to achieve 1.3 or 1.55 μm emission in a QW compared to the bulk case. The assumed 75 meV total confinement energy is close to that obtained in the optimised structure discussed later in this chapter.

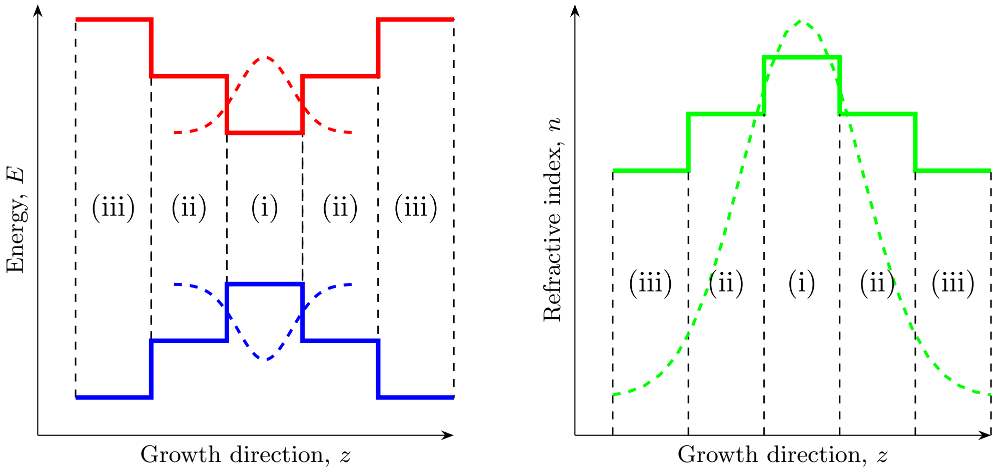

FIGURE 4.3: Schematic representation of the distribution of the conduction band minimum and valence band maximum (red and blue line respectively, left panel) and refractive index profile (green line, right panel) of the active region of the laser heterostructure along the growth direction. The Quantum Well (QW), barrier and Separate-Confinement Heterostructure (SCH) are denoted by (i), (ii) and (iii) respectively. A larger conduction (valence) band offset between the barrier and the QW brings about an improved confinement of the electron (hole) wavefunction, denoted by the dashed red (blue) line on the left panel. A larger difference between the refractive index of the SCH and of the barrier brings about an improved confinement of the optical mode in the active region, denoted by the dashed green line on the right panel.

20%) compared to the InP substrate ($\epsilon_{xx} = 0$ for $y = 53\%$). Examining Fig. 4.2(b) we see that compressively strained In$_y$Ga$_{1-y}$As bulk-like epilayers with a 1.3 μm band gap can be grown on an In$_{0.2}$Ga$_{0.8}$As MBL for $y \approx 40\%$ ($\epsilon_{xx} \approx 1.5\%$). As we will see when confinement effects are taken into account in Section 4.2, compressively strained In$_y$Ga$_{1-y}$As QWs can be grown on the In$_{0.2}$Ga$_{0.8}$As MBL with In compositions (compressive strains) $y \gtrsim 45\%$ ($\epsilon_{xx} \gtrsim 1.8\%$).

Secondly, we see that the growth of an unstrained quaternary barrier having a 1 μm band gap requires significantly less Al in the case of the In$_{0.2}$Ga$_{0.8}$As MBL ($x \approx 15\%$) as compared to the InP substrate ($x \approx 40\%$). The largest Al composition that can be achieved in an unstrained cladding layer on an InP substrate is 48%, for which the room temperature energy gap is 1.41 eV. By comparison, we find that it is possible to grow direct gap Al$_x$In$_y$Ga$_{1-x-y}$As alloys on an In$_{0.2}$Ga$_{0.8}$As MBL up to $x \approx 62\%$ and an energy gap of 1.95 eV. This crossover to an indirect gap is denoted by the closed blue circle in Fig. 4.2(b). This then makes it possible to engineer a greater band gap difference and refractive index contrast between the QW and the cladding layers for the In$_{0.2}$Ga$_{0.8}$As MBL, which introduces the possibility to improve both the carrier and optical confinement compared to the InP case. A schematic diagram of the band gap and refractive index distribution in the active region is depicted in Fig. 4.3.

Finally, we note that tensile strained quaternary barriers can be grown with strains of up to approximately 1% on an In$_{0.2}$Ga$_{0.8}$As MBL. It is therefore possible to grow compensated strain or zero net strain AlInGaAs metamorphic laser structures having compressively strained QWs and tensile strained barriers, which increases the number of QW-barrier repeats that can be grown before plastic relaxation becomes problematic.

The material parameters we use for our calculations are provided in Appendix A. In order to calculate the band offsets at the barrier-QW interface, we find the absolute energy position of the CB minima and VB maxima which are calculated using model solid theory [124, 125] for an unstrained semiconductor layer as:

$$E_v = E_v^{avg} + \frac{1}{3}\Delta_{\text{so}} \tag{4.1}$$

$$E_c = E_v + E_g\,. \tag{4.2}$$

The band edge energies in a strained epilayer are then calculated using the $\mathbf{k}\cdot\mathbf{p}$ (2.32) and strain Hamiltonian (2.56) from Chapter 2. The calculation of the average valence band energy E_v^{avg} is outside of the scope of this thesis and we rely on existing values which are calculated using Density Functional Theory (DFT) methods [124–130]. The calculated QW band structure and eigenstates, using the method we derived in Section 3.1.2, are used directly to calculate the laser optical properties. The interband momentum matrix elements, calculated using the method in Section 3.4 are then used to calculate the gain and spontaneous emission spectra. For the calculations of spontaneous emission and material gain spectra (cf. Section 2.4) we assume a homogeneous linewidth broadening described using a hyperbolic secant lineshape having an interband relaxation time of $\tau_{\text{in}} = 100$ fs [32, 131].

The threshold current density J_{th} is assumed to include two components, one due to radiative recombination (J_{rad}) and the second due to non-radiative Auger recombination (J_{Auger}) [24, 83, 132]

$$J_{\text{th}} = J_{\text{rad}} + J_{\text{Auger}}\,. \tag{4.3}$$

J_{rad} is calculated directly for each laser structure by integrating over the calculated spontaneous emission spectrum at threshold as a function of temperature [133]. We do not calculate the Auger recombination rate directly, but instead follow the commonly used Boltzmann approximation where the Auger current density is assumed to vary with threshold carrier density n_{th} as $J_{\text{Auger}} = eCn_{\text{th}}^3$ [24, 83, 132]. The Auger recombination coefficient C is taken to vary with temperature T as [134]

$$C(T) = C_{300}\exp\left(-\frac{E_a}{k_{\text{B}}}\left(\frac{1}{T} - \frac{1}{300}\right)\right)\,, \tag{4.4}$$

where C_{300} is the Auger recombination coefficient at $T = 300$ K and E_a is the Auger activation energy. We take $C_{300} = 8.67 \times 10^{-17}$ cm^4 s^{-1} and $E_a = 30$ meV in all of the calculations presented below. The chosen C_{300} and E_a lie well within the range of values quoted in the literature, and were chosen so as to match our best performing laser structures to the results of Ref. [28]. Equations (4.3) and (4.4) can then be used to provide an estimate of the Auger current density and its temperature dependence in each device. This approach should reproduce well trends in the Auger contribution to the total current density, which is expected in all cases to increase superlinearly with increasing n_{th} and J_{rad}.

For the calculation of the threshold gain we assume internal cavity losses of 6 cm^{-1}, choose an unstrained AlInGaAs SCH with an Al composition of 40%, and take an overall cavity length of 750 μm for all of the devices considered [83]. The confinement factor Γ of the fundamental (TE-polarised) optical mode was calculated for each laser structure using an effective index approach [117]. By varying the thickness of the barrier layers it was found for all structures considered that Γ is maximised for 160 – 180 nm thick (Al)InGaAs barriers. As such, all calculations presented below were performed for laser structures having 180 nm wide barriers.

Having outlined our theoretical model we now turn to present the results of the theoretical calculations, which we use to elucidate general trends in the gain and threshold characteristics of 1.3 μm metamorphic QWs, as well as to identify optimised laser structures.

4.2 Variable strain and well width

The solid blue and dashed red lines in Fig. 4.4 show the calculated variation of the QW width with strain required to maintain peak gain at 1.3 μm for a ternary InGaAs QW, with unstrained $\text{In}_{0.2}\text{Ga}_{0.8}\text{As}$ and $\text{Al}_{0.12}\text{In}_{0.2}\text{Ga}_{0.68}\text{As}$ barriers respectively. We first discuss in this section the results for $\text{In}_{0.2}\text{Ga}_{0.8}\text{As}$ barriers, before turning to consider the effects of varying the barrier composition in Section 4.3. We calculate that 1.3 μm $\text{In}_x\text{Ga}_{1-x}\text{As}$ QWs can be grown with compressive strains between 1.8 and 2.6%, corresponding to In compositions between 46 and 58%, and with QW widths varying from $d_{\text{QW}} = 9.8$ nm for $\epsilon_{xx} = 1.8\%$, to narrow QWs having $d_{\text{QW}} = 3.8$ nm for $\epsilon_{xx} = 2.6\%$.

Since the In composition can be varied over a relatively large range in these QW structures while maintaining a 1.3 μm band gap, there is significant scope to engineer the density of states (DOS) at the VB edge so that n_{th} is minimised. The effect on the VB structure of varying the strain in this series of QWs is shown in Fig. 4.5, where we compare the band structure (left panel) and DOS (right panel) in the vicinity of the VB edge for the structures having the lowest strain (widest QW) and highest strain (narrowest QW). We firstly note that all of the zone-centre bound states calculated in this series of QWs are heavy-hole- (HH) like along the

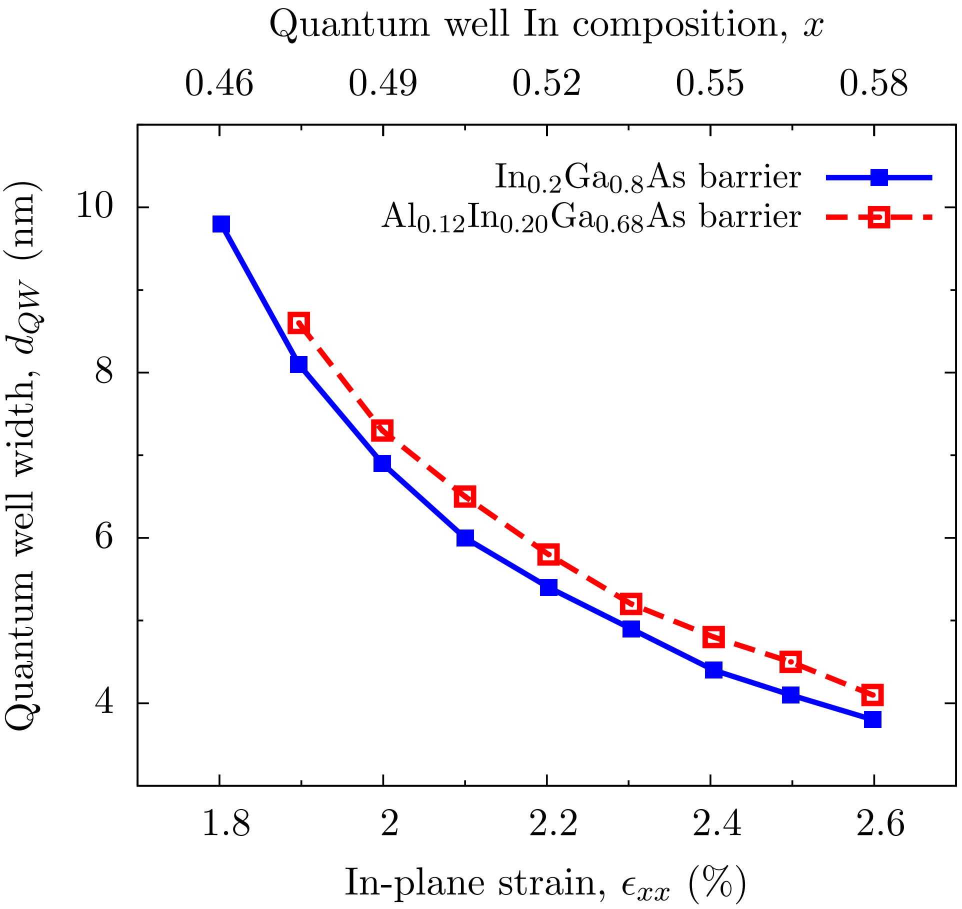

FIGURE 4.4: Calculated variation of the quantum well (QW) width required to maintain 1.3 μm peak gain at $T = 300$ K as a function of in-plane strain and QW In composition, for a series of compressively strained $In_xGa_{1-x}As$ QWs grown on an $In_{0.2}Ga_{0.8}As$ metamorphic buffer layer. The QWs have either ternary $In_{0.2}Ga_{0.8}As$ (blue solid lines, closed squares) or quaternary $Al_{0.12}In_{0.20}Ga_{0.68}As$ (red dashed lines, open squares) unstrained barriers.

growth direction. We calculate that the QW having 1.8% compressive strain has a relatively large DOS for energies $\gtrsim$ 20 meV from the VB edge, due to the relatively small separation in energy between the two highest energy hole subbands in this 9.8 nm wide well. As the strain in the QW is increased to 2.6% we see a dramatic reduction in the DOS at energies further away from the VB edge, due to the reduction in QW width, d_{QW}, to 3.8 nm in this case. Confinement effects in this narrowest QW lead to a large splitting of approximately 80 meV between the two highest energy hole subbands.

To elucidate the effects of these differences in the VB structure on the laser performance we have calculated the variation of n_{th} and J_{th} for the series of QW structures represented by the blue line in Fig. 4.4. The results of the calculations for n_{th} are shown in Fig. 4.6, where the solid (dashed) blue lines correspond respectively to the calculated variation of n_{th} at $T = 300$ K (360 K). The green, red and black lines in Figs. 4.6 depict the corresponding results for QWs having quaternary (AlInGaAs) barriers – we reserve discussion of these results for Section 4.3. Examining first the solid blue line in Fig. 4.6, we see that the carrier density required to reach

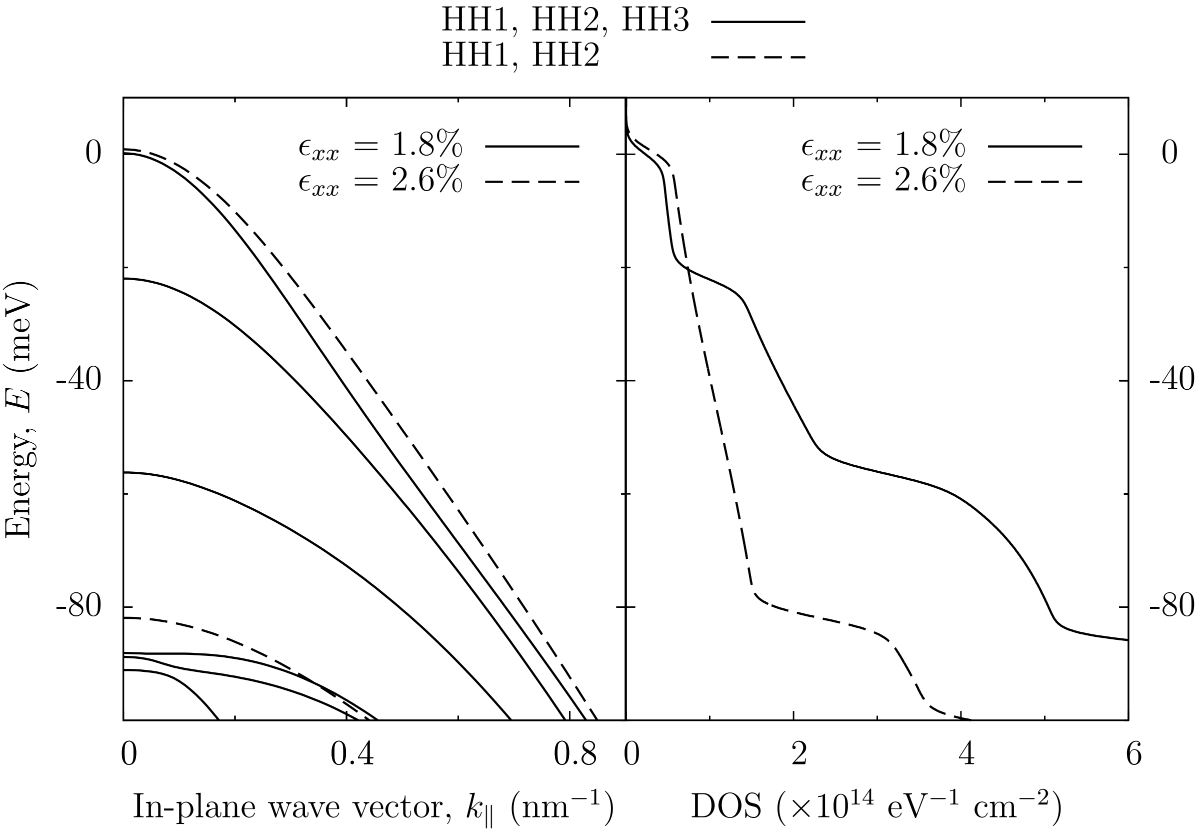

Figure 4.5: Calculated valence band structure (left panel) and density of states (DOS; right panel) for 1.3 μm InGaAs quantum wells (QWs) having 1.8 and 2.6% compressive strain (solid and dashed lines, respectively) on an $In_{0.2}Ga_{0.8}As$ metamorphic buffer layer. Both QWs have unstrained $In_{0.2}Ga_{0.8}As$ barriers. The zero of energy is taken in each case at the energy of the highest bound hole state, in order to facilitate a comparison of the DOS in the vicinity of the band edge. All of the bound hole states in each case are heavy-hole- (HH) like along the growth direction at the QW Brillouin zone centre.

threshold reduces rapidly with increasing strain up to $\epsilon_{xx} \approx 2.2\%$, consistent with the reduction of the DOS in the vicinity of the VB edge discussed above. Calculations were undertaken in Ref. [131] to estimate the gain characteristics of an ideal 1.3 μm InGaAs/GaAs QW structure, with $\epsilon_{xx} = 3.8\%$ and $d_{\text{QW}} = 7$ nm, for which a value of $n_{\text{th}} = 1.65 \times 10^{12}$ cm^{-2} was obtained at 300 K. Although the QW width and strain in this GaAs-based structure are beyond what can be achieved in strained QW growth, this hypothetical GaAs-based structure can nevertheless serve as a useful benchmark for the metamorphic structures considered here. Encouragingly, we calculate that $n_{\text{th}} = 1.46 \times 10^{12}$ cm^{-2} at $\epsilon_{xx} = 2.2\%$, so that the performance of the metamorphic devices under consideration then compares very favourably with the GaAs-based benchmark device.

We note that there is only minimal reduction in the calculated room temperature value of n_{th} for QW widths $\lesssim 5.4$ nm (strains $\gtrsim 2.2\%$), suggesting that there is little benefit to be obtained from growing highly strained QWs having $\epsilon_{xx} \gtrsim 2.2\%$ ($d_{\text{QW}} \lesssim 5.4$ nm) considering

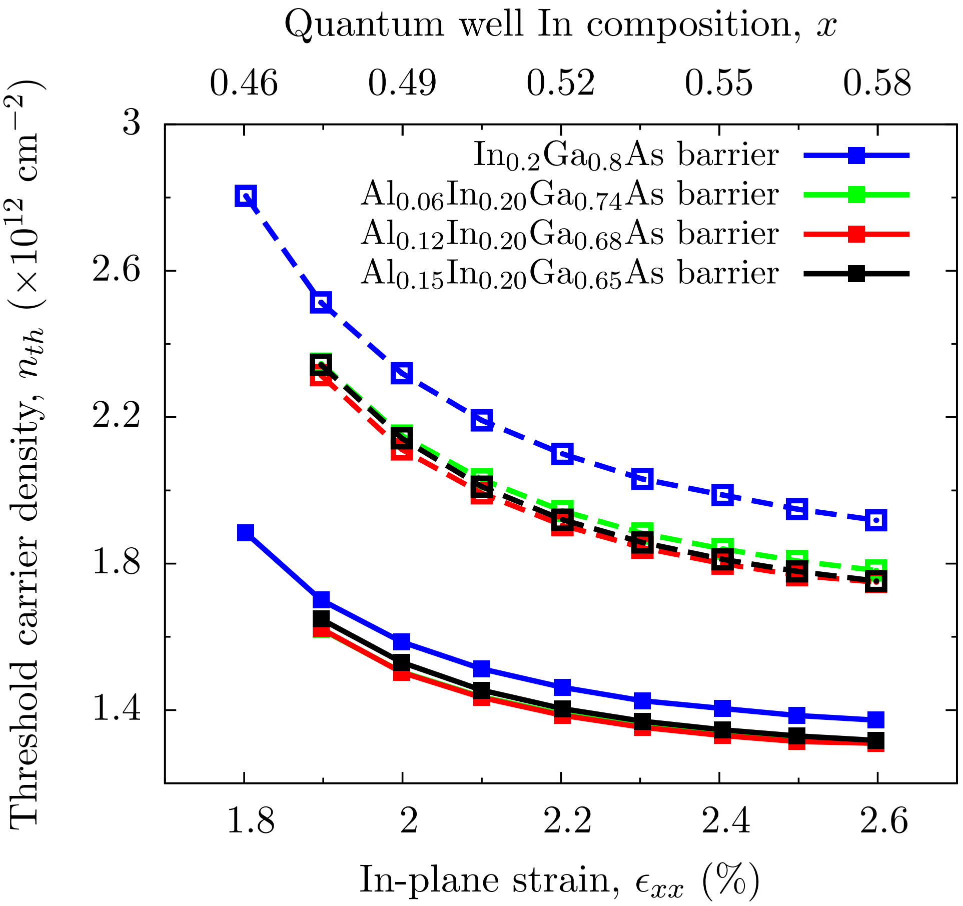

FIGURE 4.6: Calculated variation of the (areal) threshold carrier density as a function of in-plane strain and quantum well (QW) In composition at $T = 300$ K (solid lines, closed squares) and 360 K (dashed lines, open squares), for the same series of compressively strained 1.3 μm InGaAs QWs as in Fig. 4.4. The QWs have unstrained $Al_yIn_{0.2}Ga_{0.8-y}As$ barriers with $y = 0$, 6, 12 or 15% (blue, green, red and black lines/squares, respectively).

the potential relaxation of highly strained layers [135]. A similar trend is shown by the dashed blue line in Fig. 4.6, which shows the variation of n_{th} as a function of strain at 360 K.

We calculate that the optical transition strength at the QW Brillouin zone centre for the fundamental TE-polarised electron to HH1 transition decreases slowly over the strain range considered, with the calculated value of 23.1 eV at $\epsilon_{xx} = 2.6\%$ being approximately 89% of its value at $\epsilon_{xx} = 1.8\%$. This weak variation in the transition strength is due to the fact that while d_{QW} decreases with increasing strain, the corresponding increase in the QW In composition is sufficient to increase the CB offset – from 141 meV at $\epsilon_{xx} = 1.8\%$ to 200 meV at $\epsilon_{xx} = 2.6\%$ – so that the electron-hole overlap remains approximately constant for $1.8\% \leq \epsilon_{xx} \leq 2.6\%$. As such, we conclude that the calculated reduction of n_{th} as a function of compressive strain is primarily due to the reduction in the DOS in the vicinity of the VB edge, which is in turn brought about primarily as a result of the reduced QW width required to maintain peak gain at 1.3 μm.

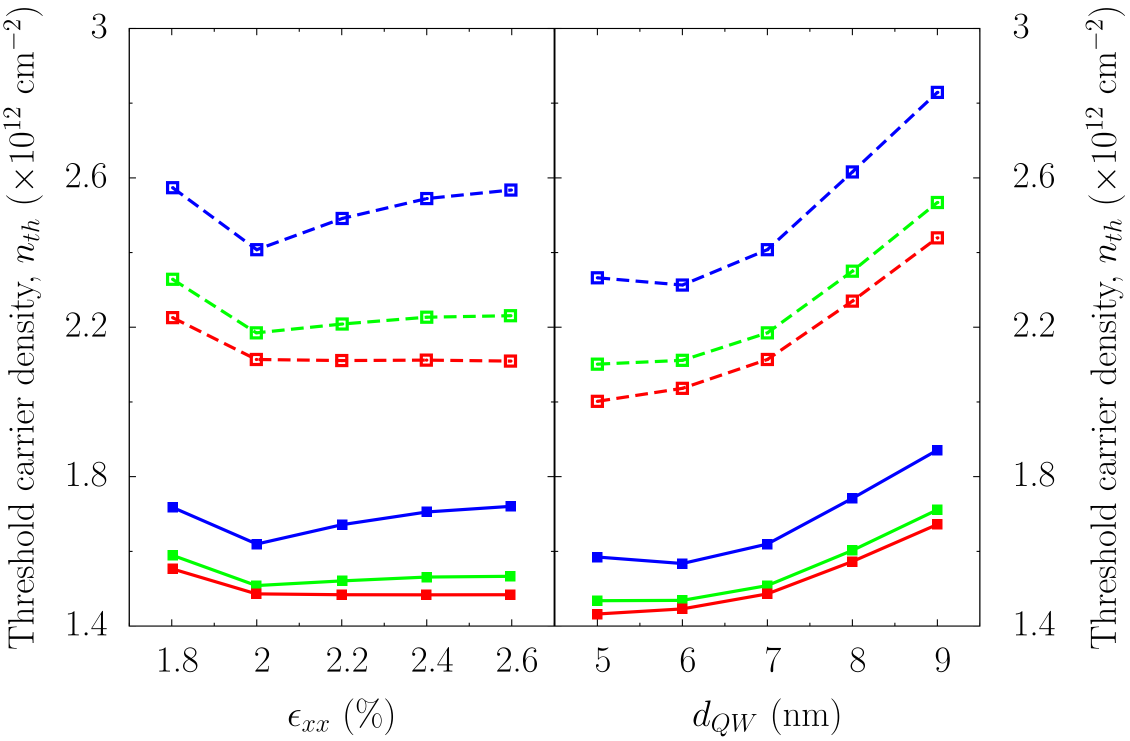

FIGURE 4.7: Calculated variation of the (areal) threshold carrier density as a function of in-plane strain at a fixed quantum well (QW) width of 7 nm (left panel) and QW width at a fixed strain of 2.0% (right panel) at $T = 300$ K (solid lines, closed squares) and 360 K (dashed lines, open squares), for a series of AlInGaAs QWs with the peak gain at 1.3 μm. The QWs have unstrained Al$_y$In$_{0.2}$Ga$_{0.8-y}$As barriers with $y = 0$, 6 or 12% (blue, green and red lines/squares, respectively), as in Fig. 4.6.

Further calculations where we kept a fixed QW width of 7 nm but used a quaternary AlInGaAs QW to vary the strain confirm this conclusion. The threshold carrier density at a fixed d_{QW} was much less sensitive to a change in ϵ_{xx} compared to the opposite case, as shown in Fig. 4.7. We note that the n_{th} minimum at $\epsilon_{xx} = 2.0\%$ from the blue lines is associated with a minor reduction in the conduction band DOS at energies in the vicinity of the ground electron state. By contrast, there is a much larger increase in n_{th} associated with increased QW width d_{QW} at a constant strain ϵ_{xx} since a larger number of HH bound states are allowed in the QW valence band. We speculate here that the threshold characteristics of the laser will be negatively impacted by having a compressively strained AlInGaAs QW with $\epsilon_{xx} < 1.8\%$. However it is not possible to reduce the strain in such a QW without increasing its thickness d_{QW} in order to maintain the 1.3 μm emission, since the 1.8% QW in this context is InGaAs-based. A wider QW then, as we have shown, will lead to a dimished laser performance.

The solid (dashed) blue curve in the left panel of Fig. 4.8 shows the calculated variation of the total threshold current density J_{th} as a function of strain for the series of InGaAs QW structures from Fig. 4.4 at 300 K (360 K), calculated using the corresponding values of n_{th}

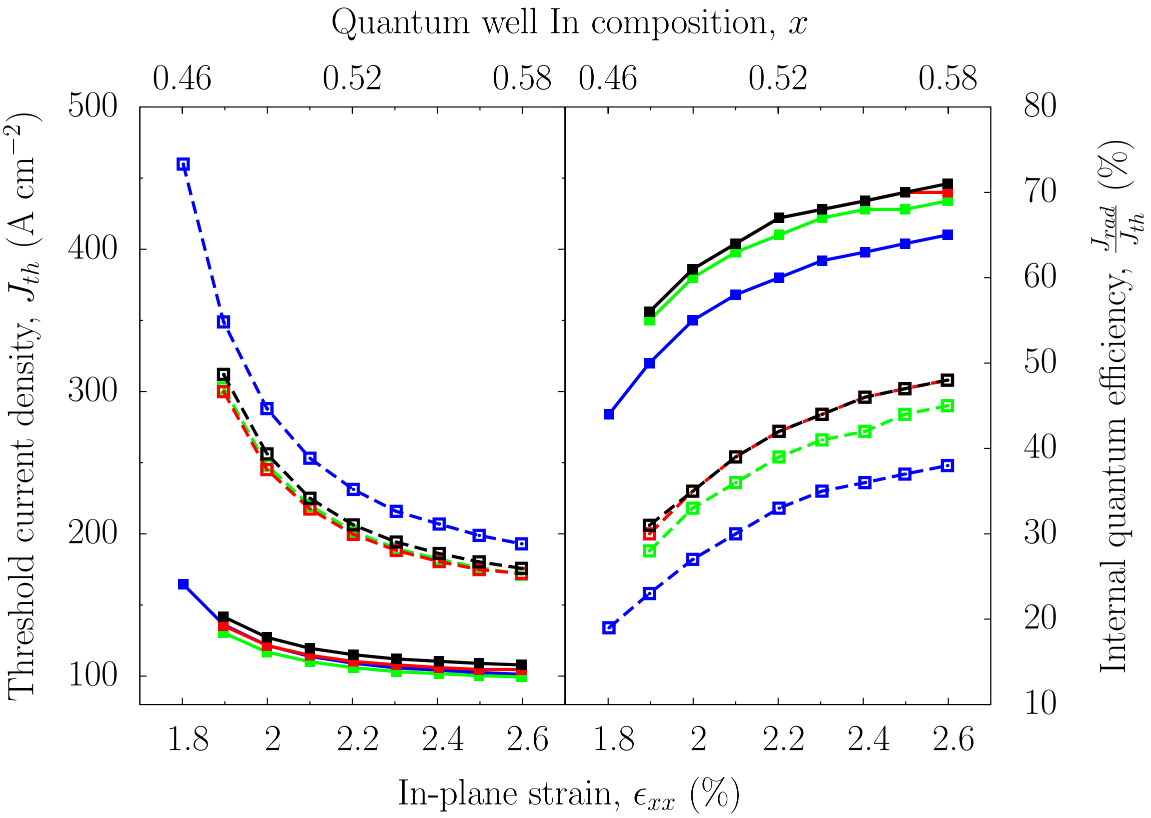

FIGURE 4.8: Calculated variation of the threshold current density (left panel) and the ratio of the radiative current density to the total current density at threshold (the internal quantum efficiency; right panel) as a function of in-plane strain and quantum well (QW) In composition at $T = 300$ K (solid lines, closed squares) and 360 K (dashed lines, open squares), for the same series of compressively strained 1.3 μm InGaAs QWs as in Figs. 4.4 and 4.6. The QWs have unstrained Al$_y$In$_{0.2}$Ga$_{0.8-y}$As barriers with $y = 0$, 6 or 12% (blue, green and red lines/squares, respectively), as in Fig. 4.6.

from Fig. 4.6 in Eq. (4.3). At 300 K we see that there is a reduction in J_{th} as ϵ_{xx} (d_{QW}) is increased (decreased), with the calculated value of 165 A cm^{-2} at $\epsilon_{xx} = 1.8\%$ decreasing to 109 A cm^{-2} at $\epsilon_{xx} = 2.2\%$. At 300 K we find that there is little benefit to having strains $\gtrsim 2.2\%$ (QW widths $\lesssim 5.4$ nm), with J_{th} decreasing only by 8 A cm^{-2} between $\epsilon_{xx} = 2.2\%$ and 2.6%. The situation at $T = 360$ K is somewhat similar. The calculated value of $J_{\text{th}} = 466$ A cm^{-2} at $\epsilon_{xx} = 1.8\%$ is relatively large, and we calculate that J_{th} decreases extremely rapidly with increasing strain in the QW, decreasing by a factor of approximately two to 231 A cm^{-2} for a QW having $\epsilon_{xx} = 2.2\%$.

The reasons for these calculated trends in J_{th} at 360 K can be understood in light of Eqs. (4.3) and (4.4), as well as the calculated variation of n_{th} shown in Fig. 4.6. We assume in our calculations that the non-radiative (Auger) component of J_{th} varies as the cube of n_{th}, with the larger carrier densities at threshold at 360 K then leading to strongly increased values of J_{th} at high temperature. In addition, we calculate using Eq. (4.4) that the Auger coefficient C increases by approximately 21% between 300 and 360 K. Based on this value of C, and the assumption that $J_{\text{Auger}} \propto n_{\text{th}}^3$, we then estimate that J_{th} at 360 K is dominated by its non-radiative component. This can be seen from the dashed blue curve in the right panel of Fig. 4.8, which shows the calculated variation of the internal quantum efficiency (IQE) – i.e. the ratio of the radiative current density to the total current density at threshold – as a function of strain for the structures depicted by the blue curve in Fig. 4.4. Examining the calculated variation of the IQE at threshold as a function of strain at 360 K (shown by the dashed blue curve) we estimate, based on the value of C used here, that J_{th} is dominated at $\epsilon_{xx} = 1.8\%$ by non-radiative recombination, which accounts for approximately 80% of the total current density in the device at threshold. The calculated IQE at 360 K increases with increasing strain in the QW. We estimate that non-radiative recombination increases from approximately 35% of J_{th} at room temperature to 62% at 360K in the narrowest, highly strained QW having $d_{\text{QW}} = 3.8$ nm and $\epsilon_{xx} = 2.6\%$. This suggests that GaAs-based 1.3 μm metamorphic QW lasers should have favourable temperature dependence of J_{th} due to the fact that non-radiative Auger recombination could play a less important role than radiative recombination at room temperature for $\epsilon_{xx} \gtrsim 2.2\%$.

We note that the quantitative aspects of these results for J_{th} depend upon the assumed value of the room temperature Auger recombination coefficient used in Eq. (4.4). Furthermore, the high density of threading dislocations present in metamorphic laser structures [9] may provide a large number of recombination centres, which could lead to there being an appreciable defect-related contribution to J_{th} that has not been taken into account in Eq. (4.3). The values of J_{th} here include radiative and Auger recombination only, while measurements of J_{th} and the characteristic temperature T_0, given by [136]

$$T_0 = \left[\frac{\text{dln} J_{\text{th}}(T)}{\text{d}T} \right]^{-1} . \tag{4.5}$$

include additional contributions from defect-related recombination and carrier leakage, calculation of which is beyond the scope of our current analysis. However, assuming on the basis of our calculations that $J_{\text{th}} = 100$ A cm^{-2} per QW and $T_0 = 85$ K (cf. Fig. 4.8) for radiative and Auger recombination, we estimate that the combined defect-related/leakage current accounts respectively for 50 and 70% of the measured values of J_{th} at room temperature for the devices studied in Refs. [17] and [54]. We note that defect-related contributions to J_{th} of this magnitude are comparable to those previously reported for GaInNAs-based 1.3 μm devices [41]. Measurements performed on GaInNAs-based lasers indicate that devices having higher J_{th} tend to have higher values of T_0, suggesting that strong defect-related recombination leads to an artificially high T_0 [137]. Our analysis here suggests that this conclusion may also be extended to metamorphic lasers, which may account for the large T_0 values reported for some devices. The best high temperature performance obtained to date was in a triple QW device, which displayed a J_{th} of order 7 kA cm^{-2} at 200 °C, and a T_0 value of order 220 K over a

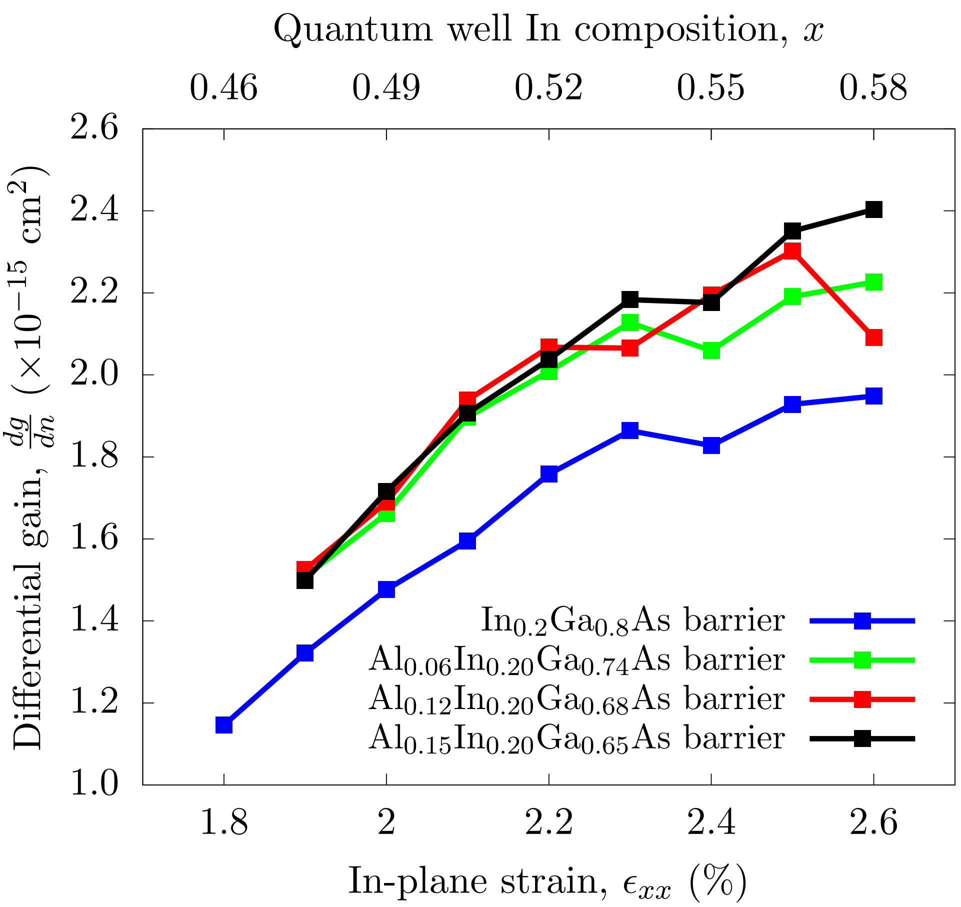

FIGURE 4.9: Calculated variation of the differential gain at threshold as a function of in-plane strain and quantum well (QW) In composition at T = 300 K, for the same series of compressively strained 1.3 μm InGaAs QWs as in Figs. 4.4, 4.6 and 4.8. The QWs have unstrained $Al_yIn_{0.2}Ga_{0.8-y}As$ barriers with y = 0, 6, 12 or 15% (blue, green, red and black lines/squares, respectively). We note that the differential gain has been calculated with respect to the three-dimensional (as opposed to areal) carrier density, so that any explicit dependence on the QW width has been removed.

wide temperature range [54]. If we assume that the T_0 value for Auger and radiative current remains close to 85 K over the full temperature range, the combined defect-related/leakage current would then account for approximately 60% of the total J_{th}, suggesting that there remains opportunity to further improve the performance of metamorphic QW devices.

The calculated variation of the differential gain at threshold, $\frac{\text{d}g}{\text{d}n}$, as a function of strain at 300 K is shown by the blue curve in Fig. 4.9, for the same series of InGaAs QWs having unstrained $In_{0.2}Ga_{0.8}As$ barriers (cf. Fig. 4.4). The differential gain, which plays a key role in determining the bandwidth of a semiconductor laser through its relationship to the modulation response frequency ($\omega_r \propto \sqrt{\frac{\text{d}g}{\text{d}n}}$), is presented in conventional three-dimensional units here, so that any explicit dependence on d_{QW} has been removed. We calculate a differential gain of approximately 1.1×10^{-15} cm^2 in the widest QW having $\epsilon_{xx} = 1.8\%$, and note that this single QW value is comparable to that calculated in Ref. [83] for an optimised InP-based InGaAsP laser structure containing 4 QWs. We note that the values of differential gain presented in

Ref. [83] were calculated at transparency (or at zero gain) as opposed to threshold, with $\frac{\mathrm{d}g}{\mathrm{d}n}$ being typically larger at the former. As such, the fact that our calculated values of $\frac{\mathrm{d}g}{\mathrm{d}n}$ at threshold are comparable to those calculated at transparency for InP-based devices containing $\gtrsim 4$ QWs suggests that significantly enhanced differential gain can be obtained in ideal 1.3 μm metamorphic devices.

As the strain is increased we calculate that $\frac{\mathrm{d}g}{\mathrm{d}n}$ increases strongly up to $\epsilon_{xx} \approx 2.3\%$, due primarily to a combination of (i) the decrease of the DOS at the VB edge with increasing strain brought about by the reduction in d_{QW} required to maintain peak gain at 1.3 μm, and (ii) the associated reduction in n_{th} (cf. Fig. 4.6). At $\epsilon_{xx} = 2.3\%$ $\frac{\mathrm{d}g}{\mathrm{d}n}$ attains a value of approximately 1.8×10^{-15} cm^2, which is equal to that calculated in Ref. [83] for an 8 QW device, reinforcing that compressively strained metamorphic InGaAs QWs offer increased differential gain as compared to equivalent InP-based heterostructures. In Ref. [131] a value of 2.1×10^{-15} cm^2 was calculated for $\frac{\mathrm{d}g}{\mathrm{d}n}$ at threshold for the aforementioned hypothetical 1.3 μm InGaAs/GaAs QW, where the strain and QW width are beyond what can be achieved experimentally. This value of $\frac{\mathrm{d}g}{\mathrm{d}n}$ is slightly larger than the values we have obtained here for devices having ternary barriers but, as we will show in Section 4.3, an appropriate choice of barrier materials can be used to further increase $\frac{\mathrm{d}g}{\mathrm{d}n}$. As was the case for n_{th} above, we again conclude that the performance of the metamorphic devices under consideration should be equivalent to, or slightly improved over that of an idealised GaAs-based benchmark device. We finally note that the improvement in $\frac{\mathrm{d}g}{\mathrm{d}n}$ begins to saturate for strains $> 2.3\%$, so that there appears to be little benefit to growing QWs with $\epsilon_{xx} \gtrsim 2.3\%$.

In addition to the analysis of single QW devices presented here, we have also calculated the variation of J_{th} and $\frac{\mathrm{d}g}{\mathrm{d}n}$ as a function of the number of QWs in the structure with the following approximation:

$$J_{\mathrm{th}_q} = n_q J_{\mathrm{rad}_q} + n_q C n_{\mathrm{th}_q}^3 \tag{4.6}$$

$$\left.\frac{\mathrm{d}g}{\mathrm{d}n}\right|_q = \frac{\mathrm{d}g}{\mathrm{d}n}\left(n_{\mathrm{th}_q}\right) , \tag{4.7}$$

where n_q is the number of QWs, and J_{rad_q}, n_{th_q} and $\left.\frac{\mathrm{d}g}{\mathrm{d}n}\right|_q$ are evaluated at the carrier density corresponding to $g_{\mathrm{th}_q} = g_{\mathrm{th}}/n_q$. We find that J_{th} increases with the number of QWs, so that the minimum values of J_{th} are obtained in devices containing $1-2$ QWs as shown in Fig. 4.10. This is in marked contrast to the InP-based 1.3 μm InGaAsP devices studied in Ref. [83], where is was determined that an optimised laser structure should contain 6 QWs. Similar to the analysis in Ref. [83], we also find that $\frac{\mathrm{d}g}{\mathrm{d}n}$ at threshold increases with the number of QWs. However, since the enhancement in $\frac{\mathrm{d}g}{\mathrm{d}n}$ brought about by increasing the number of QWs in the

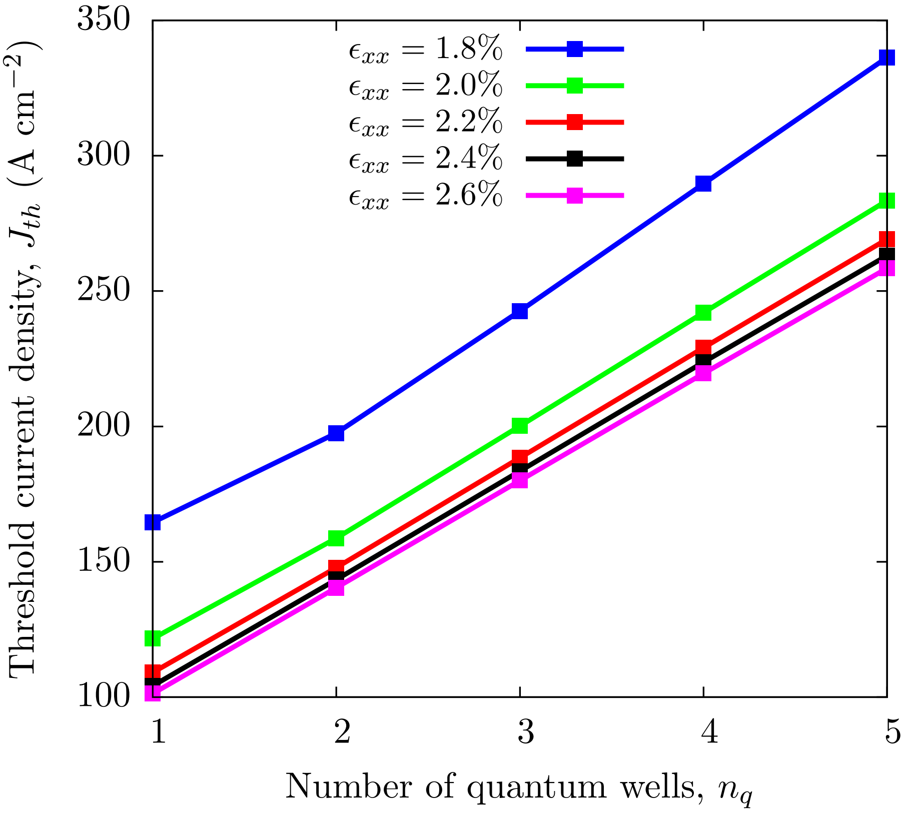

FIGURE 4.10: Calculated variation of the threshold current density as a function of number of quantum wells (QWs) at $T = 300$ K, for the series of supercells that contain a 1.8% (blue), 2.0% (green), 2.2% (red), 2.4% (black) and 2.6% (pink) compressively strained 1.3 μm InGaAs QWs corresponding to the blue solid line in Figs. 4.4, 4.6 and 4.8. The QWs have unstrained $\text{In}_{0.2}\text{Ga}_{0.8}\text{As}$ barriers.

device comes at the expense of increasing J_{th}, we conclude that an optimised device – in which J_{th} and $\frac{\text{d}g}{\text{d}n}$ are simultaneously optimised – should contain $\lesssim$ 3 QWs.

In summary, we calculate that compressively strained 1.3 μm InGaAs QWs can be grown on $\text{In}_{0.2}\text{Ga}_{0.8}\text{As}$ MBLs for strains $1.8\% \lesssim \epsilon_{xx} \lesssim 2.6\%$, corresponding to QW widths $3.8 \text{ nm} \lesssim d_{\text{QW}} \lesssim 9.8$ nm. We have calculated that J_{th} decreases rapidly with increasing strain to values less than those calculated previously for optimised InP-based devices [83]. We find that there is no clear minimum in the calculated variation of J_{th} with strain and that there is little benefit to having strains $\gtrsim 2.2\%$. However, we calculate that the IQE and differential gain at threshold can be expected to continue to increase with further increases in the strain. Based on the results of this analysis we conclude that optimised 1.3 μm InGaAs lasers grown on an $\text{In}_{0.2}\text{Ga}_{0.8}\text{As}$ MBL should contain $\lesssim$ 3 QWs having compressive strains $2.0\% \lesssim \epsilon_{xx} \lesssim 2.3\%$, corresponding to QW widths (In compositions) $5 \text{ nm} \lesssim d_{\text{QW}} \lesssim 7$ nm ($49\% \lesssim x \lesssim 54\%$).

4.3 Variable barrier composition

Having determined the optimum QW parameters for compressively strained InGaAs QWs with unstrained ternary $\mathrm{In}_{0.2}\mathrm{Ga}_{0.8}\mathrm{As}$ barriers, we now turn our attention to the composition of the barrier materials. By considering quaternary AlInGaAs barriers with variable Al composition we show that it is possible to engineer the carrier and optical confinement in such a way as to minimise the carrier and current densities at threshold, while simultaneously maximising the differential gain. We focus our attention here on unstrained quaternary barriers, but also provide some general comments on compensated strain structures containing tensile strained barriers.

We consider unstrained $\mathrm{Al}_y\mathrm{In}_{0.2}\mathrm{Ga}_{0.8-y}\mathrm{As}$ barriers, for which the Al composition y is varied between 0 and 24%. Incorporation of Al in the barrier layers produces a slight increase in the energy separation between the lowest energy electron and highest energy hole states in the QW, so that the QW width then must be increased slightly as compared to a QW having Al-free barriers in order to maintain peak gain at 1.3 μm. This effect is relatively minor, but leads to an InGaAs QW with $d_{\mathrm{QW}} \gtrsim 10$ nm for $\epsilon_{xx} = 1.8\%$. We omit this structure from our analysis here, limiting our calculations to structures with $d_{\mathrm{QW}} < 10$ nm, given the rapid increase in n_{th} and J_{th} observed for wider QWs with Al-free barriers.

Taking as an example the structure containing a 2% compressively strained QW ($\mathrm{In}_{0.49}\mathrm{Ga}_{0.51}\mathrm{As}$, $d_{\mathrm{QW}} = 7$ nm) with Al-free barriers we calculate in this case a conduction band to valence band offset ratio of $\Delta E_c : \Delta E_v \approx 60 : 40$, with the separation in energy between the lowest energy electron (highest energy hole) bound state and the barrier conduction (valence) band edge then being equal to 105 (88) meV. Adding 12% Al to the barrier increases both the conduction and valence band offsets, and raises this energy separation to 143 (150) meV. The total difference in energy between the barrier band gap and the ground state transition energy of the QW is approximately 193 meV for Al-free barriers, which increases to 293 meV for a laser structure having barriers containing 12% Al, thereby improving the carrier confinement in the QW.

The upper portion of Fig. 4.11 shows the calculated variation of the electron confinement factor at 300 K and at 360 K (solid and dashed blue lines, respectively), as well as the optical confinement factor Γ (solid green line), given in Eq. (2.78), as a function of the barrier Al composition for a 7 nm wide InGaAs QW having $\epsilon_{xx} = 2\%$. The electron confinement factor η_e is calculated at each temperature as the fraction of the total electron charge density lying within the QW at threshold, assuming thermally occupied conduction subbands described by a quasi-Fermi distribution function [81], and is given by

$$\eta_e = \frac{\displaystyle\int_{\mathrm{QW}} n(z)\mathrm{d}z}{n_{th}}\,, \tag{4.8}$$

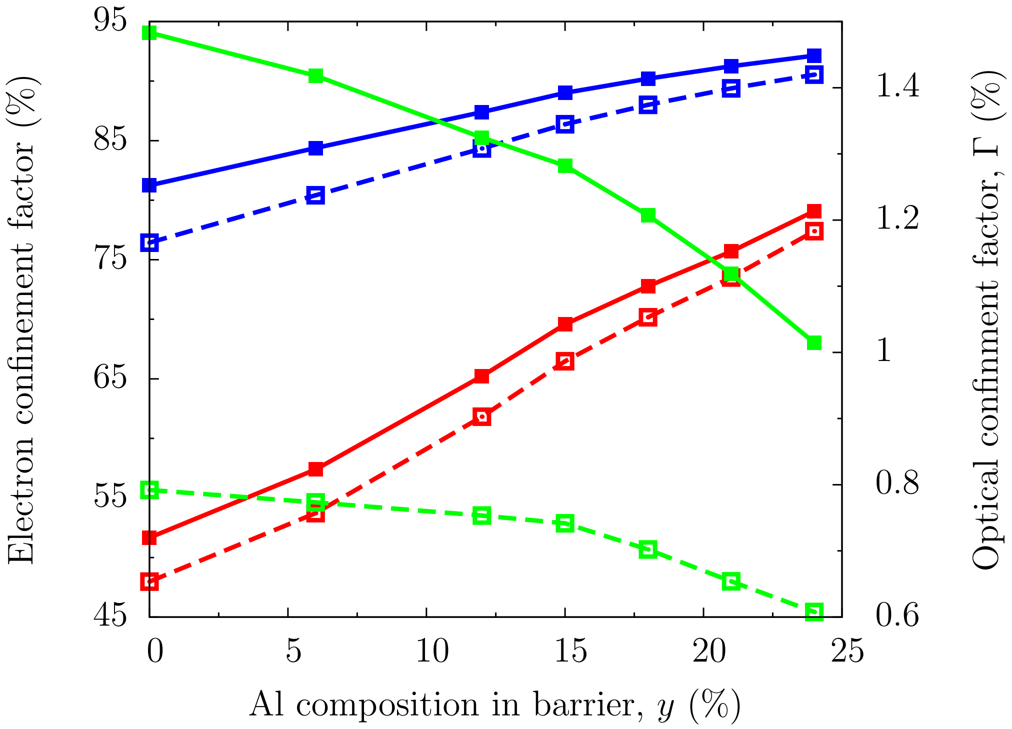

FIGURE 4.11: Calculated variation of the electron confinement factor η_e (at threshold) and optical confinement factor as a function of barrier Al composition for 2% compressively strained InGaAs quantum wells (QWs) having peak gain at 1.3 μm and unstrained AlInGaAs barriers. Blue solid (dashed) lines and closed (open) squares show the calculated variation of the electron confinement factor at 300 K (360 K) for QWs grown on an $\text{In}_{0.2}\text{Ga}_{0.8}\text{As}$ metamorphic buffer layer (MBL). Red solid (dashed) lines and closed (open) squares show the calculated variation of the electron confinement factor at 300 K (360 K) for QWs grown on an $\text{In}_{0.25}\text{Ga}_{0.75}\text{As}$ MBL. Green solid (dashed) lines show the calculated variation of the optical confinement factor for QWs grown on an $\text{In}_{0.2}\text{Ga}_{0.8}\text{As}$ ($\text{In}_{0.25}\text{Ga}_{0.75}\text{As}$) MBL.

where $n(z)$ is given by Eq. (3.79) and the integration is performed over the QW. At 300 K we see that $>$ 80% of the electron charge density lies within a QW having ternary (Al-free) barriers, and we calculate that the electron confinement increases approximately linearly with increasing barrier Al composition y, reaching 93% for $y = 24\%$, due to the associated increase in the CB offset (which increases from 156 meV to 259 meV between $y = 0$ and 24%). At 360 K we calculate that the electron confinement increases more strongly with increasing y, from 76% at $y = 0$ to 91% at $y = 24\%$. In addition to confirming that these metamorphic QWs have strong carrier (and optical) confinement, these results suggest that barrier materials with higher Al compositions should be of benefit at higher temperature, where they play an important role in limiting temperature-dependent carrier spillover. Over the same range of barrier Al compositions we calculate that the optical confinement factor Γ decreases, from 1.5% at $y = 0$ to 1.3% at $y = 12\%$, and to 1% at $y = 24\%$, as the refractive index contrast between the barrier and SCH layer is reduced.

The effects of varying the barrier Al composition on n_{th}, J_{th}, and $\frac{\text{d}g}{\text{d}n}$ are shown in Figs. 4.6 – 4.9

using solid (dashed) lines at 300 K (360 K), for 1.3 μm InGaAs QWs having $\mathrm{Al}_y\mathrm{In}_{0.2}\mathrm{Ga}_{0.8-y}\mathrm{As}$ barriers with $y = 6$, 12 and 15% (shown using green, red and black lines respectively). We calculate that the enhanced carrier confinement for $y > 0\%$ at fixed strain leads to (i) a decrease in n_{th}, (ii) a decrease in J_{th}, (iii) an increase in IQE, and (iv) significant enhancement of $\frac{\mathrm{d}g}{\mathrm{d}n}$, with the latter reaching values in excess of 2.0×10^{-15} cm^2 for a single QW device. We note that the calculated values of n_{th}, J_{th}, the IQE, and $\frac{\mathrm{d}g}{\mathrm{d}n}$ vary little for $6\% \lesssim y \lesssim 15\%$, suggesting that there is a wide window within which the barrier alloy composition can be engineered in order to optimise the laser performance.

We have performed additional calculations for compensated strain structures incorporating 2.0% compressively strained 7 nm InGaAs QWs and tensile strained AlInGaAs barriers having $-0.5\% \leq \epsilon_{xx} \leq 0.0\%$. Overall, our calculations suggest that the use of up to -0.5% tensile strained barriers leads to a minor degradation in the threshold characteristics, i.e. a 3.3% and 4.9% increase in n_{th} and J_{th} respectively, suggesting that unstrained barriers are favourable for the design of optimised devices. However, we note that the incorporation of a small amount of tensile strain in the barrier layers may be beneficial in a real device, since this may serve to facilitate dislocation-free growth of the optimised QWs identified above, which have relatively high values of compressive strain.

To summarise, our calculations have shown that the incorporation of Al in the $\mathrm{Al}_y\mathrm{In}_{0.2}\mathrm{Ga}_{0.8-y}\mathrm{As}$ barrier layer may be beneficial for the threshold characteristics of the 1.3 μm laser. This however introduces a trade-off between the carrier and optical confinement since we consider the same $\mathrm{Al}_{0.4}\mathrm{In}_{0.2}\mathrm{Ga}_{0.4}\mathrm{As}$ SCH layer. We find that n_{th} and J_{th} vary little for $6\% \lesssim y \lesssim 15\%$ at both 300 and 360 K. We note that by using an SCH layer with a larger fraction of Al up to 62% (compared to 40% in our calculations) for an enhanced refractive index contrast may further improve the optical confinement in metamorphic devices, but we do not address this possibility further in this thesis.

4.4 Variable metamorphic buffer layer composition

Having investigated 1.3 μm InGaAs/(Al)InGaAs QW lasers grown on $\mathrm{In}_{0.2}\mathrm{Ga}_{0.8}\mathrm{As}$ MBLs, we now turn our attention to the effect of varying the InGaAs MBL alloy composition on the laser performance. Specifically, we consider InGaAs QWs with well widths close to 4 nm (and 2.0% compressive strain) grown on $\mathrm{In}_{0.25}\mathrm{Ga}_{0.75}\mathrm{As}$ MBLs and calculate the associated changes in the carrier and optical confinement, and the theshold carrier density n_{th} and current density J_{th} as compared to the $\mathrm{In}_{0.2}\mathrm{Ga}_{0.8}\mathrm{As}$ laser structures studied above.

The lower portion of Fig. 4.11 shows the calculated variation of the electron confinement factor η_e at 300 K and at 360 K (solid and dashed red lines, respectively), as well as the optical

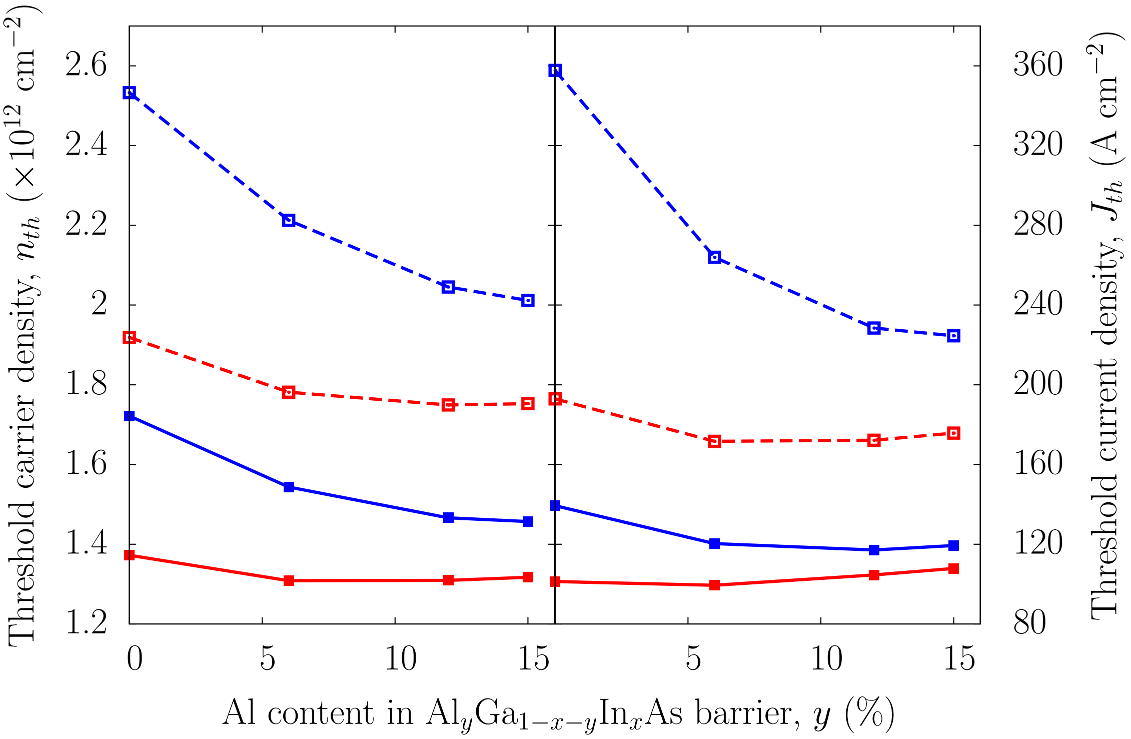

Figure 4.12: Calculated variation of the threshold carrier density n_{th} (left panel) and the threshold current denstiy J_{th} (right panel) as a function of Al content y in the $\mathrm{Al}_y\mathrm{In}_x\mathrm{Ga}_{1-x-y}\mathrm{As}$ barrier on an $\mathrm{In}_x\mathrm{Ga}_{1-x}\mathrm{As}$ MBL with $x = 20\%$ (red lines) and $x = 25\%$ (blue lines) at $T =$ 300 K (solid lines, closed squares) and 360 K (dashed lines, open squares). The QW in the structure grown on $\mathrm{In}_{0.2}\mathrm{Ga}_{0.8}\mathrm{As}$ ($\mathrm{In}_{0.25}\mathrm{Ga}_{0.75}\mathrm{As}$) MBL is 2.6% (2.0%) compressively strained and 3.8 nm $\lesssim d_{\mathrm{QW}} \lesssim$ 4.3 nm (3.7 nm $\lesssim d_{\mathrm{QW}} \lesssim$ 4.4 nm).

confinement factor Γ (dashed green line), as a function of the barrier Al composition for an InGaAs QW having $\epsilon_{xx} = 2\%$ and grown on an $\mathrm{In}_{0.25}\mathrm{Ga}_{0.75}\mathrm{As}$ MBL. The electron confinement is strongly reduced compared to an equivalent QW grown on an $\mathrm{In}_{0.2}\mathrm{Ga}_{0.8}\mathrm{As}$ MBL, with only 52% of the electron charge density residing within the QW at 300 K for a laser structure incorporating unstrained ternary barriers. This is primarily caused by the reduced energy difference between the $\mathrm{In}_{0.2}\mathrm{Ga}_{0.8}\mathrm{As}$ barrier CB edge and the electron ground state in the InGaAs QW from 105 meV with $x = 20\%$ in the $\mathrm{In}_x\mathrm{Ga}_{1-x}\mathrm{As}$ MBL to 58 meV with $x = 25\%$. We calculate that the electron confinement increases strongly with increasing Al composition y in the barrier layers, reaching 77% at $y = 24\%$. However, this is still less than the electron confinement calculated for an InGaAs QW with Al-free barriers grown on an $\mathrm{In}_{0.2}\mathrm{Ga}_{0.8}\mathrm{As}$ MBL. At 360 K we calculate that $< 50\%$ of the electron charge density lies within a QW having ternary barriers, suggesting that carrier spillover from the QW at high temperature increases strongly with increasing In composition in the MBL. While the net degradation in the optical confinement factor Γ between $y = 0$ and 24% is reduced by a factor of approximately two compared to the devices grown on $\mathrm{In}_{0.2}\mathrm{Ga}_{0.8}\mathrm{As}$ MBLs, we note that the overall optical confinement factor Γ is significantly smaller in the case of an $\mathrm{In}_{0.25}\mathrm{Ga}_{0.75}\mathrm{As}$ MBL, with $\Gamma \lesssim 0.8\%$ for all of the laser structures considered.

The change in the calculated variation of the threshold carrier density n_{th} and current density J_{th} with the InGaAs MBL composition is shown in Fig. 4.12. We saw earlier that, for sufficiently high strain, n_{th} and J_{th} vary more strongly with well width than with strain. In order to therefore compare structures with similar well width, we compare quantum wells with 2% compressive strain on an $\mathrm{In}_{0.25}\mathrm{Ga}_{0.75}\mathrm{As}$ MBL (3.7 nm $\lesssim d_{\mathrm{QW}} \lesssim$ 4.4 nm), with QWs with 2.6% compressive strain on an $\mathrm{In}_{0.20}\mathrm{Ga}_{0.80}\mathrm{As}$ MBL (3.8 nm $\lesssim d_{\mathrm{QW}} \lesssim$ 4.3 nm).

The left panel (right panel) of Fig. 4.12 shows a strong increase in n_{th} (J_{th}) at 300 K by growing the device with unstrained $\mathrm{In}_x\mathrm{Ga}_{1-x}\mathrm{As}$ barriers for $x = 25\%$ compared to $x = 20\%$, as a consequence of (i) reduced electron-hole overlap due to a reduced CB offset and (ii) reduced optical confinement factor Γ. We find that by growing the laser on the $\mathrm{In}_x\mathrm{Ga}_{1-x}\mathrm{As}$ MBL the threshold carrier density n_{th} increases by 25%, i.e. from 1.37×10^{12} for $x = 20\%$ to 1.72×10^{12} cm^{-2} for $x = 25\%$, at 300 K by having ternary InGaAs barriers. In terms of total current density at threshold J_{th} we estimate a 30% increase by growing the laser on an $\mathrm{In}_{0.25}\mathrm{Ga}_{0.75}\mathrm{As}$ MBL, with the IQE decreasing from 65% to 49%. We find that the relative increase in n_{th} can be reduced to 10%, i.e. from 1.31×10^{12} for $x = 20\%$ to 1.45×10^{12} cm^{-2} for $x = 25\%$, at 300 K by having 15% Al in the $\mathrm{Al}_y\mathrm{In}_x\mathrm{Ga}_{1-x-y}\mathrm{As}$ barrier, thereby minimising the change in J_{th} and IQE.

By increasing the temperature from 300 to 360 K we see a minor change in the relative increase of n_{th}. However, due to the overall larger magnitude of n_{th}, by growing the device on an $\mathrm{In}_x\mathrm{Ga}_{1-x}\mathrm{As}$ MBL with $x = 25\%$ instead of $x = 20\%$ we estimate an increase of almost a factor of two for J_{th}, from 193 to 358 A cm^{-2}, at 360 K when having ternary barriers. Similarly to 300 K, we find that this increase in J_{th} can be reduced down to 28% by having an $\mathrm{Al}_y\mathrm{In}_x\mathrm{Ga}_{1-x-y}\mathrm{As}$ barrier with $y \approx 15\%$. Overall these results suggest that a larger barrier band gap is required for an optimised performance of 1.3 μm lasers when they are grown on an InGaAs MBL with a larger fraction of In.

In summary, we have shown that by growing the 1.3 μm laser on an $\mathrm{In}_x\mathrm{Ga}_{1-x}\mathrm{As}$ MBL with $x = 25\%$ the electronic and optical properties are diminished compared to $x = 20\%$, mainly due to (i) smaller band gap difference and (ii) poorer refractive index contrast between the QW, barrier and SCH layers. Our results indicate that the variation of the threshold characteristics of the 1.3 μm laser with the $\mathrm{In}_x\mathrm{Ga}_{1-x}\mathrm{As}$ MBL composition can be reduced, especially at higher temperatures, by using an $\mathrm{Al}_y\mathrm{In}_x\mathrm{Ga}_{1-x-y}\mathrm{As}$ barrier having $y \approx 15\%$. By contrast, our calculations also suggest that the threshold characteristics of the 1.3 μm laser can be (in principle) improved by growing the heterostructure on an $\mathrm{In}_x\mathrm{Ga}_{1-x}\mathrm{As}$ MBL with $x < 20\%$. However highly strained and/or wide InGaAs QWs are expected to be required for a 1.3 μm peak emission (cf. Fig. 4.1). Thus we conclude that optimised electronic and optical

x in $\text{In}_x\text{Ga}_{1-x}\text{As}$ MBL	$x = 20\%$
y in $\text{Al}_y\text{Ga}_{0.8-y}\text{In}_{0.2}\text{As}$ barrier	$6\% \lesssim y \lesssim 15\%$
z in $\text{In}_x\text{Ga}_{1-x}\text{As}$ QW	$49\% \lesssim x \lesssim 54\%$
QW width, d_{QW}	$5\text{ nm } \lesssim d_{\text{QW}} \lesssim 7\text{ nm}$
QW strain, ϵ_{QW}	$2.0\% \lesssim \epsilon_{xx} \lesssim 2.3\%$
Number of QWs, N_{QW}	$N_{\text{QW}} \lesssim 3$

TABLE 4.1: Design parameters of a laser structure grown on an InGaAs Metamorphic Buffer Layer (MBL) for an optimised 1.3 μm emission. The table includes (i) InGaAs MBL composition, (ii) AlInGaAs barrier composition, (iii) InGaAs Quantum Well (QW) composition, (iv) QW thickness d_{QW}, (v) in-plane strain in the QW ϵ_{xx}, and (vi) number of QWs N_{QW}.

properties of 1.3 μm emitting lasers will be achieved by growing the heterostructure on an $\text{In}_{0.2}\text{Ga}_{0.8}\text{As}$ MBL, thereby avoiding the need for pseudomorphic growth of highly strained layers with (potentially) wide InGaAs QWs.

4.5 Conclusions

We have presented a theoretical investigation and optimisation of the properties and performance of GaAs-based 1.3 μm InGaAs/(Al)InGaAs quantum well lasers grown on InGaAs metamorphic buffer layers. Beginning with a consideration of the strained AlInGaAs band structure we demonstrated that there is large scope for the design of 1.3 and 1.55 μm metamorphic quantum well heterostructures, using compressively strained ternary (InGaAs) or quaternary (AlInGaAs) quantum wells with unstrained or tensile strained ternary or quaternary barriers.

Following the general analysis of the available laser structures in Section 4.1 we focused our attention on devices consisting of compressively strained ternary InGaAs quantum wells having unstrained (Al)InGaAs barriers. We calculated the variation of the gain and threshold characteristics as a function of strain and quantum well width in Section 4.2, and showed that metamorphic 1.3 μm laser structures offer reduced threshold current density, comparable internal quantum efficiency and enhanced differential gain compared to those calculated previously for optimised InP-based devices. We also considered quantum wells having quaternary AlInGaAs barriers in Section 4.3 and showed that the barrier Al composition can be varied to optimise the trade-off between the carrier and optical confinement in such a way as to enhance the laser performance, leading to reduced carrier and current densities at threshold, as well as improved internal quantum efficiency and differential gain, with the effects of quaternary barriers becoming increasingly beneficial with increasing temperature.

Through our analysis we identified that an optimised 1.3 μm device grown on an $\text{In}_{0.2}\text{Ga}_{0.8}\text{As}$ metamorphic buffer layer should consist of $\lesssim 3$ quantum wells, with the InGaAs quantum wells having compressive strains $2.0\% \lesssim \epsilon_{xx} \lesssim 2.3\%$, corresponding to quantum well widths 5 nm $\lesssim d_{\text{QW}} \lesssim$ 7 nm (In compositions $49\% \lesssim x \lesssim 54\%$). We further identified that the optimum barrier materials are unstrained $\text{Al}_y\text{In}_{0.2}\text{Ga}_{0.8-y}\text{As}$ alloys having Al compositions $6\% \lesssim y \lesssim 15\%$. Finally, by varying the composition of the InGaAs metamorphic buffer layer in Section 4.4 we found that the devices should be grown on virtual substrates having low In composition for improved gain characteristics. Although this is consistent with the expected improvement in device performance in going from InP-based to GaAs-based heterostructures, our analysis indicates that for optimised laser performance the devices should be grown on an $\text{In}_{0.2}\text{Ga}_{0.8}\text{As}$ metamorphic buffer layer. Our guidelines for an optimised 1.3 μm laser design are summarised in Table 4.1.

Overall, our theoretical analysis has identified important trends in the performance of GaAs-based metamorphic quantum well lasers, has provided design parameters for optimised laser structures, and has confirmed the promise of these novel heterostructures for the development of high performance GaAs-based 1.3 μm semiconductor lasers.

Chapter 5

AlGaInP 610 nm quantum wire based emitters on GaAs

In this chapter we perform an analysis on the electronic properties of lattice-mismatched [110]-oriented AlInP Quantum Wire (QWR) based heterostructures for 610 nm emission.

We begin in Section 5.1 with an overview of the structural properties of the AlGaInP QWR nanostructures that were grown at Tyndall National Institute and whose characteristics are investigated later in the chapter. We then investigate in Section 5.2 the effects of strain on the electronic properties of QWR-based supercells using the Hamiltonian derived in Section 2.3. Unlike QW-based systems, where the strain Hamiltonian (2.56) can be simplified due to vanishing components of the stress and strain tensors, most of these elements become non-zero in a QWR-based heterostructure.

Following this we turn our attention to the photoluminescence (PL) measurements performed on a series of AlGaInP QWR-based structures in Section 5.3. Having understood the behaviour of the electronic structure of AlGaInP-based QWRs under strain, we analyse the accuracy of our method by comparing the ground state transition energy with the measured PL energies. We then examine the efficiency of the radiative emission of our structures from the integrated PL measurements. Here we also discuss the trends in the photoluminescence response of AlGaInP-based QWR systems due to variable direction of the linearly polarised excitation.

In Section 5.4 we discuss the electroluminescence measurements performed on QWR-based samples under hydrostatic pressure at University of Surrey, UK. The pressure measurements are used primarily to determine the importance of Γ-related radiative recombination and Γ–X electron leakage in the QWR structures considered. Finally, we conclude in Section 5.5.

5.1 Nanostructure formation

For the devices being investigated in this chapter, the original intention was to develop AlInP QD-based emitters using the self-assembled Stranski-Krastanov growth technique [11]. The main advantage of a QD-based system over QW-based active regions consists in (i) potentially reduced carrier leakage due to the localisation of the carrier in the QDs, and (ii) the reduced density of states due to atomic-like electronic properties of the QDs with discrete energy states. At the same time, the self-assembled growth is preferred over, e.g., site controlled growth [138], due to its ability to create a relatively dense array of QDs with a Gaussian-like size and shape distribution, thereby resulting in a broad emission spectrum, favourable for LED applications.

In order to achieve a noticeable emission from such heterostructures, the devices were grown on GaAs substrates tilted by 6° towards the (111)A plane which allowed high quality growth of numerous QD layers (up to 200) in one structure. AFM measurements performed on these structures indicate, however, that the self-assembled growth results in the formation of ordered (both vertically and horizontally) QWRs instead, which are elongated along the [110] direction with a length of $0.5 - 2.0$ μm and a thickness around 20 nm. We speculate that the QWR formation is caused primarily by the bunched surface organisation [139]. Although, compared to QDs, the QWRs have a larger size due to their elongation along the [110] direction, it is expected that their optical properties will still be superior to QW-based heterostructures. Due to the tilt of the substrate, the calculation of electronic and optical properties require, ideally, the rotation of the $\mathbf{k}\cdot\mathbf{p}$ and strain Hamiltonians, as well as the strain tensor. In our calculations however we consider only perfectly oriented heterostructures grown along the [001] direction and we assume that the impact of the substrate tilt on the electronic and optical properties is negligible.

The periodic horizontal and vertical ordering of the grown QWRs, as can be seen from the TEM scan in Fig. 5.1, suggests that the plane wave method with periodic boundary conditions is a very suitable approximation for the evaluation of the electronic (and optical) properties of such a superlattice. In Section 3.2 we derived the general form of the plane wave method, which can be directly applied to QD-based heterostructures; we apply it directly here for the calculation of the electronic (and optical) properties of [110] QWR-based systems. Unlike the discrete energy levels in a QD, the [110] QWRs require, ideally, the calculation of energy dispersion along the wire direction. Because we however are primarily interested in the ground state properties, we therefore simplify our calculations by determining the energy levels only at $k = 0$. Because the calculations are undertaken using a quantum dot code the calculations at $k = 0$ also give results for a regular grid of k points determined by the QD supercell size. This allows us therefore to also use the $k = 0$ calculations to estimate spectral properties as a function of energy. In addition, due to the much larger length of the [110] QWRs compared to their thickness, in our calculations we consider the wires to have an infinite length according

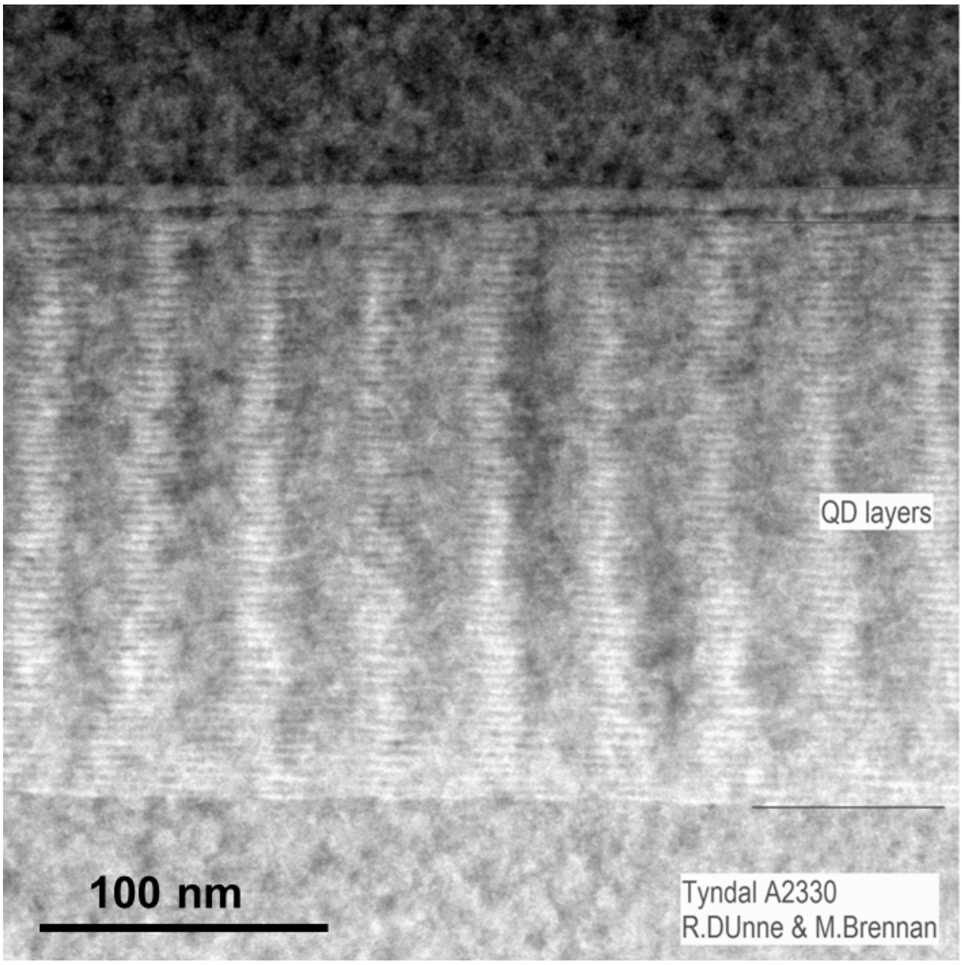

FIGURE 5.1: HAADF TEM image of a 60-layer $Al_{0.22}In_{0.78}P/(Al_{0.6}Ga_{0.4})_{0.52}In_{0.48}P$ heterostructure. The stacked AlInP QWRs are visible as bright columns. The TEM is performed at Intel Ireland Labs.

to the periodic boundary conditions. The top-view diagram of the QWR in the supercell and its characteristic function are given in Appendix D.

For the calculation of electronic and optical properties in this chapter we consider compressively-strained [110] AlInP QWRs surrounded by an AlGaInP barrier lattice-matched to the GaAs substrate. Although the self-assembled growth brings about a distribution of QWR cross-sections that may impact the electronic and optical properties, we simplify our analysis here by considering QWRs with a rectangular cross-section only.

5.2 Strain distribution in a [110] QWR based supercell

The weak electron confinement and significant electron leakage in 610 nm emitters is associated with the direct-to-indirect band gap crossover in the $(Al_xGa_{1-x})_{0.52}In_{0.48}P$ barrier lattice-matched to GaAs, which occurs at $x \approx 0.6$ [140] with the largest direct band gap $E_g \approx 2.3$ eV.

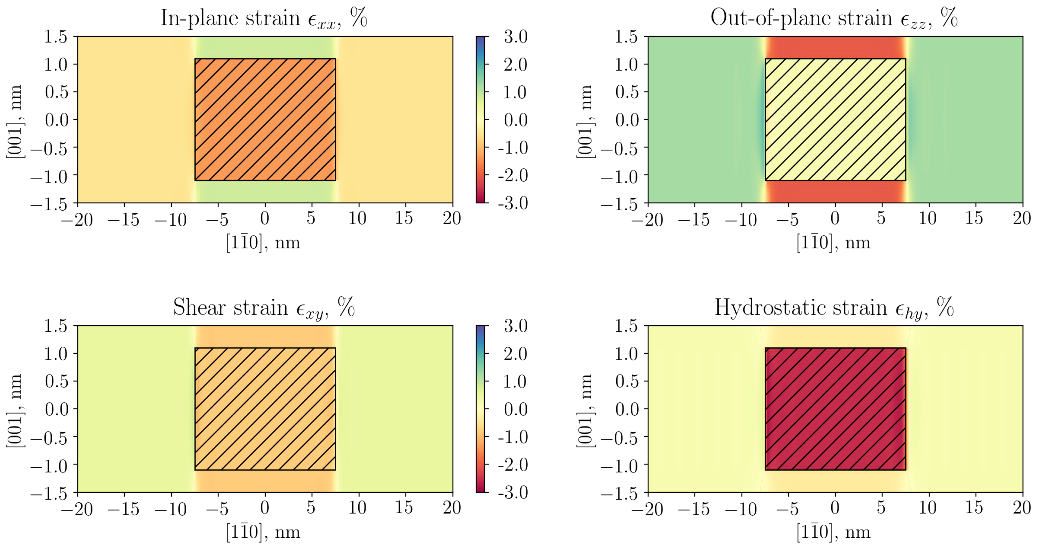

FIGURE 5.2: Calculated distribution of the in-plane (upper left panel) and out-of-plane (upper right panel) component of the strain tensor, ϵ_{xx} and ϵ_{zz} respectively, the shear component of the strain tensor ϵ_{xy} (bottom left panel), and the hydrostatic strain $\epsilon_{hy} = \epsilon_{xx} + \epsilon_{yy} + \epsilon_{zz}$ (bottom right panel), in the (110) plane of a $Al_{0.316}Ga_{0.212}In_{0.472}P$ supercell on GaAs with the size 56.6×56.6×3 nm. The supercell contains a 15 nm thick and 2.2 nm tall [110] $Al_{0.22}In_{0.78}P$ QWR, denoted by the hatched black rectangle. Note that the in-plane dimensions (or [1$\bar{1}$0]) are one order of magnitude larger than along the growth direction (or [001]).

While the band gap can be slightly increased by going beyond the crossover composition, the optical properties in this case will tend to be strongly diminished since most of the electrons will be located in a different position of the wave vector space with a much larger effective mass compared to the CB minimum at Γ. In this section we consider the best case scenario, where the unstrained AlGaInP barrier material on GaAs is at the $\Gamma - X$ crossover at 300 K with the assumed band gap $E_g = 2.284$ eV. For the heterostructures with x in the $(Al_xGa_{1-x})_{0.52}In_{0.48}P$ barrier larger than 0.6 the PL response is much weaker, indicating the indirect band gap nature of the material.

The anisotropic strain associated with the QWR will tend to split the energies of the X states both in the wire and in the barrier layer. The strain associated with a [110] QWR has been analysed previously by Ma *et al.* [141], and is worth to summarise here, before we consider our model wires in further details.

It is relatively straightforward to derive expressions for the strain components using a coordinate system where the axes 1, 2 and 3 are pointing along the [1$\bar{1}$0], [110] and [001] directions respectively. In this coordinate system, there is no shear strain in the growth plane ($\epsilon_{12} = 0$). Likewise, there is no strain in the barrier along axis 2 ($\epsilon_{22} = 0$) while the strain in the wire along axis 1 is given by $\epsilon_{22} = -\epsilon_0$, where ϵ_0 is the (positive) lattice mismatch between the wire and substrate lattice constants. If we assume isotropic elastic constants that are equal in the well and the barrier, then the hydrostatic strain is zero in the barrier, so that $\epsilon_{11} = -\epsilon_{33}$ for the barrier material, where ϵ_{11} is negative (barrier compressed) along axis 1 and ϵ_{33} is positive along axis 3 (barrier lattice constant stretched along the growth direction). Converting to Cartesian coordinates yields $\epsilon_{xx} = \epsilon_{yy} = (\epsilon_{11} + \epsilon_{22})/2$, $\epsilon_{zz} = \epsilon_{33}$ and $\epsilon_{xy} = (\epsilon_{11} - \epsilon_{22})/2$. If we assume that the wire is continuous along the growth (z) direction, which based on Figure 5.1 is a reasonable first approximation, then the strain tensor in Cartesian coordinates is given by [141]:

$$\epsilon_{\mathrm{QWR}} = \begin{pmatrix} (\epsilon_{11} - \epsilon_0)/2 & (\epsilon_{11} + \epsilon_0)/2 & 0 \\ (\epsilon_{11} + \epsilon_0)/2 & (\epsilon_{11} - \epsilon_0)/2 & 0 \\ 0 & 0 & \epsilon_{33} \end{pmatrix} \tag{5.1}$$

Fig. 5.2 shows the calculated distribution of the in-plane (upper left panel) and out-of-plane (upper right panel) strain, ϵ_{xx} and ϵ_{zz} respectively, as well as the shear strain ϵ_{xy} (bottom panel), in the (110) plane of a 56.6×56.6×3 nm $\mathrm{Al}_{0.316}\mathrm{Ga}_{0.212}\mathrm{In}_{0.472}\mathrm{P}$ supercell, that contains a 15 nm thick and 2.2 nm tall [110] $\mathrm{Al}_{0.22}\mathrm{In}_{0.78}\mathrm{P}$ QWR. We find a very good agreement between calculated distribution of strain in the AlInP QWR and the expected values from the model above. We firstly notice that the hydrostatic strain ϵ_{hy}, which is shown on the bottom right panel in Fig. 5.2, given by $\epsilon_{hy} = \epsilon_{xx} + \epsilon_{yy} + \epsilon_{zz}$, is applied primarily to the AlInP QWR, as expected based on the analysis above. The resulting compressive hydrostatic strain in the QWR increases the band gap by shifting the conduction band minimum at the Γ point of the Brillouin zone upwards in energy (as well as the valence band maximum downwards in energy), as we indicated in Section 2.3. The overall shallow electron confinement in the QWR for 610 nm emission, which is believed to be the dominant factor that influences the leakage related losses of the radiative recombination [142], is further weakened due to the reduced conduction band offset. The ground hole state, on the other hand, remains almost fully localised in the AlInP QWR because of (i) a larger magnitude of the valence band offset compared to the conduction band, and (ii) a much larger effective mass.

Our calculations show there is minimal hydrostatic strain ϵ_{hy} applied to the barrier layer due to anisotropy of the elastic constants. This is in a good agreement with the assumptions in our model above, and overall it has a negligible effect on the electronic structure. The effects of strain on the band structure of an $\mathrm{Al}_{0.316}\mathrm{Ga}_{0.212}\mathrm{In}_{0.472}\mathrm{P}$ supercell with an $\mathrm{Al}_{0.22}\mathrm{In}_{0.78}\mathrm{P}$ QWR are shown in Fig. 5.3, where we only include the effects of the axial strain components on the Hamiltonian. Due to the biaxial strain in the term q of the Hamiltonian (2.56) the HH (orange line) and LH (purple line) band edges at Γ, originally degenerate in an unstrained material, will split, and the confined ground hole state in the QWR would then posess mostly a HH-like character, which is expected for a compressively strained nanostructure. In addition, the shear strain component ϵ_{xy} introduces a further mixing between the HH and LH states, increasing the band edge splitting in Fig. 5.3, and leading to the highest valence state being predominantly

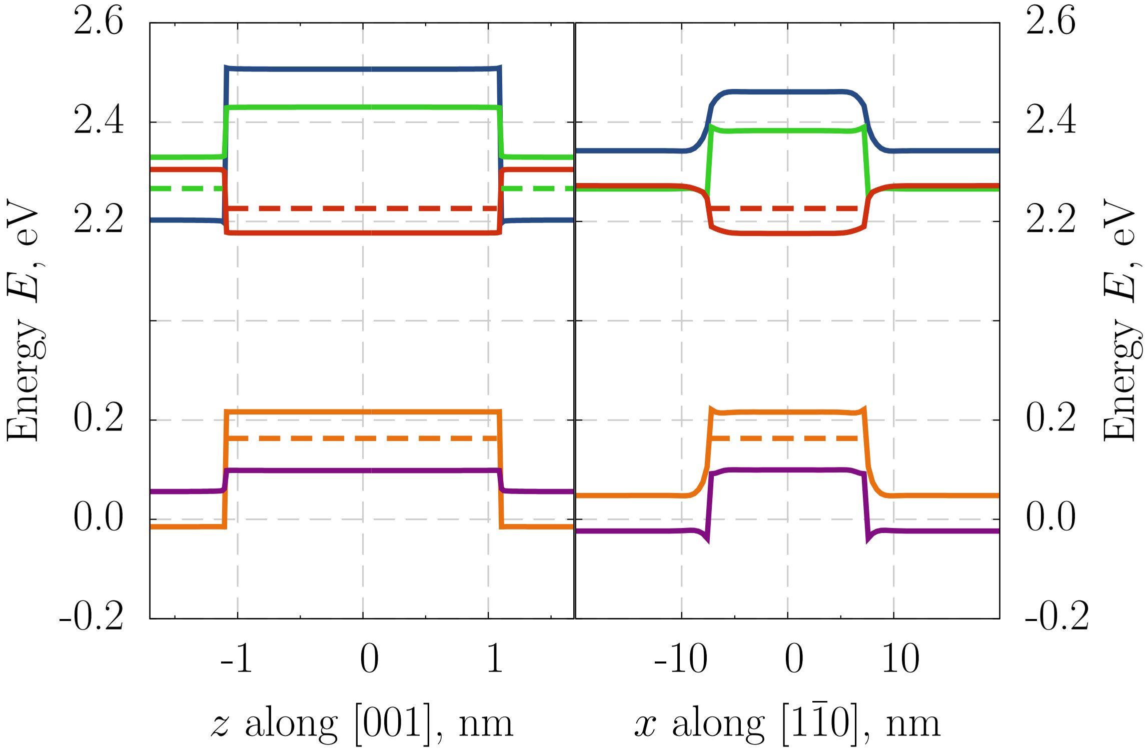

FIGURE 5.3: Calculated distribution of the conduction band minima at Γ (solid red line), $X_\parallel$ (blue line), $X_\perp$ (solid green line), and heavy-hole (solid orange line) and light-hole (purple line) valence band maxima at the supercell wave vector $\mathbf{k} = 0$ through the centre of a 15 nm thick and 2.2 nm tall [110] $Al_{0.22}In_{0.78}P$ QWR in a 56.6×56.6×3.4 nm $Al_{0.316}Ga_{0.212}In_{0.472}P$ supercell along the growth direction (left panel) and along the $[1\bar{1}0]$ direction (right panel). The dashed red, green and orange lines denote the ground electron states at Γ and X, and the hole state respectively.

associated with p-like states pointing along the QWR axis. We consider this mixing further, when we analyse the polarisation characteristics of the emitted light in Section 5.3 below.

The strain also affects the three conduction band minima at the X point of the Brillouin zone, which are degenerate in an unstrained material. We label the three X states as X_x, X_y and X_z along the [100], [010] and [001] direction of $\mathbf{k}$ respectively. However, due to (i) the symmetry of the supercell with respect to the axis of the AlInP QWR and (ii) the growth being along the [001] direction, we use here the following labeling: $X_x = X_y = X_\perp$; $X_z = X_\parallel$. The effects of strain on the conduction band minima at X of a [110] QWR are given by [124]:

$$\begin{aligned} X_\perp &= X_0 + \Xi_h \epsilon_{hy} + \frac{1}{3}\Xi_{ax}(\epsilon_\parallel - \epsilon_\perp) \\ X_\parallel &= X_0 + \Xi_h \epsilon_{hy} + \frac{2}{3}\Xi_{ax}(\epsilon_\perp - \epsilon_\parallel)\,, \end{aligned} \tag{5.2}$$

where X_0 is the unstrained conduction band edge at X, Ξ_h and Ξ_{ax} denote the hydrostatic and axial deformation potentials of the X band edge respectively, $\epsilon_{\|} = \epsilon_{xx} = \epsilon_{yy}$ and $\epsilon_{\perp} = \epsilon_{zz}$. The compressive (tensile) hydrostatic strain pushes these three bands to lower (higher) energies, and the effect is very similar to the VB maximum. Due to the biaxial strain these states split causing either $X_{\perp}$ or $X_{\|}$ to be at a lower energy. Using Eq. (5.2), the magnitude of this splitting in energy equals to $\Delta X = \left|X_{\perp} - X_{\|}\right| = \left|\Xi_{ax}(\epsilon_{\|} - \epsilon_{\perp})\right|$. The conduction band edge at X in the QWR-based supercells is almost unaffected by the hydrostatic strain ϵ_{hy}. However we find that the biaxial strain pushes the $X_{\|}$ ($X_{\perp}$) states in the barrier downwards in energy by 84 (21) meV along the [001] ($[1\bar{1}0]$) direction, thereby reducing the barrier potential energy for the electrons to overcome to thermally leak from the QWR; this effect will be discussed in Section 5.4 in more detail. Consequently the barrier material, originally at the $\Gamma - X$ crossover, has an indirect band gap, with the ground X state located below the barrier Γ CB.

Because the heterostructure in Fig. 5.3 has a type-I $\Gamma - \Gamma$ band alignment, i.e. the CB (VB) edge at Γ of the barrier has a higher (lower) potential energy compared to the AlInP QWR, the confined Γ electrons and holes are located in the QWR. However due to the band alignment, the X conduction states in the AlInP QWR are located at a higher energy compared to the AlGaInP barrier, thereby acting as a potential "barrier" for the X states in the surrounding barrier material. This results in a set of delocalised X energy levels located in the barrier with a very large density of states due to the large effective mass of the X electrons. The barrier X states for the structure in Fig. 5.3 are calculated to be about 40 meV above the lowest confined Γ state in the QWR. Carrier leakage from the QWR to the barrier is then expected to be an increasing problem as the temperature increases, as is already known to be the case for red QW devices [70]. This issue will be discussed further below.

5.3 Optical properties and photoluminescence measurements

The goal of this section is to use our 8-band **k·p** model to analyse trends in optical properties, both qualitatively and quantitatively, of QWR-based heterostructures. Consequenty, it becomes necessary to determine whether there is good agreement between (i) the electronic and optical properties calculated using the 8-band **k·p** model, and (ii) the measured PL response of existing QWR-based structures. The blue curve in Fig. 5.4 shows the measured PL spectrum of a 60-layer AlInP QWR-based system at 300 K. We note here that all of the measured PL properties presented in this section were, for consistency, measured on this sample. The measurements show a relatively broad emission from this QWR-based structure, with a Full Width Half Maximum (FWHM) of about 163 meV, and the peak emission wavelength around 618 nm. Although for the calculation of the spontaneous emission spectrum in our work we consider the effects of inhomogeneous broadening, it is important nonetheless to explicitly investigate

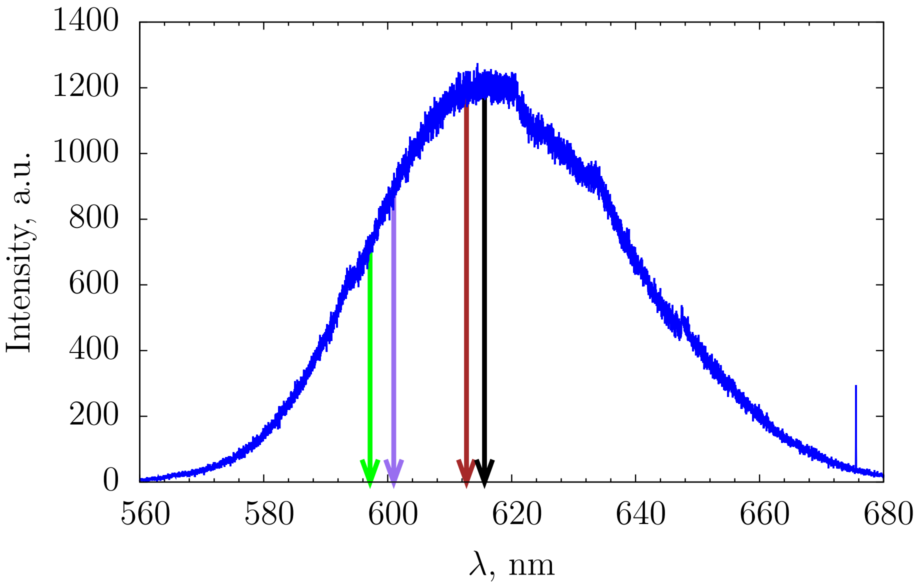

FIGURE 5.4: Measured PL spectrum of a $Al_{0.22}In_{0.78}P/(Al_{0.60}Ga_{0.40})_{0.52}In_{0.48}P$ QWR-based structure (blue line) and calculated transition energy for the QWR-based supercell specified in Table 5.1 at 300 K.

the expected variation in ground state emission wavelength due to geometry and possible composition variations. Table 5.1 includes the set of supercells we performed calculations on for the analysis of the emission broadening. The green arrow in Fig. 5.4 denotes the calculated ground state transition energy for a 7.5 nm wide and 2.2 nm tall $Al_{0.22}In_{0.78}P$ QWR with an in-plane and vertical spacing of 32.5 and 1.8 nm respectively, where the QWR is surrounded by $Al_{0.32}Ga_{0.20}In_{0.48}P$. The compositions of the QWR and barrier materials are taken from the nominal growth conditions. The QWR in-plane thickness is approximately extrapolated from the upper part of the TEM micrograph in Fig. 5.1, and the height of 2.2 nm has been used in order to preserve the nominal 0.4:3.0 nm growth ratio of AlInP QWR and AlGaInP barrier respectively. From our calculations we find that the ground state transition energy of 597 nm (in units of wavelength λ) for this structure is located at the high energy (short wavelength) tail of the measured PL spectrum. By considering a larger in-plane thickness of the AlInP QWR, thereby preserving the nanostructure periodicity, but breaking the assumed wire to barrier growth ratio of 0.4:3.0, we find a minor redshift in the emission towards 601 nm, denoted by the purple arrow.

To produce an additional redshift in ground state emission wavelength, we consider that a minor fraction of Ga atoms from the AlGaInP barrier diffuses into the AlInP QWR, thereby decreasing the band gap while maintaining the 0.4:3.0 wire to barrier growth ratio, i.e. migration of a small amount of Ga atoms from the barrier can give a noticeable change in QWR composition from $Al_{0.22}In_{0.78}P$ to $Al_{0.177}Ga_{0.043}In_{0.78}P$. The transition energy of this structure is denoted by the brown arrow in Fig. 5.4 with the calculated ground state emission wavelength of 613 nm. A further decrease in the QWR composition due to a further exchange of Al (Ga) atoms towards

Line colour	QWR					Barrier	λ, nm
	Composition	d_w, nm	h_w, nm	d_{xy}, nm	d_z, nm	Composition	
Green	$Al_{0.22}In_{0.78}P$	7.5	2.2	32.5	1.2	$Al_{0.32}Ga_{0.20}In_{0.48}P$	597.2
Purple	$Al_{0.22}In_{0.78}P$	15	2.2	25	1.2	$Al_{0.32}Ga_{0.20}In_{0.48}P$	601.0
Brown	$Al_{0.177}Ga_{0.043}In_{0.78}P$	15	2.2	25	1.2	$Al_{0.32}Ga_{0.20}In_{0.48}P$	612.7
Black	$Al_{0.135}Ga_{0.085}In_{0.78}P$	7.5	2.2	32.5	1.2	$Al_{0.33}Ga_{0.19}In_{0.48}P$	615.6

TABLE 5.1: Composition and geometry data used for theoretical simulations of QWR-based supercells, with d_w, h_w, d_{xy} and d_z denoting the QWR width, height, in-plane and vertical distance between the QWRs respectively. The calculated transition energies in units of wavelength λ correspond to the highlighted arrows in Fig. 5.4.

(from) the barrier material redshifts the emission towards 616 nm (black arrow). Although for the last heterostructure we preserved the nominal 0.4:3.0 layer thickness ratio by assuming a narrower QWR, from the first two structures we found that only a minor change in emission wavelength can be attributed to this change in geometry. We conclude that the inclusion of some Ga – Al interdiffusion between the wire and the barrier provides a theoretically calculated emission wavelength in good agreement with the observed experimental data. However we note that there are in addition some further factors that may contribute to the broadening of the emission, e.g. (i) partial strain relaxation of the QWRs and (ii) partial CuPt ordering [84, 85]. Although earlier PL measurements indicate that the CuPt atomic ordering should be diminished due to the high temperature growth conditions [143], we nevertheless speculate that a portion of the broad spectrum can be attributed to this effect, which is known to decrease the band gap. While there are theoretical methods that describe the effect of the CuPt ordering on the band gap [144], it is nearly impossible to accurately quantify its effect on a particular heterostructure. Nevertheless, we believe that there is good overall agreement between (i) the calculated ground state transition energies using the 8-band $\mathbf{k}\cdot\mathbf{p}$ model, and (ii) the emission wavelength of the measured PL spectrum of a representative sample, supporting the use of the model below for further calculation of trends in electronic and optical properties.

PL measurements were performed on a series of QWR-based structures with different separation between QWRs along the growth direction (or barrier thickness) in order to determine its influence on the intensity of the PL emission. It was found that by decreasing the barrier thickness from 20 nm to 3 nm an enhanced spontaneous emission can be obtained, suggesting that a minimal amount of barrier material has to be deposited to maximise the intensity and efficiency of the emission. We perform here a theoretical analysis of the impact of the barrier thickness on the QWR spontaneous emission for a better understanding of its influence. Fig. 5.5 shows the calculated variation of the radiative current density J_{rad} of the x-polarised emission (red line) and peak emission wavelength λ_p (blue line) of a 15 nm thick and 2.2 nm tall [110] $Al_{0.22}In_{0.78}P$ QWR in an $Al_{0.316}Ga_{0.212}In_{0.472}P$ supercell with in-plane base dimensions 56.6×56.6 nm^2 and supercell height between 3 and 10 nm, and injected areal carrier density

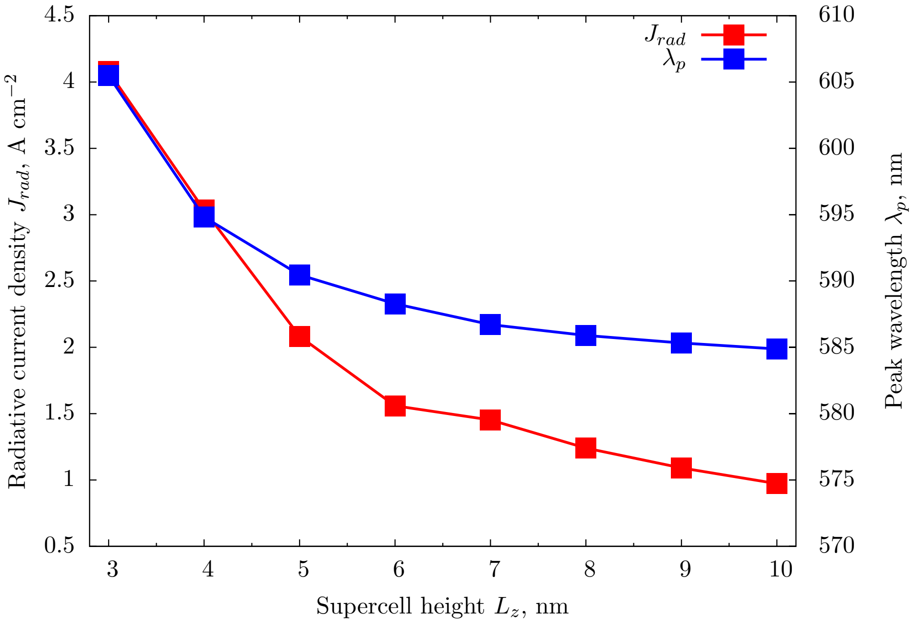

FIGURE 5.5: Calculated variation of the radiative current density J_{rad} of the $x-$polarised emission (red line) and peak emission wavelength λ_p (blue line) of a 15 nm thick and 2.2 nm tall [110] $Al_{0.22}In_{0.78}P$ QWR in an $Al_{0.316}Ga_{0.212}In_{0.472}P$ supercell with the in-plane base 56.6×56.6 base and the supercell heigh between 3 and 10 nm, and injected areal carrier density $n_{2D} = 1.56 \times 10^{11}$ cm^{-2}.

$n_{2D} = 1.56 \times 10^{11}$ cm^{-2}. Here, for the calculation of J_{rad} we consider the possibility of the injected electrons to occupy both the Γ states in the QWR as well as the delocalised X states in the barrier. Comparing the strain distribution in this set of supercells, we find that there is negligible change in the magnitude of strain tensor elements by increasing the supercell height from 3 to 10 nm. Therefore the change in peak emission wavelength from 605 to 585 nm when the supercell thickness increases from 3 to 10 nm occurs mostly due to a smaller vertical separation between the QWRs (or thinner barrier) and wavefunction coupling between the neighbouring layers.

In addition, increasing the supercell thickness from 3 to 10 nm leads to a significant reduction in the calculated radiative current density J_{rad} by a factor of 4, due to a combination of factors. Firstly, by increasing the supercell thickness from 3 to 10 nm, the wavefunction coupling between the neighbouring layers decreases; therefore the Γ electron ground state reaches the Γ band edge of the barrier. At the same time, the difference between the ground Γ and X electron states decreases from 44 to 8.7 meV when the supercell thickness changes from 3 to 10 nm, thereby allowing a smaller fraction of electrons to occupy the direct band gap states according to the Fermi-Dirac distribution, which becomes particularly important at 300 K or higher temperatures.

Secondly, the shallow ground electron confinement and a smaller supercell height compared to its in-plane base size results in the partial spillover of the electron wavefunction into the

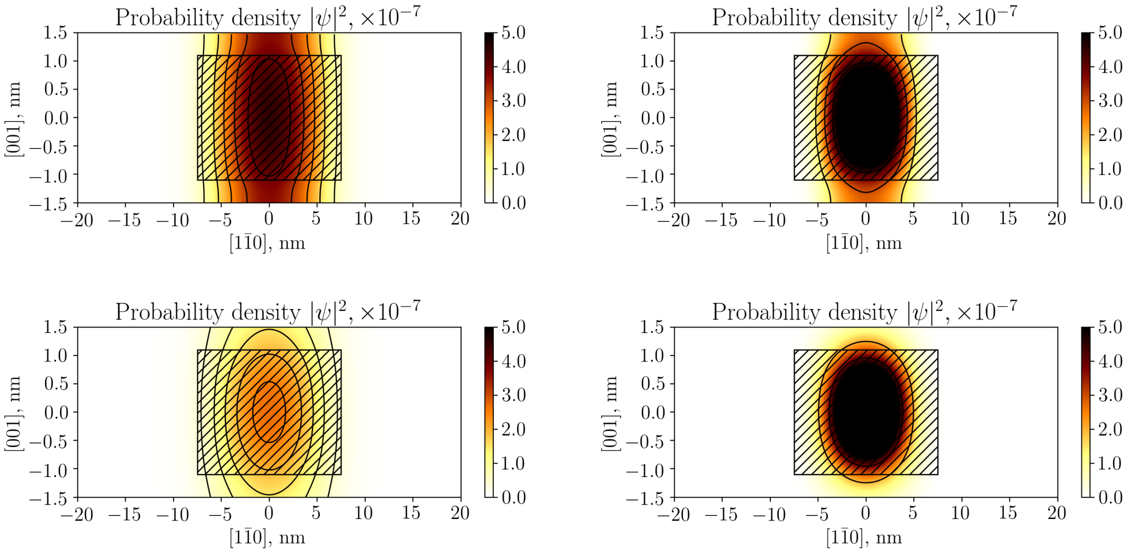

FIGURE 5.6: Calculated distribution of the probability density of the ground electron (left column) and hole (right column) states in the (110) plane of a $Al_{0.316}Ga_{0.212}In_{0.472}P$ supercell on GaAs with the in-plane base size 56.6×56.6 nm, and the height 3 nm (10 nm) in the upper row (bottom row). The supercell contains a 15 nm thick and 2.2 nm tall [110] $Al_{0.22}In_{0.78}P$ QWR, denoted by the hatched black rectangle. Note that the in-plane dimensions (or [1$\bar{1}$0]) are one order of magnitude larger than along the growth direction (or [001]).

barrier; its wavefunction confinement ratio decreases from 73 to 41% by increasing the height of the supercell from 3 to 10 nm. The wavefunction confinement ratio η_ψ is given by:

$$\eta_\psi = \int_{\Omega_Q} |\psi(\mathbf{r})|^2 \, d\mathbf{r} \,, \tag{5.3}$$

where the integration is performed over the volume of the nanostructure Ω_Q (in this case QWR) and is always smaller than 1 due to the wavefunction being normalised. This, in combination with the strongly localised ground hole state with $\eta_\psi \approx 85\%$, means that a stronger electron-hole wavefunction overlap will be achieved when the electron wavefunction will occupy the least amount of volume i.e. in a supercell with a smaller height, which is shown in Fig. 5.6. From our calculations we find that the momentum matrix element between the ground electron and hole states of 12.3 eV·Å in the 3 nm tall supercell for x-polarised light reduces to 8.15 eV·Å by increasing the height to 10 nm.

The emission efficiency of a photonic structure and its behaviour as a function of temperature can be studied by analysing the temperature dependence of the integrated PL spectrum. Such measurements can provide very useful insight into the nature of carrier leakage mechanisms by determining the activation energy (or energies) associated with thermal leakage [145, 146]. Temperature-dependent PL measurements were performed on a range of QWR-based samples grown at the Tyndall National Institute, with the measured temperature dependence of the

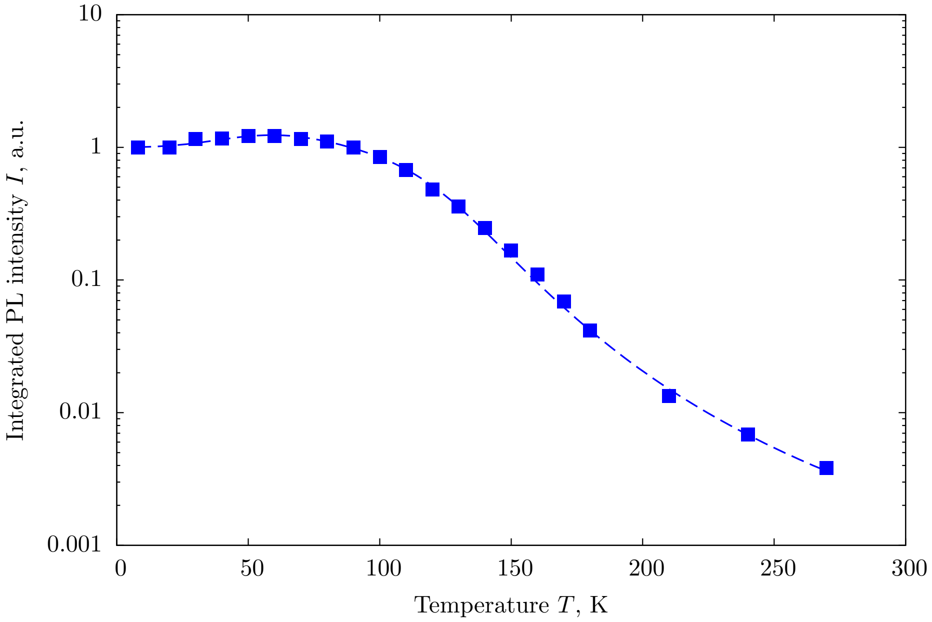

FIGURE 5.7: Measured temperature dependence of the integrated PL intensity (blue squares) of a $Al_{0.22}In_{0.78}P/(Al_{0.60}Ga_{0.40})_{0.52}In_{0.48}P$ QWR-based structure, normalised to the measurement at 8 K. The dashed line denotes the fitting of the measured integrated intensity using Eq. (5.4).

integrated PL intensity of the AlInP/AlGaInP structure discussed above shown using blue squares in Fig. 5.7. The following Arrhenius equation was used to fit the data [143]

$$I(T) \propto \frac{1}{\sqrt{T}\left(A\exp\left(-\frac{E_e}{k_BT}\right) + B\exp\left(-\frac{E_h}{k_BT}\right) - CT^2\right)} \tag{5.4}$$

where A, B, C are fitting parameters, E_e, E_h are activation energies, and k_B and T denote the Boltzmann constant and temperature respectively. Looking at the data for $T \lesssim 60$ K we find that there is an unusual increase in integrated PL intensity, which is fitted using the last term in the demonimator in Eq. (5.4). We believe that this increase is associated with the indirect band gap nature of the barrier material (cf. Fig. 5.3), whereby the intervalley transfer of electrons from the X states of the barrier into the confined Γ electron states in the AlInP QWRs is phonon-assisted. A rise in temperature from 8 K and the consequent increase in electron-phonon scattering rate, thereby promotes this transfer leading to an increased radiative recombination rate between the electrons and the localised holes in the AlInP QWR [143].

The activation energies used to fit the temperature dependent integrated PL from Fig. 5.7 are $E_e = 23$ meV and $E_h = 108$ meV. We note that there is a certain variability in the chosen set of parameters to reproduce the fit, particularly the activation energies E_e and E_h. Ignoring the term CT^2 in the denominator of Eq. (5.4), we find that a range of activation energies E_e and E_h can be used to reproduce the resulting temperature dependent integrated PL intensity.

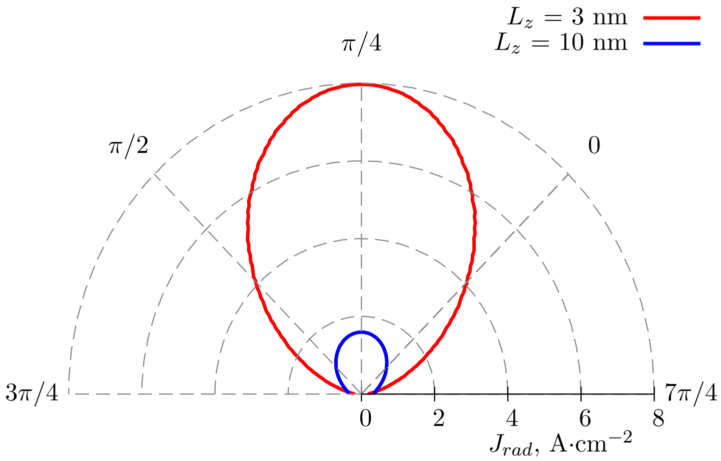

FIGURE 5.8: Calculated radiative current density J_{rad} for a single light polarisation $\widehat{e} = \widehat{x}\cos(\theta) + \widehat{y}\sin(\theta)$ as a function of the polarisation direction of the incident wave θ of a 15 nm thick and 2.2 nm tall [110] $Al_{0.22}In_{0.78}P$ QWR in a 56.6×56.6×3.4 nm $Al_{0.316}Ga_{0.212}In_{0.472}P$ supercell. At $\theta = \pi/4$ the light polarisation is along the QWR axis.

For instance, a similar fit can be obtained by choosing E_e (E_h) in the range of 17.5 – 37.5 (107 – 127) meV, while simultaneously adjusting the parameter A (B). Overall it is clear that two activation energies are necessary to accurately fit the experimental measurements, one of which is much smaller than the other. Examining the band structure in Fig. 5.3, we see that the ground hole state is located approximately 107 meV above the LH band edge of the barrier. At the same time, we calculate that the ground electron state in the AlInP QWR is located 40 meV below the ground delocalised X state in the barrier. We therefore attribute the activation energies E_e and E_h to the confinement depth[1] of the ground electron and hole states respectively, with electron leakage due to the shallow confinement then making a significant contribution to the nonradiative losses in short wavelength red emitters [70]. In Chapter 6 we propose a way to improve the efficiency of shorter wavelength red emitters by employing metamorphic substrates to give improved electron confinement and to consequently reduce the electron leakage.

Due to the fact that the active region is formed of QWRs, it is expected that the spontaneous emission will be highly anisotropic, favouring a particular polarisation direction of the emitted radiation. The polar plot in Fig. 5.8 shows the calculated radiative current densities J_{rad} of a [110] AlInP QWR as a function of the in-plane polarisation direction of the incident electromagnetic wave at a constant injected areal carrier density $n_{2D} = 1.56 \times 10^{11}$ cm^{-2}. For the calculation of the polarisation dependent emission we consider here two supercells (cf. Fig. 5.5) with height L_z = 3 nm (red line) and 10 nm (blue line). The angle $\theta = \pi/4$ is associated with the electromagnetic radiation that is linearly polarised along the QWR axis. We, again, find here that enhanced emission can be achieved by growing the multilayer structure with thinner barrier, as described earlier. When investigating the impact of barrier thickness earlier, we calculated the radiative current rate for x-polarised TE emission (cf. Fig. 5.5). We see from Fig. 5.8 that the QWR emission strength varies strongly with angle, being maximised along the [110] direction, and with the value along x direction equivalent to that obtained by averaging over all directions. From our calculations we find that rotating from the x to the [110] direction almost doubles J_{rad} for the structure in a 3 nm tall supercell from 4.07 to 7.96 A·cm^{-2} (from 0.972 to 1.592 A·cm^{-2} for the 10 nm tall supercell).

---

[1] Here and in Chapter 6 the *confinement depth* will denote the difference in energy between, e.g., the electron (hole) ground state and the barrier conduction (valence) band edge.

For the polarisation angle $\theta = 3\pi/4$, i.e. normal to the QWR axis, J_{rad} in fact decreases by surrounding the AlInP with a thinner barrier. This suggests that a larger degree of linear polarisation (DOLP) p is associated with the reduced barrier thickness, where p is defined here as:

$$p = \frac{J_{rad}^{[110]} - J_{rad}^{[\bar{1}10]}}{J_{rad}^{[110]} + J_{rad}^{[\bar{1}10]}}\,, \tag{5.5}$$

where $J_{rad}^{[110]}$ and $J_{rad}^{[\bar{1}10]}$ are the radiative current densities along the [110] (maximum J_{rad}) and $[\bar{1}10]$ (minimum J_{rad}) polarisation directions respectively. From our calculations we find that by reducing the supercell height from 10 to 3 nm p increases linearly from 0.63 to 0.95. The polarisation-dependent PL measurements performed on the QWR-based structure from Fig. 5.4 and 5.7 indicate that almost 80% of the emitted light is polarised along the QWR axis, which is in reasonably good agreement with our model. We note that the measured DOLP is intermediate between that which we calculate for the 10 nm and 3 nm supercell height, suggesting that the interwire coupling in the actual device may be lower than that which we have assumed when using a 3 nm supercell height. The fact that TE-polarised red emission with a DOLP close to 1 can be obtained by employing [110]-oriented QWRs is particularly relevant when we take into account the possibility to generate green and blue highly polarised emission using III-N based heterostructures [147, 148]. It is therefore possible to design white light sources based on red, green and blue emitters with high DOLP, thereby reducing the complexity of devices like LCD displays by, e.g., removing the requirement for polarising filters. The multilayer [110] AlGaInP QWR-based heterostructures are therefore an attractive candidate as a red emitter for such technologies.

5.4 Electroluminescence measurements under hydrostatic pressure

Hydrostatic pressure is a very useful tool to analyse loss mechanisms in semiconductor devices. When hydrostatic pressure is applied, the equilibrium lattice constant changes and the band

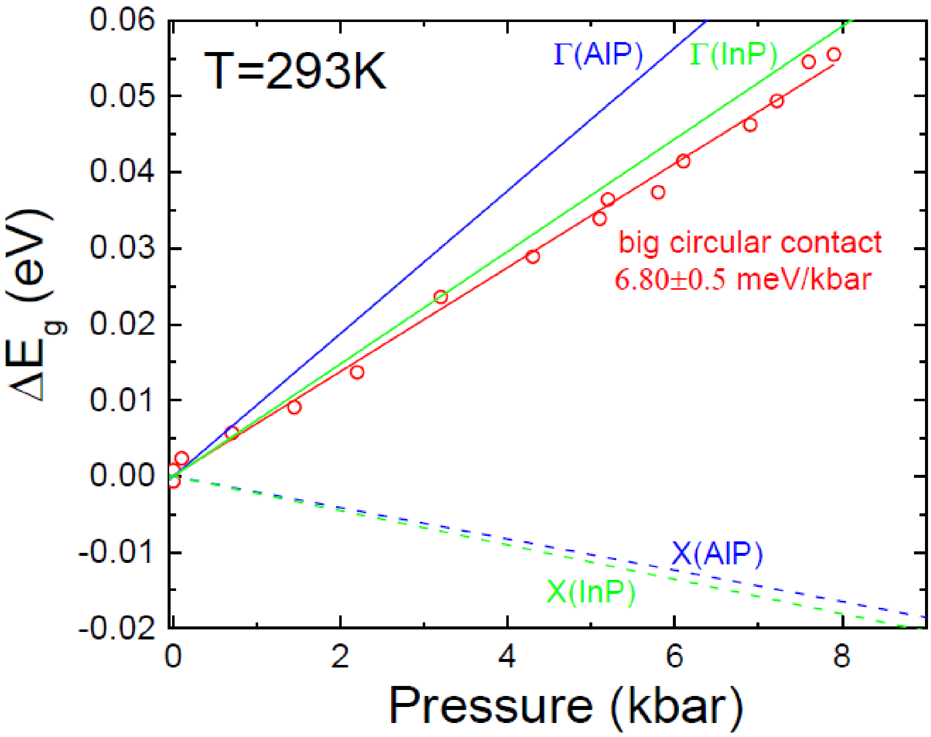

FIGURE 5.9: Measured variation of the peak electroluminescence energy of an Al(Ga)InP QWR-based LED device under hydrostatic pressure, denoted by the red open circles. The blue and green solid (dashed) lines denote the change in the direct (indirect) band gap under hydrostatic pressure of AlP and InP respectively. The measurements were performed at 293 K. The measurements indicate an increase in peak emission energy with applied hydrostatic pressure, consistent with direct band gap radiative recombination.

structure is modified in a controlled way. In particular, hydrostatic pressure increases the direct gap at Γ by about 10 meV/kbar and decreases the indirect gap at X by about 2 meV/kbar [140]. As a result the separation between Γ and X states decreases with increasing pressure. Hence if carrier escape from Γ to X is a significant loss mechanism in a semiconductor laser or LED, it can be expected that this loss becomes more significant with increasing pressure, and so the device optical efficiency will decrease as pressure is applied. Previous measurements of the red laser threshold current density as a function of hydrostatic pressure have proved to be very useful in identifying the role of carrier leakage to X states in determining overall device efficiency [71, 149]. As there has been little previous work on red QD/QWR LEDs, hydrostatic pressure measurements should also provide useful insight for these devices, and samples were therefore provided to collaborators at University of Surrey to undertake such measurements.

Figure 5.9 shows the measured variation of the energy gap with pressure for an LED structure. We see increasing peak energy with increasing pressure, which is consistent with movement of the direct band gap. The measured pressure dependence of 6.8 meV/kbar is consistent with that expected from AlInP QWRs with high In composition, as $\mathrm{d}E_g/\mathrm{d}p$ = 9.4meV/kbar and 7.4 meV for AlP and InP respectively, and strained QWRs can be expected to have a lower pressure coefficient than equivalent bulk alloys, due to third order elasticity effects [150].

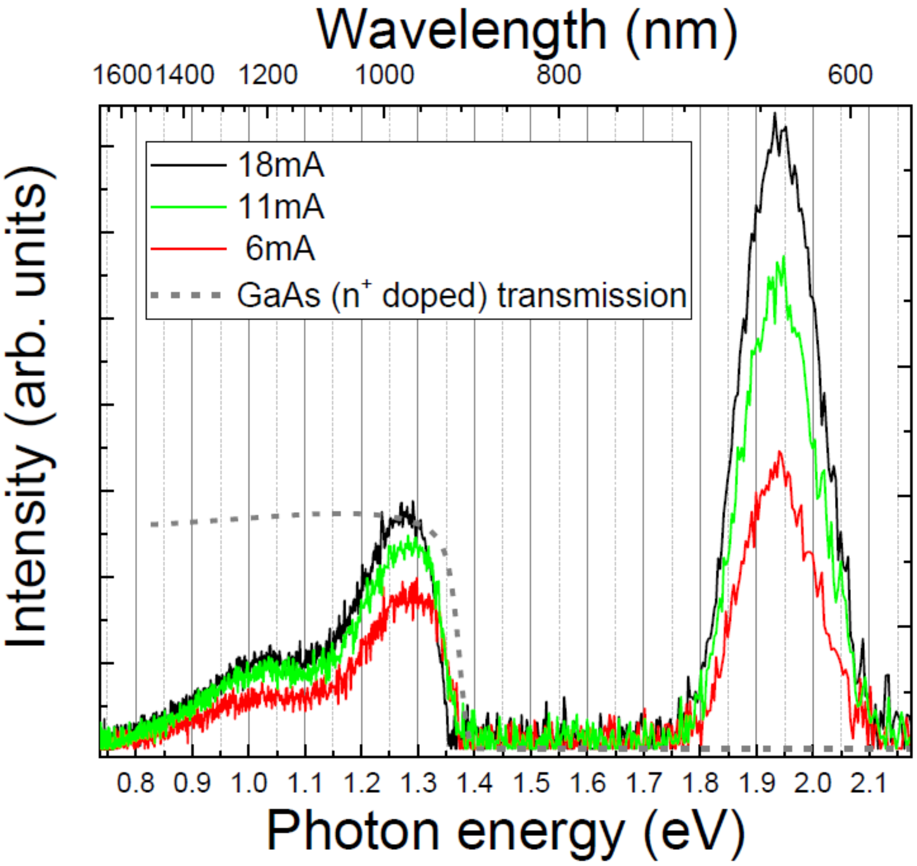

FIGURE 5.10: Measured electroluminescence spectra of an Al(Ga)InP QWR-based LED device resulting when a 6 mA (red line), 11 mA (green line) and 18 mA (solid black line) current is injected into the device at ambient pressure. The measurements were performed at 293 K. The dashed black line denotes the spectral range in which the GaAs substrate is transparent. The emission from the active region is observed around the high energy (2 eV) peak, while the spectrum below 1.4 eV is due to emission from the n-doped GaAs substrate.

Figure 5.10 shows the room temperature PL spectra measured across a wide spectral range for a sample LED structure. Interestingly, some broad PL emission is found below 1.4 eV, which subsequent analysis showed was due to emission from the n-doped GaAs substrate. It should be noted that the data presented in Fig. 5.10 has been spectrally corrected to account for the efficiency of the photodetector used in the spectral measurements, which is about an order of magnitude more efficient in the low energy range than it is around 2 eV.

Because the LED output decreases strongly with increasing temperature, it was not possible to undertake spectrally resolved pressure measurements at room temperature. Instead the integrated light output was measured, using both an InGaAs photodetector and a Si photodetector.

Figure 5.11 shows the integrated intensity measured as a function of drive current for the two detectors. It can be seen that the light output drops off more rapidly with drive current for the Si detector. This is most likely because the Si detector does not detect all the long wavelength near-IR band.

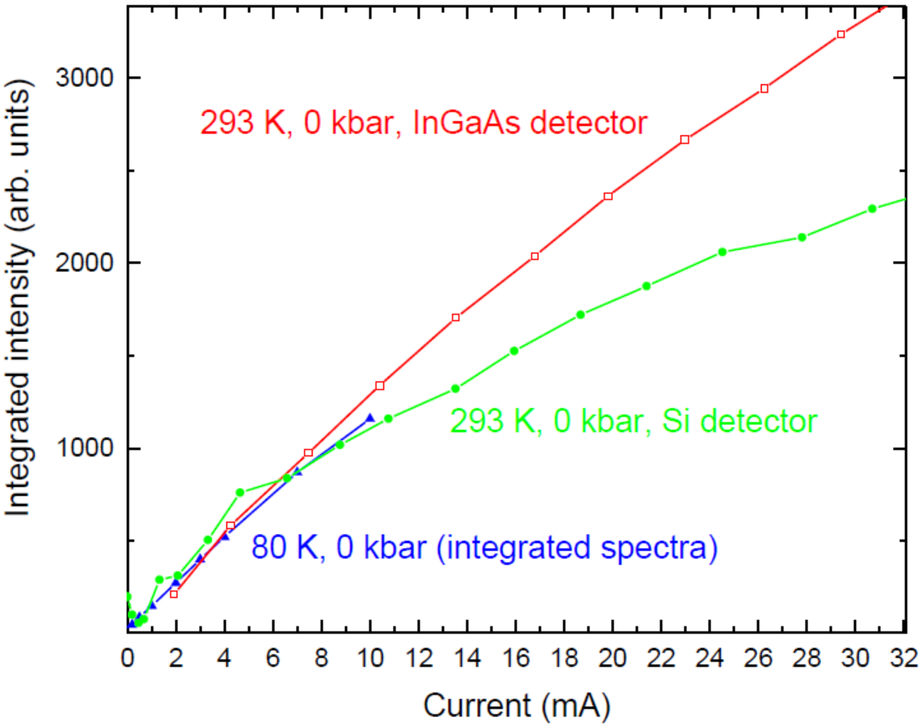

FIGURE 5.11: Measured L–I curves of an Al(Ga)InP QWR-based LED device under ambient pressure. The emission was collected using an InGaAs detector (red line) and Si detector (green line) at 293 K, while the blue solid line corresponds to the L–I curve measured at 80 K.

The left panel of Fig 5.12 shows the measured room temperature L–I curve as a function of pressure. It can be seen that the current required to achieve a given total light output increases weakly with pressure. This is investigated in further detail in the right panel of Fig. 5.12, where we plot the normalised total current required to provide a constant output intensity as a function of pressure. The black data points were obtained using the Si detector, while the red data points were obtained using the InGaAs detector. It is difficult to make an accurate quantitative analysis of the measured data. We note however that the data obtained using the Si detector tend to lie above those obtained using the InGaAs detector, presumably reflecting the greater contribution or near-IR emission in the InGaAs case. Assuming that the radiative emission and defect currents do not vary with pressure, a reasonable fit is obtained if 7% of the total current at ambient pressure is due to Γ–X leakage, using the model below [71, 151]:

$$\begin{aligned} I_{tot}(p) &= I_{def}(p) + I_{rad}(p) + I_{leak}^{\Gamma-\mathrm{X}}(p) \\ I_{rad}(p) + I_{def}(p) &= const \\ I_{leak}^{\Gamma-\mathrm{X}}(p) &\propto \exp\left[-\left(\frac{\mathrm{d}E_{\mathrm{X}}}{\mathrm{d}p} - \frac{\mathrm{d}E_{\Gamma}}{\mathrm{d}p}\right)\frac{p}{k_{\mathrm{B}}T}\right], \end{aligned} \tag{5.6}$$

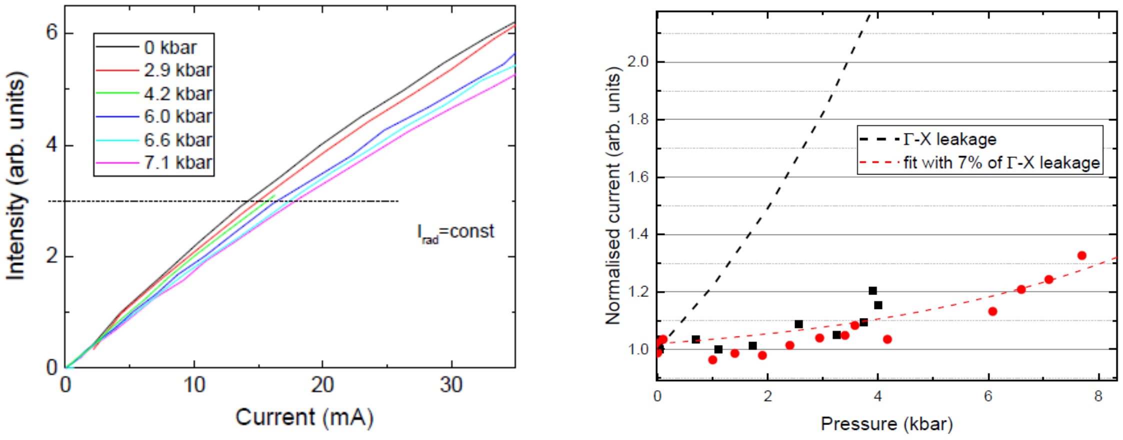

FIGURE 5.12: (Left panel) Measured L–I curves of an Al(Ga)InP QWR-based LED device under hydrostatic pressure and at 293 K temperature. The dashed black line shows how the total current varies for an arbitrary constant light output level as a function of applied pressure. (Right panel) Measured normalised injected current to achieve a constant radiative emission as a function of applied hydrostatic pressure, denoted by the dashed black line in the left panel. The black squares and red circles correspond to the injection current required to achieve a constant emission measured by a Si and InGaAs detector respectively. The dashed black line denotes the expected behaviour of the L–I curve assuming that Γ–X leakage is the dominant non-radiative loss mechanism, whereas the measured data (red circles) was fitted using the model from Eq. (5.6).

where $I_{tot}, I_{def}, I_{rad}$ and $I_{leak}^{\Gamma-X}$ denote the total, defect-related, radiative and $\Gamma - X$ leakage-related current respectively. The dashed black line shows the expected variation of the normalised current, ignoring the near-IR contribution to the L–I curve, and assuming that the radiative current is only due to red emission (close to 2 eV). It can be seen that the measured pressure dependence is significantly lower than that predicted by the dashed black line. If we allow however that a large part of the measured light output comes from the low-energy near-IR peak then the measured data are consistent with the Γ–X leakage being the dominant loss mechanism in the device active region. As noted, the detectors are up to an order of magnitude more sensitive in the near-IR range compared to the red spectral range. From Fig. 5.10, the measured response due to the substrate emission could then be close to an order of magnitude larger than that due to the red-band emission. We conclude therefore, based on Figs. 5.10 and 5.12, and wider spectral measurements undertaken at Tyndall National Institute that the dominant non-radiative loss mechanism in the devices considered is associated with non-radiative Γ–X leakage, due to the close proximity of the Γ and X states in the device being investigated.

5.5 Conclusions

In this chapter we investigated the electronic and optical properties of [110]-oriented compressively strained AlInP Quantum Wires (QWRs) for 610 nm emission, surrounded by AlGaInP barriers lattice-matched to the GaAs substrate.

In Section 5.1 we outlined the motivation for the use of, originally intended, QD-based heterostructures, which were grown using the self-assembled Stranski-Krastanov technique at Tyndall National Institute. In order to obtain high-quality multilayer QD-based heterostructures (with up to 200 layers) a 6° tilt was applied to the substrate towards the (111)A direction. The resulting step-bunched organisation consequently promoted the growth of QWRs elongated along the [110] direction, which we can model using the plane wave method with periodic boundary conditions to calculate the electronic and optical properties.

In our calculations, the QWR composition was chosen to match the nominal growth conditions, with the main QWR details extrapolated from the TEM scan, including QWR geometry and periodicity. In Section 5.2 we analysed the influence of strain on the electronic structure of compressively strained AlInP QWRs surrounded by an AlGaInP barrier grown lattice-matched on GaAs. From the calculated strain distribution we found that the band structure of the AlInP QWRs is affected the most due to the lattice mismatch, thereby reducing the CB offset and the electron confinement depth. Due to the biaxial strain in the AlGaInP barrier (i) the lowest CB edge is located at the X point in the Brillouin zone, and (ii) a significant fraction of the electrons can populate the delocalised X states in the barrier, assuming a Fermi-Dirac carrier distribution for the electrons.

We perform an analysis of the electronic and optical properties of QWR-based supercells in Section 5.3. Having found that there is reasonable agreement between our model and the measured PL energies of the QWR-based structure investigated, we examined the impact of the barrier thickness L_z on the radiative current density J_{rad} of such supercells. Our calculations show that enhanced optical properties can be achieved by separating the QWR layers with a thinner barrier due to (i) a smaller fraction of electrons occupying the barrier X states because of a deeper confinement, and (ii) a larger ground electron-hole wavefunction overlap, which is related to better confinement of the ground electron state in the wire. From the PL measurements performed on AlInP/AlGaInP-based heterostructures we found that (i) interatomic diffusion, (ii) partial relaxation, and (iii) potential CuPt ordering have to be taken into account to explain the wide PL spectra.

From the integrated PL measurements we found that thermal leakage of electrons from the QWR into the barrier is the primary cause of the large decrease in efficiency of shorter wavelength emitters. We found that the reduced symmetry of the QWRs allows to create emitters with a strong degree of linear polarisation. The radiative emission was found to be polarised nearly 100% along the QWR axis when the QWRs are surrounded by thin barrier layers ($L_z \approx$ 3 nm), making such heterostructures attractive for display applications, where polarising filters are typically employed.

Finally, we analysed the electroluminescent properties of QWR-based LED devices under hydrostatic pressure in Section 5.4, for which the experimental measurements were performed at

University of Surrey, UK. A blueshifted emission due to applied pressure confirmed the direct band gap nature of the radiative recombination. A large component of the measured response in the pressure measurements was estimated as being due to sub-band-gap optical emission from the *n*–doped substrate. Assuming that this substrate emission only has a weak dependence on pressure, we conclude that Γ–X leakage is indeed the dominant loss mechanism in the active region at room temperature.

Considering that the major drawback of these devices is carrier leakage related with the weak electronic confinement, in the next chapter we will examine a way to enhance the efficiency of shorter wavelength red emitters by employing lattice-mismatched metamorphic buffer layers.

Chapter 6

AlGaInP 610 nm metamorphic quantum well based light-emitting diodes

For this chapter we perform calculations to investigate the potential benefits of growing Al(Ga)InP QW-based light-emitting diodes (LED) with 610 nm peak emission on InGaAs Metamorphic Buffer Layers (MBL).

We start in Section 6.1 with an analysis of the range of compositions accessible for a direct band gap Al(Ga)InP alloy when grown on an $\mathrm{In}_z\mathrm{Ga}_{1-z}\mathrm{As}$ MBL. We then consider a series of heterostructure for 610 nm emission with a compressively strained AlInP QW surrounded by Al(Ga)InP barriers, which are at the direct-to-indirect band gap crossover and lattice-matched to the InGaAs MBL. Using model solid theory we estimate the change in the conduction band offset, which is crucial for the investigation of electronic confinement.

Having estimated the band alignment in the series of heterostructures considered, we then analyse the electronic properties of a series of structures in Section 6.2, where we focus primarily on the effect of the InGaAs MBL lattice constant on the electronic confinement and estimate its potential impact on the thermal leakage of electrons. We then perform an analysis of the optical properties of the series of structures in Section 6.3, to determine the effect of an InGaAs MBL lattice constant on the calculated radiative recombination rate. These are then compared to preliminary results of temperature dependent microphotoluminescence measurements performed on QW-based structures grown on $\mathrm{In}_z\mathrm{Ga}_{1-z}\mathrm{As}$ with $z = 0$ and 6%. Finally, we conclude in Section 6.4.

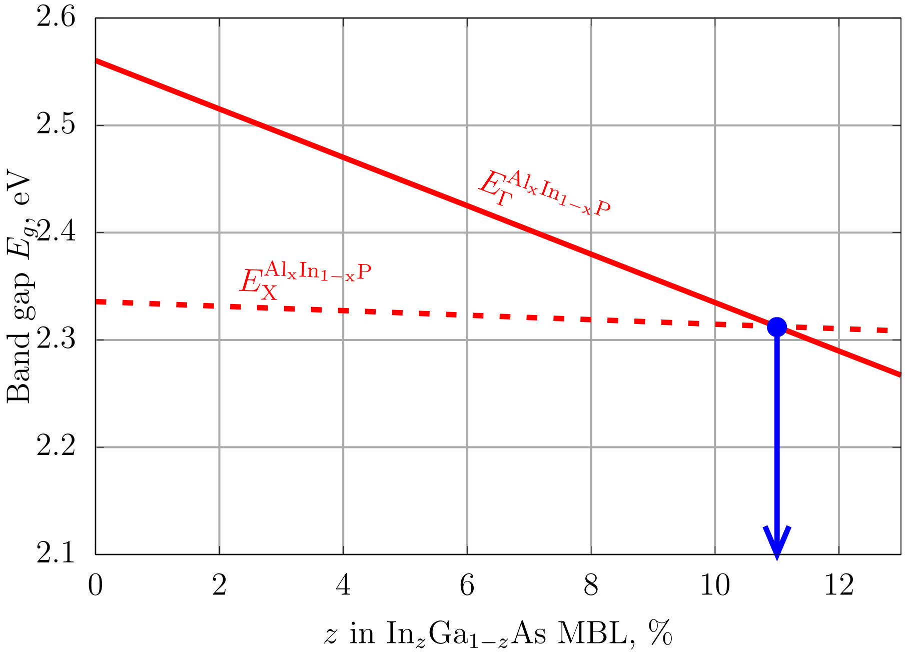

FIGURE 6.1: Calculated variation of the bulk band gap of $\mathrm{Al}_x\mathrm{In}_{1-x}\mathrm{P}$ lattice matched to the $\mathrm{In}_z\mathrm{Ga}_{1-z}\mathrm{As}$ MBL at 300 K. The solid and dashed lines denote the band gap at the Γ and X valleys respectively. The closed blue circle and vertical arrow show that $\mathrm{Al}_x\mathrm{In}_{1-x}\mathrm{P}$ can be grown with a direct band gap lattice matched to the $\mathrm{In}_z\mathrm{Ga}_{1-z}\mathrm{As}$ MBL with $z \approx 11\%$.

6.1 Band structure engineering

As we mentioned in Section 5.3, the main factor that limits the efficiency of short wavelength red LEDs on GaAs is the shallow electronic confinement due to the direct-to-indirect band gap crossover in $\mathrm{Al}_x\mathrm{Ga}_y\mathrm{In}_{1-x-y}\mathrm{P}$. The largest direct band gap E_g^Γ available for this alloy lattice-matched to GaAs is 2.33 eV at 0 K (cf. Ref. [140], Ref. 37 in [140]) and 2.253 at 300 K [140]. This, as a consequence, brings about (i) a significant thermal leakage of electrons into the barrier at 300 K or higher temperatures in 610 nm LEDs due to a small magnitude of the conduction band offset, and (ii) a reduced refractive index contrast between the barrier and the cladding layer necessary for optical confinement. The second factor is particularly important for the development of efficient 610 nm lasers, where the low optical confinement factor Γ significantly increases the threshold current density J_{th}. The early work by Bour *et al.* [70] on AlGaInP-based lasers with 614 − 663 nm emission indicates a significant rise in J_{th} when shortening the emission wavelength, and is especially noticeable when the peak gain shifts from 620 to 614 nm (J_{th} increases from 0.8 to 2.4 kA cm^{-2} at 300 K respectively). A characteristic temperature $T_0 = 22$ K was also determined for the 614 nm laser, making continuous wave operation impossible at room temperature. The optimisation of 610 nm lasers is not considered in this chapter where we focus exclusively on the electronic confinement and spontaneous emission. However we hope that the results presented here will also motivate the development of short wavelength red lasers with improved threshold characteristics.

Due to the aforementioned limitation in the direct band gap, we wish to explore the band structure of $\mathrm{Al}_x\mathrm{Ga}_y\mathrm{In}_{1-x-y}\mathrm{P}$ with a lattice constant other than that of GaAs, similar to the analysis carrier out in Section 4.1 for AlGaInAs, with the aim to identify the potential to improve electronic confinement for more efficient 610 nm emission. Fig. 6.1 shows the calculated variation of the bulk band gap at Γ (solid line) and X (dashed line) for AlInP at 300 K lattice matched to an $\mathrm{In}_z\mathrm{Ga}_{1-z}\mathrm{As}$ MBL with $0 \leq z \leq 12\%$. Details of the origins of the parameters used in this chapter are given in Appendix A. We calculate that a direct band gap can be achieved for $\mathrm{Al}_x\mathrm{In}_{1-x}\mathrm{P}$ when lattice matched to $\mathrm{In}_z\mathrm{Ga}_{1-z}\mathrm{As}$ with $z \gtrsim 11\%$, with the largest band gap E_g^Γ of 2.310 eV at $z \approx 11\%$ (blue arrow). While it may not appear significantly different than the largest direct band gap of AlGaInP lattice matched to GaAs of about 2.284 eV according to our set of material parameters, it can contribute nonetheless to a reduced thermal leakage of electrons by increasing the confinement depth ΔE_0 of electrons. In order to avoid the indirect band gap in AlInP lattice matched to $\mathrm{In}_z\mathrm{Ga}_{1-z}\mathrm{As}$ with $z \lesssim 11\%$ and bring it (at least) towards the $\Gamma - \mathrm{X}$ crossover, a fraction of AlP has to be replaced with GaP whose E_g^Γ is smaller by ≈ 0.885 eV at 300 K. However, due to an additional interplay between (i) the band gap bowing and (ii) the reduced fraction of InP at lower z to maintain the lattice-matched condition, the band gap at the $\Gamma - \mathrm{X}$ crossover increases overall by about 1 k_BT (at 300 K) in our calculations going from $z = 0$ to 11%. We note however that our calculations are likely to be a lower estimate of the increase in energy gap; experimental measurements give an estimated Γ–X crossover at 2.253 eV at 300 K on GaAs [140] and at a maximum value of 2.33 eV on $\mathrm{In}_{0.105}\mathrm{Ga}_{0.895}\mathrm{As}$ [152]. The direct band gap of AlInP lattice-matched to $\mathrm{In}_z\mathrm{Ga}_{1-z}\mathrm{As}$ with $z \gtrsim 11\%$ decreases simply due to a replacement of AlP with InP with the E_g^Γ decreasing by about 226 meV per 1% In for $z \gtrsim 11\%$. Since we find that a larger direct band gap for Al(Ga)InP can be only for $z > 0\%$, we exclude from our analysis here heterostructures grown on an MBL, e.g. GaAsP or InGaP, with a lattice constant smaller than GaAs.

We calculate the band gap of the unstrained $\mathrm{Al}_x\mathrm{Ga}_y\mathrm{In}_{1-x-y}\mathrm{P}$ alloy using the following quadratic interpolation

$$\begin{aligned} E_g^{\Gamma,\mathrm{X}}\,(\mathrm{Al}_x\mathrm{Ga}_y\mathrm{In}_{1-x-y}P) = xE_g^{\Gamma,\mathrm{X}}\,(\mathrm{AlP}) + yE_g^{\Gamma,\mathrm{X}}\,(\mathrm{GaP}) + (1-x-y)E_g^{\Gamma,\mathrm{X}}\,(\mathrm{InP}) - \\ - xyC_{\mathrm{AlGaP}}^{\Gamma,\mathrm{X}} - x(1-x-y)C_{\mathrm{AlInP}}^{\Gamma,\mathrm{X}} - y(1-x-y)C_{\mathrm{GaInP}}^{\Gamma,\mathrm{X}}\,, \end{aligned} \tag{6.1}$$

where $C_{\mathrm{AlGaP}}, C_{\mathrm{AlInP}}, C_{\mathrm{GaInP}}$ denote the band gap bowing parameters of the corresponding ternary materials[1], with the superscripts Γ and X denoting the corresponding valley minimum of the Brillouin zone. For most ternary alloys, the band gap bowing parameters C are positive, thereby producing a sublinear interpolation of the band gap between the binary components. For AlGaInP specifically, the band gap bowing arises primarily from C_{GaInP} which is taken here to be 0.66 eV, while the other two are set as zero [125, 153]. Although it is known that E_g^Γ of GaInP follows a sublinear interpolation between the binary components [154–156], to our knowledge there have been no experimental works on the (direct) band gap of AlGaInP lattice-mismatched with respect to GaAs, therefore we cannot benchmark our chosen value for bowing on the quaternary alloy with arbitrary composition.

---

[1] The interpolation of the band gap of a quaternary alloy may also include an additional term of form $-xy(1-x-y)C_{\mathrm{AlGaInP}}$. We neglect this bowing parameter from our analysis since our values of band gap for AlGaInP lattice-matched to GaAs compare very favourably with other theoretical and experimental works; this is discussed in more details in Appendix A.

Following the discussion above, the electronic and optical properties calculations in this chapter are performed on a set of compressively strained AlInP QW-based heterostructures surrounded by Al(Ga)InP barriers, which are lattice matched to the $\text{In}_z\text{Ga}_{1-z}\text{As}$ MBL with $z \leq 12\%$. The barrier is chosen to have a thickness of 20 nm on each side of the QW and the composition of the barrier is set to be at the $\Gamma - \text{X}$ crossover, to both minimise carrier leakage and maximise electronic transport. We choose to include a QW rather than a QD or QWR in the supercell, in order to simplify our analysis whereby the barrier band structure is not affected by the lattice mismatch of the AlInP QW with respect to the InGaAs MBL[2] (cf. chapter 5.2).

The $\text{Al}_x\text{In}_{1-x}\text{P}$ QW in the supercell is chosen to have a thickness of 8 nm. Depending on the composition of $\text{In}_z\text{Ga}_{1-z}\text{As}$ MBL, the composition of the QW is slightly adjusted in order to maintain the peak emission at 610 nm, with $x = 25\%$ on GaAs and up to $x = 27.2\%$ at $z = 11\%$, where the barrier band gap is the largest, and $x = 26.7\%$ at $z = 12\%$. The in-plane compressive strain ϵ_{xx} in the AlInP QW due to being lattice-mismatched to the $\text{In}_z\text{Ga}_{1-z}\text{As}$ MBL reduces from $\epsilon_{xx} \approx 2.00\%$ on GaAs to $\epsilon_{xx} \approx 1.08\%$ with $z = 11\%$ due to the negligible change in the QW's lattice constant, thereby reducing the upward (downward) shift in energy of the CB minimum (VB maxima). Excluding the effects of confinement, this minor increase in the fraction of AlP in the AlInP QW, combined with the resulting change in strain, keeps the band gap almost constant at about 2 eV. The calculations of optical properties are performed at 300 K.

The average valence band energy E_v^{avg} of the Al(Ga)InP alloy, required for the estimation of the band alignment at the QW-barrier interface, is interpolated quadratically using Eq. (6.1), where the bowing parameters C_{ABC} for E_v^{avg} are calculated as follows [124]

$$C_{\text{ABC}} = 3\left[a_v(\text{AC}) - a_v(\text{BC})\right] \frac{a_{\text{AC}} - a_{\text{BC}}}{a_{\text{MBL}}}\,, \tag{6.2}$$

where ABC denotes a ternary alloy, e.g. $\text{Al}_x\text{In}_{1-x}\text{P}$, $a_v(\text{AC}, \text{BC})$ is the hydrostatic deformation potential of the valence band maximum for the corresponding binary compound, with $a_{\text{AC,BC}}$

---

[2] Following the results from Chapter 5.3, the inclusion of a QWR (or QD) into the supercell, which may additionally improve the carrier transport, e.g. by reducing the surface recombination due to carrier localisation, is an additional step for optimisation of 610 nm emitters, which is beyond the scope of this work.

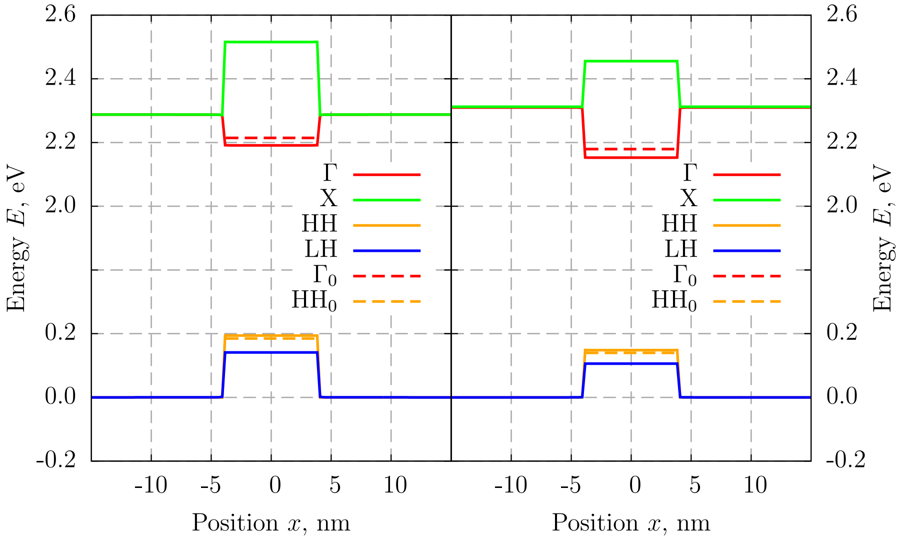

FIGURE 6.2: Calculated distribution of the bulk band edges along the growth direction in a AlInP QW surrounded by Al(Ga)InP barrier lattice-matched to $In_zGa_{1-z}As$ for $z = 0\%$ (left panel) and $z = 11\%$ (right panel). The solid red, green, orange and blue lines denote the conduction band edge at Γ, X, heavy-hole and light-hole valence bands respectively. The dashed red and orange lines denote the calculated confined ground electron and hole states respectively. The zero of energy is in each case taken at the barrier valence band maximum.

and a_{MBL} corresponding to the lattice constants of the binary material and MBL respectively. Fig. 6.2 shows the resulting calculated band alignment of the AlInP/Al(Ga)InP heterostructures grown on GaAs (left panel) and $In_{0.11}Ga_{0.89}As$ (right panel). Using our set of parameters we find that by changing the $In_zGa_{1-z}As$ MBL composition from GaAs to $z = 11\%$, the valence band offset ΔE_v of the AlInP/Al(Ga)InP heterostructure, calculated using Eq. (4.1), decreases from 194 to 148 meV when the effects of strain are considered. When looking at the evolution of E_v^{avg} of the $Al_xGa_yIn_{1-x-y}P$ barrier with z in the $In_zGa_{1-z}As$ MBL, we find, surprisingly, that the largest contribution arises from the term $x(1-x-y)C_{\text{AlInP}}$. This can be explained by the fact that (i) a_v(AlP) is almost 2.5 times larger than a_v(InP), and (ii) GaP has the lowest composition fraction, and this effect is more pronounced at $z > 0$ where the fractions of both AlP and InP increase at the expense of GaP. This change in ΔE_v and the increased E_g^Γ of the barrier from 2.284 to 2.310 eV at 300 K mentioned earlier result in a calculated increase in the conduction band offset ΔE_c by 72 meV. We therefore expect this increase in ΔE_c to significantly modify the electronic confinement for 610 nm emission, and we quantify its effect on the optical properties in the next section. We also note that the magnitude of the change in ΔE_c is sensitive to the set of chosen material parameters, and requires additional experimental investigations to be performed on such heterostructures in order to test our predictions.

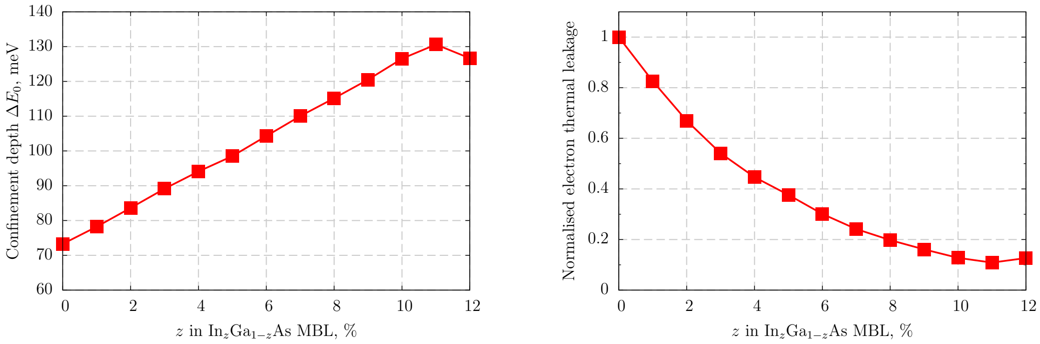

FIGURE 6.3: Calculated variation of the confinement depth ΔE_0 of the ground electron state (left panel), and normalised thermal leakage of electrons at 300 K assuming an exponential dependence upon ΔE_0 as shown in Eq. (6.3) (right panel) as a function of z in the $\mathrm{In}_z\mathrm{Ga}_{1-z}\mathrm{As}$ MBL. The calculations are performed on a series of supercells with a compressively strained 8 nm AlInP QW for 610 nm emission and surrounded by 20 nm Al(Ga)InP barriers with the band gap at the Γ–X crossover and lattice-matched to an $\mathrm{In}_z\mathrm{Ga}_{1-z}\mathrm{As}$ MBL.

6.2 Electronic confinement

Having determined the effect of the $\mathrm{In}_z\mathrm{Ga}_{1-z}\mathrm{As}$ MBL on the conduction band offset ΔE_c at the AlInP QW – AlGaInP barrier interface, we turn our attention to the consequent change in electron confinement. The left panel of Fig. 6.3 shows the calculated confinement depth ΔE_0 of the ground electron state in our set of AlInP/Al(Ga)InP supercells at 300 K. We find a linear increase in ΔE_0 when growing the AlInP/Al(Ga)InP heterostructure on the $\mathrm{In}_z\mathrm{Ga}_{1-z}\mathrm{As}$ MBL from 73 meV on GaAs to 130 meV at $z = 11\%$, with an additional increase in the InGaAs MBL lattice constant lowering this value due to a decrease in the barrier band gap (cf. Fig. 6.1). In the previous chapter we assumed that the escape rate of the carriers $1/\tau_{es}$ has the following dependence

$$\frac{1}{\tau_{es}} \propto \exp\left(-\frac{E_a}{k_B T}\right), \tag{6.3}$$

which is caused by the thermal escape of the confined carriers whose confinement depth represents the activation energy. Based on this assumption, we expect that a deeper confinement of the electrons in the QW will suppress their thermal escape into the barrier when the structure is grown on $\mathrm{In}_z\mathrm{Ga}_{1-z}\mathrm{As}$ with $z \approx 11\%$ compared to GaAs. Assuming that the coefficient A from Eq. (5.4) does not vary with temperature, this change in confinement therefore reduces the thermal escape of electrons by up to a factor of 6 at 300 K by increasing z from 0 to 11%, as shown in the right panel of Fig. 6.3.

In a similar manner, a deeper confinement of electrons reduces their probability to occupy the delocalised X states in the barrier assuming that they obey the Fermi-Dirac distribution. Using Eq. (4.8) and considering only the calculated electron bound states at Γ to compute the

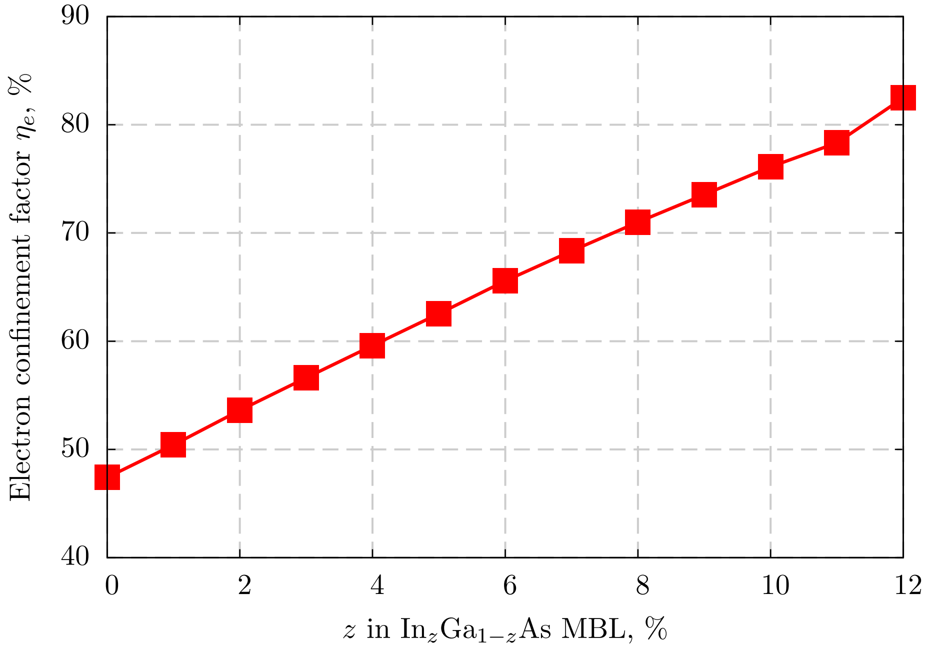

FIGURE 6.4: Calculated variation of the electron confinement factor η_e (cf. Eq. (4.8)) in the AlInP QW for 610 nm emission for an areal carrier density $n_{2\mathrm{D}} = 1.0 \times 10^{12}$ cm^{-2} as a function of z in the $\mathrm{In}_z\mathrm{Ga}_{1-z}\mathrm{As}$ MBL, for the same series of compressively strained 610 nm QWs as in Fig. 6.3.

electron confinement factor η_e, we calculate that by growing the structure on the $\mathrm{In}_z\mathrm{Ga}_{1-z}\mathrm{As}$ MBL η_e increases from 47.4% on GaAs to 78.3% when $z = 11\%$ at the areal carrier density $n_{2\mathrm{D}} = 1.0 \times 10^{12}$ cm^{-2}, thereby allowing a much larger fraction of electrons to radiatively recombine with the holes in the QW. Although ΔE_0 decreases for $z \gtrsim 11\%$ (cf. Fig. 6.3), the Γ and X valley minima of the AlInP conduction band are no longer degenerate thus providing an additional energy separation between the ground electron state and the delocalised X states in the barrier, and we find $\eta_e \approx 82.4\%$ for $z = 12\%$ at the same $n_{2\mathrm{D}}$. This case, however, introduces a trade-off between (i) a shallower electronic confinement and (ii) a larger fraction of electrons occupying the bound states in the QW. We predict that the radiative emission of a 610 nm LED at 300 K or higher temperatures will therefore be maximised in a heterostructure grown on an $\mathrm{In}_{0.11}\mathrm{Ga}_{0.89}\mathrm{As}$ MBL when the magnitude of ΔE_0 reaches its peak; however additional experimental confirmation is required to test this prediction. We also note that, although the phonon-assited intervalley transfer of electrons from the QW may reduce the actual activation energy by a few tens of meV (cf. Section 5.3), the incorporation of an $\mathrm{In}_z\mathrm{Ga}_{1-z}\mathrm{As}$ MBL with $z > 0\%$ can nonetheless facilitate an improved electronic confinement, therefore providing enhanced thermal efficiency and radiative emission at 300 K or higher temperatures.

Another side effect of the distribution of electrons into the barrier X states is the creation of an electrostatic potential across the supercell due to the spatial separation between the electrons in the barrier and the holes in the QW. Here we proceed with the following Schrödinger equation:

$$[H_{\mathbf{k}\cdot\mathbf{p}}(z,\mathbf{k}) + H_{\epsilon}(z,\mathbf{k}) - e\phi(z)]\,\psi_n(z,\mathbf{k}) = E_n(\mathbf{k})\psi_n(z,\mathbf{k})\,, \tag{6.4}$$

where $H_{\mathbf{k}\cdot\mathbf{p}}$ and H_{ϵ} are the $\mathbf{k}\cdot\mathbf{p}$ and strain Hamiltonians respectively, e is the electron charge, and the electrostatic potential $\phi(z)$ is the solution of Poisson's equation from Eq. (3.82) and is, therefore, calculated self-consistently. Although in our set of supercells this effect is not as significant as in a typical type-II heterostructure with $\Gamma - \Gamma$ carrier confinement, i.e. where the bound Γ electrons and holes are localised in separate layers, this effect nevertheless affects the carrier confinement in our structures by pushing both Γ electron and hole states downward in energy and, generally, blueshifting the emission when carriers are injected into the heterostructure. Due to a smaller η_e at lower compositions z of the $\mathrm{In}_z\mathrm{Ga}_{1-z}\mathrm{As}$ MBL, this effect is most pronounced in the structure grown on GaAs. Our calculations, however, show that there is a negligible change in the peak emission wavelength when n_{2D} is increased. Our calculations also show that η_e increases by approximately 74% when increasing n_{2D} from 1.0×10^{10} to 1.0×10^{12} cm^{-2} in the heterostructure grown on GaAs. We attribute this to (i) an increasing separation between the ground Γ electron states in the QW and the X states in the barrier (and, consequently, ΔE_0[3]) due to the electrostatic potential when increasing n_{2D}, and (ii) a slightly improved wavefunction confinement ratio η_{ψ}, given in Eq. (5.3), for the bound Γ electron states. These results suggest that a superlinear dependence of the ground state spontaneous emission rate on n_{2D} will occur, although we note that the leakage rate will also depend on the carrier density. On the other hand, the electrostatic field is strongly diminished in the heterostructure grown on the $\mathrm{In}_{0.11}\mathrm{Ga}_{0.89}\mathrm{As}$ MBL, therefore we conclude that η_e remains relatively constant within the same range of n_{2D}, which is a typical behaviour for a type-I active region.

6.3 Spontaneous emission and photoluminescence measurements

The effect of a deeper electron confinement on the optical properties of a 610 nm emitter is presented in the left panel in Fig. 6.5, which shows the calculated radiative current density J_{rad} in our set of structures for a constant injected areal carrier density $n_{\mathrm{2D}} = 1.0\times10^{12}$ cm^{-2}. We find that by growing the structure on an $\mathrm{In}_z\mathrm{Ga}_{1-z}\mathrm{As}$ MBL, J_{rad} increases by 63 % from 18.7 A cm^{-2} on GaAs to 30.4 A cm^{-2} when $z = 11\%$, due to the aforementioned increase in the fraction of electrons located in the QW. J_{rad} increases even beyond this lattice constant of the MBL, reaching 32.14 A cm^{-2} at $z = 12\%$, although leakage current may also start to increase again due to the reduction in barrier energy gap at $z \gtrsim 11\%$. These results also suggest that

---

[3] Because of this electrostatic potential, which is calculated self consistently using Schrödinger's and Poisson's equations, (i) the conduction and valence band edges across the supercell are no longer flat, and (ii) the confinement depth ΔE_0 depends on the injected carrier density. Therefore, in order to simplify the estimations of the electron confinement depth ΔE_0, the data presented in Fig. 6.3 is calculated relative to the barrier band edge when the electrostatic potential is neglected, although in reality they may be confined deeper in the QW, with this difference becoming less significant for z approaching 11%.

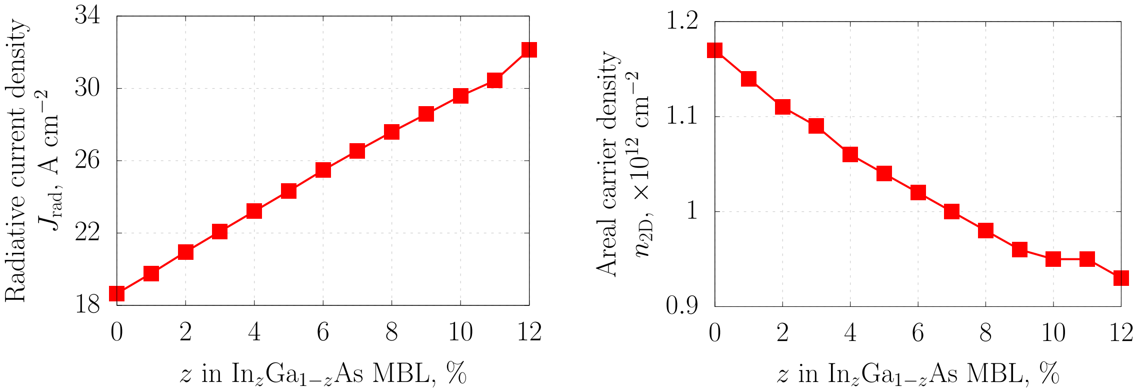

FIGURE 6.5: Calculated radiative current density $J_{\rm rad}$ at injected areal carrier density $n_{\rm 2D} = 1.0 \times 10^{12}{\rm cm}^{-2}$ (left panel), and areal carrier density $n_{\rm 2D}$ required to obtain a $J_{\rm rad} \approx 30$ A cm^{-2} (right panel), as a function of z in the In$_z$Ga$_{1-z}$As MBL, for the same series of compressively strained 610 nm QWs as in Fig. 6.3.

the incorporation of an In$_z$Ga$_{1-z}$As MBL enables the reduction of $n_{\rm 2D}$ in order to achieve a certain radiative recombination rate, which is shown in the right panel of Fig. 6.5. Here we find that by changing the lattice constant of the In$_z$Ga$_{1-z}$As MBL from the one of GaAs to $z = 11\%$, $n_{\rm 2D}$ can be reduced by 23% in order to maintain $J_{\rm rad} \approx 30$ A cm^{-2}. This reduction in $n_{\rm 2D}$ could be useful, particularly for the development of power efficient portable devices, where the display has the largest power consumption. Our calculations also show that $n_{\rm 2D}$ for any constant value of $J_{\rm rad}$ starts to saturate when the structure is grown on In$_{0.1}$Ga$_{0.9}$As and there is minimal difference by having $z = 11\%$ in the In$_z$Ga$_{1-z}$As MBL.

In order to verify our predictions of an improved efficiency in 610 nm emitters by employing an In$_z$Ga$_{1-z}$As MBL, two 5 QW AlGaInP-based samples were grown by the Epitaxy and Physics of Nanostructures group at the Tyndall National Institute. As the efficiency of the emission drops rapidly as it blueshifts towards 610 nm [70], it becomes important here to compare samples with the peak emission wavelength as similar as possible, which will then allow a direct comparison of the drop in emission efficiency with increasing temperature. The first structure was grown on GaAs, with the QWs surrounded by (Al$_{0.6}$Ga$_{0.4}$)$_{0.52}$In$_{0.48}$P (sample A) which has the band gap near the $\Gamma-$X crossover for an optimised performance of real LED (cf. Section 5.2). The QWs in the second structure were surrounded by (Al$_{0.95}$Ga$_{0.05}$)$_{0.47}$In$_{0.53}$P barriers, which were grown lattice-matched to an In$_{0.06}$Ga$_{0.94}$As MBL (sample B). The microphotoluminescence (μPL) measurements performed on these samples at 270 K show a nearly identical peak emission wavelength, as shown in the left panel of Fig. 6.6.

The right panel of Fig. 6.6 includes a comparison of the temperature dependent integrated μPL, with the red and blue lines corresponding to sample A and B respectively. Similar to the QWR-based structures from Chapter 5, the intensity of the emission in sample A (on GaAs) reduces by a factor of 300 when increasing the temperature from 8 to 270 K. By contrast, there is a significantly smaller drop in the efficiency of the emission of sample B (on an InGaAs

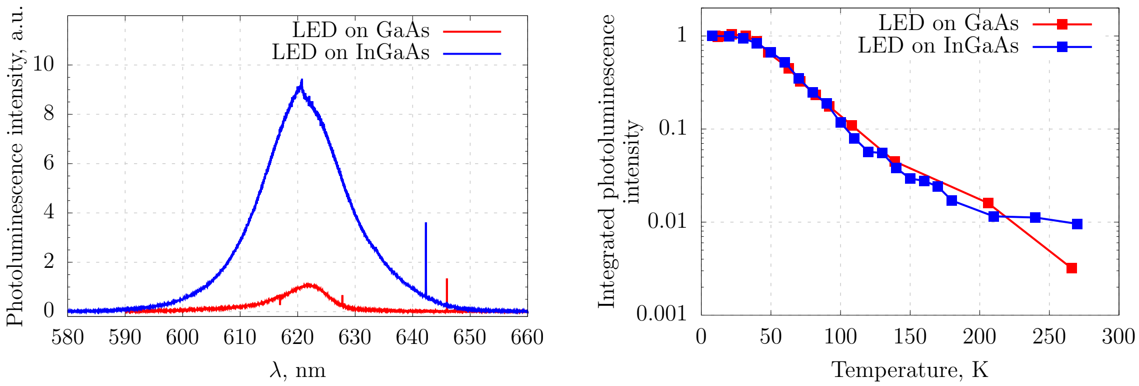

FIGURE 6.6: Measured $\mu-$photoluminescence spectra of at 270 K (left panel), and measured temperature dependent integrated photoluminescence (right panel) of a sample grown on GaAs (sample A, red line) and $In_{0.06}Ga_{0.94}As$ (sample B, blue line); each sample contains 5 QWs.

MBL) with temperature, decreasing only by a factor of 100 over the same range of temperature. Although, using our set of parameters, the barriers in sample B are expected to have an indirect band gap, we conclude that the observed improvement in optical emission efficiency for growth on an $In_zGa_{1-z}As$ MBL with $z = 6\%$ is highly encouraging [4].

There are a few things to note here. Firstly, the aforementioned barrier composition in both samples denote the nominal growth conditions, while in reality they may (slightly) differ. The shallow electronic confinement can be affected by variations in barrier and well composition primarily due to (i) changes in the composition-dependent band gap, and (ii) strain-induced effects on the QW band gap.

Secondly, there is a much larger degree of uncertainty in the composition of the AlGaInP QWs in both samples, since they are much thinner than the barrier layers. The composition of a particular layer is inferred from X-Ray Diffraction (XRD) and PL measurements, where certain assumptions, e.g. lack of relaxation, are made. Nevertheless, the critical factor is the emission wavelength, and it can be seen from Fig. 6.6 that this is nearly identical in the two samples, and possibly even at slightly shorter wavelength in the sample B. Finally, we acknowledge that the comparison of the efficiency of the temperature-dependent integrated μPL was performed only on two samples, whereas a larger sample size is required for a more accurate description.

6.4 Conclusions

In this chapter we investigated the electronic and optical properties of AlInP/AlGaInP QW-based heterostructures for use as the active region in shorter wavelength red emitters grown on InGaAs Metamorphic Buffer Layers (MBL). Here we consider a series of supercells with a

---

[4] The experimental data for sample A on the right panel of Fig. 6.6 (red line) is obtained by averaging the data of multiple μPL measurements at each temperature.

8 nm compressively strained $\mathrm{Al}_x\mathrm{In}_{1-x}\mathrm{P}$ QW surrounded by 20 nm Al(Ga)InP barriers lattice-matched to an $\mathrm{In}_z\mathrm{Ga}_{1-z}\mathrm{As}$ MBL with $0 \leq z \leq 12\%$, and perform the calculations at 300 K. The composition of the Al(Ga)InP barrier was chosen such as to have the Γ and X CB valley minima degenerate, while including minor adjustments to the QW composition to maintain 610 nm peak emission.

We started our analysis in Section 6.1 with the investigation of Al(Ga)InP band structure lattice-matched to an $\mathrm{In}_z\mathrm{Ga}_{1-z}\mathrm{As}$ MBL. Using our set of parameters presented in Appendix A we found that the use of an $\mathrm{In}_z\mathrm{Ga}_{1-z}\mathrm{As}$ MBL allows to (i) increase the direct band gap of the Al(Ga)InP barrier with the largest magnitude corresponding to AlInP lattice-matched to $\mathrm{In}_z\mathrm{Ga}_{1-z}\mathrm{As}$ MBL at $z \approx 11\%$ at 300 K, and (ii) increase the CB offset at the barrier-QW interface at the expense of the VB offset according to model solid theory [124]. A larger CB offset then allows a deeper confinement of electrons in the QW for 610 nm emission, thereby reducing what is known to be the primary loss mechanism in such structures.

In Section 6.2 we present the results of electronic confinement and optical properties calculations performed on a series of supercells. Here we calculate that by employing an $\mathrm{In}_z\mathrm{Ga}_{1-z}\mathrm{As}$ MBL the electron confinement depth can be increased from 73 meV on GaAs to 130 meV having $z = 11\%$. We expect that a deeper electronic confinement will enable the:

(i) suppression of the thermal leakage of the electrons from the QW into the barrier. Our qualitative analysis here suggests that the electron leakage can be reduced by up to a factor of 6 at 300 K (or even more at higher temperatures), assuming that the thermal leakage depends exponentially on the confinement depth;

(ii) reduction of the fraction of electrons thermally distributed into the delocalised X states in the barrier assuming the Fermi-Dirac distribution. Our calculations show that the fraction of electrons occupying the QW increases by about 79% when the device is grown on $\mathrm{In}_{0.11}\mathrm{Ga}_{0.89}\mathrm{As}$ compared to GaAs. This, therefore, allows a larger fraction of electrons to radiatively recombine with the holes in the QW, and we calculate the radiative current density J_{rad} to increase by about 63% by growing the structure on $\mathrm{In}_{0.11}\mathrm{Ga}_{0.89}\mathrm{As}$ compared to GaAs at a constant areal carrier density $n_{2\mathrm{D}} = 1.0 \times 10^{12}$ cm^{-2};

(iii) reduction of $n_{2\mathrm{D}}$ when increasing z in the $\mathrm{In}_z\mathrm{Ga}_{1-z}\mathrm{As}$ MBL from 0 to 11% to maintain a constant radiative recombination rate. This improvement is particularly important in the context of portable devices, e.g. smartphones, where the largest power consumption is attributed to the display.

In order to verify our predictions, we turned our attention to microphotoluminescence (μPL) measurements performed on two 5 QWs samples in Section 6.3, grown on GaAs (sample A) and on an $\mathrm{In}_{0.06}\mathrm{Ga}_{0.94}\mathrm{As}$ MBL (sample B). The temperature-dependent integrated μPL response of these structures, which emit at close to identical wavelengths at 270 K, show an improvement by a factor of 3 in the efficiency of the emission for sample B at 270 K.

Finally, we note that the calculated improvements in electronic and optical properties in 610 nm emitters brought about by growth on an InGaAs MBL is sensitive to the chosen set of material parameters. At the same time, the comparison of the μPL measurements made on only 2 samples is not sufficient to draw a definitive conclusion about the impact of an InGaAs MBL on the efficiency of shorter wavelength red emitters. Based on the preliminary results, we therefore strongly encourage the scientific community to investigate in more detail (i) the band structure of AlGaInP, and (ii) the effect of growth on an InGaAs MBL on the emission efficiency of 610 nm light-emitting diodes.

Chapter 7

Summary, conclusions, and future work

We present our final analysis of the thesis in this chapter. We start with Section 7.1, where we provide a summary of the thesis, and then present and discuss in Section 7.2 potential directions for future research based on the work in this thesis.

7.1 Summary and conclusions

In this thesis we performed theoretical simulation of electronic and optical properties of 1.3 μm AlInGaAs-based lasers and 610 nm AlGaInP-based LEDs grown on relaxed InGaAs Metamorphic Buffer Layers (MBLs) for optimised emission and improved efficiency compared to devices grown on conventional substrates such as InP and GaAs.

We began in Chapter 2 by presenting the theoretical model to calculate the electronic structure of zinc blende semiconductors and the optical properties of semiconductor photonic devices, such as lasers and light-emitting diodes (LEDs). Here we introduced the well established 8-band $\mathbf{k}\cdot\mathbf{p}$ model, including the effects of strain, to calculate the electronic structure of zinc blende semiconductors. We then proceeded to the theory of optical properties, where we derived the expression for gain spectrum. Starting with Fermi's golden rule, which ensures that a transition between a conduction and a valence state is at near-resonance with the energy of the incident photon, we showed that population inversion is necessary for material gain to occur. Here the optical confinement factor Γ was introduced, which describes the fraction of the incident wave "confined" in the active region, typically a few percent in a single QW-based heterostructure. This factor therefore reduces the magnitude of the amplified emission, with the device ultimately producing the *modal* gain, which, unlike the material gain, is measurable. Finally, the expression for the spontaneous emission spectrum is derived to complete our theoretical model for device simulation.

In Chapter 3 we presented the semi-analytical plane wave expansion method, which is the computational technique used in this thesis to implement our theoretical model into a set of codes. This method then enables the calculation of the electronic and optical properties of Quantum Well (QW), Quantum Wire (QWR) and Quantum Dot (QD) based heterostructures, using periodic boundary conditions. We applied the method first to the 1-band model, where we showed how the linear Schrödinger equation can be transformed into an eigenvalue problem with the position-dependent effective mass Hamiltonian becoming a square matrix using the Fourier transform approach. This matrix is then diagonalised numerically to calculate the eigenstates in the supercell. Here we introduced the characteristic function of the QW in order to calculate the Fourier expansion of the Hamiltonian matrix elements. In real space, the position-dependent characteristic function equals unity (zero) inside (outside) the QW, and its Fourier transform is the key step required to calculate the electronic structure of a QW (or other nanostructure).

We then applied the method to the 8-band $\mathbf{k}\cdot\mathbf{p}$ Hamiltonian, which we directly used to calculate the electronic structure of AlInGaAs- and AlGaInP-based heterostructures in Chapters 4, 5 and 6. The method was applied first for single and multiple QW-based supercells, where we showed that the Fourier expansion of a single-QW Hamiltonian is a simplified case of a multi-QW expansion, for which a linear combination of multiple characteristic functions is used.

We then presented the implementation of the method to calculate the electronic properties of QD- or QWR-based supercells, which are periodic along all three Cartesian coordinate axes. Here we found the plane wave expansion of the $\mathbf{k}\cdot\mathbf{p}$ Hamiltonian to be similar to the QW case, and we showed that the former is a special case of the general three-dimensional expansion. Because the strain distribution in a QWR- or QD-based heterostructure is more complex compared to the QW-based case, we presented the analytical expression for the Fourier transform of strain tensor elements in a supercell that contains a QD or QWR. We then provided the analytical solution of Poisson's equation by evaluating the Fourier transform of the carrier-induced electrostatic potential due to spatial separation of electrons and holes within a supercell. The latter is calculated self-consistently using the Fourier coefficients of the calculated eigenstates directly.

The Fourier transform of the strain tensor and carrier-induced electrostatic potential can be used to (i) estimate their real-space distribution within the supercell, and/or (ii) evaluate the plane wave expansion of the Pikus-Bir Hamiltonian matrix elements and the diagonal terms of the aforementioned electrostatic potential. We next provided analytical expressions to calculate the momentum matrix elements between a conduction and a valence energy level using the calculated Fourier coefficients of the corresponding eigenstates.

The 8-band **k·p** model and the plane wave expansion method are then used for the remainder of this thesis, where we performed a detailed analysis of the electronic structure and optical properties of (i) 1.3 μm metamorphic AlInGaAs QW-based lasers for telecom applications in Chapter 4, and (ii) 610 nm AlGaInP QWR- and QW-based LEDs for display applications in Chapters 5 and 6.

The first part of this research was presented in Chapter 4, where we performed a theoretical investigation and optimisation of the properties and performance of GaAs-based 1.3 μm InGaAs/(Al)InGaAs QW lasers grown on InGaAs MBLs, with the goal to provide detailed guidelines for the design of optimised devices.

We started our analysis by identifying the ranges of strain and QW thickness accessible for 1.3 μm emission when the heterostructure is grown on an InGaAs MBL. We then calculated the variation of gain and threshold characteristics as a function of strain and QW thickness, and showed that metamorphic 1.3 μm laser structures offer reduced threshold current density, comparable internal quantum efficiency and enhanced differential gain compared to those calculated previously for optimised InP-based devices. We also considered QWs having quaternary AlInGaAs barriers and showed that the barrier Al composition can be varied to optimise the trade-off between the carrier and optical confinement in such a way as to enhance the laser performance, leading to reduced carrier and current densities at threshold, as well as improved internal quantum efficiency and differential gain, with the effects of quaternary barriers becoming increasingly beneficial with increasing temperature.

Through our analysis we identified that an optimised 1.3 μm device grown on an $\text{In}_{0.2}\text{Ga}_{0.8}\text{As}$ MBL should consist of $\lesssim 3$ QWs, with the InGaAs QWs having compressive strains $2.0\% \lesssim \epsilon_{xx} \lesssim 2.3\%$, corresponding to QW widths $5 \text{ nm} \lesssim d_{\text{QW}} \lesssim 7 \text{ nm}$ (In compositions $49\% \lesssim x \lesssim 54\%$). We further identified that the optimum barrier materials are unstrained $\text{Al}_y\text{In}_{0.2}\text{Ga}_{0.8-y}\text{As}$ alloys having Al compositions $6\% \lesssim y \lesssim 15\%$. Finally, by varying the composition of the InGaAs MBL we found that the devices should be grown on virtual substrates having low In composition for improved gain characteristics. Although this is consistent with the expected improvement in device performance in going from InP-based to GaAs-based heterostructures, our analysis indicates that for optimised laser performance the devices should be grown on an $\text{In}_{0.2}\text{Ga}_{0.8}\text{As}$ MBL.

For the second part of this research, presented in Chapters 5 and 6, we performed a theoretical investigation of electronic and optical properties of AlGaInP-based LEDs for 610 nm emission. We started with Chapter 5, where we investigated the electronic and optical properties of [110]-oriented self-assembled AlGaInP Quantum Wires (QWRs) based heterostructures for 610 nm emission.

The TEM scans performed on QWR-based devices grown at Tyndall National Institute showed the in-plane and vertically periodic organisation of the nanostructures, the electronic and optical properties of which we calculated using the periodic boundary conditions of our model. Using the calculated strain distribution we found that the band structure of the AlInP QWRs is affected the most due to the lattice mismatch with respect to the barrier, leading to a reduced conduction band (CB) offset and reduced electron confinement.

We then performed an analysis of the electronic and optical properties of QWR-based supercells. Here we examined the impact of the barrier thickness L_z on the radiative recombination in these heterostructures, with our calculations showing that enhanced optical properties can be achieved by separating the QWR layers with a thinner barrier. This is the result of an improved electronic confinement, which then leads to (i) a smaller fraction of electrons occupying the barrier X states, and (ii) an improved ground electron-hole wavefunction overlap.

From the integrated PL measurements we found that thermal leakage of electrons from the QWR into the barrier is the primary cause of the large decrease in efficiency of shorter wavelength emitters. Our calculations also showed that the QWRs, due to being elongated along the [110] direction, can be used to create emitters with a strong degree of linear polarisation. We calculated the radiative emission to be polarised nearly 100% along the QWR axis when the QWRs are surrounded by thin barrier layers ($L_z \approx 3$ nm), in good agreement with experimental measurements. This then makes such heterostructures attractive for display applications, where, to date, filters are typically employed to achieve polarised emission.

Finally, electroluminescence measurements of QWR-based LED devices under hydrostatic pressure performed at University of Surrey, UK confirmed the direct band gap nature of the radiative recombination, while also providing evidence that Γ–X leakage is indeed the dominant loss mechanism in the active region at room temperature.

Overall, these results confirm the significant thermal leakage of electrons from the active region due to a shallow electron confinement. These results serve as a precursor to the following chapter, where we investigate the possibility of improving electron confinement for improved efficiency of 610 nm devices, by employing lattice-mismatched InGaAs MBLs.

Finally, we investigated in Chapter 6 the possibility of using AlInP/AlGaInP QW-based heterostructures grown on InGaAs MBLs as the active region for 610 nm LEDs. We started our analysis with an investigation of the band strucutre of Al(Ga)InP lattice-matched to an $\mathrm{In}_z\mathrm{Ga}_{1-z}\mathrm{As}$ MBL. We calculated that the use of an $\mathrm{In}_z\mathrm{Ga}_{1-z}\mathrm{As}$ MBL brings about (i) an increased direct band gap of the Al(Ga)InP barrier, with the largest value at 300 K found for AlInP lattice-matched to an $\mathrm{In}_z\mathrm{Ga}_{1-z}\mathrm{As}$ MBL at $z \approx 11\%$, and (ii) an increased CB offset at the barrier-QW interface at the expense of the VB offset according to model solid theory. A larger CB offset then allows better confinement of electrons in the QW for 610 nm emission, thereby reducing what was confirmed in the previous chapter as the primary loss mechanism in such devices.

We then performed calculations on a series of supercells to investigate the electronic and optical properties of these heterostructures. Our calculations showed that the electron confinement can be strongly improved by growing the heterostructure on an InGaAs MBL, thereby reducing the thermal leakage of electrons from the QW into the barrier. In a similar manner, the enhanced electron confinement is expected to reduce the fraction of thermally distributed electrons in the X bands in the barrier, thereby improving the radiative recombination rate at fixed carrier density for 610 nm emission. In order to test our predictions, microphotoluminescence (μPL) measurements were performed on two 5 QWs structures, grown on GaAs and on an $\mathrm{In_{0.06}Ga_{0.94}As}$ MBL. The preliminary temperature-dependent integrated μPL measurements performed on these devices, which emit at close to identical wavelength at 270 K, show an improvement by a factor of 3 in the efficiency of the emission at 270 K.

We note that the calculated scale of improvements in the electronic and optical properties of 610 nm emitters brought about by incorporating an InGaAs MBL are sensitive to the chosen set of material parameters. Also, we cannot make a definitive conclusion about the impact of an InGaAs MBL on the efficiency of shorter wavelength red emitters given the small sample size on which the μPL measurements were performed. Based on the preliminary results, we therefore strongly encourage the scientific community to investigate in more detail (i) the band structure of AlGaInP, and (ii) the effect of growth on an InGaAs MBL on the emission efficiency of 610 nm LEDs.

Overall, our theoretical analysis has identified important trends in the performance of GaAs-based metamorphic QW lasers and LEDs, has provided design parameters for optimised emission of the heterostructures, and has confirmed the promise of these novel heterostructures for the development of high performance GaAs-based 1.3 μm lasers and 610 nm LEDs.

7.2 Future work

Here we present some possible directions towards which research presented in this thesis can be extended.

For our analysis of electronic and optical properties of metamorphic lasers in Chapter 4 we considered an $\mathrm{Al}_x\mathrm{Ga}_{0.8-x}\mathrm{In}_{0.2}\mathrm{As}$ cladding layer with $x = 40\%$. A possible way to further optimise metamorphic lasers for 1.3 μm emission is to incorporate a larger fraction of Al x for a larger band gap. We estimate that a direct band gap $\mathrm{Al}_x\mathrm{Ga}_{0.8-x}\mathrm{In}_{0.2}\mathrm{As}$ epilayer can be grown with x up to about 62%, with the increased band gap allowing an improved carrier confinement. This, in combination with an improved refractive index contrast for a superior optical confinement, is expected to further improve the threshold and gain characteristics of 1.3 μm metamorphic lasers.

In Chapter 6 our analysis was restricted to the calculation of the electronic and optical properties of QW-based supercells. The lattice mismatch between the QW and the MBL produces a linear strain profile across the supercell, thereby simplifying the analysis of the electronic confinement. It is however expected that metamorphic 610 nm emitters could also benefit from the incorporation of self-assembled QWRs, which would produce a polarised emission (cf. Chapter 5). Also, in our previous work in Ref. [143], the electrical measurements showed that incorporation of self-assembled QWRs in the active region instead of QW(s) can further reduce the current leakage, whereby a higher degree of spatial confinement in the growth plane reduces the diffusion of carriers towards the surface of the device.

In addition, the results of our calculations in Chapter 6 are a motivation to create efficient 610 nm lasers. It is known that the significant current leakage due to the weak electron confinement has been a limiting factor on the threshold characteristics of shorter wavelength red lasers. A threshold current density J_{th} of 5.9 kA cm^{-2} for a 610 nm $p-n$ junction based laser was reported originally by Nuese *et al.* in 1972 [157]. The work by Bour *et al.* reported a reduced J_{th} to 2.4 kA cm^{-2} for a single QW-based 614 nm laser in 1994, although with a very low characteristic temperature T_0 of 22 K between 3 and 30° C, so that the device cannot operate in continuous-wave mode at room temperature [70]. Other attempts have also been made to create a semiconductor laser for red-orange emission, including conversion of a 1220–1240 nm dilute nitride GaInNAs QW-based laser into 610–620 nm using nonlinear crystal waveguides [158, 159]. Therefore, metamorphic substrates become a more attractive option since it is expected to improve the device efficiency without the incorporation of additional layers into the heterostructure, thereby simplifying the laser design.

However, as we mentioned the results presented in Chapter 6 are sensitive to the choice of material parameters. As we discuss in Appendix A, we find that the literature currently lacks a consistent set of material parameters for III-P compounds. While some theoretical and experimental analysis has been performed on the band structure of AlGaInP lattice-matched to GaAs, which is the conventional substrate for red emitting devices, to our knowledge the research focused on the bandstructure of III-P alloys with a different lattice constant is very limited. Given the intrinsicly weak electronic confinement in blueshifted red LEDs, as well as our predictions of improved optoelectronic performance for these devices by using an InGaAs MBL, there is an opportunity to investigate in more detail the bandstructure of AlGaInP alloys for efficient 610 nm (or shorter wavelength) emission.

Appendix A

Material parameters for k·p calculations

In this appendix we present the material parameters used in the calculations of electronic and optical properties of AlGaInAs QW based lasers in Chapter 4 and AlGaInP-based LEDs in Chapters 5 and 6. In Section A.1 we discuss the chosen material parameters for III-P binaries. Unlike the III-As compounds, the material parameters of which are well defined in the literature and have a relatively low degree of uncertainty, it appears that the literature lacks a consistent set of parameters for the III-P binaries. In particular, the main uncertainties are related with the direct and indirect band gap, as well as certain deformation potentials.

This leads to uncertainty regarding the material parameters for (Al)GaInP ternary (quaternary) layers grown on InGaAs MBLs. Parameters have been extracted from strained GaInP layers grown on GaAs, and from lattice-matched AlGaInP layers on GaAs, as well as limited data for lattice-matched AlInP layers on InGaAs MBLs. We use these results to benchmark the parameters that we present for AlGaInP grown on InGaAs MBL layers.

TABLE A.1: Material parameters for III-As and III-P compounds used in $\mathbf{k}\cdot\mathbf{p}$ calculations. Since we do not consider the X valley in the electronic and optical properties calculations of AlGaInAs-based lasers, certain parameters like electron effective masses or deformation potentials are omitted. The parameters presented include (i) Γ and X energy gaps at 0 K, spin-orbit splitting energy, and average energy of the three highest valence states relative to vaccuum; (ii) parameters for temperature dependence of Γ and X energy gaps; (iii) parameters for $\mathbf{k}\cdot\mathbf{p}$ model, and Γ and X effective masses; (iv) lattice constant and elastic constants; (v) deformation potentials, and (vi) bowing parameters for Γ and X band gap, and spin-orbit splitting energy. The parameters for III-As compounds are taken from Refs. [103, 125, 132], and we discuss the sources of parameters for III-P compounds in Section A.1.

Parameter	AlAs	GaAs	InAs	AlP	GaP	InP
E_g^Γ at 0 K (eV)	3.051	1.517	0.424	3.680	2.826	1.4539
E_g^X at 0 K (eV)	2.229	1.980	1.433	2.510	2.350	2.300
Δ_{SO} (eV)	0.280	0.340	0.380	0.070	0.080	0.108
E_v^{avg} (eV)	-7.38	-6.84	-6.68	-8.00	-7.47	-7.04
α_Γ (meV K^{-1})	0.67	0.5408	0.406	0.5771	0.1081[1]	0.0359[2]
β_Γ (K)	300	204	271	372	164[1]	209[2]
α_X (meV K^{-1})	0.7	0.46	0.276	0.5771	0.62	0.5771
β_X (K)	530	204	93	372	460	372
E_P (eV)	21.1	28.8	21.5	16.807	17.496	14.314
γ_1^L	3.760	6.980	20.0	3.750	6.517	6.28
γ_2^L	0.820	2.060	8.50	0.893	1.872	2.08
γ_3^L	1.420	2.930	9.20	1.494	2.672	2.76
m_e^Γ (m_0)	0.1350	0.0665	0.0223	0.170	0.0925	0.0808
$m_e^\parallel$ (m_0)	——	——	——	2.68	2.0	1.38
$m_e^\perp$ (m_0)	——	——	——	0.155	0.253	0.278
a_0 (Å)	5.6600	5.6533	6.0580	5.4672	5.4505	5.8697
C_{11} (GPa)	125.0	118.0	83.0	133.0	140.5	102.0
C_{12} (GPa)	53.0	53.8	48.0	63.0	62.03	57.6
C_{44} (GPa)	57.0	59.4	39.6	61.5	70.33	46.0
a_c (eV)	-5.64	-8.06	-5.88	-5.86	-8.57	-5.71
a_v (eV)	2.47	1.16	1.00	3.15	1.70	1.27
b (eV)	-1.50	-1.70	-1.80	-1.50	-1.50	-1.60
d (eV)	——	——	——	-4.60	-4.60	-5.00
Ξ_h (eV)	——	——	——	1.81	2.70	1.85
Ξ_{ax} (eV)	——	——	——	6.75	6.30	3.30

Parameter	AlGaAs	AlInAs	GaInAs	AlGaP	AlInP	GaInP
C_Γ (eV)	0.370	0.750	0.450	0.000	0.000	0.660
C_X (eV)	0.000	0.000	0.000	-0.130	0.000	0.220
C_Δ (eV)	0.000	0.150	0.0289	0.000	0.000	0.000

---

[1] E_g^Γ calculated using Ref. [160]

[2] E_g^Γ calculated using Ref. [161]

A.1 Review of the material parameters for III-P compounds

In our calculations the direct (indirect) band gap of AlP and InP at 300 K are taken to be 3.602 and 1.346 eV (2.432 and 2.222 eV) respectively. These values are in a very good agreement with the measurements performed by Onton *et al.* [153]. Similarly to Si, GaP is an indirect gap material with the conduction band minimum located near the X point of the Brillouin zone [162]. For our calculations we assume a direct and indirect band gap of GaP at 300 K to be 2.717 and 2.276 eV respectively, with the latter being in a good agreement with Ref. [163]. We find that the reported values of Γ and X band gaps for GaP (c.f. Refs. [155, 163–165]) are more inconsistent compared to InP and AlP. Consequently, our values were adjusted to fit the more recently reported experimentally measured band gaps for GaInP lattice-matched to GaAs from Refs. [140, 166], which also require a bowing parameter and is discussed below.

Except for the direct band gap of InP and GaP, the temperature dependence of the band gaps of the binary materials were calculated using the Varshni relation. The literature data suggests that different equations can be used to better reproduce the direct energy gap of InP [161] and GaP [160]. Another important aspect is that the band gap in the X valley decreases slower compared to the Γ minimum. For example, in the work by Beaton *et al.* [152] it was shown that by increasing the temperature from 8 to 300 K, the direct-to-indirect band gap crossover in the $\mathrm{Al}_x\mathrm{In}_{1-x}\mathrm{P}$ alloy shifts from $x \approx 40.5 \pm 0.2$ % to $x \approx 43.2 \pm 0.2$ %. A similar behaviour was found for GaP, where the difference between the band gap in Γ and X valleys decreased from 0.555 eV at 8 K to 0.538 eV at 300K [164].

Typically the band gap of a ternary alloy follows a quadratic fit and is interpolated with the relation:

$$E_\mathrm{g}\left(\mathrm{A}_x\mathrm{B}_{1-x}\mathrm{C}\right) = x \cdot E_\mathrm{g}\left(\mathrm{AC}\right) + (1-x) \cdot E_\mathrm{g}\left(\mathrm{BC}\right) - x \cdot (1-x) \cdot C_\mathrm{ABC} \tag{A.1}$$

where C_ABC is the band gap bowing parameter. The work by Onton *et al.* [153] however shows that the band gap of an AlInP alloy can be interpolated linearly between the binary extremes, thus we do not include band gap bowing for this alloy in our calculations. Using the parameters in [153] we find that the direct-to-indirect band gap crossover in $\mathrm{Al}_x\mathrm{In}_{1-x}\mathrm{P}$ alloys at 300K occurs at $x \approx 42.7$ % with the energy gap at 2.310 eV. The experimental work by Beaton *et al.* [152] shows the direct-to-indirect band gap crossover occuring at 300 K for $x \approx 43.3 \pm 0.2$ % with the measured band gap at 2.330 ± 0.005 eV, while the cathodoluminescence measurements performed by Onton *et al.* [153] determine the crossover to be at $x \approx 44$ % with a 2.33 eV band gap. While the difference between our theoretical estimations and the experimental values has a small magnitude, a 20 meV change in the band gap could impact the external quantum efficiency of 610 nm emitters by affecting the intrinsicly weak electronic confinement and barrier to electron leakage. We note however that the theoretical barrier energy gap is smaller than the experimental one, so that our results therefore provide a conservative estimate of the effect of growth on a MBL.

Unlike the AlInP alloy, multiple reports [154, 156] show that a non-zero bowing parameter is required to fit the composition dependent bandgap in GaInP for both Γ and X valleys. In our calculations we use C_{GaInP} to be 0.66 (0.22) eV for the direct (indirect) band gap in order to reproduce the experimentally measured band gap of (i) the $\text{Ga}_x\text{In}_{1-x}\text{P}$ alloy across the entire composition range from Ref. [154], and (ii) $\text{Ga}_{0.5}\text{In}_{0.5}\text{P}$ from Refs. [140, 166]. We find that there has been very limited investigation of the electronic structure of AlGaP alloys, and these suggest that the alloy does not require a bowing parameter in order to interpolate the band gap [125].

Having established a set of parameters that can provide a good description of the band gaps of AlGaInP alloys with lattice constants close to that of GaAs, we now turn our attention to the band alignment. This will help us determine the magnitude of the band offsets in order to estimate the electron confinement depth using our 8-band **k·p** model. In our calculations we calculate the valence band offset ΔE_v using model solid theory [124]. This and the calculated Γ and X band gaps for our heterostructures allow us to calculate the conduction band offset ΔE_c. The maximum of the valence band, E_v, is calculated using the position of the average valence band, E_v^{avg}, and the spin-orbit splitting, Δ_{so}, as follows:

$$E_{\text{v}} = E_v^{avg} + \frac{1}{3}\Delta_{\text{so}} \tag{A.2}$$

Several values for the average valence band energy, E_v^{avg}, determined from model solid theory, can be found in the literature. The original work by Van de Walle [124] estimates E_v^{avg} to be -8.09, -7.40 and -7.04 eV for AlP, GaP and InP respectively. The work by Qteish and Needs [126] suggests slightly different values for the III-P binaries (-8.00, -7.26 and -6.81 eV for AlP, GaP and InP respectively). In our calculations we take E_{v}^{avg} for AlP, GaP and InP to be -8.00, -7.47 and -7.04 eV respectively, based on the theoretical work by Krijn [125]. The values for Δ_{so} used in our calculations are 0.07, 0.08 and 0.108 eV for AlP, GaP and InP respectively, and are typical values used in the literature [103]. Using our set of parameters we find a very good agreement between our estimated ΔE_v for AlP/GaP/InP interfaces and the theoretical predictions by Li *et al.* [127]. We also find that the calculated ΔE_v and ΔE_c for GaInP/AlGaInP heterostructures lattice matched to GaAs in our model are in good agreement with the work by Zhang *et al.* [167], with the $\Delta E_c/\Delta E_v$ ratio being within the range of measured values [168, 169].

Because of an inconsistent set of deformation potentials available in the literature for III-P compounds, we limit the choice of compositions for AlGaInP-based heterostructures by using lattice-matched barriers. Nevertheless deformation potentials are required for our calculations to include the effect of compressive strain on the band structure of AlInP QW- and QWR-based supercells. In our calculations we assume the conduction band deformation potentials a_c for AlP, GaP, and InP to be -5.86, -8.57 and -5.71 eV respectively, and are taken from Wei's work [170]. The values for valence band deformation potential a_v, which is responsible for the strain-induced shift of the average valence band energy, are taken from Qteish's work [126] and are in agreement with other reported values [103]. Overall, we estimate the direct band gap deformation potential $a_g^\Gamma = a_c - a_v$ in our calculations to be -9.01, -10.27 and -6.98 eV for AlP, GaP and InP respectively. Earlier experimental measurements suggest a_g^Γ for GaP to be -9.9±0.3 eV [171] and -9.9 eV±10% [165], assuming in the latter a bulk modulus of 90 GPa. For InP however a broader range of a_g^Γ can be found, with values such as -6.35±0.05 [172], -6.07±0.06 [173], -6.4 [174] and -8.0±0.4 eV [175] for InP. We find this range surprising given the direct band gap nature of this compound. Using the bulk modulus of GaAs, which is estimated to be about 6% larger than the one for InP, Kobayashi *et al.* evaluate a_g^Γ to be -6.7 eV for InP [176]. The experimental work by Ernst *et al.* [177] estimates the $\Gamma - \mathrm{X}$ valley crossover in undoped InP to occur at 11.2±0.4 GPa at low temperatures, which translates into approximately 3.7% lattice compression, however the authors did not provide the magnitude of the band gap at this crossover. Using our values for a_g^Γ and the hydrostatic deformation potential for the X valley $a_g^\mathrm{X} = \Xi_h - a_v$ of 0.58 eV, where Ξ_h is the hydrostatic deformation potential for the X valley minimum, we find that this crossover occurs at 2.234 eV with a 3.9% lattice compression at 4 K. To our knowledge there are no experimental investigations of a_g^Γ for AlP, with the theoretical works estimating it to be -9.52 [170], -8.7 eV [124].

In our calculations the values considered for the shear deformation potential b, which determines the splitting of heavy- and light-hole bands, are taken from Vurgaftman's work [103] and are typical values derived from theoretical and experimental estimations. In order to investigate the effects of strain on the X minimum, the hydrostatic and axial deformation potentials (Ξ_h and Ξ_ax respectively) for the conduction band minima are included in our one-band model of the indirect band gap. We find that there is limited research on these deformation potentials in the literature, and our values are taken from Adachi [178].

Overall we note that the literature currently lacks a consistent set of material parameters for III-P compounds. Given the intrinsically weak electronic confinement in blueshifted red LEDs, as well as our predictions of improved optoelectronic performance in these devices by using an InGaAs MBL, we strongly encourage the scientific community to investigate the bandstructure of AlGaInP alloys in more details.

Appendix B

Second order perturbation theory

Here we provide the derivation of the second order perturbation theory, and we follow the method used by O'Reilly [88].

For the second order perturbation theory we estimate how the nth wavefunction changes under the $\mathbf{k}\cdot\mathbf{p}$ Hamiltonian $\widehat{H}'$, which will help us find an additional change in the energy bands E_n. Since we use the perturbation theory for a narrow range of wave vectors $\mathbf{k}$ close to the reference $\mathbf{k}_0$, the effect of the perturbed Hamiltonian $\widehat{H}'$ in (2.7) is much smaller compared to $\widehat{H}_0$ in (2.2). Therefore the total Hamiltonian $\widehat{H}$ can be expressed as a power series using a parameter λ, such as $\widehat{H} = \widehat{H}_0 + \lambda\widehat{H}'$ and $0 \leq \lambda \leq 1$. In order to estimate the second order correction to the non-degenerate energy bands E_n we require the first order correction of the wavefunction ψ_n such as

$$\psi_n(\mathbf{r}) = \psi_n^{(0)}(\mathbf{r}) + \lambda\psi_n^{(1)}(\mathbf{r})\,, \tag{B.1a}$$

$$E_n = E_n^{(0)} + \lambda E_n^{(1)} + \lambda^2 E_n^{(2)}\,. \tag{B.1b}$$

Substituting the expanded Hamiltonian $\widehat{H}$ and Eqs. (B.1a) into the Scrödinger equation (2.1) yields

$$\left(\widehat{H}_0 + \lambda\widehat{H}'\right)\left(\psi_n^{(0)}(\mathbf{r}) + \lambda\psi_n^{(1)}(\mathbf{r})\right) = \left(E_n^0 + \lambda E_n^{(1)} + \lambda^2 E_n^{(2)}\right)\left(\psi_n^{(0)}(\mathbf{r}) + \lambda\psi_n^{(1)}(\mathbf{r})\right)\,. \tag{B.2}$$

Here we assume that the equation is true for all values of λ. Therefore, the polynomials on both sides will be equal only if the coefficients next to parameter λ at the same power will be identical, i.e.

$$\widehat{H}_0\psi_n^{(0)}(\mathbf{r}) = E_n^{(0)}\psi_n^{(0)}(\mathbf{r}) \tag{B.3a}$$

$$\widehat{H}'\psi_n^{(0)}(\mathbf{r}) + \widehat{H}_0\psi_n^{(1)}(\mathbf{r}) = E_n^{(0)}\psi_n^{(1)}(\mathbf{r}) + E_n^{(1)}\psi_n^{(0)}(\mathbf{r}) \tag{B.3b}$$

$$\widehat{H}'\psi_n^{(1)}(\mathbf{r}) = E_n^{(2)}\psi_n^{(0)}(\mathbf{r}) + E_n^{(1)}\psi_n^{(1)}(\mathbf{r})\,. \tag{B.3c}$$

The first equation here is simply the unperturbed Schrödinger equation (2.1), while the second can be used to estimate the first order energy $E_n^{(1)}$ and wavefunction $\psi_n^{(1)}(\mathbf{r})$ corrections. The results can then be substituted into the third equation to determine the second order correction for the energy $E_n^{(2)}$.

A change in the wavefunction $\psi_n^{(0)}(\mathbf{r})$ due to the perturbed Hamiltonian $\widehat{H}'$ can be regarded as mixing between the other states $\psi_m^{(0)}$ with $m \neq n$, in which case the first order correction to the nth wavefunction can be written as a linear combination of individual fractional contribution of the other states, i.e.

$$\psi_n^{(1)}(\mathbf{r}) = \sum_{m\neq n} a_{nm}\psi_m^{(0)}(\mathbf{r})\,, \tag{B.4}$$

where a_{nm} is the fractional contribution of the mth state to the nth wavefunction. Substituting Eq. (B.4) into (B.3b) we obtain

$$\sum_{m\neq n}\left(\widehat{H}_0 - E_n^{(0)}\right) a_{nm}\psi_m^{(0)}(\mathbf{r}) = \left(E_n^{(1)} - \widehat{H}'\right)\psi_n^{(0)}(\mathbf{r})\,, \tag{B.5}$$

which, using Eq. (B.3a), becomes

$$\sum_{m\neq n} a_{nm}\left(E_m^{(0)} - E_n^{(0)}\right)\psi_m^{(0)}(\mathbf{r}) = \left(E_n^{(1)} - \widehat{H}'\right)\psi_n^{(0)}(\mathbf{r})\,. \tag{B.6}$$

Multiplying both sides of the equation here by $\left(\psi_n^{(0)}\right)^*$ and integrating over the the unit cell space yields

$$\sum_{m\neq n} a_{nm}\left(E_m^{(0)} - E_n^{(0)}\right)\langle\psi_n^{(0)}|\psi_m^{(0)}\rangle = \langle\psi_n^{(0)}|E_n^{(1)} - \widehat{H}'|\psi_n^{(0)}\rangle\,. \tag{B.7}$$

Due to the orthonormality of the wavefunction, i.e. $\langle\psi_n|\psi_m\rangle = \delta_{nm}$, where δ_{nm} is the Kronecker delta, the left-hand side of the Eq. (B.7) is equal to 0. Thus we obtain the first order correction $E_n^{(1)}$ of the nth energy state

$$E_n^{(1)} = \langle\psi^0_n|\widehat{H}'|\psi^0_n\rangle\,, \tag{B.8}$$

which we have also shown in Eq. (2.11). We now multiply both sides of Eq. (B.6) by $\left(\psi_{n'}^{(0)}\right)^*$ to obtain

$$\sum_{m\neq n} a_{nm}\left(E_m^{(0)} - E_n^{(0)}\right)\langle\psi_{n'}^{(0)}|\psi_m^{(0)}\rangle = \langle\psi_{n'}^{(0)}|E_n^{(1)} - \widehat{H}'|\psi_n^{(0)}\rangle\,. \tag{B.9}$$

where, due to the wavefunction orthonormality, only one term in the sum of the left-hand side is non-zero, and rearrange to find the coefficients a

$$a_{nn'} = \frac{\langle\psi_{n'}^{(0)}|\widehat{H}'|\psi_n^{(0)}\rangle}{E_n^{(0)} - E_{n'}^{(0)}}\,. \tag{B.10}$$

Substituting Eq. (B.10) into (B.4) we find the first order correction $\psi_n^{(1)}$ to the wavefunction

$$\psi_n^{(1)}(\mathbf{r}) = \sum_{m\neq n}\frac{\langle\psi_m^{(0)}|\widehat{H}'|\psi_n^{(0)}\rangle}{E_n^{(0)} - E_m^{(0)}}\psi_m^{(0)}\,. \tag{B.11}$$

In order to find the second order correction $E_n^{(2)}$ to the energy state we substitute the first order expansion of the wavefunction (B.4) into (B.3c)

$$E_n^{(2)}\psi_n^{(0)}(\mathbf{r}) = \sum_{m\neq n} a_{nm}\left(\widehat{H}' - E_n^{(1)}\right)\psi_m^{(0)}(\mathbf{r})\,, \tag{B.12}$$

multiply both sides by $\left(\psi_n^{(0)}\right)^*$, integrate over the unit cell volume, and, taking the wavefunction orthonormality into account, we find

$$E_n^{(2)} = \sum_{m\neq n} a_{nm}\langle\psi_n^{(0)}|\widehat{H}'|\psi_m^{(0)}\rangle = \sum_{m\neq n}\frac{\langle\psi_m^{(0)}|\widehat{H}'|\psi_n^{(0)}\rangle}{E_n^{(0)} - E_m^{(0)}}\langle\psi_n^{(0)}|\widehat{H}'|\psi_m^{(0)}\rangle \tag{B.13}$$

Plugging Eqs. (B.8) and (B.13) into (B.1b) yields

$$\begin{aligned} E_n &= E_n^{(0)} + \langle \psi_n^0 | \widehat{H}' | \psi_n^0 \rangle + \sum_{m \neq n} \frac{\left| \langle \psi_n^{(0)} | \widehat{H}' | \psi_m^{(0)} \rangle \right|^2}{E_n^{(0)} - E_m^{(0)}} \\ &= E_n^{(0)} + \widehat{H}'_{nn} + \sum_{m \neq n} \frac{\left| \widehat{H}'_{nm} \right|^2}{E_n^{(0)} - E_m^{(0)}} , \end{aligned} \tag{B.14}$$

and using the **k·p** Hamiltonian from Eq. (2.7) the energy dispersion with the second order correction becomes

$$E_n(\mathbf{k}) = E_n(\mathbf{k}_0) + \frac{\hbar^2}{2m_0} |\mathbf{k} - \mathbf{k}_0|^2 + \frac{\hbar}{m_0} (\mathbf{k} - \mathbf{k}_0) \cdot \mathbf{p}_{nn} + \frac{\hbar^2}{m_0^2} \sum_{m \neq n} \frac{|(\mathbf{k} - \mathbf{k}_0) \cdot \mathbf{p}_{nm}|^2}{E_n(\mathbf{k}_0) - E_m(\mathbf{k}_0)} \tag{B.15}$$

with the Hamiltonian matrix element $\widehat{H}_{nm}$

$$\widehat{H}_{nm}(\mathbf{k}) = E_n(\mathbf{k}_0)\delta_{nm} + \widehat{H}'_{nm}(\mathbf{k}) + \sum_{l \in A \neq n} \frac{\widehat{H}'_{nl}(\mathbf{k}) \widehat{H}'_{lm}(\mathbf{k})}{E_n(\mathbf{k}_0) - E_l(\mathbf{k}_0)} , \tag{B.16}$$

where δ_{nm} is the Kronecker delta. The term under summation in Eq. (B.15) represents the perturbation on a particular band E_n from the nearby bands E_m that are located relatively close in energy. According to Löwdin's renormalisation method [96] these energy states correspond to class A, which is specified in the sum in Eq. (B.16). He also introduces the class B states which denote the remote energy states, which have a much weaker interaction with the class A states compared to the interaction between the class A states themselves. By adding the perturbation of class B remote states into the Hamiltonian it becomes:

$$\widehat{H}_{nm}(\mathbf{k}) = E_n(\mathbf{k}_0)\delta_{nm} + \widehat{H}'_{nm}(\mathbf{k}) + \sum_{l \in A \neq n} \frac{\widehat{H}'_{nl}(\mathbf{k}) \widehat{H}'_{lm}(\mathbf{k})}{E_n(\mathbf{k}_0) - E_l(\mathbf{k}_0)} + \sum_{l \in B} \frac{\widehat{H}'_{nl}(\mathbf{k}) \widehat{H}'_{lm}(\mathbf{k})}{E_A(\mathbf{k}_0) - E_l(\mathbf{k}_0)} . \tag{B.17}$$

Appendix C

Fermi's golden rule

Here we provide the derivation of Fermi's golden rule, and we start by considering the time-dependent Schrödinger equation

$$\widehat{H}\psi_p(\mathbf{r},t) = i\hbar\frac{\partial}{\partial t}\psi_p(\mathbf{r},t) \tag{C.1}$$

where the Hamiltonian $\widehat{H}$ consists of the unperturbed and time-dependent perturbation, $\widehat{H}_0$ and $\widehat{H}'$ respectively:

$$\widehat{H} = \widehat{H}_0 + \widehat{H}'(\mathbf{r},t)\,. \tag{C.2}$$

Similarly to the perturbation theory in section 2.2, we assume a known wavefunction ψ_{m_0} for the unperturbed Hamiltonian $\widehat{H}_0$, and can be written as

$$\psi_m(\mathbf{r},t) = \psi_m(\mathbf{r})e^{-iE_m t/\hbar}\,. \tag{C.3}$$

The Hamiltonian $\widehat{H}'$ is assumed to have the form:

$$\widehat{H}'(\mathbf{r},t) = \begin{cases} \widehat{H}'(\mathbf{r})e^{-i\omega t} + \widehat{H}'^{*}(\mathbf{r})e^{+i\omega t}, & t \geq 0 \\ 0, & t < 0 \end{cases} \tag{C.4}$$

where the * superscript in $\widehat{H}'^{*}$ denotes the Hermitian conjugate and the perturbation Hamiltonian $\widehat{H}'(\mathbf{r},t)$ appears due to the interaction between the electron and the incident electromagnetic wave with angular frequency ω. Here we consider the time-dependent wavefunction ψ_p as a combination of fractional contributions of unperturbed wavefunctions ψ_m in the series

$$\psi_p(\mathbf{r},t) = \sum_m a_m(t)\psi_m(\mathbf{r},t) = \sum_m a_m(t)\psi_m(\mathbf{r})e^{-iE_m t/\hbar}\,, \tag{C.5}$$

where $|a_m|^2$ gives the probability density of the state n at time t. We substitute the expansion (C.5) into the Schrödinger equation (C.1) and, taking into account the fact that ψ_m is the eigenfunction of the unperturbed Hamiltonian $\widehat{H}_0$, obtain

$$\begin{aligned} &\sum_m \frac{\mathrm{d}a_m(t)}{\mathrm{d}t}\psi_m(\mathbf{r})e^{-iE_m t/\hbar} = \frac{1}{i\hbar}\sum_m \widehat{H}'(\mathbf{r},t)a_m(t)\psi_m(\mathbf{r})e^{-iE_m t/\hbar} \iff \\ &\iff \sum_m \frac{\mathrm{d}a_m(t)}{\mathrm{d}t}|\psi_m(\mathbf{r},t)\rangle = \frac{1}{i\hbar}\sum_m \widehat{H}'(\mathbf{r},t)a_m(t)|\psi_m(\mathbf{r},t)\rangle\,. \end{aligned} \tag{C.6}$$

Here we left multiply by $\langle\psi_n(\mathbf{r},t)|$ and, taking into account the orthonormality condition $\langle\psi_n(\mathbf{r})|\psi_m(\mathbf{r})\rangle = \delta_{nm}$, we obtain

$$\frac{\mathrm{d}a_n(t)}{\mathrm{d}t} = \frac{1}{i\hbar}\sum_m a_m(t)\widehat{H}'_{nm}e^{i\omega_{nm}t}\,, \tag{C.7}$$

where

$$\begin{aligned} \widehat{H}'_{nm}(t) &= \langle\psi_n(\mathbf{r})|\widehat{H}'(\mathbf{r},t)|\psi_m(\mathbf{r})\rangle = \\ &= \widehat{H}'_{nm}e^{-i\omega t} + \widehat{H}'^{*}_{nm}e^{+i\omega t}\,, \\ \omega_{nm} &= (E_n - E_m)/\hbar\,. \end{aligned} \tag{C.8}$$

We note here that the Hamiltonian matrix elements $\widehat{H}'_{nm}$ and $\widehat{H}'^{*}_{nm}$ are time- and position-independent. Here we consider the expansion of the Hamiltonian (C.2) and the fractional parameters a_n into the following power series:

$$\begin{aligned} \widehat{H} &= \widehat{H}_0 + \lambda\widehat{H}'(\mathbf{r},t) \\ a_n(t) &= a_n^{(0)} + \lambda a_n^{(1)}(t)\,, \end{aligned} \tag{C.9}$$

where $0 \le \lambda \le 1$, resulting in:

$$\begin{aligned} \frac{\mathrm{d}a_n^{(0)}}{\mathrm{d}t} &= 0 \\ \frac{\mathrm{d}a_n^{(1)}(t)}{\mathrm{d}t} &= \frac{1}{i\hbar}\sum_m a_m^{(0)}\widehat{H}'_{nm}(t)e^{i\omega_{nm}t}\,. \end{aligned} \tag{C.10}$$

Suppose at time $t = 0$, when no perturbation is applied, the electron is located in an initial state i, such as:

$$\begin{aligned} a_i^{(0)} &= 1 \\ a_n^{(0)} &= 0, n \neq i\,. \end{aligned} \tag{C.11}$$

With the perturbation included we calculated the first-order contribution to the initial state $a_i^{(1)}(t)$:

$$\begin{aligned} \frac{\mathrm{d}a_n^{(1)}(t)}{\mathrm{d}t} &= \frac{1}{i\hbar}\widehat{H}'_{ni}(t)e^{i\omega_{ni}t} = \\ &= \frac{1}{i\hbar}\left[\widehat{H}'_{fi}e^{i(\omega_{ni}-\omega)t} + \widehat{H}'^{*}_{fi}e^{i(\omega_{ni}+\omega)t}\right]\,. \end{aligned} \tag{C.12}$$

We solve this equation for a final state $m = f$ by integration with the lower and upper limits $t_1 = 0$ and $t_2 = t$ respectively:

$$a_f^{(1)}(t) = -\frac{1}{\hbar}\left[\widehat{H}'_{fi}\frac{e^{i(\omega_{fi}-\omega)t}-1}{\omega_{fi}-\omega} + \widehat{H}'^{*}_{fi}\frac{e^{i(\omega_{fi}+\omega)t}-1}{\omega_{fi}+\omega}\right]\,. \tag{C.13}$$

We now assume that the incident wave ω is near resonance, i.e. $\omega \approx \pm\omega_{fi}$, thereby yielding the probability density of the electron being in the final state

$$\left|a_f^{(1)}(t)\right|^2 = \frac{1}{\hbar^2}\left\{\left|\widehat{H}'_{fi}\right|^2\frac{\sin^2[t(\omega_{fi}-\omega)/2]}{[(\omega_{fi}-\omega)/2]^2} + \left|\widehat{H}'^{*}_{fi}\right|^2\frac{\sin^2[t(\omega_{fi}+\omega)/2]}{[(\omega_{fi}+\omega)/2]^2}\right\}\,, \tag{C.14}$$

where we ignored the cross product terms due to their relatively small magnitude. For times long enough, we can make the substitution $\frac{sin^2(xt/2)}{x^2} \rightarrow \pi\delta(x)\frac{t}{2}$, where $\delta(x)$ is the Dirac delta function, therefore for the transition probability we obtain:

$$W_{if} = \frac{\mathrm{d}}{\mathrm{d}t}\left|a_f^{(1)}(t)\right|^2 = \frac{2\pi}{\hbar}\left\{\left|\widehat{H}'_{fi}\right|^2\delta(E_f - E_i - \hbar\omega) + \left|\widehat{H}'^{*}_{fi}\right|^2\delta(E_f - E_i + \hbar\omega)\right\}\,, \tag{C.15}$$

where we used the fact that $\delta(\omega) = \delta(\hbar\omega)/\hbar$. The Eq. (C.15) is the Fermi's golden rule, where the first (second) term in the bracket represents the absorption (emission), since $E_f \approx E_i + \hbar\omega$ ($E_f \approx E_i - \hbar\omega$).

Appendix D

Useful characteristic functions for various quantum wire and quantum dot shapes

In this appendix we present a set of Fourier transform of the characteristic function $\widetilde{\chi}$ for various QD and QWR shapes, which is given by the following integral:

$$\widetilde{\chi}(\mathbf{G}) = \frac{1}{\Omega_{\mathrm{sc}}} \int_{\Omega_{\mathrm{QD}}} e^{-i\mathbf{G}\cdot\mathbf{r}} \mathrm{d}V \, . \tag{D.1}$$

Following the derivation procedure in Chapter 3.2, we consider here a rectangular cuboid supercell with the volume $\Omega_{sc} = L_x \times L_y \times L_z$. A position dependent material parameter of the supercell $\mathcal{A}(\mathbf{r})$ follows the periodic boundary condition, i.e. $\mathcal{A}(\mathbf{r}) = \mathcal{A}(\mathbf{r} + \mathbf{R})$, where $\mathbf{R} = m_x L_x \mathbf{x} + m_y L_y \mathbf{y} + m_z L_z \mathbf{z}$ and $m_x, m_y, m_z \in \mathbb{Z}$. The reciprocal space wave vector $\mathbf{G} = (G_x, G_y, G_z)$, where G_j $(j = x, y, z)$ is given by:

$$G_j = \frac{2 m_j \pi}{L_j} \tag{D.2}$$

Cuboid Quantum Dot

$$\widetilde{\chi}(\mathbf{G}) = \frac{\Omega_{qd}}{\Omega_{sc}} \mathrm{sinc}\left(\frac{G_x d_x}{2}\right) \mathrm{sinc}\left(\frac{G_y d_y}{2}\right) \mathrm{sinc}\left(\frac{G_z d_z}{2}\right) , \tag{D.3}$$

where d_x, d_y and d_z are the sides length of the cuboid QD along the x, y and z directions respectively. The body centre of the QD is situated at the origin of the coordinate system.

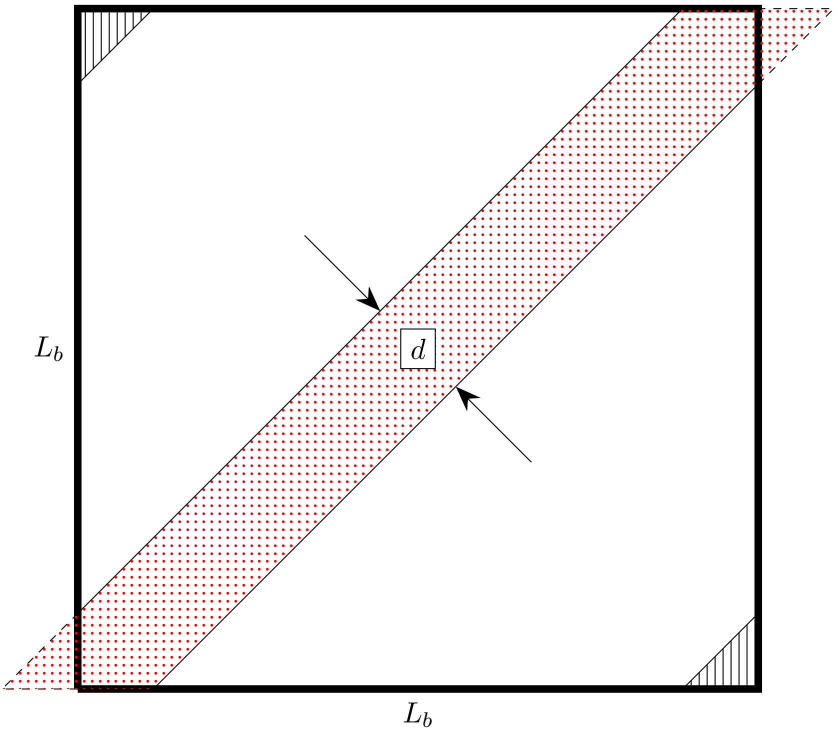

FIGURE D.1: Top view schematic representation of a supercell containing a wire along [110] direction with the thickness d. When we perform electronic and optical properties calculations on a QWR we ensure that the supercell has a shape of a square in the (x,y) plane, with sides L_b. The red hashed areas, including the triangles outside the supercell, are considered for the derivation of $\widetilde{\chi}$. Due to the periodic boundary conditions, the red hashed triangles are replicated inside the supercell, shown as black hashed triangles.

[110] and [1$\bar{1}$0] QWR with a rectangular cross section. Let the QWR have the thickness d and height h in a supercell with the sides L_b, L_b and L_z in x, y and z direction respectively. Let $a = d\sqrt{2}$, then

$$\widetilde{\chi}(\mathbf{G}) = \frac{2\sqrt{2}L_b h}{G_y} \sin\left(\frac{aG_y}{2}\right) \operatorname{sinc}\left(\frac{G_z h}{2}\right) \delta(G_x, \mp G_y)\,. \tag{D.4}$$

The minus and plus signs inside the Kronecker delta δ correspond to the QWR along [110] and [1$\bar{1}$0] direction respectively. For the derivation of $\widetilde{\chi}$ of the QWR we ensure that the top view of the supercell represents a square with the side length L, as shown in Fig. D.1. This, and the periodic boundary conditions, result in the presence of multiple structures in the supercell, which, ultimately, do not negatively impact our calculations. One way to address these concerns is to use another coordinate system (x', y') which is rotated by $\theta = \frac{\pi}{4}$ counterclockwise relative to the original system (x, y). In this case, however, we (i) are forced to introduce a new set of wave vectors k_j, therefore we need to reevaluate the plane wave expansion of the Hamiltonian matrix elements [79], and (ii) reevaluate the Fourier transform of the strain tensor. Thus we decide to use a plane wave basis set that is consistent with all QD and QWR shapes in order to simplify the implementation in a code. Here the line $x = \pm y$ at $z = 0$ goes through the centre of the wire cross section.

Additional expressions for characteristic function for various QD shapes can be found in Refs. [80, 179].

Bibliography

[1] D. K and Z. Xiang, "Optoelectronic Devices" (World Scientific Publishing Company, 2013), ISBN 9789813236714.

[2] S. Chuang, "Physics of Photonic Devices", Wiley Series in Pure and Applied Optics (John Wiley & Sons, 2009).

[3] E. P. O'Reilly, "Valence band engineering in strained-layer structures," Semiconductor Science and Technology **4**, 121 (1989).

[4] W. Chow and S. Koch, "Semiconductor-Laser Fundamentals: Physics of the Gain Materials" (Springer Berlin Heidelberg, 2013), ISBN 9783662038802.

[5] J. P. Loehr and J. Singh, "Theoretical studies of the effect of strain on the performance of strained quantum well lasers based on GaAs and InP technology," IEEE Journal of Quantum Electronics **27**, 708 (1991).

[6] M. Suzuki and T. Uenoyama, "Strain effect on electronic and optical properties of GaN/AlGaN quantum well lasers," Journal of Applied Physics **80**, 6868 (1996).

[7] J. Matthews and A. Blakeslee, "Defects in epitaxial multilayers: I. Misfit dislocations," Journal of Crystal Growth **27**, 118 (1974), ISSN 0022-0248.

[8] S. Jain, M. Willander, and R. Van Overstraeten, "Compound Semiconductors Strained Layers and Devices", Electronic Materials Series (Springer US, 2013), ISBN 9781461544418.

[9] S. M. Wang, ed., "Lattice Engineering: Technology and Applications" (Pan Stanford Publishing, 2012).

[10] Z. Wang, "Self-Assembled Quantum Dots", Lecture Notes in Nanoscale Science and Technology (Springer New York, 2007), ISBN 9780387741918.

[11] R. Nötzel, "Self-organized growth of quantum-dot structures," Semiconductor Science and Technology **11**, 1365 (1996).

[12] E. Schubert, "Light-Emitting Diodes (Second Edition, 2006)" (E. Fred Schubert, 2006), ISBN 9780986382611.

[13] J. Ayers, T. Kujofsa, P. Rago, and J. Raphael, "Heteroepitaxy of Semiconductors: Theory, Growth, and Characterization, Second Edition" (CRC Press, 2016), ISBN 9781315355177.

[14] I. Tångring, S. Wang, M. Sadeghi, A. Larsson, and X. Wang, "Metamorphic growth of 1.25–1.29 μm InGaAs quantum well lasers on GaAs by molecular beam epitaxy," Journal of Crystal Growth **301–302**, 971 (2007).

[15] Y.-C. Xin, L. G. Vaughn, L. R. Dawson, A. Stintz, Y. Lin, L. F. Lester, and D. L. Huffaker, "InAs quantum-dot GaAs-based lasers grown on AlGaAsSb metamorphic buffers," Journal of Applied Physics **94**, 2133 (2003).

[16] A. E. Zhukov, A. R. Kovsh, S. S. Mikhrin, E. S. Semenova, N. A. Maleev, A. P. Vasil'ev, E. V. Nikitina, N. V. Kryzhanovskaya, A. G. Gladyshev, Y. M. Shernyakov, et al., "Metamorphic lasers for 1.3 μm spectral range grown on GaAs substrates by MBE," Semiconductors **37**, 1119 (2003).

[17] D. Wu, H. Wang, B. Wu, H. Ni, S. Huang, Y. Xiong, P. Wang, Q. Han, Z. Niu, I. Tångring, et al., "Low threshold current density in 1.3 μm metamorphic InGaAs/GaAs quantum well laser diodes," Electron. Lett. **44**, 474 (2008).

[18] R. Olshansky, P. Hill, V. Lanzisera, and W. Powazinik, "Frequency response of 1.3μm InGaAsP high speed semiconductor lasers," IEEE Journal of Quantum Electronics **23**, 1410 (1987).

[19] J. Manning, R. Olshansky, and C. Su, "The carrier-induced index change in AlGaAs and 1.3 μm InGaAsP diode lasers," IEEE Journal of Quantum Electronics **19**, 1525 (1983).

[20] J. C. L. Yong, J. M. Rorison, and I. H. White, "1.3-μm quantum-well InGaAsP, AlGaInAs, and InGaAsN laser material gain: a theoretical study," IEEE Journal of Quantum Electronics **38**, 1553 (2002).

[21] S. R. Selmic, T.-M. Chou, J. Sih, J. B. Kirk, A. Mantle, J. K. Butler, D. Bour, and G. A. Evans, "Design and characterization of 1.3-μm AlGaInAs-InP multiple-quantum-well lasers," IEEE Journal of Selected Topics in Quantum Electronics **7**, 340 (2001).

[22] R. F. Kazarinov and G. L. Belenky, "Novel design of AlGaInAs-InP lasers operating at 1.3 μm," IEEE Journal of Quantum Electronics **31**, 423 (1995).

[23] M. C. Wang, W. Lin, T. T. Shi, and Y. K. Tu, "Ultrahigh temperature and ultrahigh speed operation of 1.3 μm strain-compensated AlGaInAs/InP uncooled laser diodes," Electronics Letters **31**, 1584 (1995).

[24] T. Higashi, S. J. Sweeney, A. F. Phillips, A. R. Adams, E. P. O'Reilly, T. Uchida, and T. Fujii, "Observation of reduced nonradiative current in 1.3-μm AlInGaAs-InP strained MQW lasers," IEEE. Photon. Tech. Lett. **11**, 409 (1999).

[25] K. Takemasa, M. Kubota, T. Munakata, and H. Wada, "1.3-µm AlGaInAs buried-heterostructure lasers," IEEE Photonics Technology Letters **11**, 949 (1999).

[26] J.-W. Pan and J.-I. Chyi, "Theoretical study of the temperature dependence of 1.3-μm AlGaInAs-InP multiple-quantum-well lasers," IEEE Journal of Quantum Electronics **32**, 2133 (1996).

[27] C.-E. Zah, R. Bhat, B. N. Pathak, F. Favire, W. Lin, M. C. Wang, N. C. Andreadakis, D. M. Hwang, M. A. Koza, T.-P. Lee, et al., "High-performance uncooled 1.3-μm $\mathrm{Al}_x\mathrm{Ga}_y\mathrm{In}_{1-x-y}\mathrm{As}$/InP strained-layer quantum-well lasers for subscriber loop applications," IEEE Journal of Quantum Electronics **30**, 511 (1994).

[28] T. Higashi, S. J. Sweeney, A. F. Phillips, A. R. Adams, E. P. O'Reilly, T. Uchida, and T. Fujii, "Experimental analysis of temperature dependence in 1.3-μm AlGaInAs-InP strained MQW lasers," IEEE. J. Sel. Top. Quant. Electron. **5**, 413 (1999).

[29] T. J. Houle, J. C. L. Yong, C. M. Marinelli, S. Yu, J. M. Rorison, I. H. White, J. K. White, A. J. SpringThorpe, and B. Garrett, "Characterization of the temperature sensitivity of gain and recombination mechanisms in 1.3-μm AlGaInAs MQW lasers," IEEE. J. Quant. Electron. **41**, 132 (2005).

[30] S. Sweeney, T. Higashi, A. Andreev, A. Adams, T. Uchida, and T. Fujii, "Superior Temperature Performance of 1.3 µm AlGaInAs-Based Semiconductor Lasers Investigated at High Pressure and Low Temperature," physica status solidi (b) **223**, 573 (2001).

[31] K. Takemasa, T. Munakata, M. Kobayashi, H. Wada, and T. Kamijoh, "High-temperature operation of 1.3 μm AlGaInAs strained multiple quantum well lasers," Electronics Letters **34**, 1231 (1998).

[32] S. Tomić, E. P. O'Reilly, R. Fehse, S. J. Sweeney, A. R. Adams, A. D. Andreev, S. A. Choulis, T. J. C. Hosea, and H. Riechert, "Theoretical and experimental analysis of 1.3-μm InGaAsN/GaAs lasers," IEEE J. Sel. Top. Quant. Electron. **9**, 1228 (2003).

[33] H. Riechert, A. Ramakrishnan, and G. Steinle, "Development of InGaAsN-based 1.3 μm VCSELs," Semicond. Sci. Technol. **17**, 892 (2002).

[34] E. Söderberg, J. S. Gustavsson, P. Modh, A. Larsson, Z. Zhang, J. Berggren, and M. Hammar, "High-temperature dynamics, high-speed modulation, and transmission experiments using 1.3-μm InGaAs single-mode VCSELs," IEEE J. Lightwave Technol. **25**, 2791 (2007).

[35] P. Sundgren, R. M. von Wurtemberg, J. Berggren, M. Hammar, M. Ghisoni, V. Oscarsson, E. Odling, and J. Malmquist, "High-performance 1.3 μm InGaAs vertical cavity surface emitting lasers," Electronics Letters **39**, 1128 (2003).

[36] D. L. Huffaker, G. Park, Z. Zou, O. B. Shchekin, and D. G. Deppe, "1.3 μm room-temperature GaAs-based quantum-dot laser," Appl. Phys. Lett. **73**, 2564 (1998).

[37] V. M. Ustinov, N. A. Maleev, A. E. Zhukov, A. R. Kovsh, A. Y. Egorov, A. V. Lunev, B. V. Volovik, I. L. Krestnikov, Y. G. Musikhin, N. A. Bert, et al., "InAs/InGaAs quantum dot structures on GaAs substrates emitting at 1.3 μm," Appl. Phys. Lett. **74**, 2815 (1999).

[38] K. Mukai, Y. Nakata, K. Otsubo, M. Sugawara, N. Yokoyama, and H. Ishikawa, "1.3-µm CW lasing of InGaAs-GaAs quantum dots at room temperature with a threshold current of 8 mA," IEEE Photonics Technology Letters **11**, 1205 (1999).

[39] A. R. Kovsh, N. A. Maleev, A. E. Zhukov, S. S. Mikhrin, A. R. Vasil'ev, Y. M. Shemyakov, M. V. Maximov, D. A. Livshits, V. Ustinov, Z. I. Alferov, et al., "InAs/InGaAs/GaAs quantum dot lasers of 1.3 μm range with high (88%) differential efficiency," Electronics Letters **38**, 1104 (2002).

[40] J. A. Lott, N. N. Ledentsov, V. M. Ustinov, N. A. Maleev, A. E. Zhukov, A. R. Kovsh, M. V. Maximov, B. V. Volovik, Z. I. Alferov, and D. Bimberg, "InAs-InGaAs quantum dot VCSELs on GaAs substrates emitting at 1.3 μm," Electronics Letters **36**, 1384 (2000).

[41] R. Fehse, S. Tomić, A. R. Adams, S. J. Sweeney, E. P. O'Reilly, A. D. Andreev, and H. Riechert, "A quantitative study of radiative, Auger, and defect related recombination in 1.3-μm GaInNAs-based quantum-well lasers," IEEE. J. Sel. Top. Quant. Electron. **8**, 801 (2002).

[42] C. A. Broderick, M. Usman, S. J. Sweeney, and E. P. O'Reilly, "Band engineering in dilute nitride and bismide semiconductor lasers," Semicond. Sci. Technol. **27**, 094011 (2012).

[43] E. Söderberg, P. Modh, J. S. Gustavsson, A. Larsson, Z. Zhang, J. Berggren, and M. Hammar, "High speed, high temperature operation of 1.28 μm singlemode InGaAs VCSELs," Electronics Letters **42**, 1 (2006).

[44] M. T. Crowley, N. A. Naderi, H. Su, F. Grillot, and L. F. Lester, "GaAs based quantum dot lasers," Semicond. and Semimet. **86**, 371 (2012).

[45] G. Park, O. B. Shchekin, D. L. Huffaker, and D. G. Deppe, "Low-threshold oxide-confined 1.3-µm quantum-dot laser," IEEE Photonics Technology Letters **12**, 230 (2000).

[46] O. B. Shchekin and D. G. Deppe, "Low-threshold high-T_0 1.3-μm InAs quantum-dot lasers due to p-type modulation doping of the active region," IEEE Photonics Technology Letters **14**, 1231 (2002).

[47] H. Y. Liu, I. R. Sellers, T. J. Badcock, D. J. Mowbray, M. S. Skolnick, K. M. Groom, M. Gutiérrez, M. Hopkinson, J. S. Ng, J. P. R. David, et al., "Improved performance of 1.3μm multilayer InAs quantum-dot lasers using a high-growth-temperature GaAs spacer layer," Applied Physics Letters **85**, 704 (2004).

[48] I. R. Sellers, H. Y. Liu, K. M. Groom, D. T. Childs, D. Robbins, T. J. Badcock, M. Hopkinson, D. J. Mowbray, and M. S. Skolnick, "1.3 μm InAs/GaAs multilayer quantum-dot laser with extremely low room-temperature threshold current density," Electronics Letters **40**, 1412 (2004).

[49] T. Uchida, H. Kurakake, H. Soda, and S. Yamazaki, "1.3 μm InGaAs/GaAs strained quantum well lasers with InGaP cladding layer," Electron. Lett. **30**, 563 (1994).

[50] H. Kurakake, T. Uchida, T. Higashi, S. Ogita, and M. Kobayashi, "1.3 μm high T_0 strained MQW laser with AlInGaAs SCH layers on a hetero-expitaxial InGaAs buffer layer," in proceedings of the 15th IEEE International Semiconductor Laser Conference p. 71 (1996).

[51] T. Uchida, H. Kurakake, H. Soda, and S. Yamazaki, "A 1.3 μm strained quantum well laser on a graded InGaAs buffer with a GaAs substrate," Journal of Electronic Materials **25**, 581 (1996).

[52] M. Arai, T. Tadokoro, T. Fujisawa, W. Kobayashi, K. Nakashima, M. Yuda, and Y. Kondo, "Uncooled (25 – 85°C) 10 Gbit/s operation of 1.3 μm-range metamorphic Fabry-Perot laser on GaAs substrate," Electron. Lett. **45**, 359 (2009).

[53] M. Arai, K. Nakashima, T. Fujisawa, T. Tadokoro, W. Kobayashi, M. Yuda, and Y. Kondo, "High-temperature operation of 1.26-μm ridge waveguide laser with InGaAs metamorphic buffer on GaAs substrate," IEEE J. Sel. Top. Quant. Electron. **15**, 724 (2009).

[54] M. Arai, W. Kobayashi, and M. Kohtoku, "1.3-μm-range metamorphic InGaAs laser with high characteristic temperature for low power consumption operation," IEEE J. Sel. Top. Quant. Electron. **19**, 1502207 (2013).

[55] H. Ishikawa, "Theoretical gain of strained quantum well grown on an InGaAs ternary substrate," Appl. Phys. Lett. **63**, 712 (1993).

[56] Y.-D. Huh, J.-H. Shim, Y. Kim, and Y. R. Do, "Optical properties of three-band white light emitting diodes," Journal of The Electrochemical Society **150**, H57 (2003).

[57] R.-J. Xie, N. Hirosaki, N. Kimura, K. Sakuma, and M. Mitomo, “2-phosphor-converted white light-emitting diodes using oxynitride/nitride phosphors,” Applied Physics Letters **90**, 191101 (2007).

[58] R. Mueller-Mach, G. Mueller, M. R. Krames, H. A. Höppe, F. Stadler, W. Schnick, T. Juestel, and P. Schmidt, “Highly efficient all-nitride phosphor-converted white light emitting diode,” physica status solidi (a) **202**, 1727 (2005).

[59] J. Y. Tsao, M. E. Coltrin, M. H. Crawford, and J. A. Simmons, “Solid-State Lighting: An Integrated Human Factors, Technology, and Economic Perspective,” Proceedings of the IEEE **98**, 1162 (2010).

[60] S. Pimputkar, J. S. Speck, S. P. DenBaars, and S. Nakamura, “Prospects for LED lighting,” Nature photonics **3**, 180 (2009).

[61] N. Matuschek and M. Duelk, in “2017 International Conference on Numerical Simulation of Optoelectronic Devices (NUSOD)” (2017), pp. 111–112.

[62] J.-I. Hwang, R. Hashimoto, S. Saito, and S. Nunoue, “Development of InGaN-based red LED grown on (0001) polar surface,” Applied Physics Express **7**, 071003 (2014).

[63] T. Yao and S. Hong, “Oxide and Nitride Semiconductors: Processing, Properties, and Applications”, Advances in Materials Research (Springer Berlin Heidelberg, 2009), ISBN 9783540888475.

[64] H. Morkoç, “Handbook of Nitride Semiconductors and Devices, Electronic and Optical Processes in Nitrides”, Handbook of Nitride Semiconductors and Devices (Wiley, 2009), ISBN 9783527628421.

[65] T. Takeuchi, C. Wetzel, S. Yamaguchi, H. Sakai, H. Amano, I. Akasaki, Y. Kaneko, S. Nakagawa, Y. Yamaoka, and N. Yamada, “Determination of piezoelectric fields in strained GaInN quantum wells using the quantum-confined Stark effect,” Applied physics letters **73**, 1691 (1998).

[66] O. Ambacher, J. Smart, J. Shealy, N. Weimann, K. Chu, M. Murphy, W. Schaff, L. Eastman, R. Dimitrov, L. Wittmer, et al., “Two-dimensional electron gases induced by spontaneous and piezoelectric polarization charges in N-and Ga-face AlGaN/GaN heterostructures,” Journal of applied physics **85**, 3222 (1999).

[67] T. Takeuchi, H. Amano, and I. Akasaki, “Theoretical Study of Orientation Dependence of Piezoelectric Effects in Wurtzite Strained GaInN/GaN Heterostructures and Quantum Wells,” Japanese Journal of Applied Physics **39**, 413 (2000).

[68] R. J. Radtke, U. Waghmare, H. Ehrenreich, and C. H. Grein, “Theoretical performance of wurtzite and zincblende InGaN/GaN quantum well lasers,” Applied Physics Letters **73**, 2087 (1998).

[69] M. R. Krames, O. B. Shchekin, R. Mueller-Mach, G. O. Mueller, L. Zhou, G. Harbers, and M. G. Craford, “Status and Future of High-Power Light-Emitting Diodes for Solid-State Lighting,” Journal of Display Technology **3**, 160 (2007).

[70] D. P. Bour, D. W. Treat, K. J. Beernink, B. S. Krusor, R. S. Geels, and D. F. Welch, “610-nm band AlGaInP single quantum well laser diode,” IEEE Photonics Technology Letters **6**, 128 (1994).

[71] S. Sweeney, G. Knowles, T. Sale, and A. Adams, “Quantifying the Effect of Indirect Carrier Leakage on Visible Al(GaInP) Lasers Using High Pressures and Low Temperatures,” physica status solidi (b) **223**, 567 (2001).

[72] J.-I. Shim, D.-P. Han, H. Kim, D.-S. Shin, G.-B. Lin, D. S. Meyaard, Q. Shan, J. Cho, E. F. Schubert, H. Shim, et al., “Efficiency droop in AlGaInP and GaInN light-emitting diodes,” Applied Physics Letters **100**, 111106 (2012).

[73] H. Hamada, K. Tominaga, M. Shono, S. Honda, K. Yodoshi, and T. Yamaguchi, “Room-temperature CW operation of 610 nm band AlGaInP strained multiquantum well laser diodes with multiquantum barrier,” Electronics Letters **28**, 1834 (1992).

[74] S. Nakamura, M. Senoh, S. ichi Nagahama, N. Iwasa, T. Yamada, T. Matsushita, H. Kiyoku, and Y. Sugimoto, “InGaN-Based Multi-Quantum-Well-Structure Laser Diodes,” Japanese Journal of Applied Physics **35**, L74 (1996).

[75] H. Hamada, R. Hiroyama, S. Honda, M. Shono, K. Yodoshi, and T. Yamaguchi, “AlGaInP strained multiple-quantum-well visible laser diodes ($\lambda_L \leq 630$ nm band) with a multiquantum barrier grown on misoriented substrates,” IEEE Journal of Quantum Electronics **29**, 1844 (1993).

[76] D. Jung, L. Yu, D. Wasserman, and M. L. Lee, “Mid-infrared electroluminescence from InAs type-I quantum wells grown on InAsP/InP metamorphic buffers,” Journal of Applied Physics **118**, 183101 (2015).

[77] E. C. Young, B. P. Yonkee, F. Wu, B. K. Saifaddin, D. A. Cohen, S. P. DenBaars, S. Nakamura, and J. S. Speck, “Ultraviolet light emitting diodes by ammonia molecular beam epitaxy on metamorphic ($20\bar{2}\bar{1}$) AlGaN/GaN buffer layers,” Journal of Crystal Growth **425**, 389 (2015).

[78] M. Ehrhardt and T. Koprucki, “Multi-Band Effective Mass Approximations: Advanced Mathematical Models and Numerical Techniques”, Lecture Notes in Computational Science and Engineering (Springer International Publishing, 2014), ISBN 9783319014272.

[79] E. P. O'Reilly, O. Marquardt, S. Schulz, and A. D. Andreev, "Plane-Wave Approaches to the Electronic Structure of Semiconductor Nanostructures" (Springer International Publishing, 2014), pp. 155–189.

[80] A. D. Andreev, J. R. Downes, D. A. Faux, and E. P. O'Reilly, "Strain distributions in quantum dots of arbitrary shape," Journal of Applied Physics **86**, 297 (1999).

[81] S. B. Healy and E. P. O'Reilly, "Influence of electrostatic confinement on optical gain in GaInNAs quantum-well lasers," IEEE J. Quant. Electron. **42**, 608 (2006).

[82] F. Szmulowicz, "Derivation of a general expression for the momentum matrix elements within the envelope-function approximation," Phys. Rev. B **51**, 1613 (1995).

[83] C. Pacey, M. Silver, A. R. Adams, and E. P. O'Reilly, "Optimization of 1.3 μm compressively strained quantum-well lasers," Int. J. Optoelectron. **11**, 253 (1997).

[84] A. Zunger, "Spontaneous Atomic Ordering in Semiconductor Alloys: Causes, Carriers, and Consequences," MRS Bulletin **22**, 20–26 (1997).

[85] A. Mascarenhas, "Spontaneous Ordering in Semiconductor Alloys" (Springer US, 2012), ISBN 9781461506317.

[86] G. Kresse and J. Furthmüller, "Efficient iterative schemes for ab initio total-energy calculations using a plane-wave basis set," Phys. Rev. B **54**, 11169 (1996).

[87] J. P. Perdew and A. Zunger, "Self-interaction correction to density-functional approximations for many-electron systems," Phys. Rev. B **23**, 5048 (1981).

[88] E. P. O'Reilly, "Quantum Theory of Solids" (CRC Press, 2002).

[89] E. O. Kane, "Band structure of indium antimonide," Journal of Physics and Chemistry of Solids **1**, 249 (1957).

[90] P. YU and M. Cardona, "Fundamentals of Semiconductors: Physics and Materials Properties", Graduate Texts in Physics (Springer Berlin Heidelberg, 2010), ISBN 9783642007101.

[91] S. B. Radhia, N. Fraj, I. Saidi, and K. Boujdaria, "The eight-level k · p model for the conduction and valence bands of InAs, InP, InSb," Semiconductor Science and Technology **22**, 427 (2007).

[92] S. Ben Radhia, K. Boujdaria, S. Ridene, H. Bouchriha, and G. Fishman, "Band structures of GaAs, InAs, and Ge: A 24-k.p model," Journal of Applied Physics **94**, 5726 (2003).

[93] R. Beresford, "Full-zone k·p method of band structure calculation for wurtzite semiconductors," Journal of Applied Physics **95**, 6216 (2004).

[94] R. Neffati, I. Saïdi, and K. Boujdaria, “Full-zone k.p model for the electronic structure of unstrained GaAs$_{1-x}$P$_x$ and strained Al$_x$In$_{1-x}$As alloys,” Journal of Applied Physics **112**, 053716 (2012).

[95] S. B. Radhia, S. Ridene, K. Boujdaria, H. Bouchriha, and G. Fishman, “Band structures of Ge and InAs: A 20 k.p model,” Journal of Applied Physics **92**, 4422 (2002).

[96] P. Löwdin, “A Note on the Quantum-Mechanical Perturbation Theory,” The Journal of Chemical Physics **19**, 1396 (1951).

[97] R. Willardson and A. Beer, “Semiconductors and Semimetals”, no. v. 12 in Semiconductors and Semimetals (Elsevier Science, 1977), ISBN 9780080864020.

[98] P. Enders, A. Bärwolff, M. Woerner, and D. Suisky, “**k·p** theory of energy bands, wave functions, and optical selection rules in strained tetrahedral semiconductors,” Phys. Rev. B **51**, 16695 (1995).

[99] E. O. Kane, in “Semiconductors and Semimetals”, edited by R. Willardson and A. C. Beer (Elsevier, 1966), vol. 1 of “Semiconductors and Semimetals”, pp. 75 – 100.

[100] J. M. Luttinger, “Quantum Theory of Cyclotron Resonance in Semiconductors: General Theory,” Phys. Rev. **102**, 1030 (1956).

[101] L. Voon and M. Willatzen, “The k p Method: Electronic Properties of Semiconductors” (Springer Berlin Heidelberg, 2009), ISBN 9783540928720.

[102] D. Gershoni, C. H. Henry, and G. A. Baraff, “Calculating the optical properties of multidimensional heterostructures: Application to the modeling of quaternary quantum well lasers,” IEEE Journal of Quantum Electronics **29**, 2433 (1993).

[103] I. Vurgaftman, J. R. Meyer, and L. R. Ram-Mohan, “Band parameters for III-V compound semiconductors and their alloys,” J. Appl. Phys. **89**, 5815 (2001).

[104] S. Birner, “The Multi-Band k·p Hamiltonian for Heterostructures: Parameters and Applications” (Springer International Publishing, Cham, 2014), pp. 193–244, ISBN 978-3-319-01427-2.

[105] M. Dresselhaus, G. Dresselhaus, and A. Jorio, “Group Theory: Application to the Physics of Condensed Matter”, SpringerLink: Springer e-Books (Springer Berlin Heidelberg, 2007), ISBN 9783540328971.

[106] M. Altarelli, U. Ekenberg, and A. Fasolino, “Calculations of hole subbands in semiconductor quantum wells and superlattices,” Phys. Rev. B **32**, 5138 (1985).

[107] G. Bir and G. Pikus, “Symmetry and Strain-induced Effects in Semiconductors”, A Halsted Press book (Wiley, 1974).

[108] J. Singh and R. Williams, "Excitonic and Photonic Processes in Materials", Springer Series in Materials Science (Springer Singapore, 2014), ISBN 9789812871312.

[109] J. Hader, J. V. Moloney, and S. W. Koch, "Microscopic evaluation of spontaneous emission- and Auger-processes in semiconductor lasers," IEEE Journal of Quantum Electronics **41**, 1217 (2005).

[110] H. Li and Z. Wang, "Bismuth-Containing Compounds", Springer Series in Materials Science (Springer New York, 2013).

[111] G. M. T. Chai, C. A. Broderick, E. P. O'Reilly, Z. Othaman, S. R. Jin, J. P. Petropoulos, Y. Zhong, P. B. Dongmo, J. M. O. Zide, S. J. Sweeney, et al., "Experimental and modelling study of InGaBiAs/InP alloys with up to 5.8% Bi, and with $\Delta_{\mathrm{SO}} > E_g$," Semiconductor Science and Technology **30**, 094015 (2015).

[112] G. Jones, A. D. Smith, E. P. O'Reilly, M. Silver, A. T. R. Briggs, M. J. Fice, A. R. Adams, P. D. Greene, K. Scarrott, and A. Vranic, "The influence of tensile strain on differential gain and Auger recombination in 1.5- μm multiple-quantum-well lasers," IEEE Journal of Quantum Electronics **34**, 822 (1998).

[113] P. Blood, "Quantum Confined Laser Devices: Optical Gain and Recombination in Semiconductors", Oxford Master Series in Condensed Matter Physics Series (Oxford University Press, 2015), ISBN 9780199644520.

[114] J. M. Hvam, "Direct recording of optical-gain spectra from ZnO," Journal of Applied Physics **49**, 3124 (1978).

[115] B. W. Hakki and T. L. Paoli, "cw degradation at 300 K of GaAs double-heterostructure junction lasers. II. Electronic gain," Journal of Applied Physics **44**, 4113 (1973).

[116] B. W. Hakki and T. L. Paoli, "Gain spectra in GaAs double−heterostructure injection lasers," Journal of Applied Physics **46**, 1299 (1975).

[117] K. Kawano and T. Kitoh, "Introduction to Optical Waveguide Analysis: Solving Maxwell's Equation and the Schrödinger Equation" (Wiley, 2001).

[118] H. Casey, "Heterostructure Lasers", pt. 1 (Elsevier Science, 2012), ISBN 9780323157698.

[119] H. Kressel, "Semiconductor Lasers and Herterojunction LEDs" (Elsevier Science, 2012), ISBN 9780323144346.

[120] Y. M. Lifshits and L. N. Rosenzweig, "On the derivation of Green's tensor for the general equation of the elasticity theory for an infinite anisotropic elastic medium (in Russian)," Journal of Experimental and Theoretical Physics **17**, 783 (1947).

[121] J. D. Eshelby, "The determination of the elastic field of an ellipsoidal inclusion, and related problems," Proceedings of the Royal Society of London A: Mathematical, Physical and Engineering Sciences **241**, 376 (1957).

[122] A. D. Andreev and E. P. O'Reilly, "Theory of the electronic structure of GaN/AlN hexagonal quantum dots," Phys. Rev. B **62**, 15851 (2000).

[123] L. D. Landau and E. M. Lifshitz, "Course of Theoretical Physics, Theory of Elasticity", vol. 7 (Pergamon Press Oxford, 1986), 3rd ed.

[124] C. G. Van de Walle, "Band lineups and deformation potentials in the model-solid theory," Phys. Rev. B **39**, 1871 (1989).

[125] M. P. C. M. Krijn, "Heterojunction band offsets and effective masses in III-V quaternary alloys," Semicond. Sci. Technol. **6**, 27 (1991).

[126] A. Qteish and R. J. Needs, "Improved model-solid-theory calculations for valence-band offsets at semiconductor-semiconductor interfaces," Phys. Rev. B **45**, 1317 (1992).

[127] Y.-H. Li, A. Walsh, S. Chen, W.-J. Yin, J.-H. Yang, J. Li, J. L. F. D. Silva, X. G. Gong, and S.-H. Wei, "Revised ab initio natural band offsets of all group IV, II-VI, and III-V semiconductors," Applied Physics Letters **94**, 212109 (2009).

[128] S.-H. Wei and A. Zunger, "Calculated natural band offsets of all II–VI and III–V semiconductors: Chemical trends and the role of cation d orbitals," Applied Physics Letters **72**, 2011 (1998).

[129] R. T. M., W. B. A., V. R. E., and B. D. P., "Energy Level Alignments in Strained-Layer GaInP/AlGaInP Laser Diodes: Model Solid Theory Analysis of Pressure-Photoluminescence Experiments," physica status solidi (b) **211**, 869 (1999).

[130] D. Vignaud and F. Mollot, "Conduction band offset in the $\mathrm{Al}_x\mathrm{Ga}_y\mathrm{In}_{1-x-y}\mathrm{P}/\mathrm{Ga}_{0.52}\mathrm{In}_{0.48}\mathrm{P}$ system as studied by luminescence spectroscopy," Journal of Applied Physics **93**, 384 (2003).

[131] S. Tomić and E. P. O'Reilly, "Optimization of material parameters in 1.3-μm InGaAsN-GaAs lasers," IEEE Photon. Tech. Lett. **15**, 6 (2003).

[132] M. Silver and E. P. O'Reilly, "Optimization of long wavelength InGaAsP strained quantum-well lasers," IEEE J. Quant. Electron. **31**, 1193 (1995).

[133] C.-S. Chang and S. L. Chuang, "Modeling of strained quantum-well lasers with spin-orbit coupling," IEEE J. Sel. Top. Quant. Electron. **1**, 218 (1995).

[134] A. F. Phillips, S. J. Sweeney, A. R. Adams, and P. J. A. Thijs, “The temperature dependence of 1.3 and 1.5 μm compressively strained InGaAs(P) MQW semiconductor lasers,” IEEE J. Sel. Top. Quant. Electron. **5**, 401 (1999).

[135] C. W. Snyder, B. G. Orr, D. Kessler, and L. M. Sander, “Effect of strain on surface morphology in highly strained InGaAs films,” Phys. Rev. Lett. **66**, 3032 (1991).

[136] Y. Arakawa and H. Sakaki, “Multidimensional quantum well laser and temperature dependence of its threshold current,” Applied Physics Letters **40**, 939 (1982).

[137] S. J. Sweeney, R. Fehse, A. R. Adams, and H. Riechert, “Intrinsic temperature sensitivities of 1.3 μm GaInNAs/GaAs, InGaAsP/InP and AlGaInAs/InP-based semiconductor lasers,” in proceedings of the 16th annual meeting of the IEEE Lasers and Electro-Optics Society (2003).

[138] O. Schmidt, “Lateral Alignment of Epitaxial Quantum Dots”, NanoScience and Technology (Springer Berlin Heidelberg, 2007), ISBN 9783540469360.

[139] A. Gocalinska, M. Manganaro, E. Pelucchi, and D. D. Vvedensky, “Surface organization of homoepitaxial InP films grown by metalorganic vapor-phase epitaxy,” Phys. Rev. B **86**, 165307 (2012).

[140] A. T. Meney, D. Prins, A. F. Phillips, J. L. Sly, E. P. O’Reilly, D. J. Dunstan, A. R. Adams, and A. Valster, “Determination of the band structure of disordered AlGaInP and its influence on visible-laser characteristics,” IEEE Journal of Selected Topics in Quantum Electronics **1**, 697 (1995).

[141] Z. Ma, T. Holden, Z. M. Wang, G. J. Salamo, L. Malikova, and S. S. Mao, “Strain-induced electronic energy changes in multilayered InGaAs/GaAs quantum wire structures,” Journal of Applied Physics **101**, 044305 (2007).

[142] S. A. Wood, P. M. Smowton, C. H. Molloy, P. Blood, D. J. Somerford, and C. C. Button, “Direct monitoring of thermally activated leakage current in AlGaInP laser diodes,” Applied Physics Letters **74**, 2540 (1999).

[143] A. Pescaglini, A. Gocalinska, S. Bogusevschi, S. T. Moroni, G. Juska, E. E. Mura, J. Justice, B. Corbett, E. P. O’Reilly, and E. Pelucchi, “Three-Dimensional Self-Assembled Columnar Arrays of AlInP Quantum Wires for Polarized Micrometer-Sized Amber Light Emitting Diodes,” ACS Photonics (published January 2018).

[144] S.-H. Wei and A. Zunger, “Fingerprints of CuPt ordering in III-V semiconductor alloys: Valence-band splittings, band-gap reduction, and x-ray structure factors,” Phys. Rev. B **57**, 8983 (1998).

[145] E. M. Daly, T. J. Glynn, J. D. Lambkin, L. Considine, and S. Walsh, “Behavior of $In_{0.48}Ga_{0.52}P/(Al_{0.2}Ga_{0.8})_{0.52}In_{0.48}P$ quantum-well luminescence as a function of temperature,” Phys. Rev. B **52**, 4696 (1995).

[146] J. D. Lambkin, D. J. Dunstan, K. P. Homewood, L. K. Howard, and M. T. Emeny, “Thermal quehching of the photoluminescence of InGaAs/GaAs and InGaAs/AlGaAs strained-layer quantum wells,” Applied Physics Letters **57**, 1986 (1990).

[147] H. Masui, N. N. Fellows, S. Nakamura, and S. P. DenBaars, “Optical polarization characteristics of light emission from sidewalls of primary-color light-emitting diodes,” Semiconductor Science and Technology **23**, 072001 (2008).

[148] H. Masui, H. Yamada, K. Iso, S. Nakamura, and S. P. DenBaars, “Optical polarization characteristics of m -oriented InGaN/GaN light-emitting diodes with various indium compositions in single-quantum-well structure,” Journal of Physics D: Applied Physics **41**, 225104 (2008).

[149] S. R. Jin, C. N. Ahmad, S. J. Sweeney, A. R. Adams, B. N. Murdin, H. Page, X. Marcadet, C. Sirtori, and S. Tomic, “Spectroscopy of GaAs/AlGaAs quantum-cascade lasers using hydrostatic pressure,” Applied Physics Letters **89**, 221105 (2006).

[150] M. D. Frogley, J. R. Downes, and D. J. Dunstan, “Theory of the anomalously low bandgap pressure coefficients in strained-layer semiconductor alloys,” Phys. Rev. B **62**, 13612 (2000).

[151] R. Willardson, E. Weber, T. Suski, and W. Paul, “High Pressure in Semiconductor Physics II”, Semiconductors and Semimetals (Elsevier Science, 1998), ISBN 9780080864532.

[152] D. A. Beaton, T. Christian, K. Alberi, A. Mascarenhas, K. Mukherjee, and E. A. Fitzgerald, “Determination of the direct to indirect bandgap transition composition in $Al_xIn_{1-x}P$,” Journal of Applied Physics **114**, 203504 (2013).

[153] A. Onton and R. J. Chicotka, “Conduction Bands in $In_{1-x}Al_xP$,” Journal of Applied Physics **41**, 4205 (1970).

[154] P. Merle, D. Auvergne, H. Mathieu, and J. Chevallier, “Conduction band structure of GaInP,” Phys. Rev. B **15**, 2032 (1977).

[155] B. W. Hakki, A. Jayaraman, and C. K. Kim, “Band Structure of InGaP from Pressure Experiments,” Journal of Applied Physics **41**, 5291 (1970).

[156] H. Lange, J. Donecker, and H. Friedrich, “Electroreflectance and Wavelength Modulation Study of the Direct and Indirect Fundamental Transition Region of $In_{1-x}Ga_xP$,” physica status solidi (b) **73**, 633 (1976).

[157] C. J. Nuese, A. G. Sigai, and J. J. Gannon, "Orange Laser Emission and Bright Electroluminescence from $\mathrm{In}_{1-x}\mathrm{Ga}_x\mathrm{P}$ Vapor-Grown p-n junctions," Applied Physics Letters **20**, 431 (1972).

[158] J. Konttinen and V.-M. Korpijärvi, "Frequency-converted dilute nitride laser diodes for mobile display applications," Nanoscale Research Letters **9**, 82 (2014).

[159] A. Härkönen, J. Rautiainen, M. Guina, J. Konttinen, P. Tuomisto, L. Orsila, M. Pessa, and O. G. Okhotnikov, "High power frequency doubled GaInNAs semiconductor disk laser emitting at 615 nm," Opt. Express **15**, 3224 (2007).

[160] T. Takizawa, "Wavelength Modulated Reflectivities of the Direct Exciton Edge in GaP," Journal of the Physical Society of Japan **52**, 1057 (1983).

[161] L. Pavesi, F. Piazza, A. Rudra, J. F. Carlin, and M. Ilegems, "Temperature dependence of the InP band gap from a photoluminescence study," Phys. Rev. B **44**, 9052 (1991).

[162] D. Bimberg, M. S. Skolnick, and L. M. Sander, "Properties of the electron-hole liquid in GaP," Phys. Rev. B **19**, 2231 (1979).

[163] D. Auvergne, P. Merle, and H. Mathieu, "Phonon-assisted transitions in gallium-phosphide modulation spectra," Phys. Rev. B **12**, 1371 (1975).

[164] P. J. Dean, G. Kaminsky, and R. B. Zetterstrom, "Intrinsic Optical Absorption of Gallium Phosphide between 2.33 and 3.12 eV," Journal of Applied Physics **38**, 3551 (1967).

[165] R. Zallen and W. Paul, "Band Structure of Gallium Phosphide from Optical Experiments at High Pressure," Phys. Rev. **134**, A1628 (1964).

[166] D. J. Mowbray, O. P. Kowalski, M. Hopkinson, M. S. Skolnick, and J. P. R. David, "Electronic band structure of AlGaInP grown by solid-source molecular-beam epitaxy," Applied Physics Letters **65**, 213 (1994).

[167] X. H. Zhang, S. J. Chua, and W. J. Fan, "Band offsets at GaInP/AlGaInP (001) heterostructures lattice matched to GaAs," Applied Physics Letters **73**, 1098 (1998).

[168] O. P. Kowalski, J. W. Cockburn, D. J. Mowbray, M. S. Skolnick, R. Teissier, and M. Hopkinson, "GaInP–AlGaInP band offsets determined from hydrostatic pressure measurements," Applied Physics Letters **66**, 619 (1995).

[169] C. T. H. F. Liedenbaum, A. Valster, A. L. G. J. Severens, and G. W. 't Hooft, "Determination of the GaInP/AlGaInP band offset," Applied Physics Letters **57**, 2698 (1990).

[170] S.-H. Wei and A. Zunger, "Predicted band-gap pressure coefficients of all diamond and zinc-blende semiconductors: Chemical trends," Phys. Rev. B **60**, 5404 (1999).

[171] H. Mathieu, P. Merle, E. L. Ameziane, B. Archilla, J. Camassel, and G. Poiblaud, "Deformation potentials of the direct and indirect absorption edges of GaP," Phys. Rev. B **19**, 2209 (1979).

[172] H. Müller, R. Trommer, M. Cardona, and P. Vogl, "Pressure dependence of the direct absorption edge of InP," Phys. Rev. B **21**, 4879 (1980).

[173] C. S. Menoni and I. L. Spain, "Equation of state of InP to 19 GPa," Phys. Rev. B **35**, 7520 (1987).

[174] D. D. Nolte, W. Walukiewicz, and E. E. Haller, "Band-edge hydrostatic deformation potentials in III-V semiconductors," Phys. Rev. Lett. **59**, 501 (1987).

[175] J. Camassel, P. Merle, L. Bayo, and H. Mathieu, "Deformation potentials of the fundamental exciton spectrum of InP," Phys. Rev. B **22**, 2020 (1980).

[176] T. Kobayashi, K. Aoki, and K. Yamamoto, "Pressure dependence of optical absorption in InP at 77 K," Physica B+C **139**, 537 (1986).

[177] S. Ernst, A. R. Goñi, K. Syassen, and M. Cardona, "Plasmon Raman scattering and photoluminescence of heavily doped n-type InP near the Γ-X crossover," Phys. Rev. B **53**, 1287 (1996).

[178] S. Adachi, "Deformation Potentials" (John Wiley & Sons, Ltd, 2009), pp. 259–273.

[179] N. Vukmirović and S. Tomić, "Plane wave methodology for single quantum dot electronic structure calculations," Journal of Applied Physics **103**, 103718 (2008).